DEPARTMENT OF PHYSICS
UNIVERSITY OF CAPE TOWN
IYUNIVESITHI YASEKAPA • UNIVERSITEIT VAN KAAPSTAD

Towards measuring the Relative Biological Effectiveness of high-energy neutrons at iThemba LABS

Elizabeth Fairall

Dissertation presented for the degree of
Master of Science
Department of Physics
University of Cape Town

February 2025

Abstract

In space, neutrons with energies of up to several TeV are produced through the interactions of primary cosmic radiation with matter such as in spacecraft shielding, and in the atmospheres and regoliths of moons and planets. The development of radiation health-risk models for space exploration requires the quantification of the biological effects of neutrons, and in the current radiation protection framework this is achieved via measurements of the neutron Relative Biological Effectiveness (RBE). The current deficiency of experimental data regarding the biological effects of high-energy neutrons calls for dedicated RBE experiments at neutron energies greater than 20 MeV for the doses, dose rates, and biological endpoints that are relevant to space travel. This project aimed to identify key knowledge gaps and improve neutron radiation risk estimates by developing a standardised approach to measure the limiting maximum value of neutron RBE at low doses (RBE_M) at the iThemba Laboratories for Accelerator Based Sciences (LABS) high-energy neutron facility.

Data from a preparatory experiment conducted with neutrons produced by a 66.48 MeV proton beam irradiating an 8.0 mm lithium target are used to illustrate the metrological methods for the characterisation of the neutron beam energy distribution and fluence at the iThemba LABS high-energy neutron facility. The metrological characterisation was combined with Monte Carlo radiation transport simulations to establish the absorbed dose delivered to vials containing human peripheral blood mononuclear cells that were irradiated during the experiment. The dosimetry results were related to the corresponding observed yield of γ-H2AX foci in the irradiated samples, to obtain dose-response relationships with linear yield coefficients of 10.12 ± 0.63 Gy^{-1} and 7.45 ± 0.66 Gy^{-1} for irradiations with neutrons with fluence-weighted average energies of 40.11 ± 0.92 MeV and 37.26 ± 0.40 MeV respectively. The results of this analysis were used to make recommendations for future neutron RBE measurements at iThemba LABS at energies relevant to space travel. Such measurements require reliable neutron beam metrology and detailed computational simulations of the experimental setup for both the neutron and reference irradiations, along with appropriate radiobiological analyses.

Acknowledgments

This research is the culmination of many contributions for which I am deeply appreciative, and I would like to express my gratitude to all those from the University of Cape Town (UCT), the South African National Space Agency (SANSA), iThemba Laboratories for Accelerator Based Sciences (LABS), and the GSI Helmholtz Centre for Heavy Ion Research (GSI), who have played a crucial role in this project and supported my work over the past two years.

Thank you to my supervisors, Andy Buffler and Tanya Hutton (UCT), for supporting me both as a student and a person, for consistently guiding me to produce quality work that I am truly proud of, and for lending me your dogs on a regular basis.

Thank you to Evan de Kock (iThemba LABS), Rendani Nndanganeni (SANSA), and Charlot Vandevoorde (GSI) for generously sharing your knowledge and providing invaluable feedback throughout this project.

Thank you to everyone involved in the measurement campaign at iThemba LABS in June 2022 that enabled the collection of the experimental data presented in this thesis. Thank you to the beam operators at iThemba LABS as well as Kutullo Maibane, Sizwe Mhlongo, and Josiah De Klerk (UCT), for staying overnight. Thank you to Charlot Vandevoorde, Randall Fisher, Shankari Nair, Julie Bolcaen, and Monique Engelbrecht, from the iThemba LABS Radiation Biophysics division, for facilitating the radiobiology aspects of the experiment. Thank you to James Dickson and the team at the UCT Workshop for your assistance and contributions throughout the project. Thank you to the National Research Foundation of South Africa for the financial support.

Thank you to Zama Katamzi-Joseph (SANSA) and the organisers of the International Space Weather Camp 2023 for providing me with a meaningful introduction to space weather research, and to SANSA for funding my participation in this event.

Thank you to Charlot Vandevoorde and Marco Durante for hosting me in the Biophysics Department at GSI, and for the time you took to discuss my work and share your invaluable insights. Special thanks to Charlot Vandevoorde, Amèlia Jansen van Vuuren, Jeannette Jansen, and Jennifer Persigehl, from the GSI Space Radiobiology group, for your efforts to involve me in your research and make me feel so welcome. Thank you to the German Academic Exchange Service (DAAD) for funding my visit to GSI.

Thank you to SANSA for funding my MSc over the past two years, thereby enabling me to fully focus on my work and proudly contribute to South Africa's involvement in space research.

Thank you to the wonderful people of the UCT Physics Department for the many happy tea-time conversations, and to my family and friends for everything else that matters.

Contents

1 Introduction

Radiation exposure in space is recognised as the primary health risk for astronauts on long-duration missions that will venture beyond Earth's protective magnetosphere [Chancellor et al., 2014]. Shielding astronauts from the harmful effects of cosmic radiation (originating from the Sun and from outside of our solar system) is challenging due to the high energies of the primary charged particles and the cascade of secondary radiation that is produced as they interact with atoms of the shielding material [Dobynde et al., 2021]. No space agency has yet issued specific recommendations for radiation protection limits in beyond Lower Earth Orbit (LEO) missions [Walsh et al., 2019], and with impending plans for deep space missions and long-term stays on the Moon and on Mars, the development of a comprehensive international space radiation protection strategy is essential. The largest source of uncertainty in current risk projection models is attributed to insufficient knowledge about the biological effects of space radiation [Fogtman et al., 2023] and the National Aeronautics and Space Administration (NASA) has identified carcinogenesis, degenerative tissue effects, central nervous system decrements, and acute radiation syndrome as the highest research priorities [Cucinotta and Durante, 2013a,b; Wu et al., 2013; Huff and Cucinotta, 2013].

The complexity of the space radiation environment makes it necessary to investigate the biological impact of the individual components of the radiation field. Of particular concern is the threat to astronaut health that is posed by neutrons due to their high penetration power and potential to induce severe biological damage [Horst et al., 2022b]. Neutrons in space are produced as secondary radiation via the interactions of primary cosmic radiation with matter, such as that in spacecraft shielding, and in the atmospheres and regoliths of moons and planets. The latest Radiation Assessment Detector (RAD) measurements of neutrons on the surface of Mars with energies in the range of 7 MeV to 740 MeV, as shown in Figure 1.1, represent the highest energy neutrons that have been measured in space to date [Guo et al., 2017]. While experimental data are limited, neutrons with a wide range of energies extending up to several TeV are expected to contribute significantly to the radiation exposure of astronauts on future deep space missions [Stricklin et al., 2021].

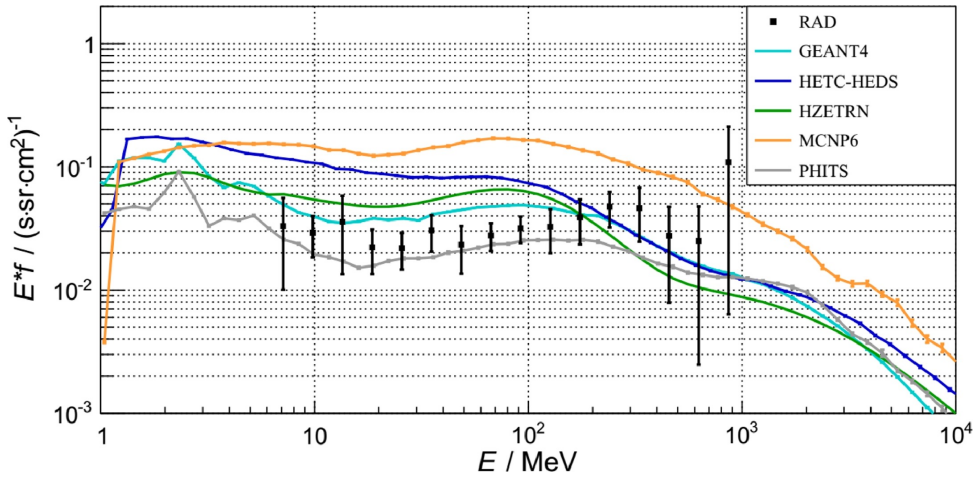

Figure 1.1: RAD measurements of neutron spectra on the surface of Mars compared to the results from various computational models [Matthiä et al., 2017].

Research on the biological effects of neutrons requires an in-depth understanding of both the physics of neutron interactions with matter and the key factors that impact the corresponding biological outcome. The damaging effects of neutrons are typically quantified via the neutron Relative Biological Effectiveness (RBE), defined as the ratio of the absorbed dose of a reference radiation to the absorbed dose of neutron radiation producing the same level of biological effect [Valentin, 2003]. Experimentally determined values of RBE are utilised by the International Commission on Radiological Protection (ICRP) to inform the selection of weighting factors that relate absorbed dose from ionising radiation to the risk of harmful effects [Valentin, 2003]. However, measuring neutron RBE is complicated given that the result depends on a number of both physical and biological factors including energy, dose, dose rate, biological system, and biological endpoint [Stricklin et al., 2021]. The currently recommended neutron weighting factors are based on a conservative pooling together of RBE results from many different experiments where the influences of these variables are not consistently reported. The uncertainties associated with these generalised results are unacceptably high given the present need to develop comprehensive neutron radiation health-risk models for space exploration [Lund et al., 2020].

The particularly significant uncertainties associated with how RBE varies as a function of neutron energy are reflected in the different ranges of radiation weighting factors for stochastic effects (including cancer) that are recommended by regulatory bodies as shown in Figure 1.2. Below 20 MeV, these weighting factors are determined from a large pool of experimental data, while RBE experiments at higher energies are extremely limited with varying results [Nolte et al., 2006]. Neutrons with energies greater than 20 MeV comprise a significant fraction of the neutron energy spectrum in space [Stricklin et al., 2021], and the current state of experimental data therefore calls for dedicated neutron RBE experiments in this energy range in order to improve astronaut radiation health-risk models.

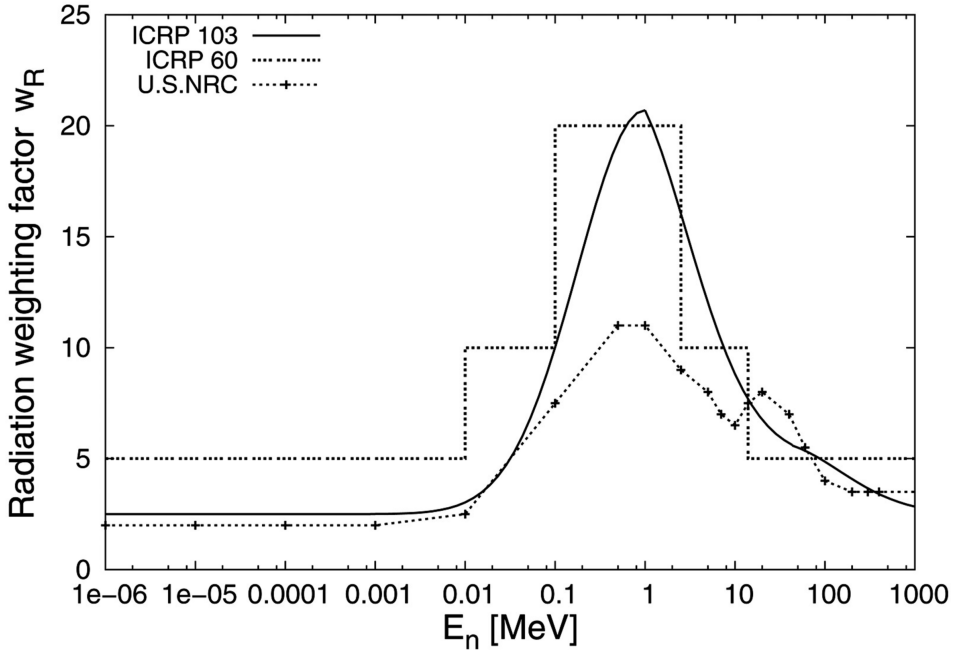

Figure 1.2: Neutron energy dependence of the radiation weighting factors for stochastic effects that are recommended by the ICRP and United States Nuclear Regulatory Commission (U.S. NRC) [Ottolenghi et al., 2015].

Beyond the context of space travel, the biological effects of high-energy neutrons are also relevant in the aviation industry and in proton therapy. At commercial aviation altitudes, the interactions of cosmic radiation particles in Earth's upper atmosphere results in the exposure

of air crew and passengers to cosmic neutrons with an energy spectrum similar to that expected in the space environment [Goldhagen et al., 2004]. During proton therapy, secondary neutrons with energies extending up to the energy of the incident protons (which typically have energies between 60 MeV and 330 MeV) are produced via proton interactions within the patient and surrounding environment, thus contributing to a whole-body dose received during treatment [Paganetti, 2018]. The results from high-energy neutron RBE experiments will therefore also contribute towards reducing the uncertainties associated with the biological impact of human exposure to neutrons within these scenarios.

The primary reason for the deficiency of experimental data for neutron RBE at energies greater than 20 MeV is the lack of experimental facilities where the relevant radiobiology experiments can be performed [Pomp et al., 2014]. The high-energy neutron facility at iThemba Laboratories for Accelerator Based Sciences (iThemba LABS) in Cape Town is one of the only facilities in the world capable of providing neutron beams with energies between 30 MeV and 200 MeV. The ns-pulsing of the beam (which enables Time-Of-Flight (TOF) measurements), combined with the available reference neutron detectors and well-established metrological techniques at this facility, allows for the characterisation of the neutron field in terms of both energy and intensity under conditions relevant to space travel. Although the radiation fields encountered within the presently considered neutron exposure scenarios will involve a complex mixture of particles, energies, and irradiation geometries, experiments with single-ion neutron beams are necessary to generate the biological datasets that are utilised in the selection of radiation weighting factors for health-risk assessment. The high-energy neutron facility at iThemba LABS therefore has the potential to be instrumental in providing a means of obtaining the required experimental data for neutron RBE within the context of future space travel, aviation, and proton therapy.

The objective of this project was to identify existing knowledge gaps and improve neutron radiation risk estimations by developing a standardised approach to measure the neutron maximum Relative Biological Effectiveness (RBE_M) at the iThemba LABS high-energy neutron facility for the assessment of carcinogenic effects at energies that are relevant to space travel.

To this end, the presented thesis comprises three main components:

1. A review of existing literature on the production and characteristics of high-energy neutrons in space, and the current understanding of their associated biological effects (Chapters 2 and 3);

2. An analysis of data obtained from an exploratory experiment at iThemba LABS focused on utilising the high-energy neutron facility to measure neutron RBE_M (Chapters 4, 5, and 6); and

3. Recommendations for future measurements of neutron RBE at iThemba LABS (Chapters 4, 5, and 6).

2 Scientific motivation

Experimentally determined values of RBE are used to inform the selection of the radiation weighting factors that form the basis upon which health risk models for certain exposure scenarios are developed. Assessments of the health risks associated with human exposure to high-energy neutrons are particularly relevant with regards to future space exploration, as well as within the contexts of air travel and proton therapy. This chapter presents an overview of existing literature on the production and characteristics of fast (0.1 MeV to 20 MeV) and high-energy (> 20 MeV) neutrons in each of these scenarios, with a particular emphasis on the current state of knowledge pertaining to high-energy neutrons in space.

It should be noted that this chapter refers to a number of different studies relating to the biological effects of ionising radiation, the results of which are often quoted in terms of various dose quantities including *absorbed dose*, *ambient dose equivalent*, *dose equivalent*, *effective dose*, and *equivalent dose*. These quantities have distinct definitions, as defined by the ICRP, that can be found in ICRP Publication 147 [Clement et al., 2021].

2.1 High-energy neutrons in space

High-energy neutrons in space are produced via the interactions of the charged particles of the primary cosmic radiation environment with matter, such as that in spacecraft shielding, the bodies of astronauts, or in the atmospheres and regoliths of moons and planets. The result is that neutrons with a wide range of energies extending up to several TeV are present in the space radiation environment to which astronauts will be exposed. This section provides a brief description of the primary radiation environment in space (Section 2.1.1), and a summary of our current state of knowledge surrounding the production of high-energy neutrons in Earth's atmosphere (Section 2.1.2), in spacecraft shielding material (Section 2.1.3), in LEO (Section 2.1.4), on the Moon (Section 2.1.5), and on Mars (Section 2.1.6).

2.1.1 The primary radiation environment in space

The primary radiation environment in space involves a complex mixture of cosmic radiation particles with a broad range of energies extending up to several TeV. These particles originate from both the Sun and outside of the solar system, and interact by various mechanisms to determine the space weather conditions at any given time and location in the heliosphere. With regards to astronaut radiation protection, the relevant components of the space radiation environment, referred to collectively as cosmic radiation throughout this thesis, are galactic cosmic radiation (GCR) and solar energetic particles (SEPs), which result in astronaut exposure to chronic and acute doses of ionising radiation respectively [Dietze et al., 2013].

The particles of GCR originate in a variety of high-energy cosmic processes that occur outside of our solar system. Pinpointing the exact origin of these particles is difficult as information about their initial location is scrambled by various magnetic fields and interactions within the interstellar medium, however it is believed that they most likely come from high-energy events such as supernova explosions and neutron stars, both inside and outside of the Milky Way Galaxy [Dietze et al., 2013; Norbury et al., 2019; Papadopoulos et al., 2023]. The result is a continuous flux of a complex mixture of particles with a broad range of energies that enter our solar system from all directions. A multitude of measurements by detectors on balloon flights

at high altitudes, in satellites, and in the International Space Station (ISS), have been used to derive information about the composition and energy spectrum of GCR [Norbury et al., 2019]. From these measurements, it has been determined that GCR is comprised of both an electron component (2%) and a baryonic component (98%). The latter is made up of $\sim$ 85% protons, $\sim$ 14% alpha particles, and $\sim$ 1% energetic, heavier ions ranging from lithium to uranium [Dietze et al., 2013]. The energy spectra of GCR are broad and vary, but tend to peak around 1 GeV/amu and extend beyond $\sim$ TeV/amu [Papadopoulos et al., 2023].

The fluence rate and particle energy distributions of GCR inside the inner heliosphere are primarily modulated by the solar wind, a magnetised plasma consisting mostly of protons, helium nuclei and electrons that are continuously emitted by the Sun and move through interplanetary space at speeds ranging between $\sim$ 300 km/s and 800 km/s [Moldwin, 2022; Dietze et al., 2013]. The intensity of the solar wind is dependent on solar magnetic activity which varies periodically according to the 11-year solar cycle with periods of high and low activity (referred to as solar maximum and solar minimum respectively). While the energies of the solar wind particles are not high enough to pose concern regarding astronaut radiation exposure, these charged particles create a magnetic field with which GCR entering our solar system interacts [Dietze et al., 2013]. The temporal variation of the solar wind (and thus the strength and structure of the interplanetary magnetic field) with the solar cycle is the main factor influencing the GCR environment in the inner heliosphere. Solar activity and GCR rates are anti-correlated such that GCR intensity is highest during solar minimum and lowest during solar maximum [Berger et al., 2020]. Figure 2.1 demonstrates the modulation of the relative fluence rate of GCR with time in the solar cycle, as measured over 50 years by a ground-based neutron monitor. Figure 2.2 shows how the energy distributions of radiance versus particle energy for four GCR particles are affected by solar activity at solar minimum and solar maximum.

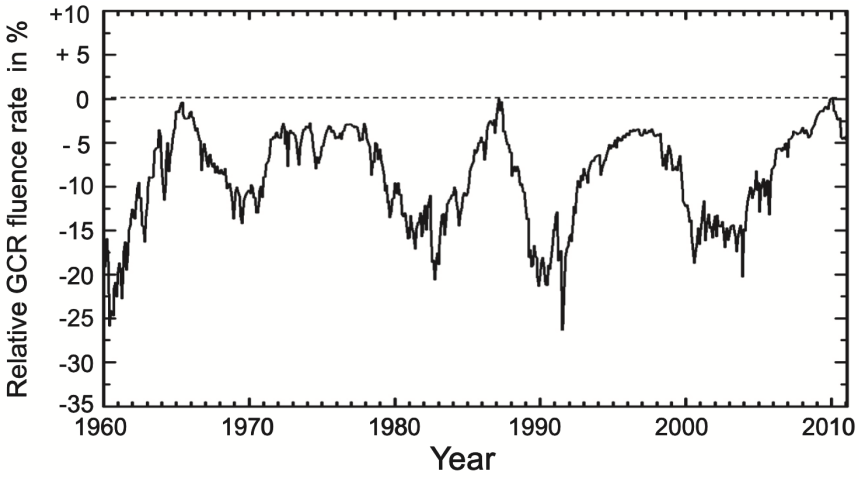

Figure 2.1: Modulation of the relative fluence rate of GCR with time in the solar cycle, as measured over several years by a ground-based neutron monitor in Kiel [Dietze et al., 2013].

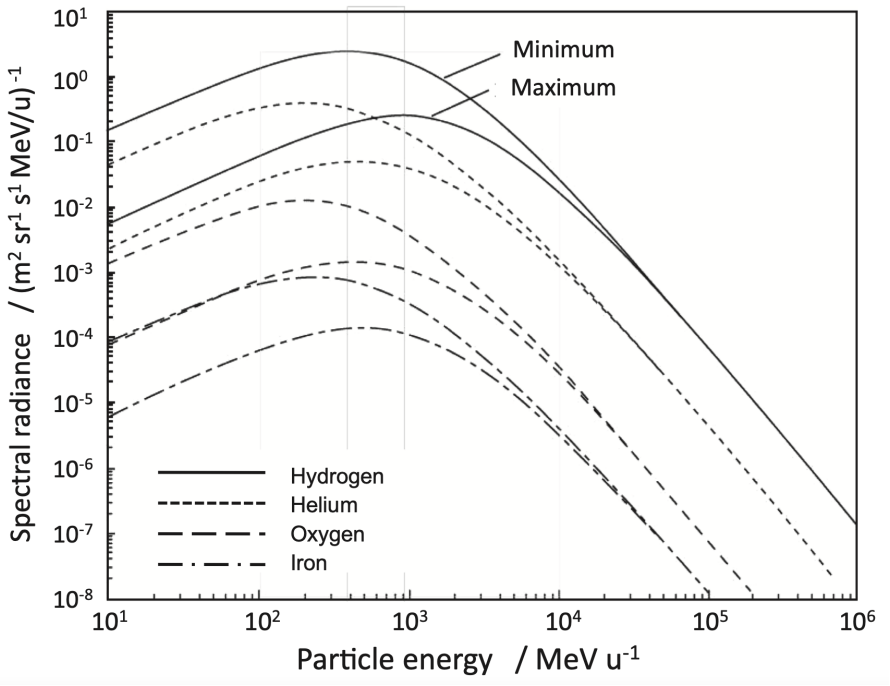

Figure 2.2: Modification of the radiance of four GCR particles with solar activity for solar minimum (1977) and solar maximum (1959) [Badhwar, 1997].

In addition to the continuous solar wind, the Sun also emits sporadic large bursts of charged particles, known as SEPs, with energies of up to several GeV, that are accelerated in association with solar particle events (SPEs), including solar flares and coronal mass ejections (CMEs) [Von Rosenvinge and Cane, 2006], and move along the interplanetary magnetic field lines in the heliosphere. Solar flares originate in localised "active regions" on the Sun's surface where the twisting of the surface magnetic field leads to a rapid energy release that accelerates solar atmospheric particles into space [Moldwin, 2022]. On the other hand, CMEs occur when large-scale reconfigurations of the Sun's magnetic field results in the expulsion of coronal material into space [Moldwin, 2022]. Fast CMEs that move away from the Sun at speeds faster than that of the solar wind can drive interplanetary shock waves that accelerate SEPs to energies of up to several GeV/amu, and are one of the most pertinent space weather phenomena regarding acute radiation effects in astronauts [Dietze et al., 2013]. Occurrences of CMEs are also often associated with temporary and rapid decreases in the intensity of GCR in the heliosphere, known as 'Forbush decreases' [Guo et al., 2018].

Although highly variable, SEPs consist mainly of protons and electrons with differing contributions from helium and heavier ions [Dietze et al., 2013; Norbury et al., 2019]. The energy distributions and fluence rates of SEPs vary tremendously, as illustrated in Figure 2.3, and are difficult to model and predict due to incomplete knowledge of the dynamics of the active regions of the Sun [Dobynde and Guo, 2021]. Although the frequency of SPEs is proportional to the solar activity and thus varies according to the solar cycle, the phase of the solar cycle does not dictate the intensity of SPEs and some of the largest SPEs ever recorded have occurred during times of solar minima [Chancellor et al., 2014]. These events are difficult to predict and may last from hours to days [Straube et al., 2010].

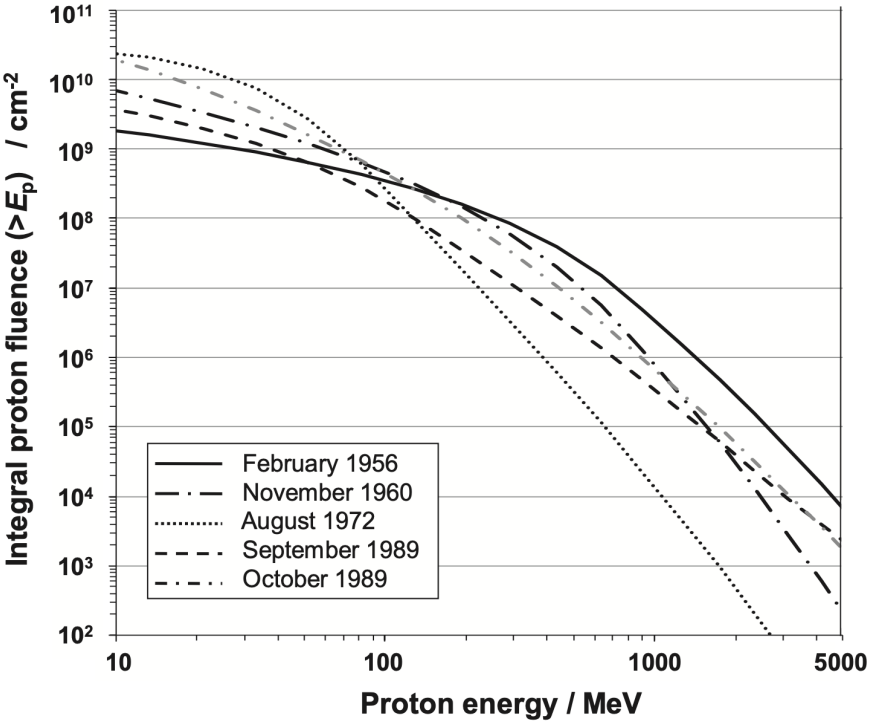

Figure 2.3: Integral fluence spectra of protons from various historical SPEs [Kim et al., 2010].

When planning for future space missions, the complexity of the primary radiation environment in space makes it necessary to assess the individual components of the ionising radiation field and their interactions that collectively influence the intensity, composition, and energy of the field at a given location over the differing temporal scales of relevant space weather events. The key characteristics of the GCR and SEPs that are relevant to astronaut radiation exposure in space are summarised in Table 2.1.

	Galactic cosmic radiation (GCR)	Solar energetic particles (SEPs)
Origin	Various high-energy events occurring outside of our solar system	Solar particle events (SPEs) including solar flares and coronal mass ejections (CMEs)
Composition	2% electrons, 98% baryons (including $\sim$ 85% protons, 14% alpha particles, and 1% heavier ions ranging from lithium to uranium)	Mostly protons and electrons with varying contribution from helium and heavier ions
Energies	Up to $\sim$ TeV/amu	Up to several GeV/amu
Duration	Continuous	Hours to days
Variation	Intensity is highest during solar minimum and lowest during solar maximum; can undergo sporadic 'Forbush decreases' in intensity that are typically associated with CMEs	Sporadic with a frequency that is highest during solar maximum and an intensity that is independent of the solar cycle
Radiation exposure	Chronic	Acute

Table 2.1: Key characteristics of SEPs and GCR relevant to astronaut radiation exposure in space.

2.1.2 Neutron production by cosmic radiation inside Earth's atmosphere

Much of our knowledge regarding neutron production in space stems from our knowledge of how neutrons are produced through cosmic radiation interactions in our own atmosphere. Although the solar system's and Earth's magnetic fields work to shield us from cosmic rays by deflecting GCR and SEPs, a fraction of these particles still reach and interact within Earth's atmosphere. The interactions of these high-energy particles with atmospheric atoms creates a complex shower of secondary particles, referred to as secondary cosmic radiation. The secondary cosmic radiation is comprised of three main components: an electromagnetic component (consisting of photons, electrons and positrons), a hadronic component (consisting of pions, protons, neutrons and heavier particles), and a muon component [Grieder, 2001]. An illustration of how these components develop in the Earth's atmosphere for an incident cosmic radiation proton is shown in Figure 2.4.

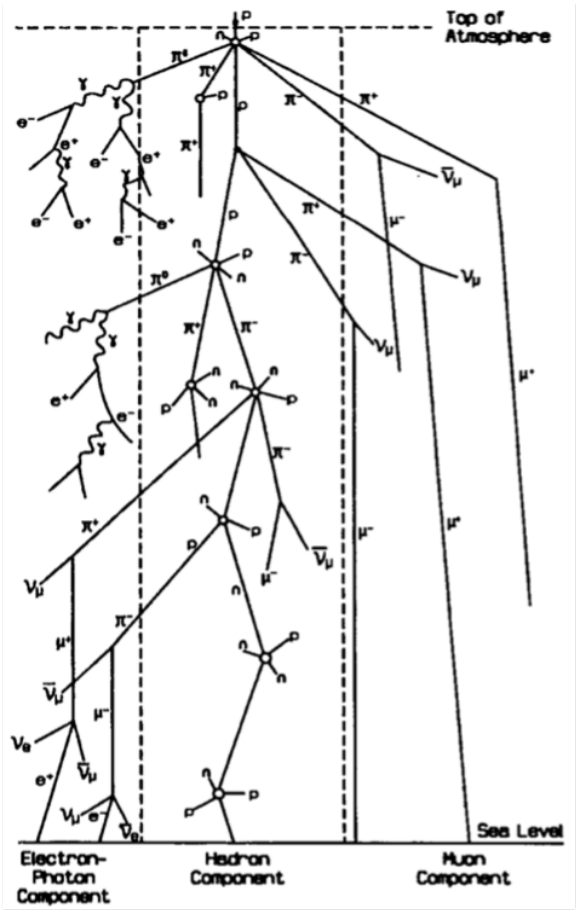

Figure 2.4: Schematic representation of the production of secondary cosmic radiation in Earth's atmosphere as a result of a primary cosmic radiation proton interacting with the nucleus of an atmospheric constituent at high altitude [Grieder, 2001].

The exact intensities and energy distributions of the secondary cosmic radiation particles are dependent on:

1. The solar cycle
   The dependence of GCR and SEPs on the solar cycle was discussed in Section 2.1.1.

2. Location in the geomagnetic field
   The number of primary cosmic radiation particles that enter Earth's atmosphere is dependent on geomagnetic latitude. Only high-energy particles can enter at equatorial latitudes where the magnetic field is strongest, while particles of all energies can enter at polar latitudes where the magnetic field is weakest [Buffler et al., 2016].

3. Altitude
   The intensity of primary particles decreases as they penetrate deeper into Earth's atmosphere and are lost through interactions that cause a build-up of secondary radiation. The result is that the fluence rate of secondary particles reaches a maximum at an altitude of about 20 km – known as the Regener-Pfotzer maximum – after which it decreases continuously due to the absorption of the primary particles [Buffler et al., 2016]. Figure 2.5 shows the results from the experiment where the Regener-Pfotzer maximum was first discovered.

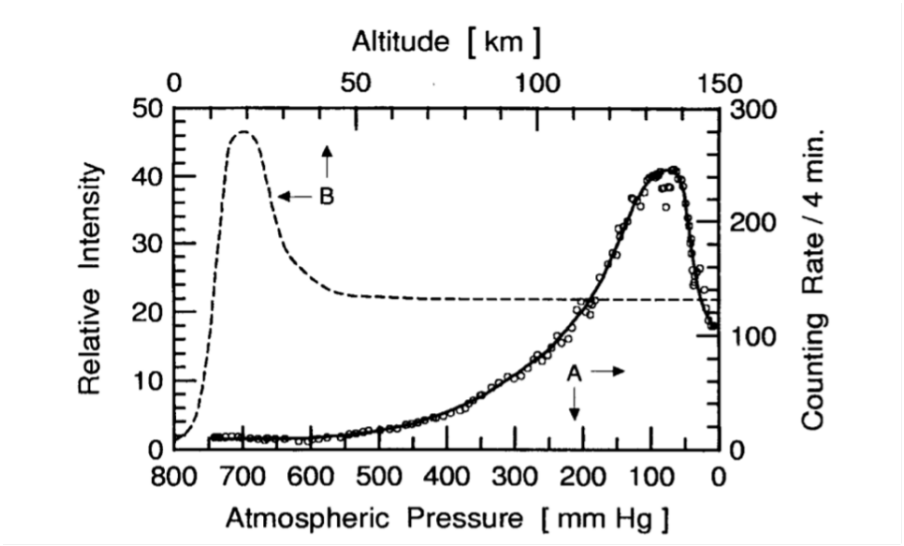

Figure 2.5: Average pressure dependence of the cosmic ray counting rate (curve A) and altitude dependence of the cosmic ray flux (curve B) demonstrating the position of the Regener-Pfotzer maximum [Grieder, 2001].

Figure 2.6 shows results from Bonner sphere measurements of the spectral fluence distributions of neutrons produced by cosmic radiation interacting in our atmosphere at different altitudes ranging from sea level to 20 km. From these results, it can be seen that the measured neutron fluence spectra in the Earth's atmosphere exhibit two distinct peaks. The large peak around 1 MeV is attributed to evaporation neutrons, that is, neutrons that are emitted during the de-excitation of a nucleus that has absorbed energy from an incident particle. These neutrons are emitted isotropically with energies that depend on the type of excited nuclei [Paganetti, 2018]. The broad peak around 100 MeV with a tail extending up to around 10 GeV is due to neutrons that originate as fragments of primary nuclei or in the spallation processes of atmospheric nuclei [Dietze et al., 2013; Matthiä et al., 2017].

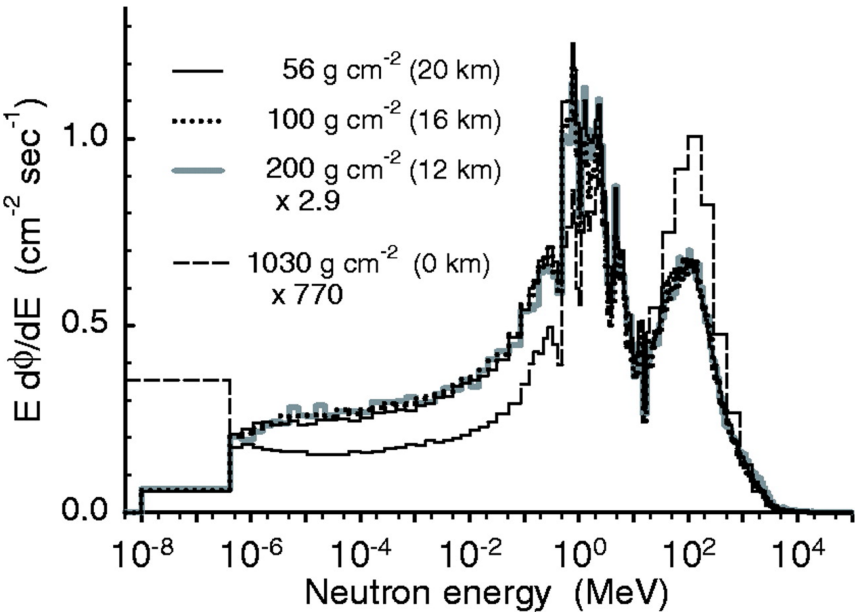

Figure 2.6: Bonner sphere measurements of the spectral fluence distributions of neutrons that are produced as secondary cosmic radiation at different altitudes in Earth's atmosphere [Goldhagen et al., 2004].

2.1.3 Neutron production by cosmic radiation in spacecraft shielding

In space, astronauts no longer benefit from the protection of Earth's atmosphere which serves to shield us from harmful cosmic radiation on Earth's surface. Furthermore, missions beyond LEO also lose the protection that is provided by Earth's magnetosphere in the deflection of many of the incoming charged particles.

The complexity of the radiation environment encountered inside spacecraft is extreme, and accurately predicting and modelling its nature presents one of the greatest challenges in the preparation for future space exploration. The radiation field inside a spacecraft is comprised of components of the primary space radiation field (as discussed in Section 2.1.1), as well as a secondary radiation field that is produced by interactions of the primary radiation with the spacecraft materials and with the bodies of astronauts. The nature of this secondary radiation field is highly variable, depending on a number of factors such as the ever-changing characteristics of the primary radiation field with time as well as the distribution and type of materials within the spacecraft [Dietze et al., 2013].

Shielding astronauts from the harmful effects of cosmic radiation is challenging due to the high energies of the charged particles and the cascade of secondary radiation that is produced as they interact with atoms of the shielding material [Dobynde et al., 2021]. There are two main classes of typical spacecraft materials [Horst et al., 2022b]: light hydrogenated materials (like water and polyethylene), which are generally considered better in terms of their shielding capabilities; and heavier materials lacking in hydrogen content (like aluminium), which are generally more readily available, and easy to manufacture.

Modern spacecraft shielding have thicknesses of 10 g/cm^2 to 40 g/cm^2 but can extend up to around 100 g/cm^2 depending on location in the spacecraft and the purpose of the mission [Horst et al., 2022b]. In the case of thicker shields, neutrons, which are negligible in the primary radiation environment, become a significant concern with regards to radiation exposure [Horst et al., 2022b]. There have been a number of studies conducted to investigate the nature of the neutron production as a result of cosmic radiation type particles interacting with typical spacecraft materials. Summaries of a few key results are outlined below.

Computational studies of neutron production by cosmic radiation in spacecraft shielding

Walker et al. [2013] conducted a computational study to compare contributions from different particles to the dose equivalent to different body organs in free space, in a variety of simple aluminium shielding geometries, and in specific locations inside aluminium models of the Space Shuttle (STS) and the ISS. The Badwahr-O'Neill model of the 1977 GCR solar minimum spectrum was used as the incident radiation environment. Their results for the blood forming organs are shown in Figure 2.7 where it can be seen for most of the ISS Liulin locations, the neutron contribution to the dose equivalent is greater than the sum of the dose from heavy ions. It was concluded that while heavy ions ($Z > 2$) contribute significantly ($\sim 50\%$ or more) to the organ dose equivalent behind thin shields, in the case of thicker shields (≥ 20 g/cm^2), up to $\sim 85\%$ or more of the dose equivalent comes from neutrons and light ions.

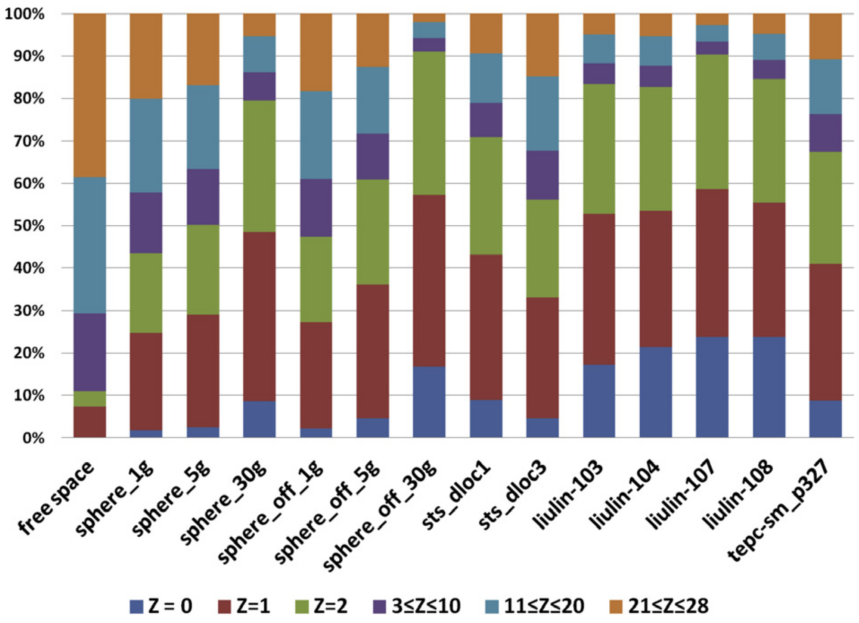

Figure 2.7: Calculated contribution to blood forming organ dose equivalent by different charged particles for free space, spherical geometries in free space, and different detector locations inside the STS and ISS in free space [Walker et al., 2013].

Slaba et al. [2017] performed a computational study to investigate the optimization of shielding designs on spacecraft and found that the GCR dose equivalent behind aluminium shielding goes through a minimum at a thickness of around 20 g/cm^2 to 30 g/cm^2 before increasing, indicating that increasing the thickness of the shielding beyond this point is actually counterproductive for astronaut radiation protection purposes. The occurrence of this minimum caused a significant shift in the space radiation shielding paradigm, where it had previously been assumed that increased shielding thickness would result in better shielding [Norbury et al., 2019]. The increase in dose equivalent at greater thicknesses is primarily attributed to the increase in the production of secondary neutrons, as confirmed by further investigations by [Dobynde et al., 2021], who used GEANT4 simulations to calculate the dependence of GCR effective dose in a spherical water phantom on the thickness of aluminium shielding at solar maximum and minimum conditions. Their results are shown in Figure 2.8 where a local minimum in the effective dose behind aluminium shielding is observed and it is shown that the existence of this minimum is due to the decreasing contribution of primary particles and increasing contribution from secondary particles with increasing shielding thickness. In particular, secondary neutrons provide the most significant contribution to the increasing effective dose at thicknesses greater than that at the position of the local minimum. No such minimum was found for polyethylene shielding, for which the dose equivalent decreases with increasing shielding thickness [Slaba et al., 2017].

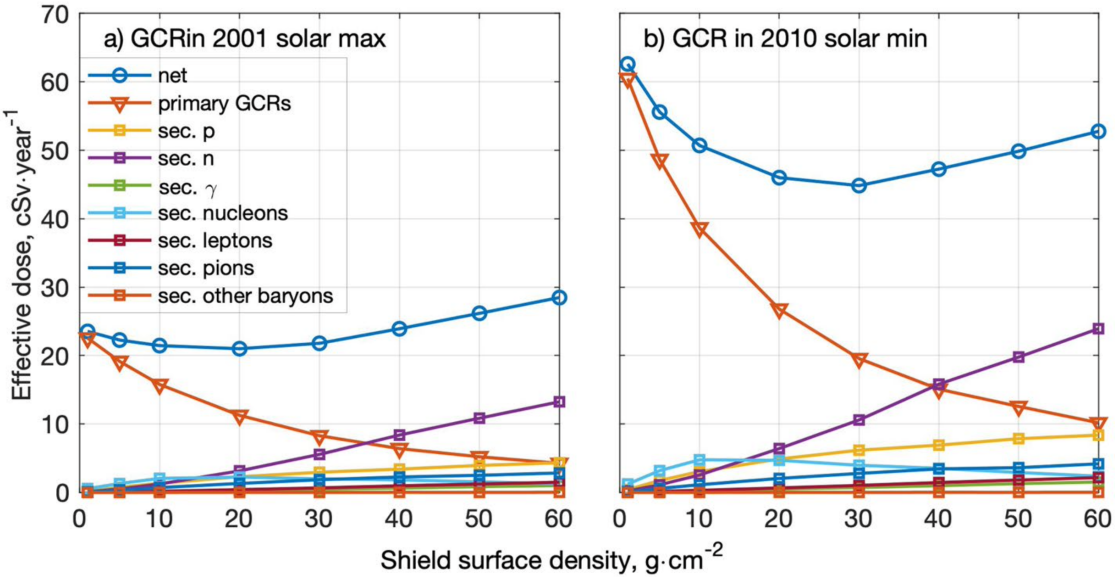

Figure 2.8: Effective dose from simulated GCR as a function of aluminium shielding thickness during the period of (a) the 2001 solar maximum and (b) the 2010 solar minimum [Dobynde et al., 2021].

Horst et al. [2022b] performed Monte Carlo simulations using the FLUKA code to study the production of secondary neutrons from GCR interactions in aluminium and polyethylene shields at solar maximum and minimum conditions. Their investigations built on the observations of Slaba et al. [2017] and Dobynde et al. [2021], but the thickness of the shielding was extended to 400 g/cm^2. Figure 2.9 shows their results for the dependence of the calculated relative dose at a 1 cm depth inside an International Commission on Radiation Units and Measurements (ICRU) sphere on the thicknesses of aluminium and polyethylene shields respectively. The significance of the neutron contribution to the absorbed dose build-up is highlighted via comparisons of the results with and without the inclusion of neutrons in the radiation field. Their results show that while introducing thicker aluminium shielding beyond 20 g/cm^2 is initially counter-productive, for sufficiently thick shielding (beyond around 200 g/cm^2), the contribution from secondary neutrons to the ambient dose equivalent does begin to decrease again as the primary charged particles are attenuated in the shielding material (this behaviour is analogous to the Regener-Pfotzer maximum of secondary cosmic radiation that is observed in Earth's atmosphere as discussed in Section 2.1.2).

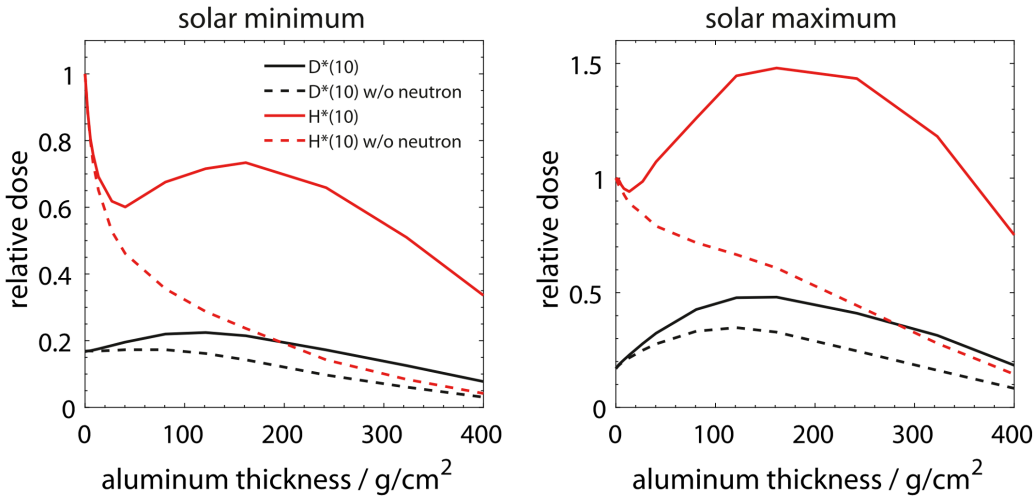

(a)

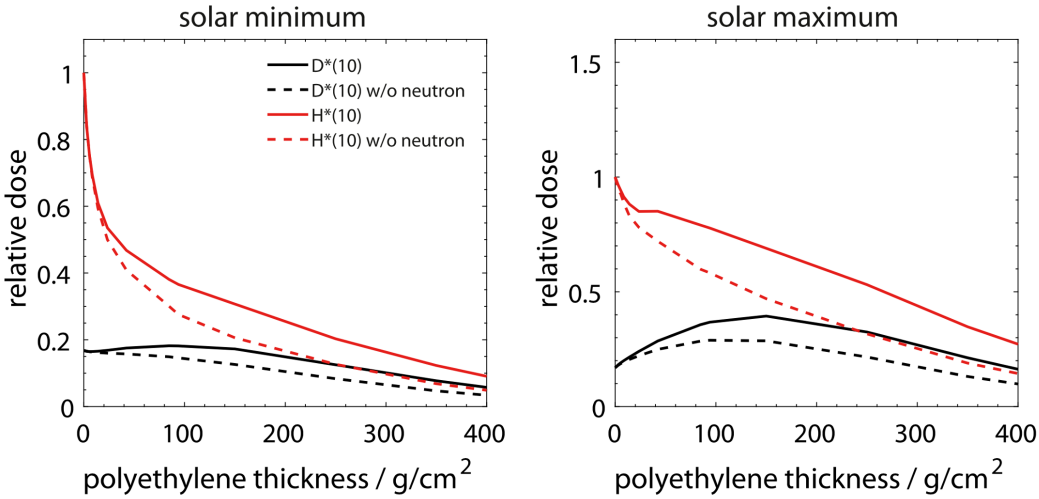

(b)

Figure 2.9: Absorbed dose $D^*(10)$ and ambient dose equivalent $H^*(10)$ as a function of (a) aluminium, and (b) polyethylene shielding thickness for simulated GCR solar minimum and maximum conditions [Horst et al., 2022b].

The reasons for the differences in the shielding properties of aluminium versus polyethylene spacecraft shielding have been illuminated by computational simulations of the energy spectra of the neutrons that are produced by GCR interacting in various thicknesses of these materials. The results from Heilbronn et al. [2015] for GCR interactions in 2.7 g/cm^2 of aluminium and water are shown in Figure 2.10. Their results indicate that in analogy with the interactions of cosmic radiation with atoms in Earth's atmosphere (as discussed in Section 2.1.2), the neutrons that are produced by proton and heavy ion interactions in shielding material usually occur in three distinct energy ranges extending from thermal energies up to several GeV: neutrons with thermal energies have generally been moderated by interactions with the shielding material; evaporation neutrons occur with energies in the range of nuclear binding energies (around 1 MeV to 10 MeV); and neutrons with energies extending up to the maximum incident particle energy are produced in knock-on or projectile fragmentation reactions [Köhler et al., 2015; Horst et al., 2022b]. The results from the study by Heilbronn et al. [2015] (which are consistent

over a range of thicknesses) indicate that a significant fraction of the neutron fluence and neutron effective dose behind typical spacecraft shielding materials comes from neutrons with energies extending up to several hundred MeV. For example, they calculated that for 13 g/cm^2 of shielding, neutrons with energies > 100 MeV contribute to $\sim 30\%$ and $\sim 50\%$ of the neutron effective dose behind aluminium and water shielding respectively.

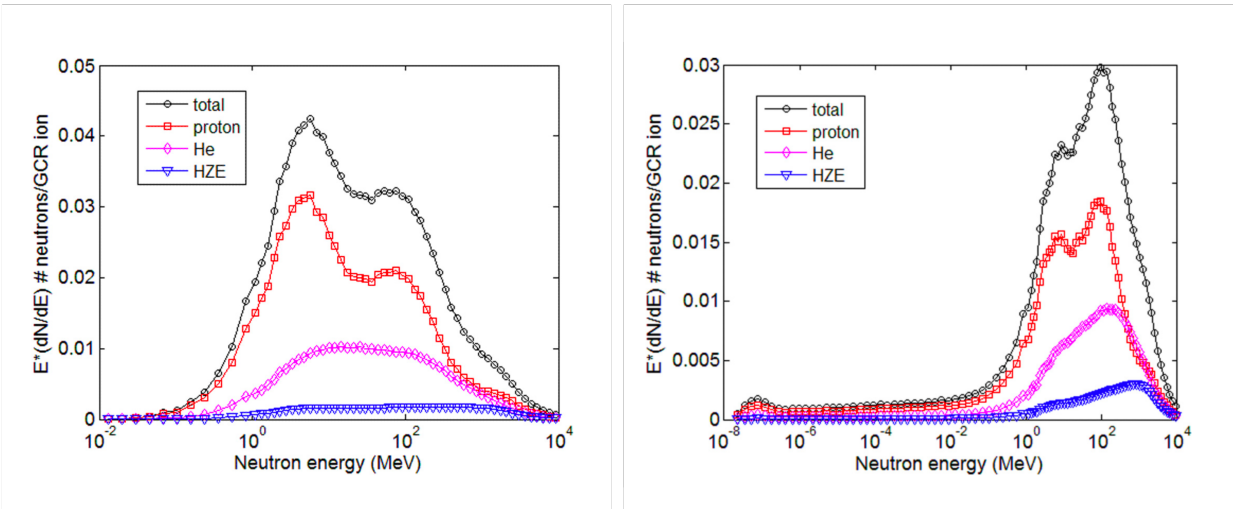

(a) **(b)**

Figure 2.10: Neutron lethargy spectra above 0.01 MeV from simulated GCR interactions in 2.7 g/cm^2 of (a) Al and (b) water, including contributions from protons, helium nuclei, and higher charge and energy particles [Heilbronn et al., 2015].

The results from further computational investigations of neutron energy spectra behind different thicknesses of aluminium and polyethylene shielding by Horst et al. [2022b], as shown in Figure 2.11, highlight that the differing shielding properties of aluminium and polyethylene are not only due to their different neutron production yields, but also due to their relative capabilities in moderating the neutrons produced:

- At 1 g/cm^2, while the total neutron yields are of the same order, a significantly larger proportion of the produced high-energy neutrons are moderated to thermal energies in polyethylene than is observed in aluminium;
- At 10 g/cm^2, the shape of the spectrum behind polyethylene is comparable to that observed at 1 g/cm^2, while an accumulation of neutrons around 1 MeV is observed behind aluminium; and
- At 100 g/cm^2, the neutron yield behind polyethylene is significantly lower than that behind aluminium and there is a noticeable accumulation of neutrons around 1 MeV behind the aluminium shielding (which also happens to be the region where neutrons have the highest biological effectiveness).

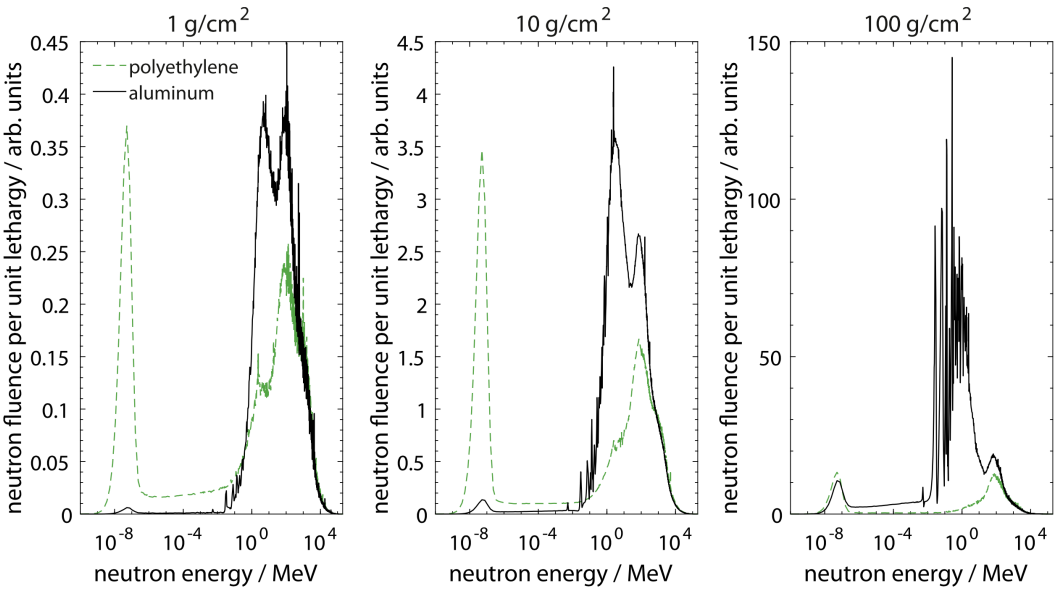

Figure 2.11: Neutron energy spectra incident on an ICRU sphere shielded with different thicknesses of aluminium and polyethylene for simulated GCR at solar maximum conditions [Horst et al., 2022b].

Experimental studies of neutron production by cosmic radiation in spacecraft shielding

There are very limited experimental data directly relating to the production of neutrons in typical spacecraft materials through the interactions of primary cosmic radiation. Köhler et al. [2015] used measurements from the Radiation Assessment Detector (RAD) to assess the neutral particle radiation environment inside the Mars Science Laboratory (MSL) spacecraft during its journey from Earth to Mars in 2011/2012. They calculated neutron spectra from the measurements by applying an inversion method, and the results are shown in Figure 2.12 along with results from GEANT4 simulations of GCR-aluminium and GCR-hydrazine interactions (note that the simulated GCR environment is an approximation that excluded particles with $Z > 2$, and the exact spacecraft geometry and materials were not included in the simulations). Using conversion values provided by the U.S. NRC, the measured neutron spectrum (in the range of 12 MeV to 436 MeV) was calculated to correspond to a neutron dose rate of 3.8 ± 1.2 μGy/d and a dose equivalent of 19 ± 5 μSv/d. Extrapolating the spectrum from 0.1 MeV to 1000 MeV resulted in a total neutron dose rate of 6 ± 2 μGy/d and a dose equivalent rate of 30 ± 10 μSv/d (which over a year would result in more than ten times the ICRP-recommended total annual dose limit for the general public of 1 mSv [Valentin, 2003]).

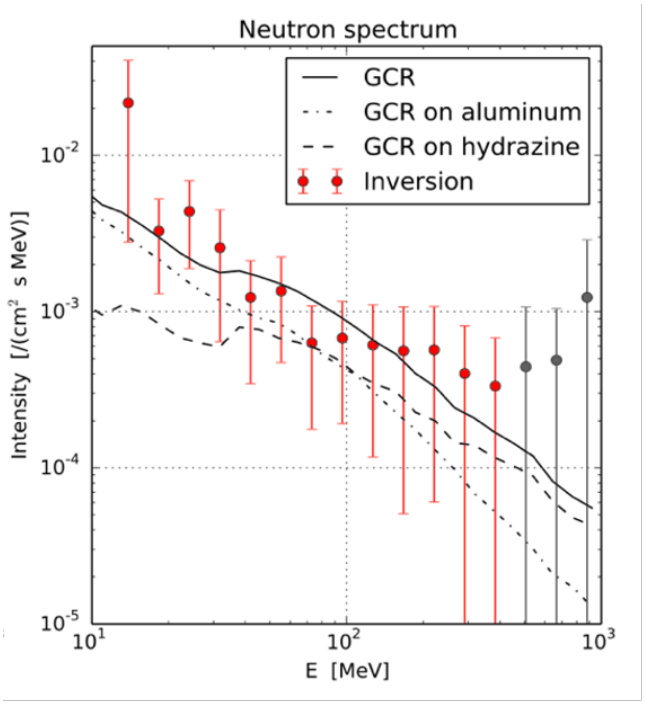

Figure 2.12: Neutron spectra measured by RAD inside the MSL during its journey from Earth to Mars in 2011/2012. The measurements are compared to the expected neutral particle spectra based on simulations of GCR interacting in aluminium and hydrazine shielding [Köhler et al., 2015].

Boscolo et al. [2020] conducted experiments at the GSI Helmholtz Centre for Heavy Ion Research (GSI) to investigate the neutron field that is produced by 1 GeV/u ^{56}Fe ions ("GCR-like radiation") fully stopping in a thick aluminium target. Their experimental setup and results for the neutron energy spectra at various positions relative to the incident beam are shown in Figure 2.13. Their results indicating the angular dependence of the produced neutron spectra provide nice illustrations on the mechanisms involved in the production of neutrons by GCR-like radiation in aluminium shielding. In the forward direction, the spectra are dominated by a peak at around 560 MeV, followed by a peak at around 1 MeV, and a peak at thermal energies. The high-energy peak is a result of neutrons produced in knock-on or projectile fragmentation reactions, and therefore has a strong forward directional dependence. At larger angles, this peak becomes less pronounced and vanishes completely in the backwards direction. Meanwhile the peaks due to largely isotropically emitted evaporation neutrons (at around 1 MeV) and thermalised neutrons that homogenously fill the experimental area, remain evident at all angles.

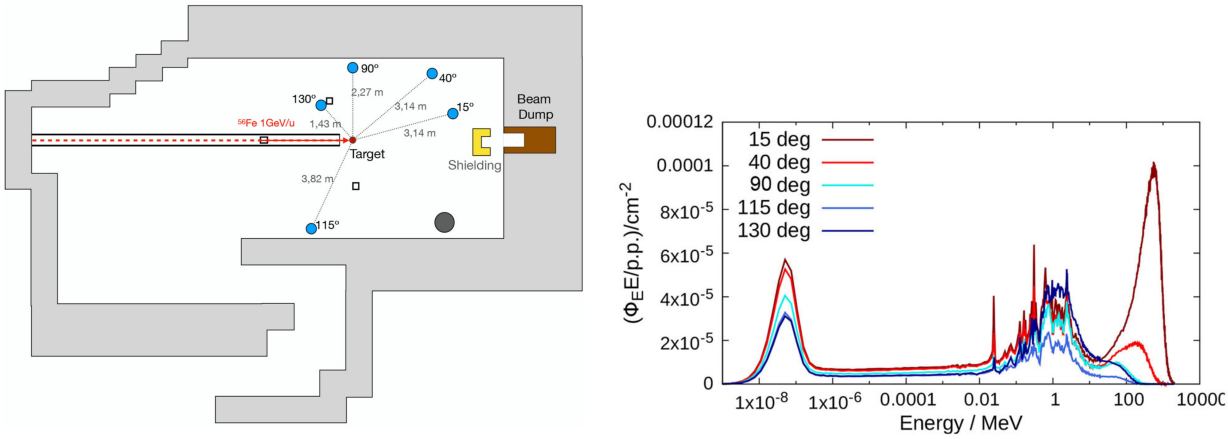

(a) (b)

Figure 2.13: (a) The experimental setup at GSI, and (b) the resulting measured neutron energy spectra at various positions relative to an incident 1 GeV/u ^{56}Fe ion beam fully stopping in a thick aluminium target [Boscolo et al., 2020].

2.1.4 Neutrons in Lower Earth Orbit (LEO)

The radiation environment in LEO (loosely defined as the region at altitudes between 300 km and 1600 km [Straube et al., 2010]) is comprised of four main components:

1. GCR and SEPs (attenuated by Earth's protection)
   In LEO, astronauts are protected from primary cosmic radiation by the geometric shielding of Earth (which blocks a significant fraction of the sky), as well as shielding by Earth's magnetic field (which deflects a fraction of GCR and all but the most energetic SEPs) [Norbury et al., 2019; Matthiä et al., 2023]. Owing to this shielding by Earth, the effective dose rate from cosmic radiation has been measured to be lower in LEO than in deep space by a factor of about two, although this is hugely dependent on the inclination and altitude of the orbit [Papadopoulos et al., 2023].

2. Particles of trapped radiation belts
   Another dominant contribution to the radiation environment in LEO comes from charged particles in the dynamic Van Allen radiation belts. These belts range from altitudes of $\sim$ 200 km to 75 000 km and contain electrons (with energies of up to 7 MeV), protons (with energies up to 700 MeV), and some heavier ions (with energies up to 50 MeV/u) [Dietze et al., 2013; Restier-Verlet et al., 2021]. The particles in these belts are a result of the interactions of cosmic radiation with the Earth's magnetic field and the atmosphere. Charged particles become trapped in the belts as they spiral along the lines of Earth's magnetic field and bounce back and forth between the magnetic poles. A complex variety of different processes work to produce the particles in the radiation belts, but there are two distinct regions:

   - The inner belt, at an altitude of $\sim$ 4000 km [Carroll and Ostlie, 2017], is comprised dominantly of energetic protons that mostly originate from the decay of albedo neutrons passing through this region [Dietze et al., 2013]. Due to the displacement of the geomagnetic dipole axes from Earth's centre, this belt extends down to an altitude of $\sim$ 200 km in a region located over South America and the Atlantic Ocean known as the South Atlantic Anomaly. Particles trapped in this belt therefore contribute significantly to radiation exposure in LEO for satellites (including the ISS) that cross this region [Dietze et al., 2013; Norbury et al., 2019; Matthiä et al., 2023].

- The outer belt, at an altitude of $\sim$ 16 000 km [Carroll and Ostlie, 2017], is composed dominantly of electrons that mostly originate from solar wind [Dietze et al., 2013; Matthiä et al., 2023].

3. Secondary particles generated in Earth's atmosphere
   As discussed in Section 2.1.2, cosmic ray interactions in Earth's upper atmosphere produce secondary particles, including neutrons with energy distributions corresponding to those shown in Figure 2.6. These neutrons can also escape into the exosphere and contribute to the radiation field in LEO, where they are known as albedo neutrons [Dietze et al., 2013].

4. Secondary particles generated in spacecraft shielding
   Secondary radiation is produced in spacecraft shielding in LEO by the interactions of cosmic radiation particles, particles trapped in the radiation belts, and albedo particles produced in Earth's atmosphere.

The nature of the space radiation environment in LEO is clearly complex and depends on the location, altitude, and solar activity. Neutrons encountered in spacecraft in LEO are produced by interactions of charged particles from cosmic radiation and trapped particles in Earth's radiation belts with the spacecraft material, or are albedo neutrons produced by interactions of cosmic radiation in the Earth's atmosphere.

Badhwar et al. [2001] presented a review of various neutron measurements that were made on Space Shuttle (STS) missions at different inclinations and altitudes in LEO. Instruments used included activation foils, track detectors, nuclear emulsions, passive (thermoluminescent) dosimeters, and Bonner spheres. For example, measurements with Bonner spheres and gold foils were made at solar maximum on STS-31 (April 1990) and STS-36 (Feb 1990) and corresponded to neutron dose equivalent rates ranging from 45 μSv/d to 345 μSv/d depending on the inclination (between 28.5° and 62.0°) and altitude (between 246 km and 617 km) of the flight [Keith et al., 1992]. However, the reported range of neutron energies from these measurements only extended up to 10 MeV and model calculations done by Badhwar et al. [2001] predicted that $\sim$ 50% of the neutron dose equivalent comes from neutrons with energies $>$ 10 MeV.

The ISS orbits the Earth at an average altitude of 400 km and an inclination of 51.6°, where the Earth's magnetic field is calculated to reduce total GCR exposure by a factor of ten relative to free space [Straube et al., 2010]. Armstrong and Colborn [2001] used Monte Carlo calculations to predict the secondary neutron spectrum inside the ISS over the energy range from 10^{-7} MeV to 10^{5} MeV as shown in Figure 2.14.

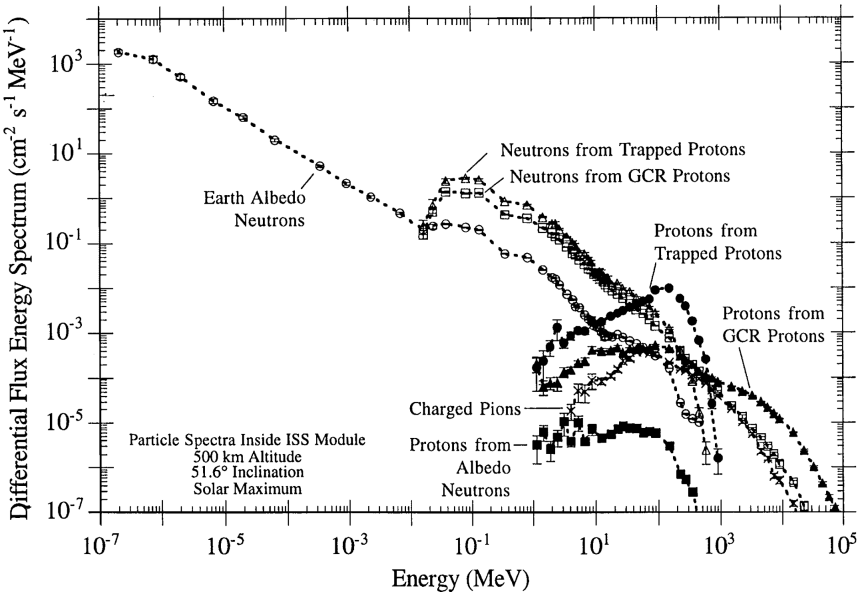

Figure 2.14: Simulated predicted secondary particle spectra inside ISS modules [Armstrong and Colborn, 2001].

Koshiishi et al. [2007] reported on the first active measurement of neutrons inside the ISS made using the Bonner Ball Neutron Detector (BBND), which is sensitive to neutrons with energies from thermal up to 15 MeV. Reported neutron dose equivalent rates were 69 μSv/d and 88 μSv/d for two different locations (as shown in Figure 2.15(b)), demonstrating a 30% difference that is just due to different localised shielding environments in the same pressurised module. The measured neutron spectra at the two locations are shown in Figure 2.15(a) and compared to the model prediction made by Armstrong and Colborn [2001]. It is noted that based on the models, neutrons with energies greater than 10 MeV extending up to several hundred MeV are expected to contribute to $\sim$ 50% of the total neutron dose equivalent, and therefore a characterisation of the neutron environment at these energies is still required.

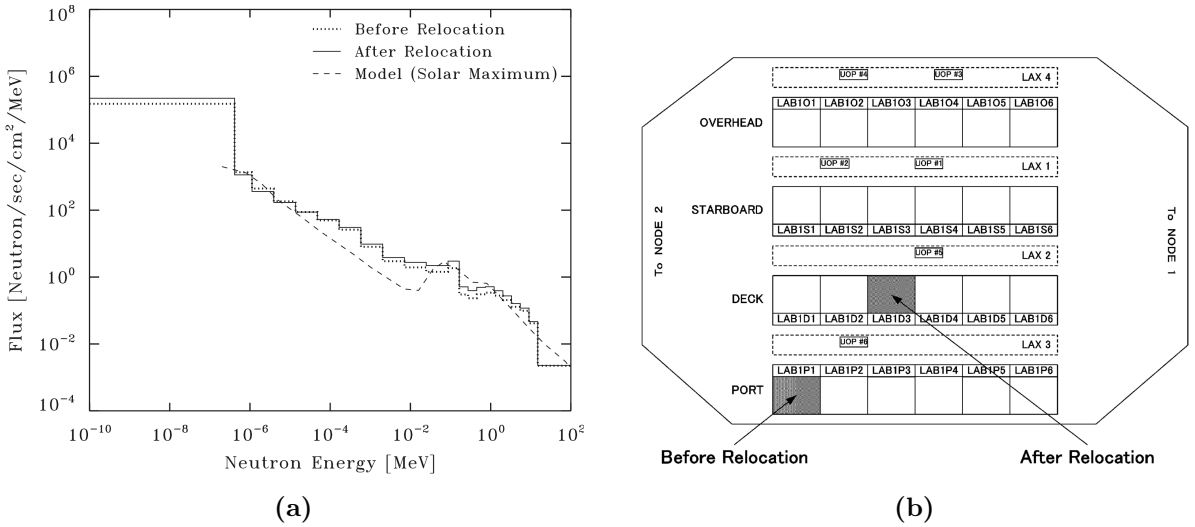

(a) **(b)**

Figure 2.15: (a) Comparison of the model predicted neutron spectrum (from Figure 2.14) with the the orbit-averaged neutron spectra measured inside the ISS US Laboratory Module with the BBND instrument at the locations indicated in (b) [Koshiishi et al., 2007].

Bubble detectors have also been used to determine neutron spectra and dose for higher neutron energies inside different ISS modules [Smith et al., 2013, 2016]. An example of an unfolded

energy spectrum is shown in Figure 2.16. Despite large uncertainties due to poor counting statistics, the measured data consistently suggest that $\sim 40\%$ of the neutron dose equivalent inside the ISS is due to neutrons with energies > 15 MeV (which is consistent with earlier predictions). More measurements on the ISS have been made at energies < 15 MeV, as a part of the "BTN-Neutron" project [Litvak et al., 2022; Li et al., 2023]. Zeitlin et al. [2023] recently reported the results of measurements of neutrons in the 0.2 MeV to 8 MeV energy range that were taken with the ISS-RAD between 2016 and 2022, which indicate that neutrons account for 29% to 43% of the total dose equivalent on the ISS depending on different shielding levels. These estimates are based on a combination of simulations and extrapolation from measurements at relatively low neutron energies (< 15 MeV), and the need for a detailed characterization of the higher energy neutron environment is repeatedly emphasized [Litvak et al., 2022; Li et al., 2023; Zeitlin et al., 2023].

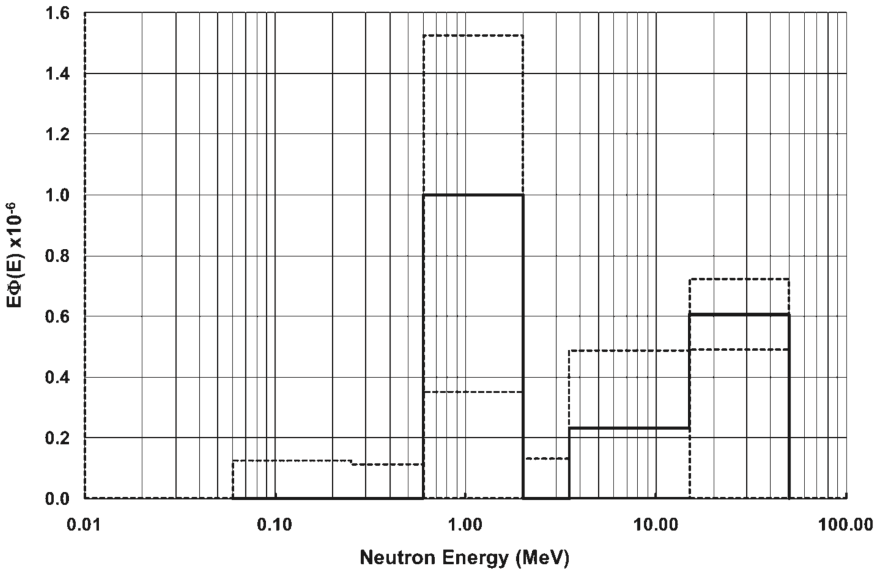

Figure 2.16: Unfolded neutron energy spectrum from the sum of five sessions on ISS-20 and ISS-21 as measured using bubble detectors [Smith et al., 2013].

2.1.5 Neutrons on the Moon

Human presence on the Moon has and will continue to play an influential part in space exploration. In contrast to the previous relatively brief Apollo missions, the plans for the future establishment of lunar bases will involve astronauts remaining on the Moon for extended periods of time. As with other space missions, exposure to the lunar radiation environment may be one of the key limiting factors in these plans [Miller et al., 2009]. Unlike Earth, the Moon does not possess an atmosphere or a magnetosphere and therefore the lunar surface is directly exposed to the primary cosmic radiation environment, as well as secondary radiation that is produced as a result of the energetic primary particles interacting in the lunar soil [Dobynde and Guo, 2021]. Among the 'backscattered', or 'albedo' particles that are produced, neutrons present particular concerns with regards to astronaut radiation exposure due to their relatively high biological effectiveness.

The Lunar Lander Neutron and Dosimetry (LND) instrument on-board Chang'E-4 recently made measurements of the radiation exposure to charged and neutral particles on the lunar surface [Zhang et al., 2020]. The results for the neutral particle dose rate recorded over two lunar days are presented in Figure 2.17. Although the individual contributions from neutrons and gamma rays were not separated, the 'dip' in the neutral particle dose rate that is ob-

served in Figure 2.17 corresponded to the activation of a liquid NH_3 thermal control system which modulates high-energy neutrons, suggesting that high-energy neutrons were a dominant component of the neutral particle doses that were measured. The measured average absorbed dose rate for neutral particles in silicon was 3.1 $\pm$ 0.5 μGy/hr, contributing 23 $\pm$ 8% to the total dose. The measured neutral particles included those produced in the shielding around the detector, as well those produced in the lunar regolith.

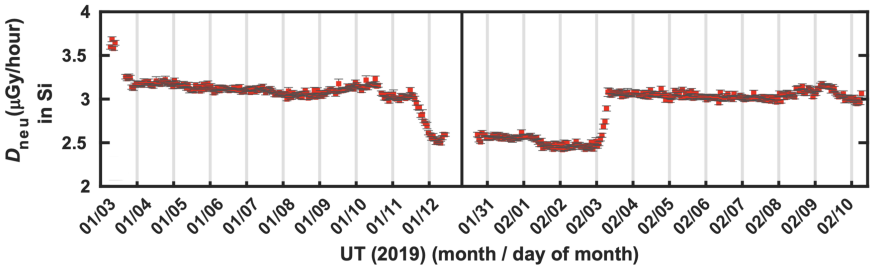

Figure 2.17: Neutral particle dose rate recorded in the LND C1 silicon detector over two separate lunar days [Zhang et al., 2020].

There have been a number of studies conducted to investigate the nature of the energy spectra of albedo neutrons on the Moon. Slaba et al. [2011] performed a computational study to investigate the albedo neutron contribution to the effective dose equivalent on the surface of the Moon within shielding that is exposed to both SEPs and GCR. The results are shown in Figure 2.18 where the relative effectiveness of polyethylene in reducing the neutron exposure compared to aluminium is evident. From these results, it can be seen that the contribution of albedo neutrons is sensitive to the spectral characteristics of the incident SEPs, while for GCR, the contribution is sensitive to the type of shielding and stage of the solar cycle. In both cases, the albedo neutrons present a non-negligible contribution to the effective dose equivalent on the surface of the Moon.

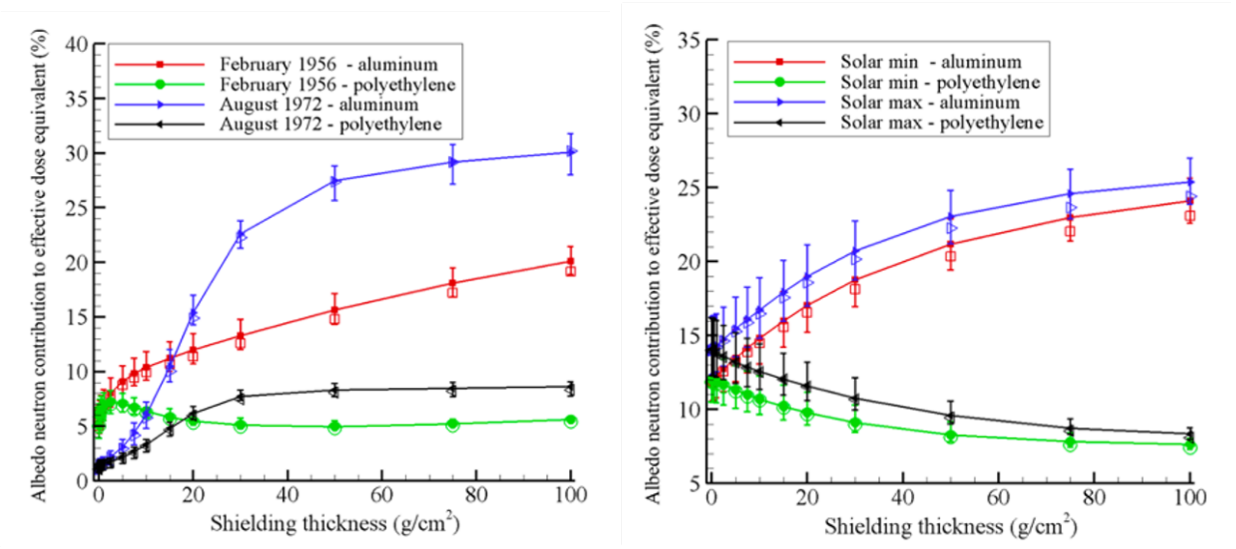

(a) **(b)**

Figure 2.18: Contribution of simulated albedo neutrons to the effective dose equivalent on the surface of the Moon in aluminium and polyethylene shielding exposed to (a) SEPs and (b) GCR [Slaba et al., 2011].

Aside from the measurements made by the neutron spectrometer on the Lunar Prospector

(LP) in 1998 to 1999, which measured albedo neutrons with energies between 0.4 eV and 8 MeV [Maurice et al., 2000], experimental data are very limited. There have been a number of computational studies conducted to investigate the matter further, one of the most recent being that done by Dobynde and Guo [2021] in which they developed a model called *REDMoon* in GEANT4 to describe the lunar radiation environment. A comparison of their results for the albedo neutron flux with the LP experimental data and previous numerical studies is shown in Figure 2.19.

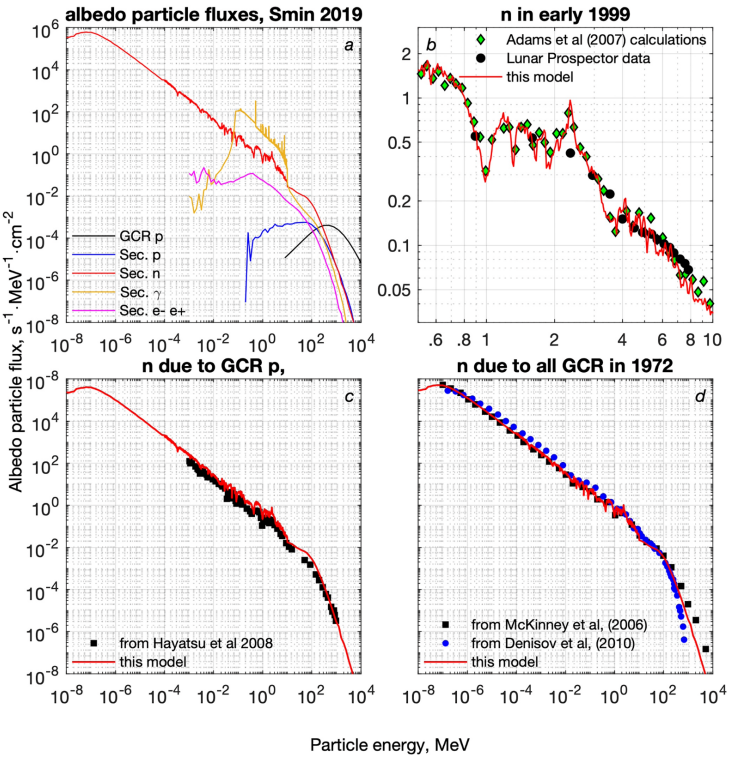

Figure 2.19: (a) Albedo particle energy-differential flux on the surface of the Moon as modelled in *REDMoon* integrated over the upward 2π angle during the period of the 2019 solar minimum. The albedo neutron flux from the *REDMoon* model is compared to (b) the experimental LP data, and (c)/(d) previous numerical results [Dobynde and Guo, 2021].

Naito et al. [2023] evaluated radiation exposure due to albedo neutrons on the lunar surface by combining GEANT4 Monte Carlo simulations of GCR interactions in different lunar surface compositions with spatially resolved data that was measured by the gamma ray spectrometer on board the Kaguya Japanese lunar orbiter in 2009. Figure 2.20 shows their results for the global neutron ambient dose distributions on the surface of the Moon, which vary between 58.7 mSv/yr and 71.5 mSv/yr depending on the differing surface compositions and geological features. Their results indicate that secondary neutrons produced in the lunar surface contribute a non-negligible additional dose of 12% to 14% of that from the primary GCR particles depending on location. Such findings are useful for the optimisation of site selection and radiation shielding strategies for future long-term missions to the Moon.

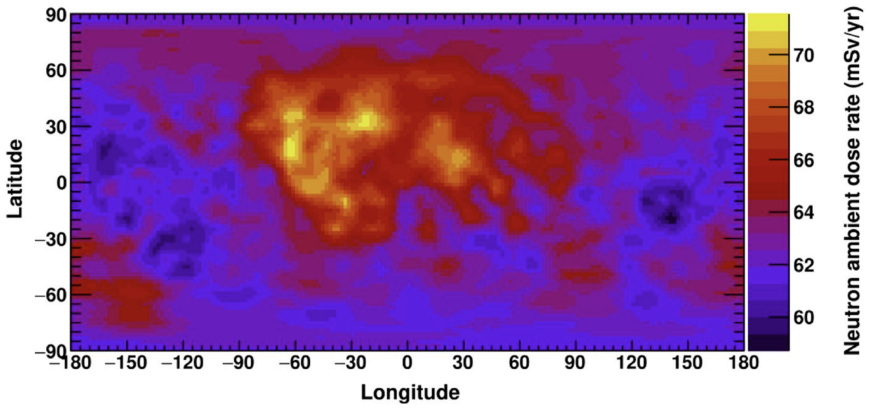

Figure 2.20: The albedo neutron ambient dose distributions on the lunar surface as determined by Naito et al. [2023].

To reduce the difficulties involved in transporting sufficient quantities of shielding materials to the Moon, it is likely that future lunar bases will utilise the widely available lunar regolith as a shielding material. In a similar manner to their investigations of the shielding performances of typical spacecraft materials (as discussed in Section 2.1.3), Horst et al. [2022b] performed Monte Carlo simulations using the FLUKA code to study the production of secondary neutrons from GCR interactions in lunar regolith at solar maximum and minimum conditions. Figure 2.21 shows their results for the dependence of the calculated relative dose factor at a 1 cm depth inside an ICRU sphere behind varying thicknesses of lunar regolith shielding. The significance of the secondary neutron contribution to the absorbed dose build-up is highlighted via comparisons of the results with and without the inclusion of neutrons in the simulated radiation field. Based on the simulation results, it is concluded that the shielding performance of lunar regolith as a thick shield against GCR is slightly better than, but qualitatively comparable to, that of aluminium. The lack of hydrogen content in both aluminium and Moon regolith leads to a significant build-up of secondary neutron dose compared to that observed in polyethylene which has superior fast and high-energy neutron moderation properties (as discussed in Section 2.1.3).

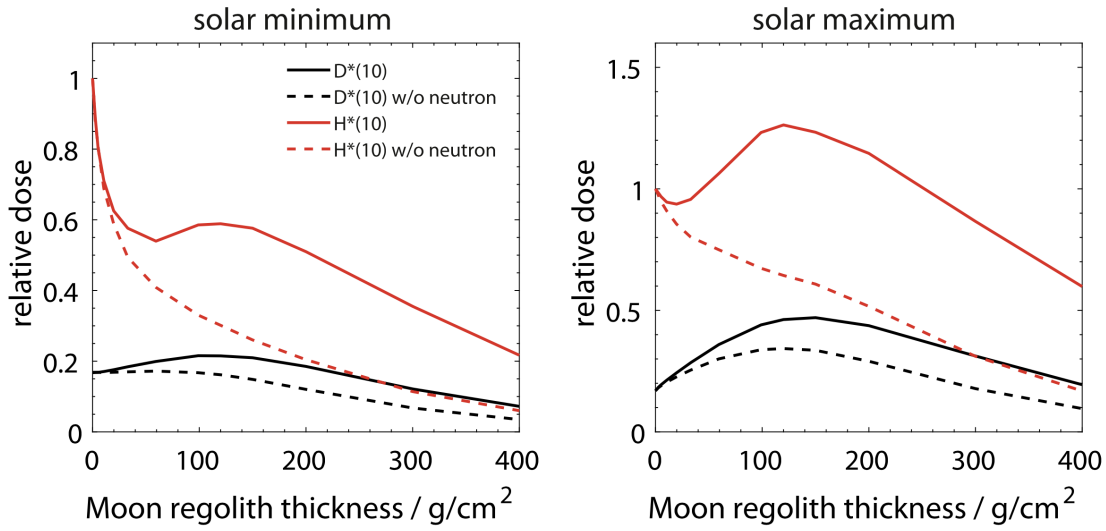

Figure 2.21: Absorbed dose $D^*(10)$ and ambient dose equivalent $H^*(10)$ as a function of Moon regolith shielding thickness for simulated GCR solar minimum and maximum conditions [Horst et al., 2022b].

2.1.6 Neutrons on Mars

Sending humans to Mars and establishing settlements on the planet are among the most exciting plans for future space exploration. Unlike Earth, Mars lacks a protective global magnetosphere and possesses a relatively thin atmosphere. The result is a complex radiation field on the planet surface comprised of a mixture of primary cosmic radiation, as well as secondary particles that are produced by interactions of cosmic radiation both in the atmosphere and in the top layer of the Martian soil. Among these secondary particles, neutrons are a source of particular concern with regards to astronaut radiation exposure [Ehresmann et al., 2021].

Although the Martian atmosphere is relatively thin ($\sim$ 50 times lower atmospheric depth than Earth at sea level), it still plays a significant role in modifying the spectra of the incoming cosmic radiation and determining the characteristics of the radiation field at the surface of the planet. In analogy to cosmic ray interactions in the upper atmosphere of Earth, cosmic ray interactions in the Martian atmosphere produce a cascade of secondary radiation, including neutrons, with characteristics that depend on the atmospheric depth [Ehresmann et al., 2021]. In addition, albedo neutrons are produced as a result of interactions of incoming radiation particles that reach and interact with the top layers of the Martian soil.

Cosmic ray interactions with atoms both in the atmosphere and in the Martian regolith produce neutrons with different energy distributions and directional dependencies. High-energy neutrons are produced as projectile fragments (with very high energies extending up to the initial energy of the incident particle) and as target fragments (which generally have lower energies). These neutrons tend to preserve the forward momentum of the incident ion and are therefore not expected to contribute significantly to the albedo neutron spectrum as they are unlikely to backscatter to the surface when they are produced in the Martian soil [Matthiä et al., 2017]. In contrast, lower energy evaporation neutrons are isotropically produced and consequently, evaporation neutrons produced both in the atmosphere and in the soil contribute to the radiation environment on the Martian surface. The neutron spectrum at the surface of Mars is therefore comprised of neutrons with a broad energy range coming from above and relatively low energy neutrons coming from below [Köhler et al., 2014].

There have been a number of studies performed with the aim of simulating the radiation environment on Mars, however the complexity of the neutron spectrum presents many challenges to the task of modelling it accurately [Köhler et al., 2014]. The RAD onboard the MSL Curiosity Rover has provided the first experimental data against which these simulations can be validated. Köhler et al. [2014] presented the first RAD measurements of the neutron spectrum on the surface of Mars, from which the radiation dose rate from neutrons with energies between 8 MeV and 740 MeV was calculated to be 14 ± 4 μGy/d (7% of the total surface dose rate) with a corresponding dose equivalent rate of 61 ± 15 μSv/d (10% of the total surface dose equivalent rate). Guo et al. [2017] presented the results for similar RAD detector measurements of the neutron spectrum from which they calculated a neutron dose rate between 7 MeV and 740 MeV of 5.1 ± 1.0 μGy/d (2.2% of the total surface dose rate) and a corresponding dose equivalent rate of 23.6 ± 4.1 μSv/d (3.8% of the total surface dose equivalent rate). The disparity in these results from those obtained by Köhler et al. [2014] is attributed to improved methodologies in the analysis procedure. Extrapolation of the measured neutron spectra to the range of 1 MeV to 1000 MeV, resulted in a calculated 6.76 μGy/d dose rate ($\sim$ 3% of the total) and 31.24 μSv/d dose equivalent rate ($\sim$ 5% of the charged particle dose equivalent rate) from neutrons with these energies. Matthiä et al. [2017] compared the measured neutron spectra presented by Guo et al. [2017] with various computational models used to model the neutron radiation field on the surface of Mars (which predict a neutron dose equivalent rate of $\sim$ 30% of the

total [Matthiä et al., 2016]). Their results are shown in Figure 2.22 and revealed some possibly significant differences between the experimental and modelled data for the neutron spectra, highlighting the sensitivity of the models to variables such as atmospheric conditions, the composition of the Marian regolith, and the modelling techniques used [Matthiä et al., 2017].

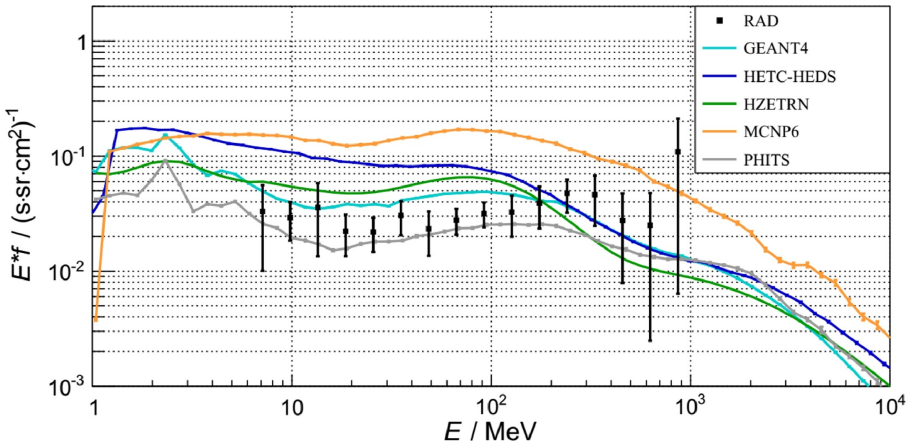

Figure 2.22: The RAD measurements of neutron spectra on the surface of Mars compared to various model results [Matthiä et al., 2017].

Martinez Sierra et al. [2023] provided the first estimate of the neutron flux spectrum on the surface of Mars over a broader energy range (10 eV to 1 GeV) by combining datasets from RAD and the High Energy Neutron Detector (HEND) aboard the Mars Odyssey orbiter (which is sensitive to neutrons with energies less than ∼10 MeV) with Monte Carlo simulations to model atmospheric effects and subsurface interactions. The resulting derived neutron spectrum is shown in Figure 2.23, from which they determined that neutrons with energies > 10 MeV contribute $\sim 50\%$ to the total neutron dose. Based on a combination of measured and simulated datasets, Martinez Sierra et al. [2023] estimated that the neutron dose equivalent rate on the surface of Mars can range from 120 μSv/d to 180 μSv/d (depending on seasonal variations, atmospheric density, and geological features present) corresponding to about 20% of the total dose equivalent at the Martian surface.

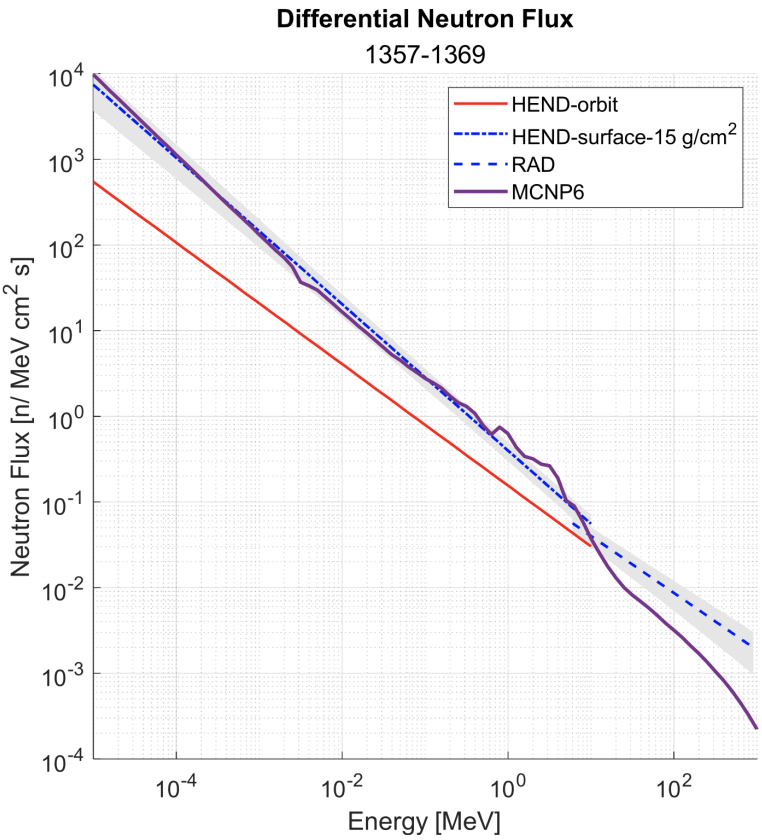

Figure 2.23: Neutron fluxes obtained by combining RAD and HEND data approximations for Martian solar days 1 357 to 1 369. The shaded grey bars represent the standard deviations from power-law fits to HEND-surface and RAD data and the purple line shows the result from MCNP6 simulations carried out using initial conditions for the measurement period [Martinez Sierra et al., 2023].

A number of studies have been conducted to investigate the radiation shielding properties of Martian regolith, which would provide a convenient and cost-effective shielding material from which structures could be constructed in order to protect humans from the harmful radiation environment on Mars [Röstel et al., 2020; Guo et al., 2021]. In these investigations, it has been noted that one of the biggest challenges in shielding design is preventing the build-up of secondary neutrons which contribute significantly to the effective dose behind thick shielding [Röstel et al., 2020]. In a computational study, Zhang et al. [2022] investigated the depth-dependence of the total effective dose in the Martian atmosphere and regolith. Their results for the contribution by secondary neutrons generated in the Martian environment under different surface pressures are shown in Figure 2.24, where it is observed that neutrons are responsible for the peak of the effective dose at a depth of 30 cm to 40 cm underneath the surface. These results illustrate that while more regolith shielding reduces the contribution of primary cosmic radiation to the effective dose, insufficient shielding may actually be counter-productive due to the significant biological effects of the accumulated secondary neutrons. Ehresmann et al. [2021] presented the first measurements taken with the RAD detector on Mars to directly investigate the shielding properties of Martian regolith. While the Curiosity Rover was parked up close to a butte blocking 19% of the sky, the RAD detector measured a 4% decrease in radiation dose. The neutral particle count rates were measured separately and were found to decrease by $\sim 7.5\%$, indicating that in this case, the butte shielding was thick enough to offset the production of secondary neutral radiation by a sufficient loss of primary cosmic radiation intensity.

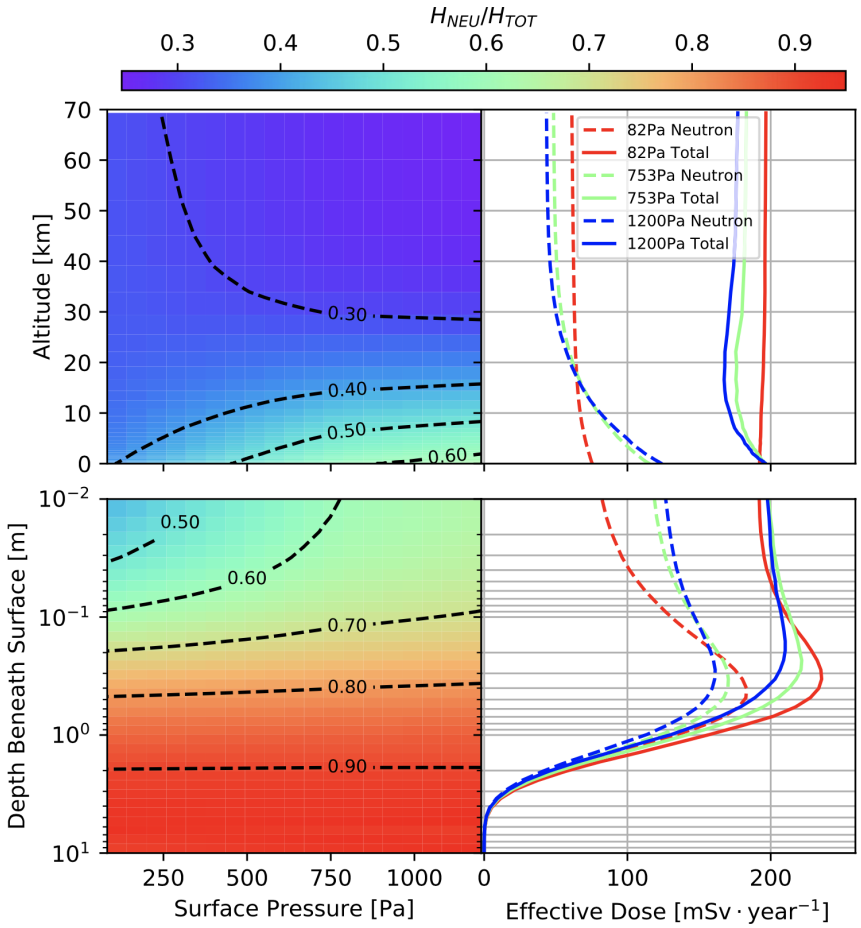

Figure 2.24: Total and neutron contributions to the total body effective dose rate from simulated primary and secondary GCR under different surface pressures as a function of atmospheric altitude and subsurface depth on Mars [Zhang et al., 2022].

2.1.7 Summary of the current state of knowledge surrounding the production of high-energy neutrons in space

Figure 2.25 provides a brief summary of the key characteristics of the production of neutrons in space, as derived from the relevant studies that have been discussed in detail in Sections 2.1.2 to 2.1.6. Results indicate that despite neutrons not being a dominant source of primary radiation in space, neutrons with a wide range of energies extending up to several TeV are expected to contribute significantly to astronaut exposure to ionising radiation during space exploration missions.

Charged particles with energies of up to several TeV

- Galactic cosmic radiation (GCR)
- Solar energetic particles (SEPs)
- Trapped energetic particles in the Van Allen radiation belts

↓

Interactions in matter

- Spacecraft in 'free space': shielding, human body
- Lower Earth Orbit (LEO): shielding, human body, Earth's atmosphere
- Moon: shielding, human body, lunar regolith
- Mars: shielding, human body, Martian atmosphere, Martian regolith

↓

Neutrons with energies of up to several TeV

- Different interaction mechanisms result in the production of neutrons in three main energy ranges:
  - Thermal neutrons (from moderation of higher energy neutrons in various materials);
  - Evaporation neutrons with energies between 1 and 10 MeV (emitted during the de-excitation of a nucleus that has absorbed energy from an incident particle);
  - Neutrons with energies extending up to the maximum incident particle energy (produced in knock-on or projectile fragmentation reactions).
- Measured/extrapolated neutron dose equivalent rates range between 7.3 mSv/yr [Köhler et al., 2015] and 71.5 mSv/yr [Naito et al., 2023] for GCR interactions in spacecraft in 'free space', LEO, on the Moon, and on Mars (note that the ICRP-recommended total annual dose limit for the general public from all types of ionising radiation is 1 mSv [Valentin, 2003]). These dose rates are expected to vary depending on the specific exposure scenario and would increase significantly during solar particle events (SPEs).
- Neutrons with energies > 10 MeV and extending up to several hundred MeV have been predicted to contribute $\sim 50\%$ of the total neutron dose equivalent in these scenarios [Armstrong and Colborn, 2001; Martinez Sierra et al., 2023].

Figure 2.25: Summary of the key characteristics of the production of neutrons in space, as derived from the relevant studies discussed in sections 2.1.2 to 2.1.6.

2.2 High-energy neutrons at commercial aviation altitudes

The ICRP considers aircrew involved in the operation of commercial aircraft to be occupationally exposed as a result of cosmic radiation, and recommends that individual exposure be monitored and practical regulations applied [Valentin, 2007]. The production of neutrons in Earth's atmosphere as secondary cosmic radiation was discussed in Section 2.1.2. Figure 2.26 illustrates the strong altitude dependence of secondary cosmic radiation by showing the calculated contributions to the dose equivalent by different particles as a function of altitude. From this plot, it can be seen that neutrons contribute around 40% of the total dose equivalent at typical commercial aviation altitudes (about 10 km), although this can vary depending on the location in the geomagnetic field and the Sun's magnetic activity. As illustrated in Figure 2.6, typical spectral distributions of neutrons in Earth's atmosphere include neutrons with a wide range of energies and distinct peaks around 1 MeV and 100 MeV. High-energy neutrons therefore contribute significantly to the radiation field to which air crew and passengers are routinely exposed, and their associated biological effects should be considered in the development of related health-risk models.

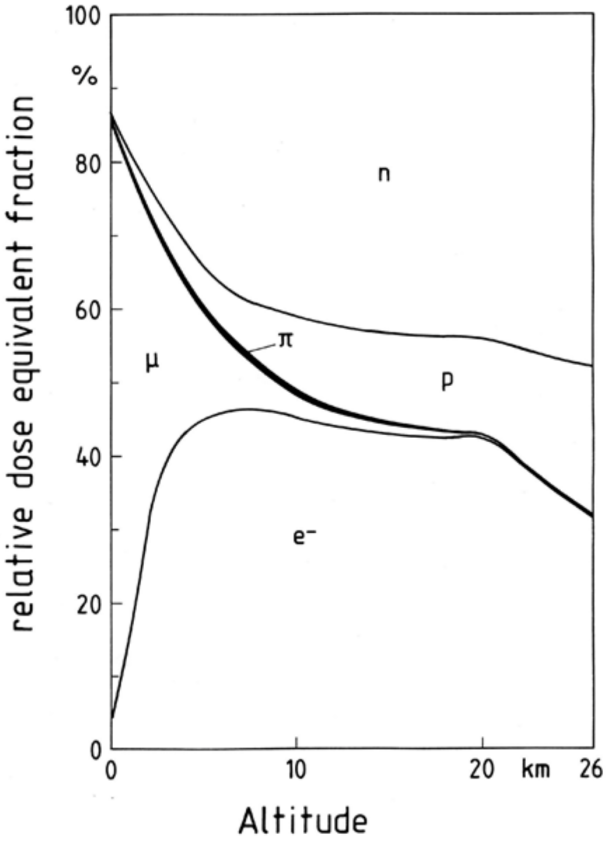

Figure 2.26: Calculated contributions of neutrons, protons, pions, muons and electrons to dose equivalent as a function of altitude [Bizzarri and Cucina, 2008].

.

2.3 High-energy neutrons in proton therapy

Proton therapy involves the irradiation of cancerous tumours by a beam of protons with typical energies between 60 MeV and 330 MeV [Paganetti, 2018]. This radiotherapy technique offers the distinct advantage that the region of highest energy deposition, characterised by the Bragg peak, can be precisely controlled to maximise dose delivered to the target area while minimising damage to the surrounding healthy tissue. However, the interactions of high-energy protons within the patient and the surrounding environment results in the production of a secondary radiation field comprised mainly of neutrons and gamma rays that contribute to a whole-body dose exposure [Paganetti, 2018]. The significance of the dose contribution from secondary neutrons is controversial [Schneider and Hälg, 2015] and while it is unlikely that the associated risks will outweigh the relative benefits of proton therapy, measured neutron doses from different proton therapy facilities vary significantly as a result of differing beam delivery system geometries and measurement techniques [Hälg and Schneider, 2020].

A number of experimental studies have been conducted within the context of proton therapy to investigate the nature of neutron spectra produced by protons with energies up to $\sim$ 200 MeV interacting in different materials. Examples of such spectra are shown in Figure 2.27. These plots illustrate that the shapes of the neutron spectra observed within the context of proton therapy, are almost analogous to those observed in space and in Earth's atmosphere and include neutrons with high energies extending up to the energy of the incident protons. Assessments of the biological effects of these high-energy neutrons are therefore necessary in order to assess the importance of the neutron dose contribution to the long term side-effects of proton therapy treatment.

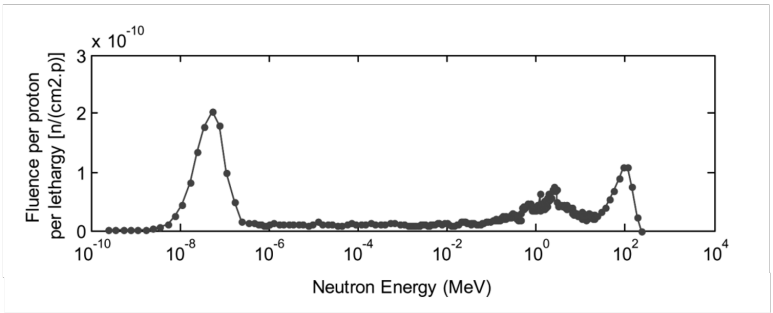

(a)

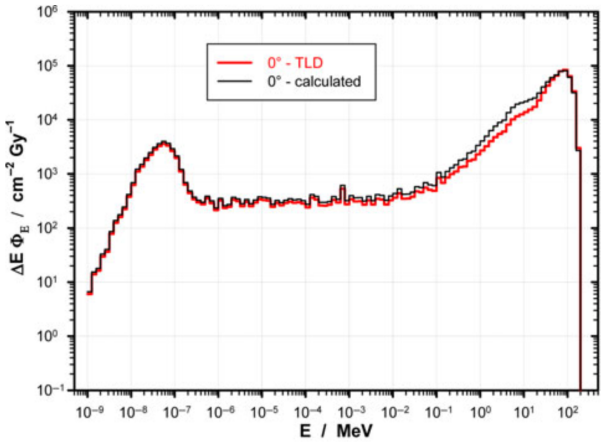

(b)

Figure 2.27: Measured neutron spectrum produced in (a) a water phantom for 227 MeV incident protons [De Saint-Hubert et al., 2016], and (b) a nylon phantom for 200 MeV incident protons [Vykydal et al., 2016], in a proton therapy facility.

3 The Relative Biological Effectiveness (RBE) of high-energy neutrons

As discussed in Chapter 2, astronauts in space will be exposed to neutrons with a wide range of energies extending up to several TeV. The development of radiation health-risk models for space exploration therefore requires the quantification of the biological effects of neutrons, and in the current radiation protection framework this is achieved via measurements of the neutron RBE. This chapter introduces the concept of neutron RBE and outlines the current state of knowledge and key challenges surrounding measurements within the context of future space exploration.

3.1 The biological effects of ionising radiation

On a physical basis, the primary outcome of the interaction of radiation with matter is the deposition of energy that causes ionisation and excitation of atoms and molecules. In general, the principle target for the biological effects of ionising radiation is the deoxyribonucleic acid (DNA) molecule. Damage to DNA from ionising radiation can be direct (where energy is deposited directly in the DNA) or indirect (where the energy deposited induces Reactive Oxygen Species which in turn react with the DNA molecule) [Arena et al., 2014].

The DNA molecule consists of two complementary strands that are linked by hydrogen bonds to form a double-helical structure. Each strand consists of a linear chain of four bases (adenine, cytosine, guanine and thymine) that are connected via a backbone of alternating sugar and phosphate groups [Hall and Giaccia, 2019]. The order of these bases along the backbone defines the genetic information that is encoded in the DNA [Joiner and van der Kogel, 2019]. Damage to DNA due to ionising radiation can occur in the form of base damage, single-strand breaks (SSBs), double-strand breaks (DSBs), and DNA protein crosslinks. Due to the importance of DNA, mammalian cells have developed special pathways to sense, respond to, and repair DNA damage. Figure 3.1 illustrates the main types of radiation-induced DNA damage, repair mechanisms and consequences in mammalian cells. Base damage and SSBs are usually (although not always) repaired successfully via the base excision repair (BER) mechanism, which utilizes the opposite undamaged complementary strand as a template. On the other hand, DSBs and DNA protein crosslinks are repaired via the mechanisms of homologous recombination (HR) or non-homologous end-joining (NHEJ). The HR pathway is an error-free process, but requires the presence of an undamaged homologous chromatid to act as a template. The NHEJ pathway is an error-prone process and is the most prominent pathway for the repair of DSBs, which it achieves via the orchestration of end-to-end joining. Although DNA DSBs can be successfully repaired, the chances of unsuccessful repair are higher, and for this reason, DSBs are considered to be the most lethal form of radiation-induced damage [Hall and Giaccia, 2019].

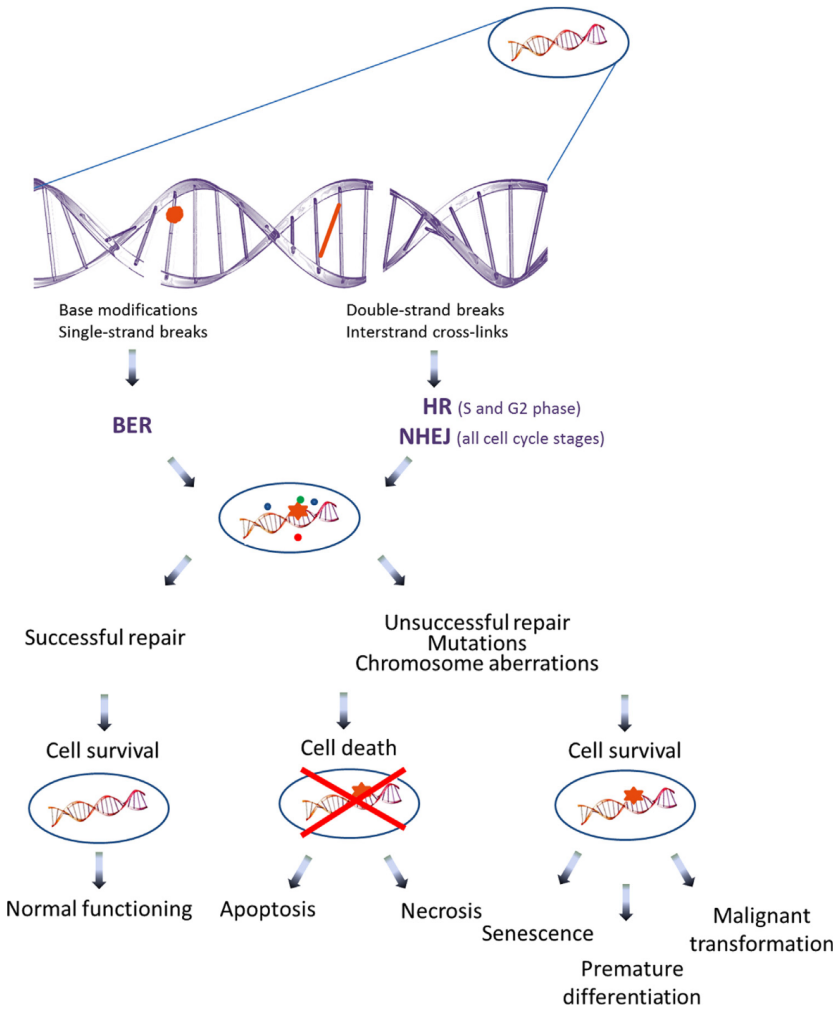

Figure 3.1: The different types of radiation-induced DNA damage in mammalian cells, repair mechanisms and potential consequences [Arena et al., 2014].

The unsuccessful repair of DNA damage following exposure to ionising radiation can result in two main types of harmful effects, as illustrated in Figure 3.2.

1. Deterministic effects (tissue reactions)
   Damaged cells are ultimately removed from the proliferative pool when the unsuccessful repair of DNA damage results in the cell undergoing apoptosis or necrosis, becoming senescent or differentiating prematurely [Arena et al., 2014]. Most organs or tissues in the body are unaffected by the loss of a few cells and therefore the effect only becomes noticeable once a critical number of cells are lost. Deterministic effects are therefore characterised by a certain threshold dose, beyond which the severity and probability of occurrence increases rapidly [Valentin, 2007].

2. Stochastic effects
   The unsuccessful repair of DNA damage can also result in cells that are changed and mutated, which can lead to the development of cancer or heritable effects. These stochastic effects occur with a probability that increases with dose but with a severity that does not depend on the dose. Based on the molecular mechanisms involved, it is believed that stochastic effects do not have a dose threshold and therefore it is considered prudent to assume that no dose is too small to potentially be effective – this assumption is known as the linear no-threshold hypothesis [Valentin, 2007; Hall and Giaccia, 2019].

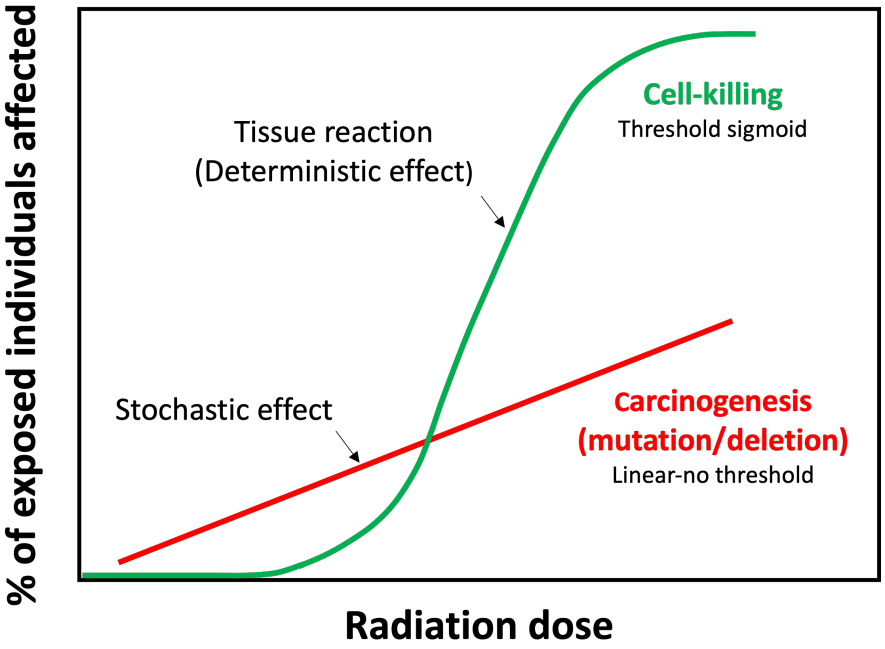

Figure 3.2: The relationships between radiation dose and biological effect for deterministic and stochastic effects [Hall and Giaccia, 2019].

3.2 The radiation protection framework for astronauts

Exposure to radiation in space has been recognized as the main risk to astronaut health on extended space exploration missions that are planned to venture beyond the protective magnetosphere of the Earth [Chancellor et al., 2014].

The ISS has been operating in LEO since 1998. Although the exposure that the crew receives is substantially higher than, and of a different nature to that received by typical terrestrial radiation workers, the basic principles of Earth-based radiation protection remain valid [Straube et al., 2010]. The ISS participating partner agencies (NASA for the United States, Roscosmos for Russia, the Japanese Aerospace Exploration Agency (JAXA) for Japan, the European Space Agency (ESA) for Europe, and the Canadian Space Agency (CSA) for Canada) work with a mutually agreed upon radiation protection framework in order to assure the safety of their crew [Walsh et al., 2019]. All radiation exposures are planned in accordance with the conventional As Low As Reasonably Achievable (ALARA) principle of radiological protection as outlined by the ICRP [Valentin, 2007].

The fundamental physical quantity that is used as the basis of the ICRP system of protection quantities is the absorbed dose D, measured in grays (Gy) and defined as

$$D = \frac{dE}{dm}, \tag{3.1}$$

where dE is the mean energy that is imparted by ionising radiation to matter of mass dm [Dietze et al., 2013]. For the purposes of setting limits for radiological protection, deterministic and stochastic effects are treated separately.

Deterministic effects only appear above a certain dose threshold with a severity that is proportional to the absorbed dose [Valentin, 2007]. Exposure limits for deterministic effects are defined in terms of specific organ damage, which is quantified in terms of a mean absorbed dose in an organ/tissue that is multiplied by an appropriate coefficient of RBE that incorporates the type of radiation field, the biological effect reported, the duration of exposure, and the tissue involved. The ICRP recommends that these limiting factors for deterministic effects are quoted using the units of gray (the same units as absorbed dose) [Ferrari et al., 2023].

In contrast to deterministic effects, stochastic effects occur with a likelihood that is related to dose, but with a severity that is independent of dose [Ferrari et al., 2023]. Limits for stochastic effects are expressed in terms of effective dose E, measured in sieverts (Sv) and defined as

$$E = \sum_T w_T \sum_R w_R D_{T,R}, \tag{3.2}$$

where $D_{T,R}$ is the mean absorbed dose in an organ/tissue, w_R are weighting factors for different radiation types, and w_T are tissue weighting factors evaluated for a standard human body. Defined in this way, the effective dose represents the stochastic health risk to the whole body for exposure to varying levels and types of ionising radiation [Dietze et al., 2013].

On the ISS, there is general consensus among the different agencies involved regarding the Aeromedical Flight Rules which include protocols for responding to contingency events like transient high ionising radiation events. However, the different agencies still maintain separate career exposure limits for their astronauts [Shavers et al., 2023]. Furthermore, no space agency has yet issued any specific recommendation for the radiation protection limits in beyond LEO missions [Walsh et al., 2019]. With impending mission plans, the development of a comprehensive international space radiation protection strategy is essential.

The largest source of uncertainty in current space radiation risk projection models is attributed to insufficient knowledge surrounding the biological effects of space radiation [Fogtman et al., 2023]. NASA has identified the following as the highest research priorities regarding space radiation health risks:

1. Carcinogenesis [Cucinotta and Durante, 2013b];
2. Degenerative tissue effects [Huff and Cucinotta, 2013];
3. Central nervous system decrements [Cucinotta and Durante, 2013a]; and
4. Acute radiation syndrome [Wu et al., 2013].

Accurately assessing and mitigating these health risks requires the development of space radiation risk models that are based on a combination of radiation transport physics and radiobiology. The current significant knowledge gaps in these fields calls for dedicated experiments and the development of corresponding theoretical models and simulations in order to better understand and quantify the risks associated with the long-term chronic radiation exposure of astronauts in space [Horst et al., 2022a].

The nature of the space radiation environment is complex and therefore it is necessary to investigate the biological impact of the individual components of the field. Of particular concern is the significant threat to astronauts' health that is posed by neutrons due to their high penetration power and biological effectiveness [Horst et al., 2022a]. As discussed in Chapter 2, neutrons with a wide range of energies extending up to several TeV are present in the space radiation environment to which astronauts will be exposed. In particular, the lack of comprehensive experimental data for neutrons with energies > 20 MeV contributes significantly to the uncertainties in radiation risk estimations.

3.3 Neutron Relative Biological Effectiveness (RBE)

An understanding of the biological effects of neutrons stems from a knowledge of the physical characteristics of their interactions in the human body and their corresponding classification as indirectly ionising, high linear energy transfer (LET) radiation.

Indirectly ionising radiation interacts in such a way that the primary particle transfers energy to secondary charged particles that subsequently deposit energy in the medium via the ionization and excitation of atoms and molecules. Neutrons are neutral and therefore do not interact with matter via the Coulomb force, which is the main mechanism of energy loss for charged particles. Rather, neutrons can travel through many centimetres of matter without any type of interaction, and thus are highly penetrating. When a neutron does interact, it interacts with the nuclei of the absorbing material to produce secondary radiation particles which deposit energy in the medium via Coulomb interactions. In the human body (composed primarily of hydrogen, carbon, nitrogen and oxygen), neutrons can undergo a large variety of nuclear reactions resulting in the production of a mixed field of secondary charged particles. These particles are produced from either neutron-induced nuclear reactions or they are the nuclei of the absorbing material that have gained energy from a neutron collision. The type of interactions that occur and the amount of energy that is deposited in matter depends strongly on the neutron energy and the nature of the material with which they interact [Knoll, 2010].

Linear energy transfer (LET) is defined as

$$\text{LET} = \frac{dE}{dl}, \tag{3.3}$$

where dE is the mean energy deposited by a charged particle as it moves a distance dl in matter [Dietze et al., 2013]. Defined in this way, the term LET describes the density of ionisations along particle tracks inside a particular medium. In general, fast electrons are relatively sparsely ionising and therefore are classified as 'low-LET' radiation, as are indirectly ionising X-rays and gamma rays because they transfer their energy to electrons. Heavy charged particles constitute 'high-LET' radiation, as they are relatively densely ionising. Neutrons are also classified as high-LET radiation, as their LET spectrum is determined by the combination of all the LET spectra of the secondary particles they produce, which tend be densely ionising [Joiner and van der Kogel, 2019].

The biological effects of ionising radiation are strongly linked to the physical pattern of energy deposition at the microscopic level, as characterised by the LET [Valentin, 2003]. In general, high-LET radiations produce more biological damage than low-LET radiations at the same absorbed dose level. The reason for this is illustrated in Figure 3.3, which compares the ionisation density along the paths of recoil electrons produced by X-rays, and recoil protons produced by neutrons, at the scale of a segment of DNA. The low-LET electrons deposit most of their energy as single isolated ionizations or excitations and therefore the induced DNA damage is relatively simple and can be efficiently repaired as discussed in Section 3.1. In contrast, the relatively intense ionization along the path of high-LET radiation means that it is more likely that complex DNA damage will be produced which is more difficult for the cell to repair [Joiner and van der Kogel, 2019].

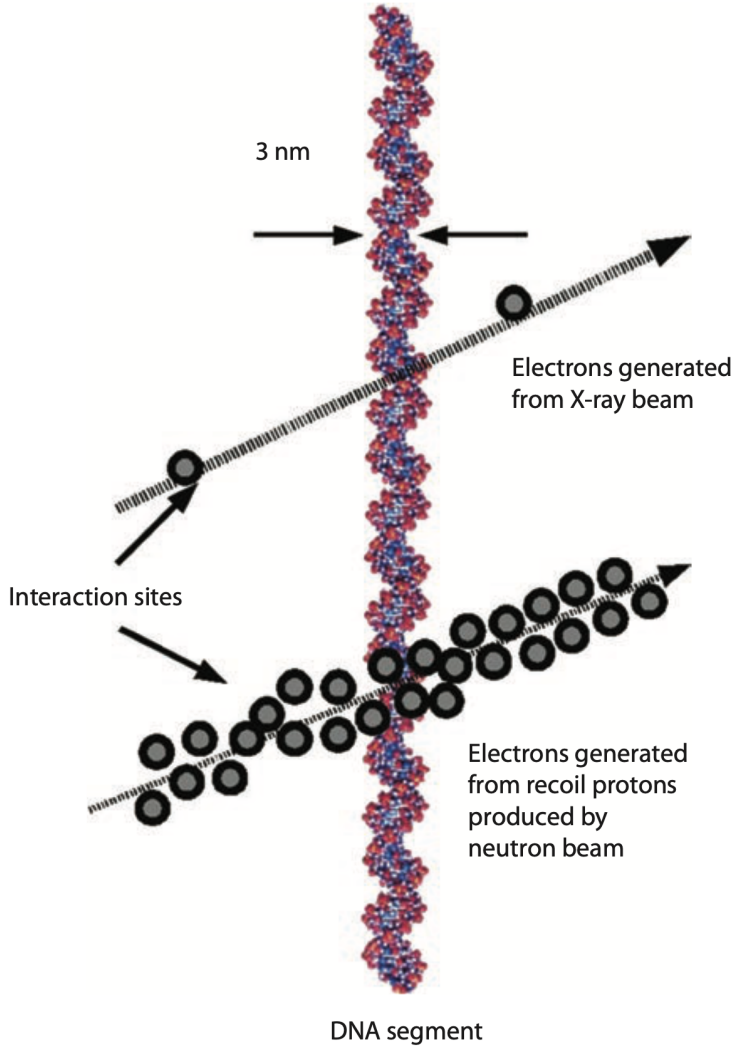

Figure 3.3: Ionization density of a low-LET radiation (electrons produced by an X-ray beam) versus a high-LET radiation (protons produced by a neutron beam) at the scale of a segment of DNA [Joiner and van der Kogel, 2019].

The considerably more damaging effects of neutrons relative to low-LET radiation have been observed in a variety of experimental systems and these observations are consistent with expectations given the knowledge that dose deposited in human tissue by neutrons occurs via secondary charged particles with well-established biologically damaging effects [Goodhead, 2019]. Differences in the effectiveness of different types of radiation for inducing a particular biological endpoint are quantified by the relative biological effectiveness (RBE), defined as [Valentin, 2003]

$$\mathrm{RBE} = \frac{\text{absorbed dose of reference radiation producing effect } Z}{\text{absorbed dose of test radiation producing effect } Z}. \tag{3.4}$$

In assessments of neutron RBE, the 'test radiation' is neutron radiation and the 'reference radiation' is typically gamma ray or X-ray radiation for which the associated health risks are well known [Ottolenghi et al., 2015].

Values of RBE determined in a variety of radiobiological experiments are utilized by the ICRP to inform the selection of the weighting factors that relate absorbed dose from ionising radiation in human tissue to the risk of both stochastic and deterministic effects, as discussed in Section 3.1 [Valentin, 2003; Stricklin et al., 2021]. For the induction of stochastic effects at low doses, it is typically experimentally determined values of the neutron $\mathrm{RBE_M}$ that are used in the selection

of the relevant radiation weighting factors. The $\mathrm{RBE_M}$ is defined as the limiting maximum value of RBE that is approached at low doses and is equal to the ratio of the initial slopes of the neutron and reference radiation dose-response curves, denoted

$$\mathrm{RBE_M} = \frac{\alpha_n}{\alpha_{ref}}, \tag{3.5}$$

where α_n and α_{ref} are the initial slopes of the dose-response curves, referred to as the 'linear yield coefficients', for the neutrons and reference radiation respectively [Valentin, 2003]. The motivation behind the use of $\mathrm{RBE_M}$ is discussed in more detail in Section 3.3.2.

Establishing comprehensive risk-related models regarding human exposure to neutron radiation is extremely complicated, given that values for neutron RBE depend on a number of both physical and biological variables. Due to the variety of parameters that can influence the results, currently reported numerical values of neutron RBE range from less than 1 to over 200 [Goodhead, 2019; Hälg and Schneider, 2020]. A comprehensive interpretation of these results for the purposes of developing neutron health-risk-related models inevitably involves substantial uncertainty given the result dependence on specific biological parameters, the varied radiation exposures, and in many cases, the inconsistent reports of radiation type, dose and dose rate. The currently recommended ICRP neutron radiation weighting factors for radiation protection purposes are based on a conservative pooling together of the RBE results from many different experiments [Lund et al., 2020]. However, the uncertainties associated with these generalised results are unacceptably high given the current need to develop accurate neutron radiation health-risk models to advise mitigation strategies for future space exploration. As discussed in the following sections, particular attention needs be paid to the knowledge of neutron RBE for the energies, doses, dose rates and biological endpoints that are relevant for astronauts.

3.3.1 The dependence of neutron RBE on energy

Neutron RBE is strongly energy dependent. This is a direct consequence of the dependence of nuclear reaction cross sections and hence of the induced secondary particle radiation field on the incident neutron energy. The energy dependence of neutron RBE has been verified in a range of experimental and epidemiological studies and it is generally accepted that the maximum RBE occurs around 1 MeV, however the exact values vary significantly. The existing uncertainties in how neutron RBE varies as a function of energy are reflected in the different ranges of neutron weighting factors for stochastic effects that are recommended by the ICRP and U.S. NRC, as illustrated in Figure 3.4. These weighting factors are primarily based on old experimental data from *in vitro* cell killing, chromosome aberrations and animal experiments for neutrons with energies < 20 MeV. Significant uncertainties remain for higher energy neutrons [Stricklin et al., 2021; Engelbrecht et al., 2021].

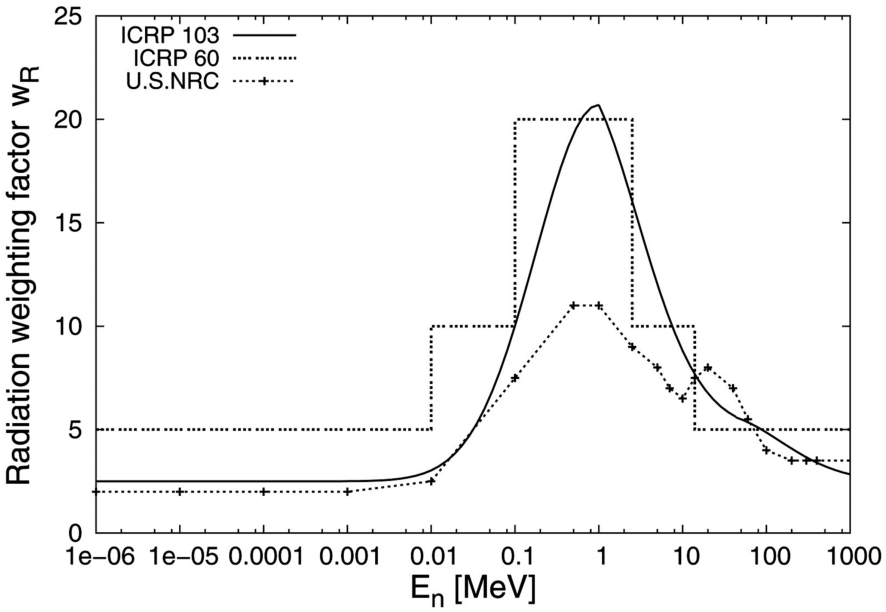

Figure 3.4: The neutron energy dependence of the radiation weighting factors for stochastic effects that are recommended by the ICRP and U.S. NRC [Ottolenghi et al., 2015].

The energy-dependence of neutron RBE is a result of the relationship between RBE and LET that has been well-established in radiobiology for a variety of different types of radiations. Of particular interest is the existence of an optimal LET at which RBE tends to reach a peak, and the reason for this is illustrated in Figure 3.5: in general, DNA DSBs are the basis of most biological effects and the most biologically effective LET is that where the average separation between ionising events corresponds to the diameter of a DNA double helix. Below this optimal value, low-LET radiation is inefficient because the induction of DNA DSBs requires more than one particle to pass through the cell. Beyond the optimal value, high-LET radiation becomes inefficient because more energy is deposited than is needed to induce DNA DSBs, and therefore this radiation is less effective per unit dose – a phenomenon known as 'overkilling' [Hall and Giaccia, 2019; Joiner and van der Kogel, 2019]. The exact location of the optimum LET varies between different cell types, and for the case of neutrons, the situation is further complicated by the fact that the LET depends on the combined LET of all the different types of secondary radiation that is produced.

Baiocco et al. [2016] conducted a computational study with the goal of tracing the energy dependence of neutron RBE back to the first principles of the physical interactions. Through a comprehensive modelling approach in which they calculated microdosimetric parameters for a range of neutron energies interacting in a standard human tissue phantom, they were able to reveal the interplay of the key mechanisms of nuclear interactions that are responsible for the energy variation of neutron RBE. The results for their *ab initio* neutron RBE model based on the induction of complex DNA damage over a range of neutron energies are shown in Figure 3.6, where the simulation results are compared to the current standards for radiation weighting factors (for stochastic effects) as recommended by the ICRP and U.S. NRC. These comparisons provide a useful validation of, and explanation for, the shape of the curve of the weighting factors used for radiation protection purposes. The region of maximal RBE around 1 MeV is attributed to the damage induced by slow secondary protons, while the second peak around 20 MeV is attributed to the damage induced by heavier charged particles produced by neutrons at this energy.

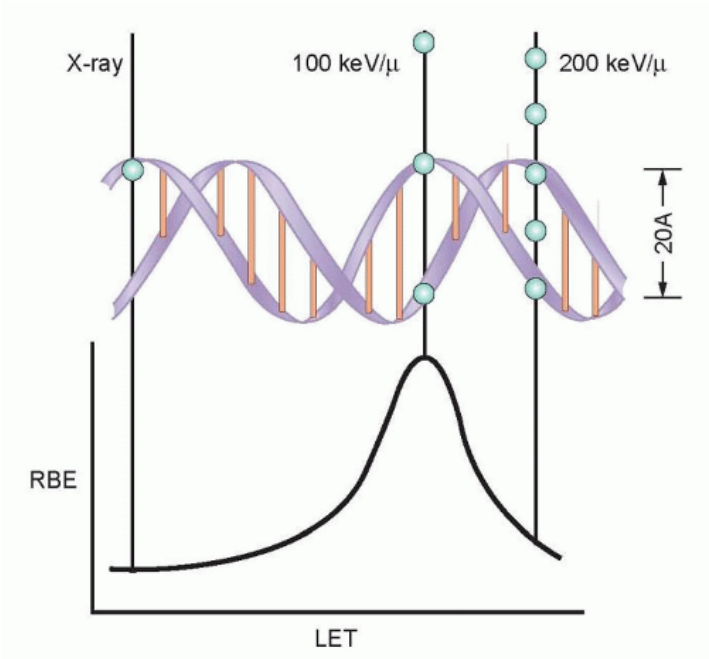

Figure 3.5: Generalised relationship between RBE and LET to illustrate why RBE tends to reach a peak for radiation with an 'optimal LET' of around 100 keV/μm where the average separation between ionising events corresponds to the diameter of a DNA double helix [Hall and Giaccia, 2019].

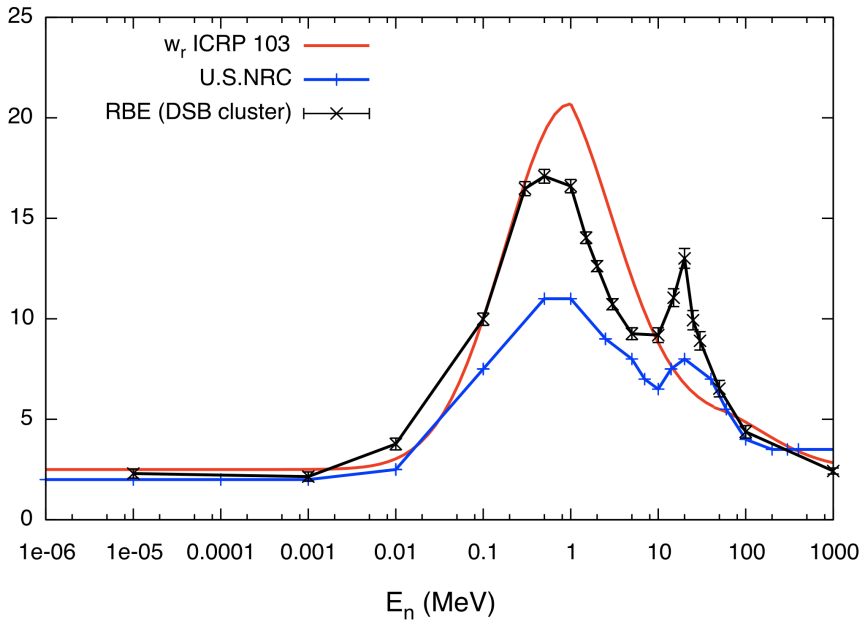

Figure 3.6: Results from the *ab initio* model for neutron RBE as a function of energy evaluated from DNA DSBs cluster induction. The model results (black) are compared to the ICRP (red) and U.S. NRC (blue) standards for radiation weighting factors for stochastic effects [Baiocco et al., 2016].

Neutron RBE measurements at high energies

While extensive studies on the biological effects of neutrons have been conducted for neutrons with energies < 20 MeV, the available data on neutron RBE for higher energies are extremely limited. As discussed in Chapter 2, neutrons with energies > 20 MeV pose a relevant health risk within the context of future space exploration (as well as aviation and proton therapy), and dedicated radiobiology research is therefore required to reduce the large uncertainties associated with neutron radiation weighting factors at these energies. An overview of the limited neutron RBE studies that have been conducted for neutrons with energies > 20 MeV is outlined below, and the key results are summarised in Table 3.1.

Heimers [1999] conducted an experiment to measure the RBE for the induction of dicentric chromosome aberrations in human lymphocytes exposed to the neutron component of the CERN-CEC reference radiation field, intended to simulate cosmic radiation. The neutron spectrum used in this study is shown in Figure 3.7 - it is a mixed radiation field with prominent peaks in the neutron spectrum around 1 MeV and 70 MeV. The measured neutron RBE_M (for ^{60}Co gamma rays as the reference radiation) was reported to be 96 for measurements conducted with a fractionated dose of 5.81 mGy delivered over 72 hours, and 113 for measurements conducted with a continuous dose exposure of 2.39 mGy delivered over 16 hours. It should be noted that the accuracy of these results have raised significant debate, as the measured values are significantly higher than the RBE_M value of 8 that was predicted for the investigated neutron spectrum based on the ICRP and National Council on Radiation Protection and Measurements (NCRP) extrapolations from high neutron doses [Mitaroff and Silari, 2002; Nolte et al., 2005, 2006; Brenner and Hall, 2008].

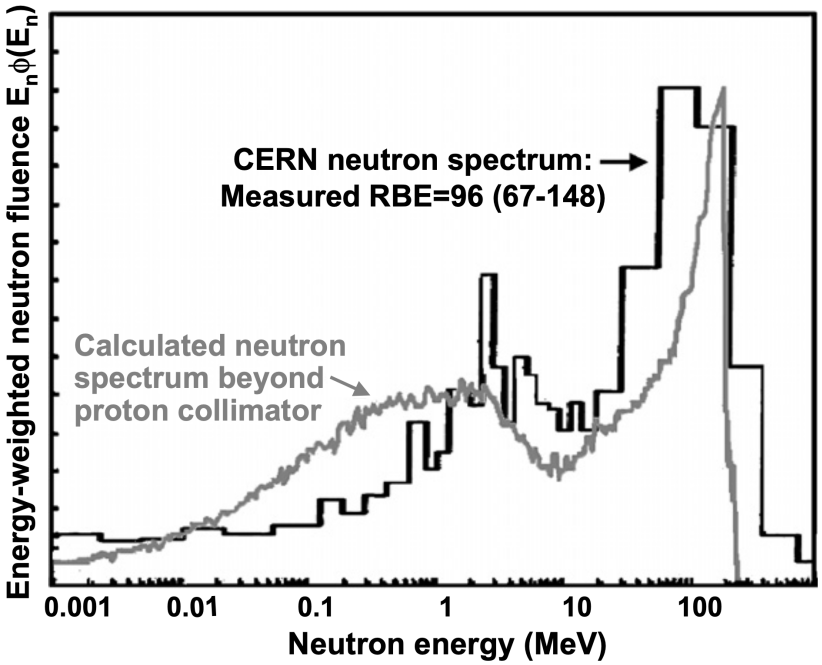

Figure 3.7: The energy spectrum of the neutron field at CERN that was used for the RBE measurements by Heimers [1999]. It is shown alongside the estimated neutron spectrum downstream of the final patient collimator at the MD Anderson clinical proton facility [Brenner and Hall, 2008].

There have been a number of neutron RBE studies that have been conducted at the Los Alamos Nuclear Science Centre (LANSCE) neutron facility's ICE House 30L beamline, which generates neutrons that simulate the secondary neutron spectra in Earth's atmosphere, with

energies ranging from 1 MeV to 800 MeV, as shown in Figure 3.8:

- Gersey et al. [2007] made measurements of neutron RBE for micronuclei induction in human cultured fibroblasts cells that were irradiated with a neutron dose rate of around 25 mGy/hr. The measured neutron RBE_M value (relative to ^{137}Cs gamma rays) was reported to be 10.0 ± 1.0 and 16.4 ± 1.4, without and with a 9.9 cm water shield present, respectively.

- Kuhne et al. [2009] carried out the first neutron RBE study of an intact vertebrate in the energy range of the LANSCE neutron facility, using Japanese medaka fish embryos. For neutron irradiations with dose rates of between 12 mGy/hr and 15 mGy/hr, they reported RBE_M values (relative to ^{137}Cs gamma rays) of 24.9 for apoptosis in defined regions in the head (primarily the brain and eyes), 147 for apoptosis in the tail (primarily muscle tissue), and 48.1 for overall survival of the embryo until ten days after hatching.

- Hada et al. [2010] used the same facility to investigate the fraction of human epithelial cells with chromosome aberrations following irradiations with neutrons at a dose rate of around 25 mGy/hr, and reported a RBE_M result (relative to ^{137}Cs gamma rays) of 26 ± 4.

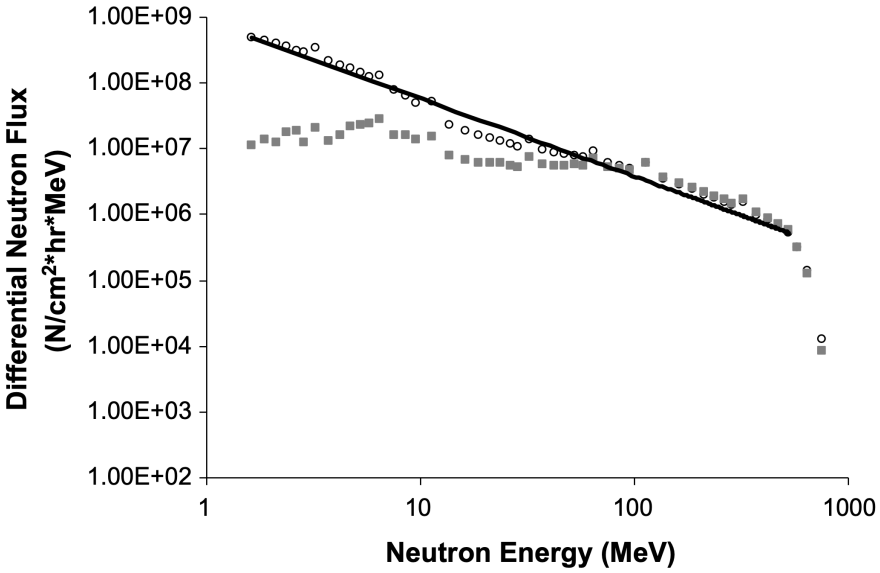

Figure 3.8: The energy spectrum of the neutrons from the LANSCE neutron facility's ICE House 30L beamline that was used for the neutron RBE experiments by Gersey et al. [2007], Kuhne et al. [2009], and Hada et al. [2010]. The open circles and solid squares represent the neutron spectrum measured without and with the presence of a 9.9 cm water shield respectively, and the solid line represents the shape of the spectrum of neutrons in Earth's atmosphere at an altitude of 12 km.

Various neutron RBE studies have been conducted using the clinical neutron beam - p(66)/Be(40) - at iThemba LABS which produced neutrons via the reaction of a 66 MeV proton beam on a beryllium target, resulting in a neutron spectrum with a fluence weighted average energy of approximately 29 MeV [Vandersickel et al., 2014]:

- Slabbert et al. [2000] reported a neutron RBE_M range of 1.6 to 3.5 evaluated for cell survival of human tumour cell lines, irradiated with 0 Gy to 5 Gy of p(66)/Be(40) neutrons and compared to ^{60}Co gamma rays.

- Using the same facility, Slabbert et al. [2010] reported a neutron RBE_M range of 1.8 to 8.0, assessed for micronuclei formation in human T-lymphocytes from different donors with varying sensitivities relative to ^{60}Co gamma ray exposure.

- Vandersickel et al. [2014] conducted a study to investigate micronuclei formation and γ-H2AX foci induction following exposure of human lymphocytes to p(66)/Be(40) neutrons and ^{60}Co gamma rays. Reported RBE_M values for micronuclei formation ranged between 3.57 and 1.56 for neutron doses of 0.05 Gy to 2.00 Gy respectively. Reported RBE_M values for γ-H2AX foci induction were between 0.70 and 0.64 for neutron doses in the range of 0.0 Gy to 0.5 Gy.

Juerß et al. [2017] measured RBE values for clonogenic survival and γ-H2AX residual foci induction following exposure of MCF10A normal human breast cells to X-rays and a mixed gamma-neutron field produced by the interaction of 190 MeV protons in water, resulting in neutrons with a mean energy of 70.5 MeV contributing 65% to the total dose. For an endpoint of 10% clonogenic cell survival, the measured RBE value for this field was 2.09. For γ-H2AX residual foci induction after 24 hours, the measured RBE value was 4.47.

To date, the only studies of neutron RBE for energies > 20 MeV that have been conducted in quasi-monoenergetic neutron fields were carried out by Nolte et al. [2005] and Nolte et al. [2006], who investigated the production of dicentric chromosomes in human lymphocytes by quasi-monoenergetic 60 MeV and 192 MeV neutron beams relative to ^{60}Co gamma ray radiation:

- Nolte et al. [2005] reported an RBE_M value of 14 ± 4 for neutrons of a mixed energy field with a dose-weighted average energy of 41 MeV (as shown in Figure 3.9). A correction procedure, based on an interpolation and extrapolation of RBE data obtained at lower neutron energies, was applied to correct for the effects of the low-energy continuum of the neutron spectrum and determine an RBE_M value of 11.4 ± 4.0 for quasi-monoenergetic 60 MeV neutrons.

- Nolte et al. [2006] reported an RBE_M value of 9 ± 3 for neutrons of a mixed energy field with a dose-weighted average energy of 162 MeV (as shown in Figure 3.10). A correction procedure, based on making measurements at different angles relative to the incident proton beam to correct for the effects of the low-energy continuum of the neutron spectrum, was applied to in order to determine an RBE_M value of 12 ± 4 for quasi-monoenergetic 192 MeV neutrons.

The results from the neutron RBE_M studies conducted by Nolte et al. [2005] and Nolte et al. [2006] are shown in Figure 3.11, along with the results from earlier measurements carried out at lower energies. The correction procedures used in these studies to obtain the results for quasi-monoenergetic neutrons from the mixed neutron energy spectra will be discussed in more detail in Section 6.3.

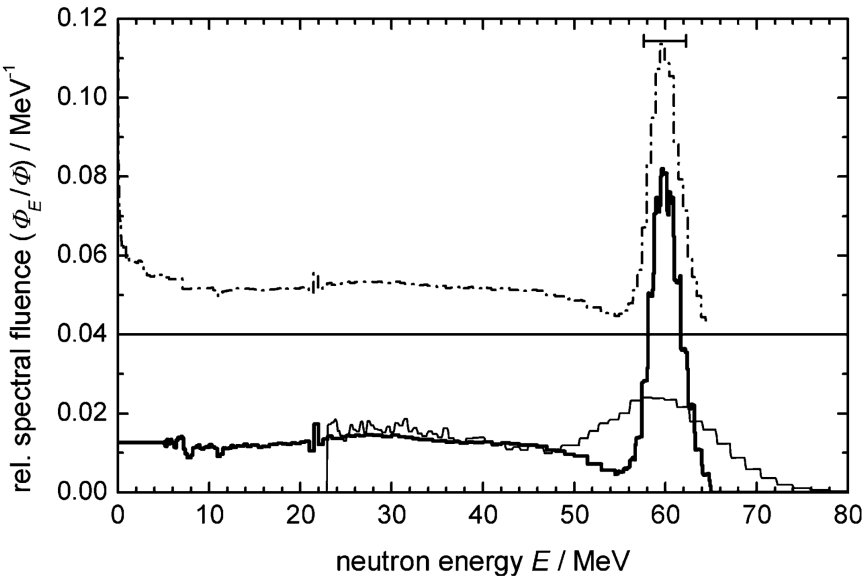

Figure 3.9: Measured neutron fluence spectrum (thick histogram), with a dose-weighted average energy of 41 MeV, used for the neutron RBE experiment by Nolte et al. [2005].

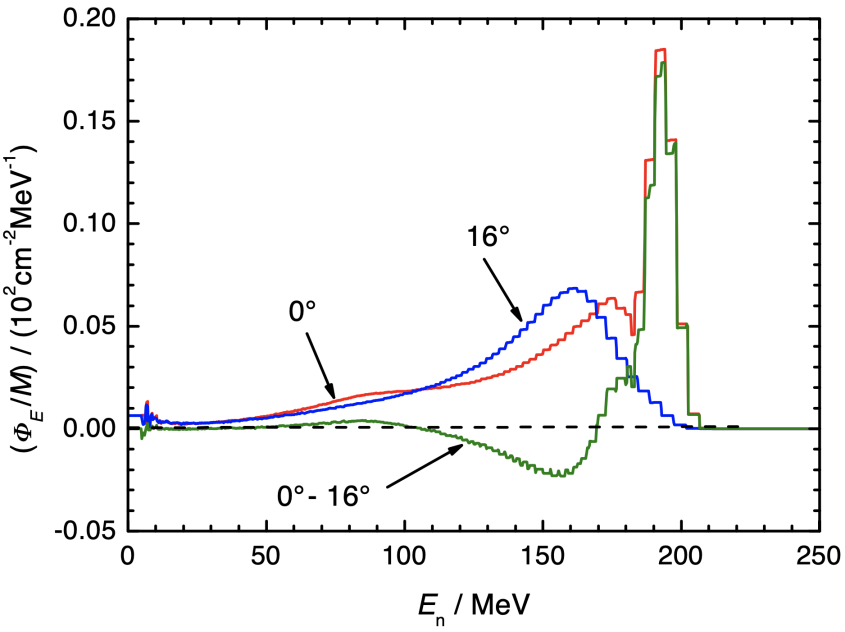

Figure 3.10: Measured neutron fluence spectra (at different angles relative to the incident proton beam) used for the neutron RBE experiment by Nolte et al. [2006]. The 0° spectrum has a dose-weighted average energy of 162 MeV.

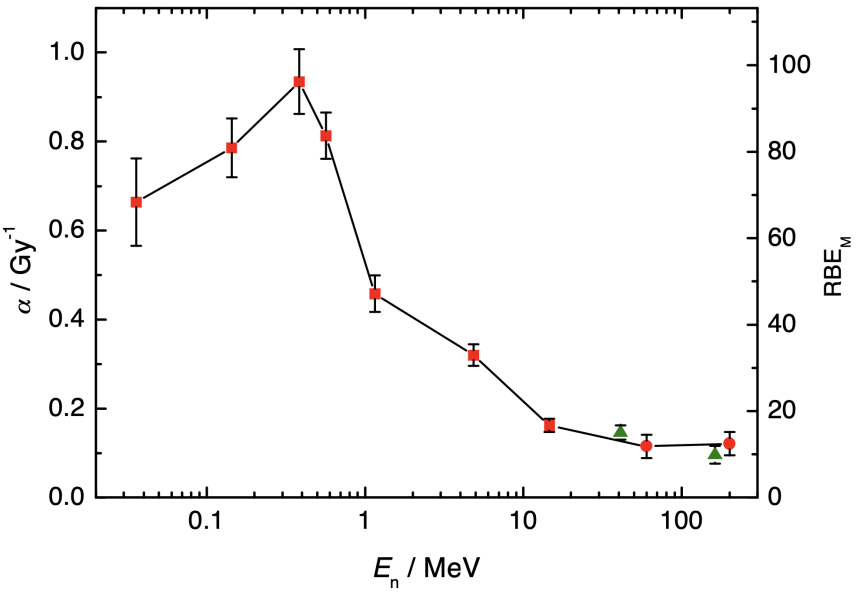

Figure 3.11: Results for the linear yield coefficient α and corresponding RBE_M at low dose for the induction of dicentric chromosomes over a range of neutron energies as reported by Nolte et al. [2005] and Nolte et al. [2006]. The squares indicate data measured using monoenergetic neutrons while the triangles indicate results obtained using quasi-monoenergetic neutron beams at the corresponding dose-weighted mean energies. The circles show the same quasi-monoenergetic data with corrections that were applied to account for the effects of neutrons from the low-energy continuum in order to determine the RBE for neutrons from the respective virtually monoenergetic high-energy peaks.

Table 3.1 summarises the results from the key neutron RBE experiments that have been conducted at energies > 20 MeV as discussed in this Chapter. It is evident that RBE results in this energy range are limited, and challenging to interpret given the variety of neutron energy fields, exposure conditions, biological systems, and biological endpoints that have been investigated. Given that neutrons with a wide range of energies extending up to several TeV are expected to contribute significantly to the radiation exposure of astronauts on missions planned to venture beyond LEO, the current state of experimental data for the biological effects of high-energy neutrons therefore calls for dedicated RBE experiments across this energy range.

Study	**Neutron radiation**	**Reference radiation**	**Biological system**	**Biological endpoint**	**RBE_M result**
Heimers [1999]	Mixed energy field with peaks around 1 MeV and 70 MeV	^{60}Co gamma rays	Human lymphocytes *in vitro*	Dicentric chromosome induction	96 - 113
Slabbert et al. [2000]	Mixed energy field with fluence-weighted average energy of around 29 MeV	^{60}Co gamma rays	Human tumour cell lines *in vitro*	Cell survival	1.6 - 3.5

Study	Neutron radiation	Reference radiation	Biological system	Biological endpoint	RBE_M result
Nolte et al. [2005]	Mixed energy field with dose-weighted average energy of 41 MeV	^{60}Co gamma rays	Human lymphocytes *in vitro*	Dicentric chromosome induction	14 ± 4
	Quasi-monoenergetic 60 MeV neutrons				11.4 ± 4.0
Nolte et al. [2006]	Mixed energy field with dose-weighted average energy of 162.1 MeV	^{60}Co gamma rays	Human lymphocytes *in vitro*	Dicentric chromosome induction	9 ± 3
	Quasi-monoenergetic 192 MeV neutrons				12 ± 4
Gersey et al. [2007]	Mixed energy field between 1 MeV and 800 MeV	^{137}Cs gamma rays	Human cultured fibroblast cells *in vitro*	Micronuclei induction	16.4 ± 1.4 (without water shield); 10.0 ± 1.0 (with water shield)
Kuhne et al. [2009]	Mixed energy field between 1 MeV and 800 MeV	^{137}Cs gamma rays	Japanese medaka fish embryos *in vivo*	Apoptosis for defined regions of the head (brains and eyes)	24.9 (95% confidence interval (CI): 13.6 - 40.7)
				Apoptosis for defined regions of the tail (mostly muscle tissue)	147 (95% CI: 29 - 240)
				Overall survival of embryos until ten days after hatching	48.1 (95% CI: 30.0 - 66.4)
Hada et al. [2010]	Mixed energy field between 1 MeV and 800 MeV	^{137}Cs gamma rays	Human epithelial cells *in vitro*	Fraction of cells with chromosome aberrations	26 ± 4

Study	Neutron radiation	Reference radiation	Biological system	Biological endpoint	RBE_M result
Slabbert et al. [2010]	Mixed energy field with fluence-weighted average energy of around 29 MeV	^{60}Co gamma rays	Human T-lymphocytes *in vitro*	Micronuclei induction	1.8 - 8.0
Vandersickel et al. [2014]	Mixed energy field with fluence-weighted average energy of around 29 MeV	^{60}Co gamma rays	Human lymphocytes *in vitro*	Micronuclei induction	1.56 - 3.57
				γ-H2AX foci induction	$0.64 - 0.70$
Juerß et al. [2017]	Mixed energy field with a mean energy of 70.5 MeV	X-rays	MCF10A normal human breast cells *in vitro*	Cell survival	2.09
				γ-H2AX foci induction	4.47

Table 3.1: Summary of the key results from neutron RBE experiments that have been conducted at energies greater than 20 MeV.

3.3.2 The dependence of neutron RBE on dose and dose rate

The dependence of neutron RBE on dose

Values for neutron RBE vary with the dose at which it is evaluated. In general, measured values for neutron RBE increase with decreasing dose, and the primary reason for this lies in the differing shapes of the dose-response relationships for neutron radiation versus the low-LET reference radiation with which it is compared [Valentin, 2003]. This effect is illustrated in Figure 3.12 which shows a comparison of the cell survival curves resulting from neutron and X-ray irradiations. In radiobiology, the differing shapes of such dose-response curves are interpreted (at least in the low dose region) according to the statistical linear-quadratic dose-response model which states that the risk of a biological effect E (at least for primary lesions [Valentin, 2003]) depends on the absorbed dose D according to,

$$E = \alpha D + \beta D^2, \tag{3.6}$$

where α represents the linear dependence of the biological effect on dose due to single-track events, and β represents the quadratic dependence of the biological effect on dose due to two-track events [Niwa et al., 2015].

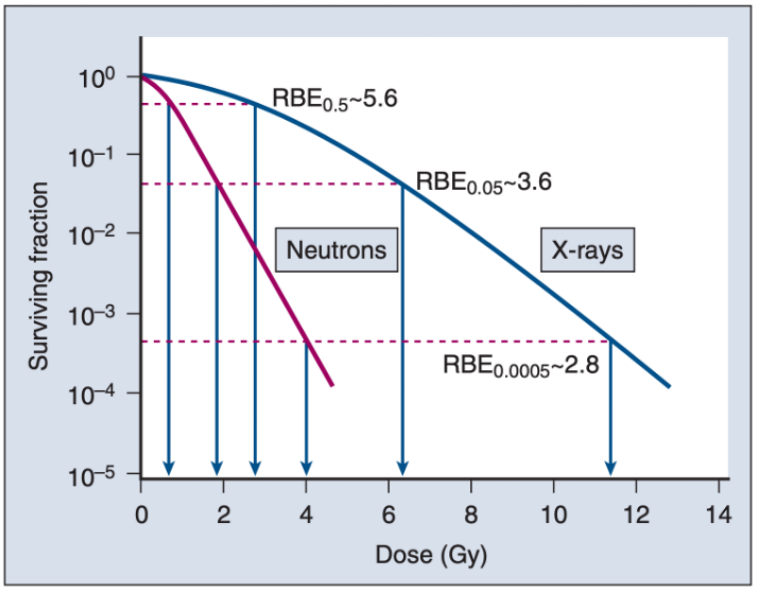

Figure 3.12: Comparison of typical cell survival curves for exposure to neutron and X-ray radiation to illustrate the increase of neutron RBE with decreasing dose [Zeman et al., 2020].

The interpretation of the linear-quadratic dose-response model is based on an understanding of the physics of energy deposition by ionising radiation and the assumption that biological response results from DNA receiving random "hits" in a probabilistic manner [Zeman et al., 2020]. High-LET radiation, like neutrons, tend to have higher α/β ratios than low-LET radiation, indicating a higher relative effectiveness of single-track events per dose [Joiner and van der Kogel, 2019]. On dose-effect plots such as that shown in Figure 3.12, low-LET radiation therefore exhibits a more significant "shoulder" at low doses than high-LET radiation, indicating that for low-LET radiation, the damage has to "accumulate" before the biological effect becomes significant [Zeman et al., 2020]. The idea behind this model was first understood based on the nature of chromosome aberrations, as illustrated in Figure 3.13.

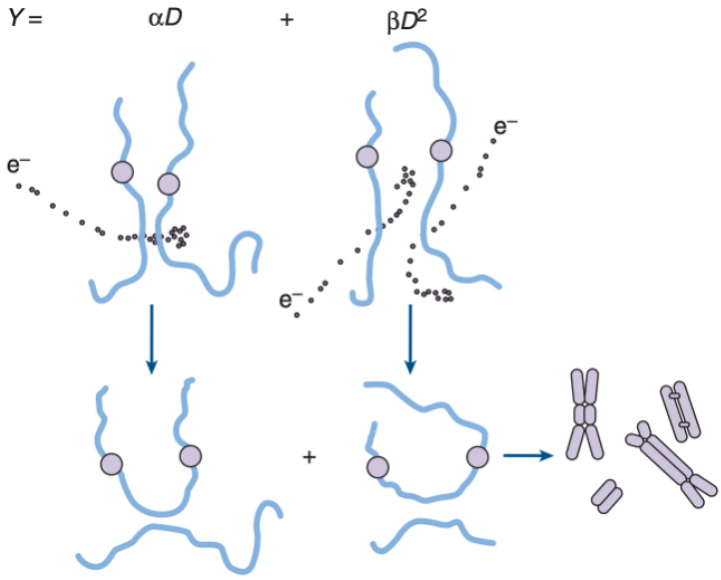

Figure 3.13: Diagram demonstrating how average chromosomal aberration yield Y can be modelled according to the linear quadratic dose-response relationship [Zeman et al., 2020]. The α-component describes chromosome aberrations that result from a single electron producing a break in each of two different chromosomes. The β component describes chromosome aberrations that result from two different electrons producing breaks in two different chromosomes.

It is therefore primarily due to the different shapes of the dose-response curves of neutrons versus the low-LET reference radiation that the value for neutron RBE generally increases as the dose is decreased. The neutron RBE reaches a limiting maximum value at low doses called the RBE_M, as defined in Equation 3.5. Measured values of RBE_M are used by the ICRP to determine the selection of the radiation weighting factors w_R for inducing stochastic effects at low doses [Valentin, 2003].

It should be noted that deterministic effects are characterised by a threshold dose and therefore corresponding maximum RBE values are not characterised by RBE_M. The maximum RBE values for deterministic effects are denoted by RBE_m and the resulting weighted dose values for the purposes of radiation protection are expressed in grays (Gy) rather than sieverts (Sv) [Valentin, 2003; Ferrari et al., 2023].

Owing to a lack of human data from epidemiological observations, most neutron RBE_M values used to select the ICRP weighting factors w_R have been determined from measurements of dicentrics in human lymphocytes [Schmid et al., 2003]. There are many practical problems in the determination of neutron RBE at low doses, as discussed in detail in ICRP Publication 92 [Valentin, 2003], and it has been noted that the large uncertainty for these measurements arises predominantly from the poorly known initial slope of the dose-response for the reference radiation [Schmid et al., 2003]. The issues in measuring the dose-response of low-LET radiations at low doses, along with the fact that there is no international recommendation for the specific photon sources that should be used as reference radiations, contribute significantly to the difficulties in determining comprehensive health risk-related models based on existing neutron RBE experimental data [Valentin, 2003].

For radiation protection purposes on Earth, the dose-range of interest for the induction of stochastic effects is usually below a few hundred mGy, and therefore the maximum value at low doses RBE_M is relevant for the selection of radiation weighting factors for use in cancer-risk models. It has however been suggested that cancer risk for doses larger than 1 Gy will become important when considering long-term space missions [Schneider and Walsh, 2009; Walsh et al., 2019]. In this case, it will become necessary to consider the shape of the dose-response for radiation induced cancer at higher doses and using the low-dose limit is no longer appropriate. Schneider and Walsh [2009] determined that use of a dose-dependent neutron RBE could lower current projected cancer risks for long-term space missions by 15% to 20%.

The dependence of neutron RBE on dose rate

It is generally accepted that neutron RBE increases as the dose rate decreases and this observed behaviour is largely attributed to the reduced effectiveness of the low-LET reference radiation at low dose rates, rather than a significant enhancement in neutron-induced damage. The reason for the reduced effectiveness of low-LET radiation relative to neutrons at low dose rates is illustrated in Figure 3.14, which shows typical survival curves for mammalian cells that are exposed to single and fractionated doses of X-rays and fast neutrons. Dose-response curves of low-LET radiation exhibit a more significant "shoulder" at low doses than high-LET radiation (as discussed above), and Figure 3.14 shows that as the fractionated regime allows for the repair of sublethal damage between doses, this shoulder is repeated with each fraction and hence neutron RBE will be progressively larger for fractionated treatments as the number of fractions increases and the dose per fraction decreases. Continuous low-dose-rate radiation exposure is analogous to receiving an infinite number of infinitely small fractions, and hence it is expected that neutron RBE would increase at low dose rates [Hall and Giaccia, 2019].

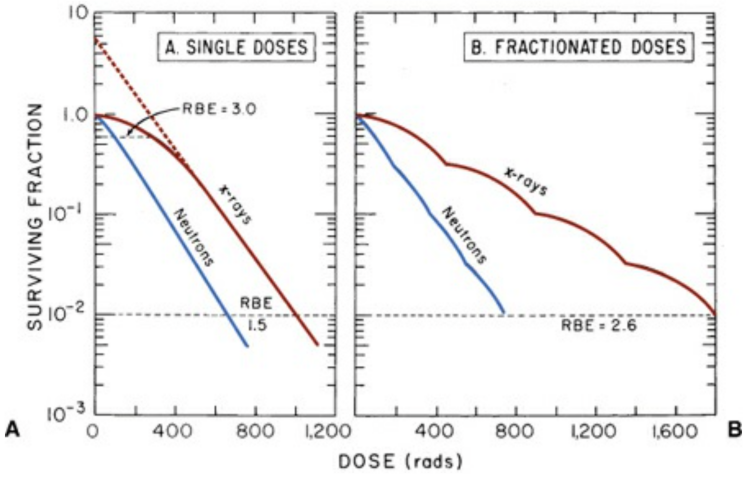

Figure 3.14: Comparison of typical cell survival curves for exposure to single and fractionated doses of neutron and X-ray radiation to illustrate the increase of neutron RBE with decreasing dose rate [Hall and Giaccia, 2019].

Most of our knowledge regarding the induction of stochastic effects from exposure to external ionising radiation, comes from the epidemiological Life Span Studies of Japanese atomic bomb survivors. These studies provide the only consensual source of data for cancer risk as a function of dose albeit at high dose rates [Restier-Verlet et al., 2021]. Significant uncertainties remain at lower dose limits and the validity of the linear no-threshold hypothesis (discussed in Section 3.1) and its independence of dose and dose rate is a controversial topic [Hall and Giaccia, 2019]. In order to avoid the substantial uncertainties inherent in studies of radiation effects at low doses and low dose rates [Valentin, 2003], the radiation risks associated with the exposures relevant to radiation protection are generally extrapolated from data obtained at high doses and dose rates using a recommended dose and dose-rate effectiveness factor (DDREF), although this remains a subject of active debate [Nair et al., 2019].

Currently, regulatory bodies only apply a DDREF to low-LET radiation, while the effects of high-LET radiation are considered to have negligible dependence on dose and dose rate [Nair et al., 2019]. As discussed above, the dependence of neutron RBE on dose rate is traditionally attributed to the dose-rate dependence of the effects of the reference low-LET radiation, rather than differences in the severity of the damage induced by neutrons. However, an increasing number of studies investigating the biological effects of high-LET radiation have demonstrated an inverse dose-rate effect for carcinogenesis or other biological effects, implying that an increasing effect is observed with decreasing dose rate under particular circumstances [Stevens et al., 2014].

In a recent study, Nair et al. [2019] investigated DNA DSBs and repair following irradiation of human lymphocytes with a p(66)/Be(40) neutron beam for high and low dose-rate exposures. Figure 3.15(a) shows their results for the investigation of DNA DSBs induction for a range of neutron doses at 30 minutes post exposure. The γ-H2AX foci assay is one of the most sensitive endpoints used in low dose and dose-rate studies and the number of γ-H2AX foci observed closely correlates with the number of DNA DSBs [Rühm et al., 2018]. The results in Figure 3.15(a) indicate that on average, the high-dose-rate neutron irradiation induced 40% more DNA DSBs per cell than at low dose rates. Results for the subsequent investigation of the DNA DSBs repair kinetics studied at different time points following a 1 Gy neutron dose are shown in Figure 3.15(b). The rate of foci loss corresponds to the repair of DSBs, and it was found that the half-life of foci disappearance was longer for low-dose-rate than for high-

dose-rate neutron irradiation. The results from this study demonstrated a significant effect of neutron dose rate on DNA damage and provided the first indication that the dose rate should be considered in the evaluation of neutron RBE and the development of corresponding cancer risk models.

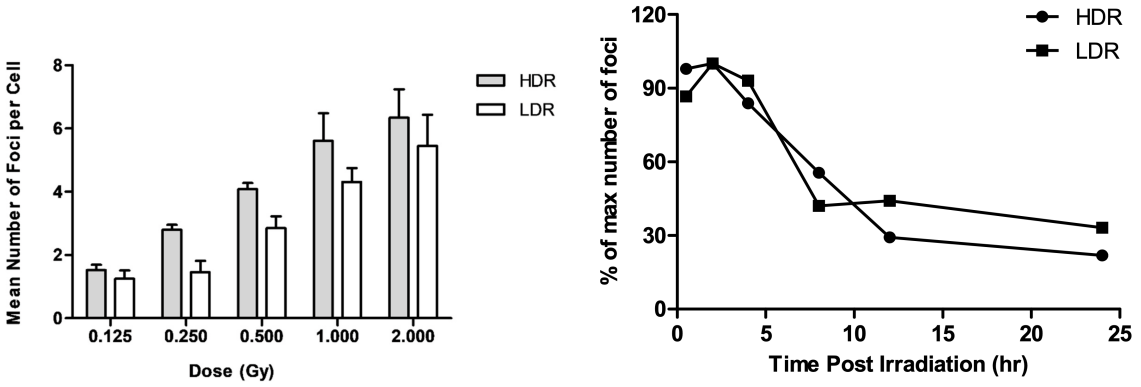

(a) (b)

Figure 3.15: Results from a study investigating DNA DSBs and repair following the irradiation of human lymphocytes with a p(66)/Be(40) neutron beam for high (0.400 Gy/min) and low (0.015 Gy/min) dose rate (HDR and LDR) exposures [Nair et al., 2019]: (a) The average yield of γ-H2AX foci as a function of dose at 30 minutes post exposure, and (b) the average yield of γ-H2AX foci at different time points following the irradiation to 1 Gy.

During long-term space missions, astronauts will be exposed to chronic low doses and low dose rates of secondary neutrons. The use of DDREF for the extrapolation from measurements of results relevant to radiation protection scenarios, and the lack of knowledge pertaining to the low dose rate effects of neutrons, are among the largest sources of uncertainties in the evaluation of neutron RBE and the development of health risk models for space travel [Nair et al., 2019; Fisher et al., 2020].

3.3.3 The dependence of neutron RBE on the target composition and geometry

One of the most significant challenges in a comprehensive evaluation of neutron RBE results is the lack of direct data pertaining to human exposure to neutron radiation [Schmid et al., 2003]. The only significant epidemiological data comes from the Life Span Studies of Japanese atomic bomb survivors who were exposed to a mixture of neutrons and gamma rays, however the neutron contribution to the total dose is calculated to be too small (at most 1%) to allow for neutron-specific carcinogenic risks to be extrapolated without considerable uncertainties [Goodhead, 2019]. As a result, the evaluation of neutron RBE is reliant on measurements with animals and cellular systems.

While human data are lacking, there is a wealth of experimental evidence for cancer induction, as well as other biologically damaging effects, in animal models by neutron radiation [Goodhead, 2019; Stricklin et al., 2021]. The International Agency for Research on Cancer classified neutrons as a Group 1 carcinogen primarily on the strong evidence of carcinogenic effects in a variety of animal experiments with mice, rats and monkeys [Goodhead, 2019]. However, the extrapolation of animal data to an evaluation of neutron effects in humans requires extreme caution. In addition to differences that may arise due to the different biological mechanisms involved, neutron radiation can be particularly problematic because of the substantial difference of the resulting radiation field inside receptors of different compositions, geometries and

sizes [Valentin, 2003]. As discussed in Section 3.3.1, the secondary particle radiation field produced in a particular target, and hence the neutron RBE, depends on the incident neutron energy spectrum. The situation is further complicated by how that spectrum and the resulting secondary radiation field is modulated in biological targets of different dimensions and compositions. Indeed, the most significant changes in neutron radiation weighting factors from ICRP Publication 60 to ICRP Publication 103 (as shown in Figure 3.4) arose from a re-evaluation of the increased contribution from the photon component of the neutron dose when low-energy neutrons interact in larger receptors [Baiocco et al., 2016]. Such effects must therefore be carefully considered when extrapolating results from small receptors, like mice or *in vitro* cell systems, to larger receptors, like humans.

The importance of taking these considerations into account was illustrated in the results of a study by Baiocco et al. [2018], where they applied the *ab initio* neutron RBE model (as shown in Figure 3.6) to an experimental setup used for stem cell irradiations. The model was used to predict RBE values for cell exposures to monoenergetic beams and to a broad energy distribution neutron field. Comparisons of these results to those determined by Baiocco et al. [2016] for a 30 cm sphere irradiated in an isotropic field are shown in Figure 3.16. The discrepancies (due to the different target and irradiation geometries) emphasize the necessity of fully characterising neutron fields in terms of physical interactions in order to understand neutron biological effects over a range of energies and reduce the current uncertainties surrounding radiation protection standards [Baiocco et al., 2018].

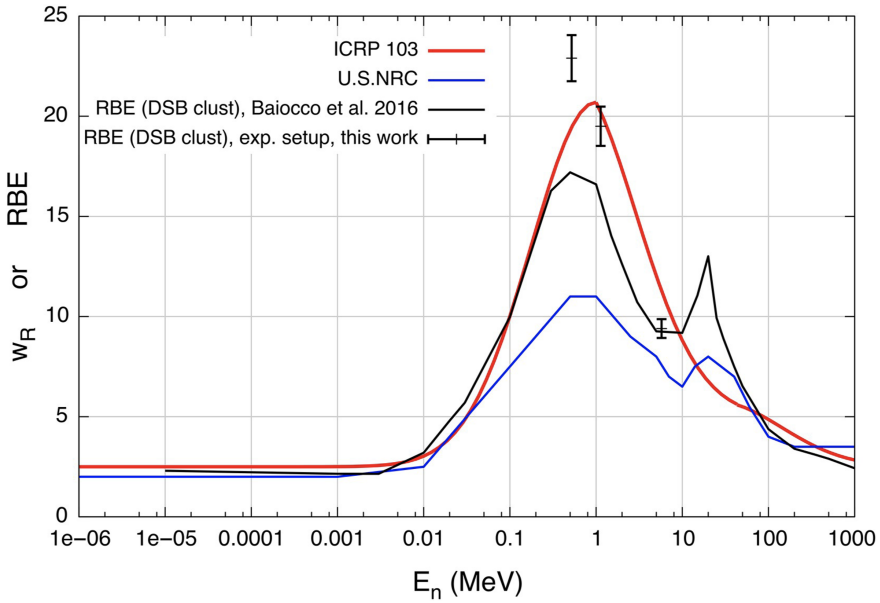

Figure 3.16: Results for an *ab initio* neutron RBE model applied to a particular experimental setup for cell exposures to monoenergetic beams and to a broad energy distribution neutron field (black points) [Baiocco et al., 2018]. The model results are compared to those determined for a 30 cm sphere irradiated in an isotropic field (black line), and to the ICRP (red line) and U.S. NRC (blue line) standards for radiation weighting factors for stochastic effects.

3.3.4 The dependence of neutron RBE on biological factors

Measured values for neutron RBE are strongly dependent on the biological system and specific biological endpoints investigated. The complexity of these dependencies must be carefully considered when interpreting the reported experimental results. The currently recommended ICRP neutron radiation weighting factors are based on a conservative pooling together of RBE

results from many experiments in different biological systems for various biological endpoints [Lund et al., 2020]. Based on the range of different biological studies and results available, the selection of these radiation factors involves a considerable element of judgement. As such, current radiation weighting factors are necessarily non-specific and are only intended for use in general radiation protection recommendations, rather than for detailed individual risk assessment [Lund et al., 2020]. Given the potential severity of the damaging health effects of neutron radiation in space, carefully considered and detailed RBE measurements involving specific biological endpoints relevant to space radiation health risks, are required.

Biological endpoints for stochastic effects

Radiation weighting factors for stochastic effects are generally based on neutron RBE measurements involving cytogenetic analysis, that is, the analysis of chromosome aberrations that are observed in exposed cells during metaphase of the cell cycle. As discussed in Section 3.1, DNA is the principle target for radiation-induced damage, with DNA DSBs being the most important and difficult lesions to repair. The mechanisms of DNA repair are complicated and depend on a variety of biological factors, including the nature and location of the DSBs, the phase of the cell cycle, the cell-type investigated, and the micro-environmental conditions [Joiner and van der Kogel, 2019]. Within cells, the consequences of incomplete and improper repair become visible in the form of chromosome aberrations. Chromosome aberrations are a sensitive and measurable indication of radiation exposure, and are generally considered to provide information on associated health risks, particularly with regards to cancer induction. As a result, the neutron weighting factors for stochastic effects are based primarily on experimental results for neutron RBE obtained via cytogenetic analysis – that is, the analysis of chromosome aberrations in human peripheral blood lymphocytes *in vitro* [Stricklin et al., 2021; Horst et al., 2022a].

To respond to DNA damage (whether it be spontaneous or induced by ionising radiation) mammalian cells have developed complex signal transduction, cell-cycle checkpoint and repair pathways. Furthermore, molecular checkpoints at various stages of the cell cycle, as shown in Figure 3.17, work to stop the cell cycle to enable repair and prevent passing the damage onto subsequent daughter cells [Ainsbury et al., 2011]. Human peripheral blood lymphocytes are popular for cytogenetic analysis and represent a cell population that is predominantly in the G0 phase of the cell-cycle. Samples are easy to extract from human donors with minimally invasive techniques, and following irradiation, these cells can be stimulated *in vitro* via the addition of phytohaemagglutinin to enter the M phase of the cell cycle where chromosomes are condensed to form the characteristic 'X-shape' appearance consisting of two sister chromatids joined together by the centromere, as illustrated in Figure 3.18. A metaphase arrest agent drug, like colcemid, is then applied to allow for the investigation of DNA damage in cells in the metaphase where chromosome aberrations can be detected and analysed [Ainsbury et al., 2011].

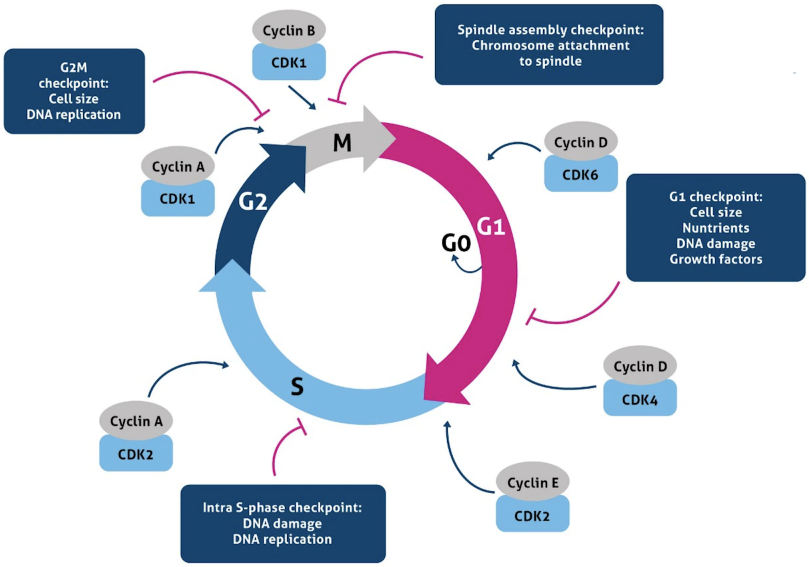

Figure 3.17: The cell cycle and its checkpoints [Proteintech, 2024].

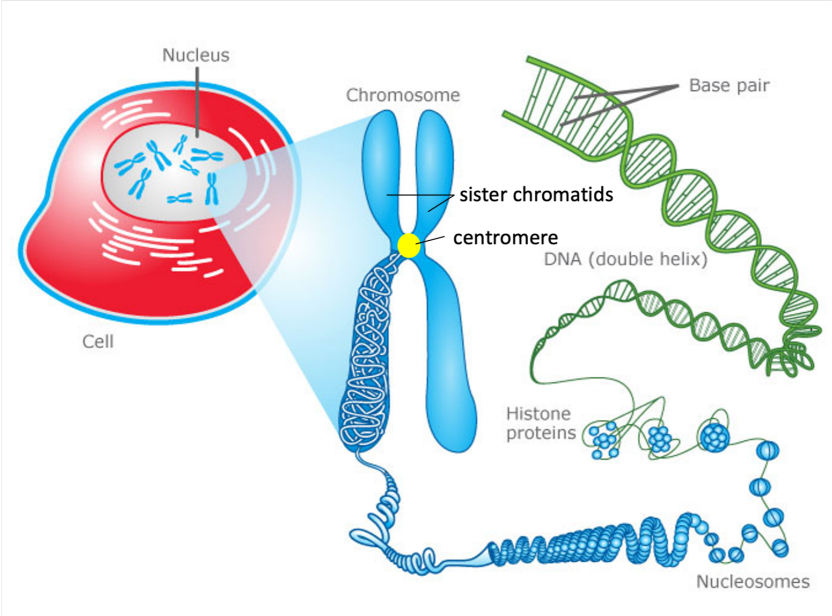

Figure 3.18: Characteristic form of chromosomes during the metaphase of the M phase [University of Waikaito, 2011].

Dicentric analysis (unstable aberrations)

The most commonly occurring chromosomal aberrations are dicentric chromosomes. These are formed when two chromosomes get interconnected with each other to form an aberrant chromosome with two centromeres [Ainsbury et al., 2011]. Figure 3.19 shows an example of a dicentric chromosome and its accompanying acentric fragment, visualised through Giemsa staining. While exact methods and standard protocols for the analysis of dicentric chromosomes vary, as discussed in detail by Ainsbury et al. [2011], dicentric chromosomes can generally be visualised relatively easily by simple staining methods that have become routine in many radiobiology laboratories. The reliability of these techniques, along with the verified sensitivity of the assay to doses as low as 100 mGy, have contributed to dicentric chromosome analysis

becoming widely recognized as a gold standard in biodosimetry [Herate and Sabatier, 2020].

Dicentric chromosomes are unstable aberrations, meaning that they are generally lost at mitosis and so affected cells are eliminated from the proliferative pool at the rate at which cell renewal occurs [Ainsbury et al., 2011]. Although dicentric chromosomes themselves are therefore unlikely to survive long enough to directly contribute to the development of long term effects like cancer, they are induced at an initial frequency similar to more persistent forms of chromosomal damage and thus are generally accepted as a reliable biomarker for the severity of radiation exposure and form the basis for many RBE experiments pertaining to stochastic effects [Stricklin et al., 2021].

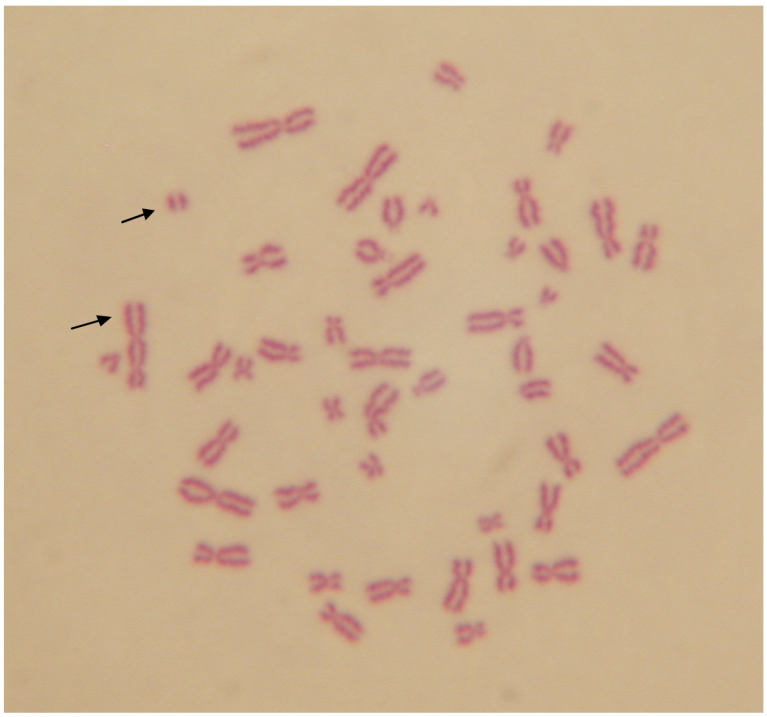

Figure 3.19: Example of a dicentric chromosome and its accompanying acentric fragment (indicated by the arrows), visualised through Giemsa staining [Ainsbury et al., 2011].

Translocation analysis (stable aberrations)

Translocation aberrations are formed when segments of one chromosome are transferred to another chromosome. The detection of translocation aberrations requires a more sophisticated analysis than those traditionally used for asymmetric aberrations like dicentrics, and is now possible through the technique of Fluorescence In-Situ Hybridization (FISH) coupled with various chromosome staining methods as described in detail by Ainsbury et al. [2011]. Figure 3.20 shows an example of translocation aberrations as detected using the multicolour fluorescence in-situ hybridization (mFISH) procedure. The lower detection limit of this technique is generally estimated to be around 300 mGy, however its applicability at lower doses still needs to be further investigated [Herate and Sabatier, 2020].

One of the drawbacks of the dicentric assay is that dicentrics are 'unstable' aberrations, which means that they are not able to pass through repeated cell divisions and into the daughter cells of the subsequent generations. In contrast, translocation aberrations are stable – they can survive through multiple cell divisions and as a result be detected many years after exposure [Ainsbury et al., 2011]. The persistence of translocation aberrations in a cell population over time makes them a more interesting endpoint to investigate as their presence can be directly

linked to long term health effects like cancer development [Gasparini et al., 2007]. The study of translocation aberrations is particularly relevant with regards to space travel, as this endpoint could be observed in an astronaut's blood sample years after returning from space travel and directly compared to data from Earth-based experiments on the impact of different types of radiation exposure.

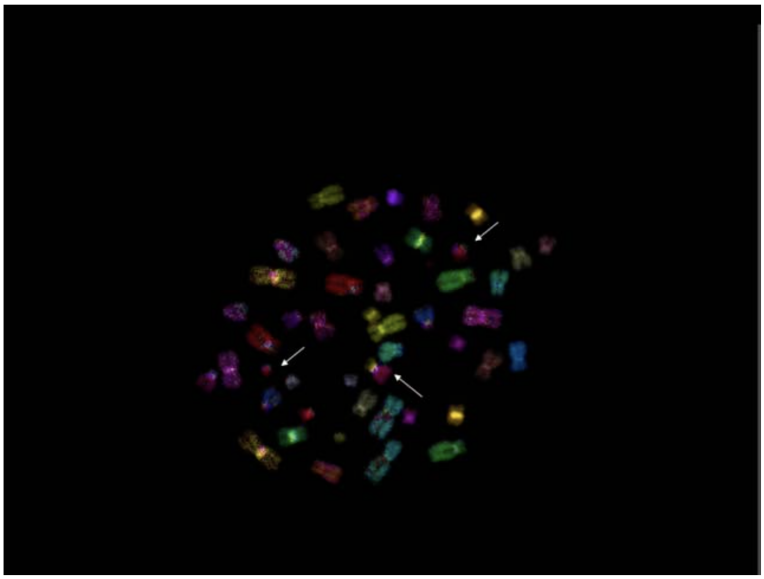

Figure 3.20: Example view of translocation aberrations (indicated by the arrows) in a metaphase stained by mFISH where a pseudocolour has been associated to each pair of chromosome [Ainsbury et al., 2011].

3.3.5 Summary of the current state of knowledge surrounding neutron RBE within the context of space exploration

A comprehensive evaluation of the biological effects of neutron radiation is extremely challenging given the complexity of the dependence of neutron RBE on a combination of both physical and biological factors, as summarised in Table 3.2.

Physical	**Biological**
Energy	Biological end point
Dose	Tissue type (sensitivity)
Dose rate	Tissue volume and depth
Material composition	Microenvironment
Target geometry	Cell-cycle phase

Table 3.2: Summary of the physical and biological factors that impact neutron RBE [Stricklin et al., 2021].

Current radiation health risk models developed within the context of future space exploration involve considerable uncertainties surrounding our knowledge of the biological effects of neutron radiation at relevant energies, doses, dose-rates, biological systems and endpoints. Based on the preceding detailed discussions on the nature of the dependence of neutron RBE on these factors, it is clear that any meaningful measurement of neutron RBE should be accompanied by a carefully considered evaluation of how each of these variables have influenced the final result.

Such a goal can only be achieved via the harmonisation of both physics (in terms of a detailed characterisation of the measured neutron field) and radiobiology (in terms of understanding and quantifying the associated biological effects).

This project aims to address the existing knowledge gaps pertaining to the biological effects of high-energy neutrons and improve neutron radiation carcinogenesis risk estimations by building on the previous experiments by Nolte et al. [2005] and Nolte et al. [2006] to develop a standardised approach to measure neutron RBE_M at iThemba LABS. As will be discussed in the following chapters, the high-energy neutron facility at iThemba LABS has the potential to be uniquely instrumental in providing impactful experimental data regarding neutron RBE within the context of future space exploration.

4 Neutron beam production and metrology at iThemba LABS

The iThemba LABS fast neutron facility (D-line) is capable of producing quasi-monoenergetic neutron beams with energies between 30 MeV and 200 MeV. The facility first became operational in the 1980s and recently underwent a major infrastructural upgrade, which was completed in 2020/2021 and included a redesign of the vault geometry, the installation of a new target ladder, and the installation of a new harp to improve proton beam focusing [Ndlovu et al., 2019]. The National Metrology Institute of South Africa (NMISA) has officially designated the D-line to be developed as a 'medium to high-energy neutron metrology' facility in line with the International Committee for Weights and Measures Mutual Recognition Arrangement (CIPM MRA) requirements. It is one of the only facilities in the world capable of providing quasi-monoenergetic neutron beams with energies of up to 200 MeV [Pomp et al., 2014].

This chapter provides a description of neutron beam production in the D-line and the metrological methods that are used for the characterisation of the neutron beam energy distribution and fluence via Time-Of-Flight (TOF) spectroscopy using a BC501A liquid scintillation detector (for high energy resolution spectral fluence measurements at low beam intensities) and a ^{238}U fission ionisation chamber (FC) (for standardised neutron fluence measurements at high beam intensities), in combination with monitor detectors that record the charge of the proton beam and neutron yield during experiments. These metrological methods are illustrated via their application to measurements of neutrons with a peak energy of 62.34 ± 0.37 MeV and gamma rays produced by a 66.48 MeV proton beam irradiating an 8.0 mm lithium target at an emission angle of 0° relative to the incident beam.

4.1 Neutron beam production

The Separated Sector Cyclotron (SSC) at iThemba LABS can accelerate protons with energies between 30 MeV and 200 MeV. Figure 4.1 illustrates the position of the D-line experimental vault relative to the SSC at iThemba LABS and Figure 4.2 illustrates the layout of the D-line experimental vault. Quasi-monoenergetic neutron beams with energies in the range of 30 MeV to 200 MeV are produced in the D-line through (p, n) reactions of protons from the SSC on lithium, beryllium, or carbon targets. The targets, with varying thicknesses, are mounted on a remotely operated ladder inside a scattering chamber. Proton beams that have passed through the neutron production targets are deflected by a dipole magnet into a beam dump. The experimental area is separated from the neutron production area by thick steel shielding. The steel collimator has openings at angles of 0° and 16° relative to the direction of the incident proton beam and is lined with a layer of borated wax and polyethylene. The collimator openings have rectangular cross-sections of 4.5 cm × 4.5 cm with exits into the experimental area at 4.00 m from the target.

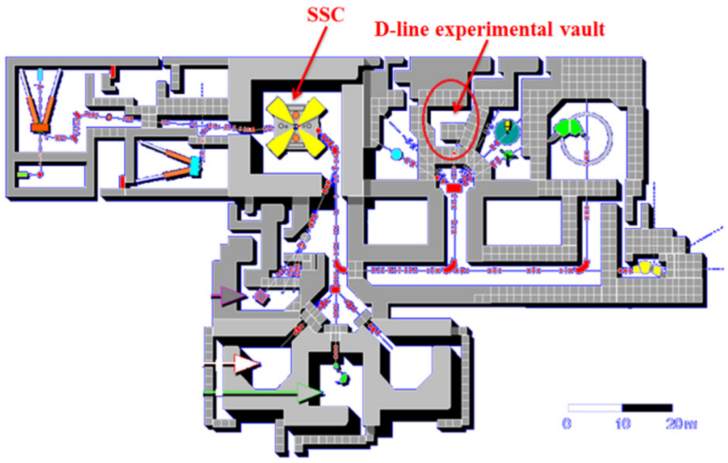

Figure 4.1: The position of the D-line experimental vault relative to the SSC at iThemba LABS [Ndlovu et al., 2019].

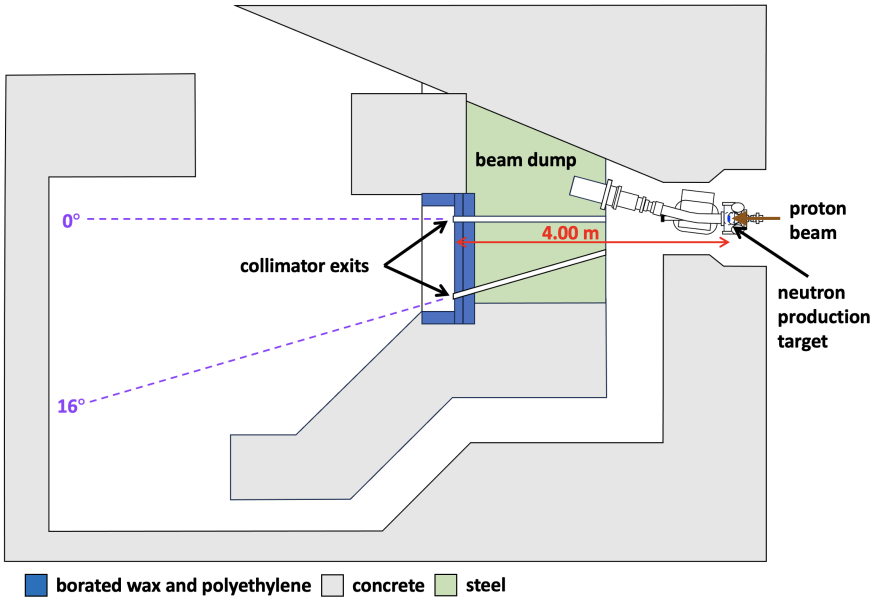

Figure 4.2: An overview of the layout of the D-line experimental vault at iThemba LABS.

In neutron metrology, Time-Of-Flight (TOF) spectroscopy is a technique used to determine the energy of neutrons by measuring the time that they take to travel a known distance. The conditions required for conducting TOF measurements at iThemba LABS are achieved via utilisation of a beam pulse selector that suppresses a certain fraction of proton bunches in order to increase the time separation between pulses. The time spread of a singular proton bunch is around 1 ns and the maximum pulse separation is 360 ns. Enlarging the time interval between pulses allows for the time at which a neutron is detected at a certain distance to be related to the time at which a suitable pulse selector reference signal occurs, so that the TOF of the neutron, and correspondingly the neutron energy can be calculated.

Figure 4.3 shows the spectral distribution of high-energy neutrons measured via TOF spectroscopy at iThemba LABS for different energies of incident protons interacting in a lithium target [Nolte et al., 2007]. Neutrons are produced in the lithium target via the ^{7}Li(p, n)^{7}Be reaction with energy spectra that comprise two distinctive components: a high-energy peak and an adjacent low-energy continuum. The high-energy peak corresponds to direct reaction

transitions to the ground or low-lying excited states of the product ^{7}Be nuclei, while the lower-energy continuum is largely attributed to neutrons that are emitted in break-up reactions in the target. The intensity of the high-energy peak is maximal in the forward direction and decreases significantly with increasing angle relative to the incident proton beam. The dependence of the intensity of the lower-energy continuum on emission angle is far less pronounced, and this feature can in principle be used to discriminate between the effects of the respective components of the spectrum [Nolte et al., 2002]. This is demonstrated in Figure 4.4(a), which shows the neutron energy spectra measured at 0° and 16° for 100 MeV protons on a 6 mm lithium target. A quasi-monoenergetic neutron spectrum is then obtained as a "difference spectrum" via the subtraction of the spectrum measured at 16° from that measured at 0°. This is illustrated in Figure 4.4(b), where the lower-energy continuum is evidently strongly suppressed. The measured high-energy peak exhibits a width that is associated with energy loss of protons in the target, as well as the energy resolution of the detector.

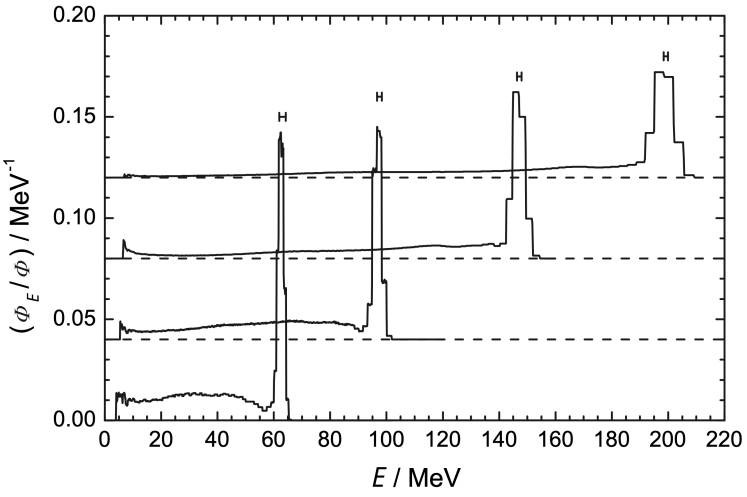

Figure 4.3: Normalised spectral distribution of neutrons measured at different energies using TOF spectroscopy at iThemba LABS [Mosconi et al., 2010]. The horizontal bars indicate the intrinsic energy widths of the high-energy peaks due to the energy loss of incident protons interacting in the lithium target.

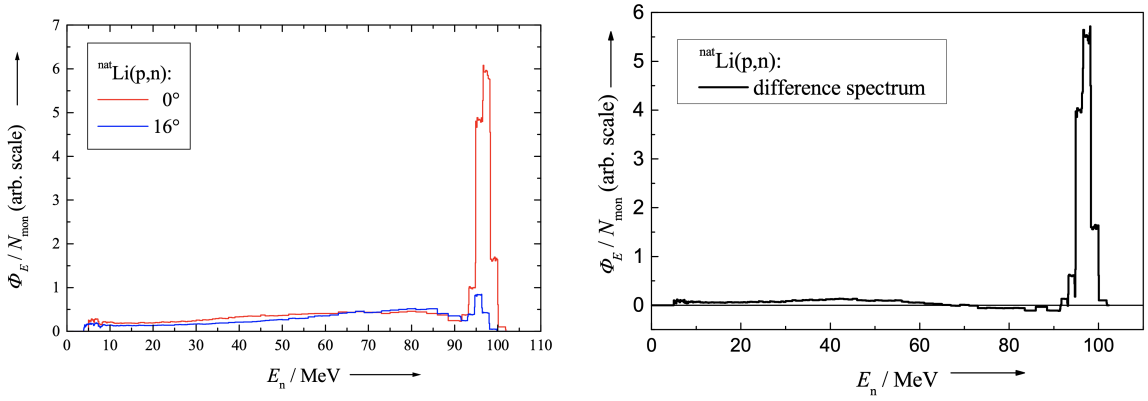

(a) **(b)**

Figure 4.4: (a) Measured neutron spectra at emission angles of 0° and 16° relative to the incident beam of 100 MeV protons interacting in a 6.0 mm lithium target at iThemba LABS. (b) The difference spectrum that is obtained via subtraction of the 16° spectrum from the 0° spectrum [Ndlovu et al., 2019].

4.2 Monitoring of the neutron beam conditions

In the D-line, the properties of the neutron beam are monitored continuously throughout experiments in order to ensure their traceability for metrology purposes. The "monitor detectors" include a Faraday cup placed in the proton beam dump, and a disc-like NE102 scintillation detector placed at the exit of the 0° collimator.

As mentioned in Section 4.1, proton beams that have passed through the neutron production targets are deflected by a dipole magnet into a beam dump. A Faraday cup is used to monitor the beam current by measuring the charge of this deflected proton beam. The integrated beam current or 'beam charge' Q is recorded in 60 s intervals during experiments.

The beam current is proportional to the neutron fluence rate if the proton beam is stable and well-focused, however this relationship is used with caution as leakage currents and the beam focus on the target can vary with time. For this reason, the neutron fluence rate at the 0° collimator exit is directly monitored using a 100.0 mm diameter, 2.0 mm thick, disc-like NE102 scintillation detector that is operated in transmission mode and utilizes a system based on synchronized light-emitting diode (LED) pulses in order to stabilise gain changes that are caused by sudden variations in count rate [Mosconi et al., 2010]. The scintillation detector is optically coupled to an XP2020 photomultiplier tube and directed through the electronics modules as shown in Figure 4.5. A pulse-height threshold chosen to suppress gamma ray events is set, and the counts from the slow dynode M_{slow} and fast anode M_{fast} signals from the NE102 detector are recorded within 60 s time-intervals. These counts are compared to the corresponding integrated beam current that is measured by the Faraday cup in order to ensure constancy.

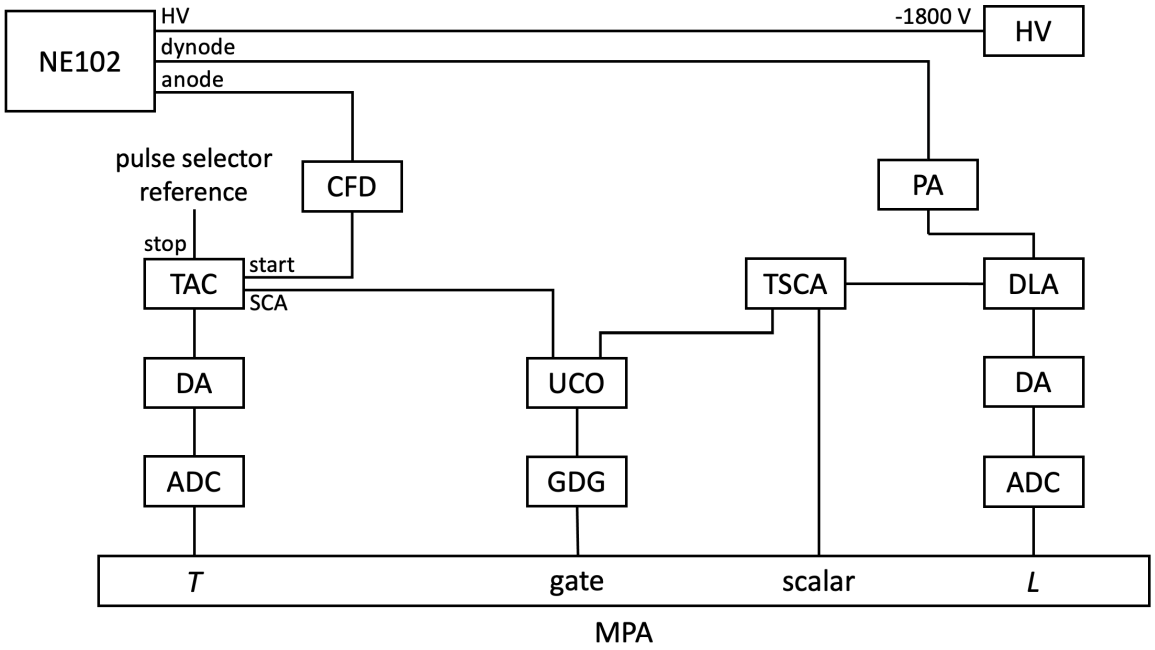

Figure 4.5: Schematic of the arrangement of the electronic modules for acquisition of data from the NE102 monitor detector. Table 4.1 contains a key to the abbreviations used in this diagram.

ADC	analogue-to-digital converter	MPA	multiparameter data acquisition system
CFD	constant fraction discriminator	PA	pre-amplifier
DA	delay amplifier	SCA	single channel analyser
DLA	delay line amplifier	T	time-of-flight parameter
GDG	gate and delay generator	TAC	time-to-amplitude converter
HV	high voltage	TSCA	timing single channel analyser
L	light output parameter	UCO	coincidence unit

Table 4.1: Key to the abbreviations used in Figure 4.5.

The stability of the neutron spectral distribution throughout measurement runs is also monitored through TOF measurements made with the NE102 detector, using the pulse selector signal as a reference timing signal. A typical TOF spectrum recorded by the NE102 monitor detector during a single measurement run is shown in Figure 4.6. The TOF spectra are used to determine two additional monitor values: the total number of counts recorded in the TOF spectrum M, and the total number of counts recorded in the fitted high-energy peak M_{peak}. In this analysis, M_{peak} is estimated by taking the integral of a Gaussian function fitted to the peak region of the measured TOF spectra.

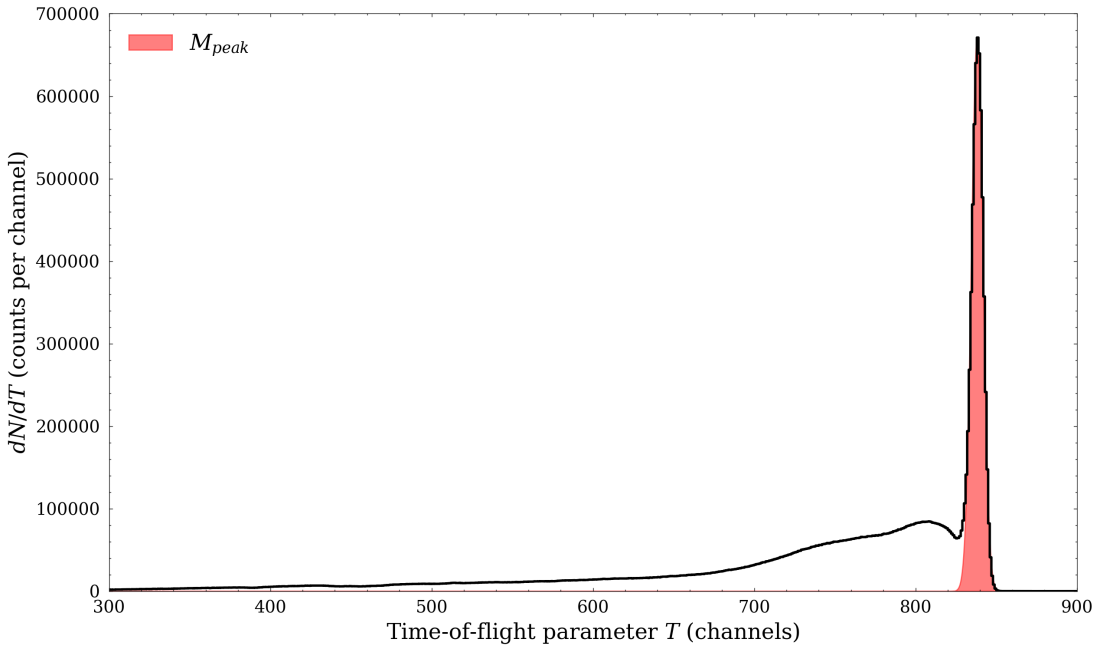

Figure 4.6: Typical TOF spectrum recorded by the NE102 monitor detector during a run with a 66.48 MeV proton beam irradiating an 8.0 mm lithium target. These spectra are used to determine the monitor values M and M_{peak}.

Table 4.2 provides a summary of the quantities measured by the monitor detectors that are used to monitor the neutron beam conditions in the D-line during experiments.

Quantity	Detector	Description
Q	Faraday cup	Integrated beam current / beam charge (recorded over 60 s intervals)
M_{slow}	NE102	Counts from slow dynode (recorded over 60 s intervals)
M_{fast}	NE102	Counts from fast anode (recorded over 60 s intervals)
M	NE102	Total counts in the TOF spectrum (recorded over a measurement run)
M_{peak}	NE102	Total counts in fitted high-energy peak of the TOF spectrum (recorded over a measurement run)

Table 4.2: Quantities measured by the monitor detectors that are used to monitor the neutron beam conditions in the D-line.

4.3 Characterisation of the neutron spectral fluence with the BC501A liquid scintillation detector

4.3.1 The BC501A liquid scintillation detector

High-energy resolution measurements of the neutron relative spectral fluence Φ_E/Φ at low beam intensities in the D-line are conducted with a BC501A liquid scintillation detector, shown in Figure 4.7.

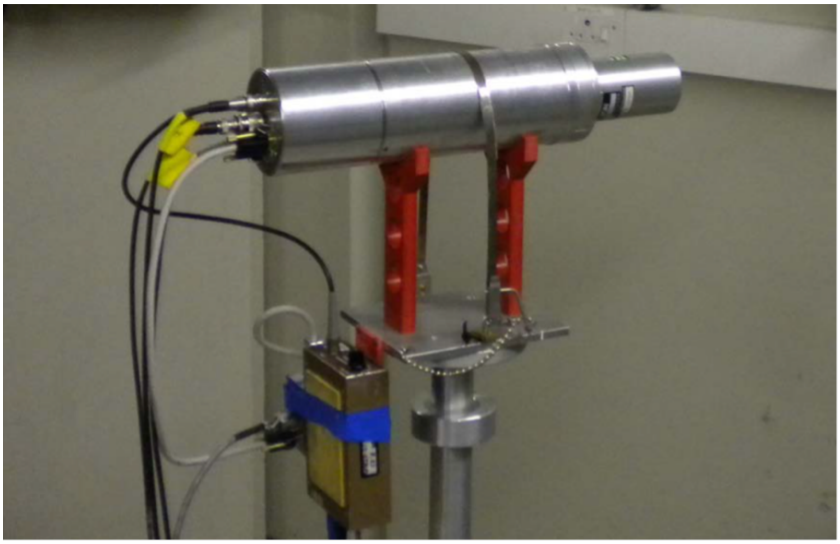

Figure 4.7: The BC501A liquid scintillation detector in the D-line experimental vault.

Table 4.3 describes the composition of the scintillation material of the BC501A detector. It is a hydrocarbon-based liquid organic scintillation detector comprised of benzene ring structures, and its detection of high-energy neutrons relies predominantly on n-p elastic scattering reactions in the detection material. Scintillation detectors operate based on the principle that when ionising radiation passes through the detection material, a fraction of the radiation's energy is absorbed and re-emitted in a burst of light, or 'scintillation', which is subsequently detected in a photomultiplier and converted into an electrical signal. The scintillation material of the detector at iThemba LABS is contained within a cylindrical volume with a diameter and length of 5.08 cm and 10.16 cm respectively. This volume is optically coupled to an XP2020 model photomultiplier tube via a light guide with a gain-stabilizing LED.

Detector	**BC501A liquid scintillator**
No. of H atoms per cm^3 ($\times 10^{22}$)	4.82
No. of C atoms per cm^3 ($\times 10^{22}$)	3.98
No. of electrons per cm^3 ($\times 10^{23}$)	2.27

Table 4.3: Composition of the BC501A liquid scintillation detector [Eljen Technology, 2016].

In an organic scintillation detector, the scintillation photons are produced via transitions of free electrons in the molecular energy states, and the way in which these states are populated, and the processes that occur between absorption and re-emission of the incident ionising radiation energy, are what characterise the detector response [Brooks, 1979]. The BC501A detector is a very popular neutron detector largely due to its exceptional pulse shape discrimination (PSD) properties that enable the distinction between neutron and gamma ray events within

the energy range of interest in a mixed field. It has good timing resolution, efficiency and light output properties that make it suitable for high-energy neutron spectrometry and counting [Eljen Technology, 2016].

4.3.2 Experimental setup and data acquisition

The electrical signal from the BC501A detector is directed through the electronics modules as illustrated in Figure 4.8. For each detected event, a FAST ComTec multiparameter data acquisition system (MPA) is used to record the light output parameter L, pulse shape parameter S, and time-of-flight parameter T, each binned into 1024 channels for further offline analysis. Descriptions of how each of these parameters were obtained and used for the purposes of pulse shape discrimination (PSD) and TOF measurements respectively, are given in the following sections. For the presented measurements, the front face of the BC501A detector was placed 8.0000 ± 0.0028 m from the centre of the lithium target, and measurements were made at proton beam currents of around 100 nA at a neutron emission angle of 0°.

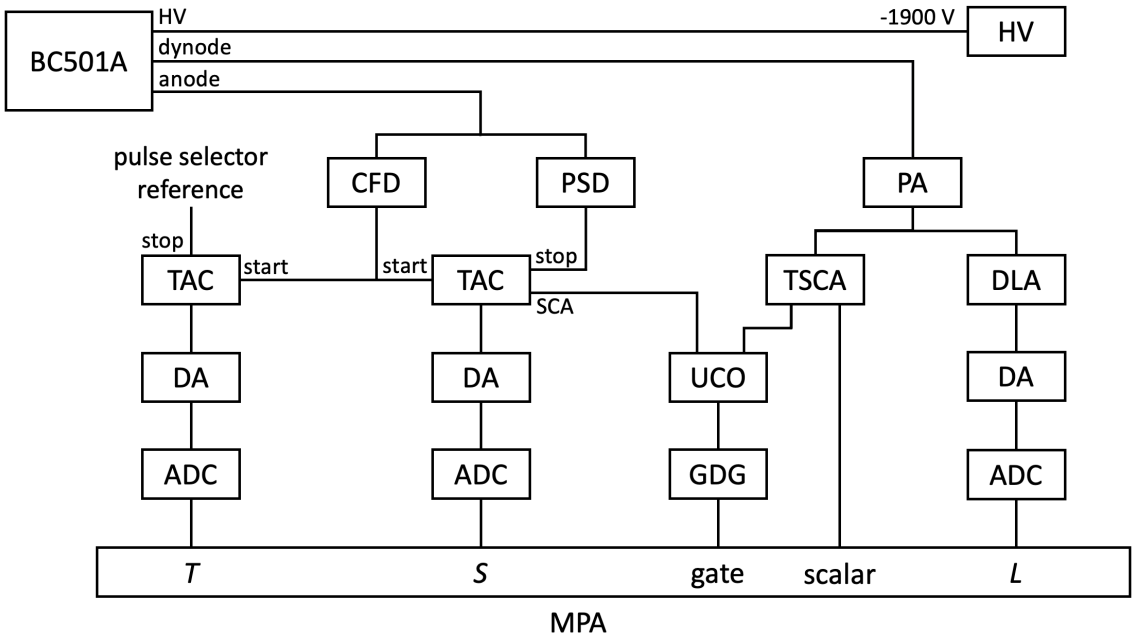

Figure 4.8: Schematic of the arrangement of the electronic modules for acquisition of data from the BC501A detector. Table 4.4 contains a key to the abbreviations used in this diagram.

ADC	analogue-to-digital converter	PA	pre-amplifier
CFD	constant fraction discriminator	PSD	pulse shape discriminator
DA	delay amplifier	S	pulse shape parameter
DLA	delay line amplifier	T	time-of-flight parameter
GDG	gate and delay generator	TAC	time-to-amplitude converter
HV	high voltage	TSCA	timing single channel analyser
L	light output parameter	UCO	coincidence unit
MPA	multiparameter data acquisition system		

Table 4.4: Key to the abbreviations used in Figure 4.8.

4.3.3 Pulse shape discrimination (PSD)

The technique of pulse shape discrimination (PSD) is used to distinguish between events associated with gamma rays and neutrons in the BC501A detector. Neutrons and gamma rays are indirectly ionising radiation, and their detection therefore relies on detecting the energy that is deposited by the secondary radiation particles that are produced via interactions of the primary particles in the detection medium. In the hydrocarbon-based BC501A detector, gamma rays interact through Compton scattering to produce recoil electrons, while neutrons interact via n-p elastic scattering or by n-C reactions to produce heavier charged particles, such as protons, deuterons, tritons and alpha particles. The method of PSD is based on the principle that the shape of a scintillation pulse from an organic liquid scintillation detector is dependent on the type of ionising particle that produced the scintillation, and this makes it possible to distinguish between neutron and gamma ray induced events. The light output of a single scintillation pulse, plotted as a function of time, exhibits a prompt and a delayed component. Due to the excitation of different emission mechanisms within the scintillator, the relative magnitudes of these components depend on the specific energy loss and thus on the type of ionising particle [Brooks, 1979]. Identifying differences in the characteristics of the scintillation decay therefore allows for the identification of different types of charged particles interacting in the detector.

The light output per event detected by a scintillation detector is observed to have a strong dependence on the energy and type of incident particle that produces the scintillation. As illustrated in Figure 4.8, this parameter is determined by directing the dynode signal from the detector through a pre-amplifier (PA) and into a delay line amplifier (DLA) that determines the pulse height. The signal is then directed through a delay amplifier (DA) to an analogue-to-digital converter (ADC) for acquisition of the light output parameter L in terms of pulse height, which can then be calibrated in terms of electron equivalent energy ($\mathrm{MeV_{ee}}$) using measurements made with gamma ray sources. Figure 4.9(a) shows the measured values of L, for the measurements of neutrons and gamma rays produced by a 66.48 MeV proton beam irradiating an 8.0 mm lithium target, binned into 1024 channels, and calibrated in terms of electron equivalent energy using a measurement of the 4.439 MeV gamma rays produced by an AmBe source.

As shown in Figure 4.8, the anode signal from the BC501A detector is split between a constant fraction discriminator (CFD) and a ComTec 2160A pulse shape discriminator module, which utilizes the "zero-crossing" method for PSD. The zero-crossing method exploits the differences in the rise times of scintillation pulses that are associated with different types of particles in-

teracting in the detector. On entering the module, the anode pulse from the detector is shaped into a bipolar signal via integration and differentiation in a PA. The time at which the shaped signal switches polarity, or the "zero-crossing," is dependent on the fall time of the input pulse which in turn depends on the type of particle that induced the scintillation. The shaped signal is fed to a high-gain limiting amplifier to enhance the separation of zero-crossing points corresponding to neutrons or gamma rays [ComTec, 1974]. The output logic pulse from the CFD that is produced from the leading edge of the input signal is used to start a time-to-amplitude converter (TAC), which is subsequently stopped by the output from the pulse shape discriminator module when the "zero-crossing" occurs. The resultant TAC output pulse is then directed through a DA to an ADC for acquisition of the pulse shape parameter S. Figure 4.9(b) shows the measured values of S binned into 1024 channels.

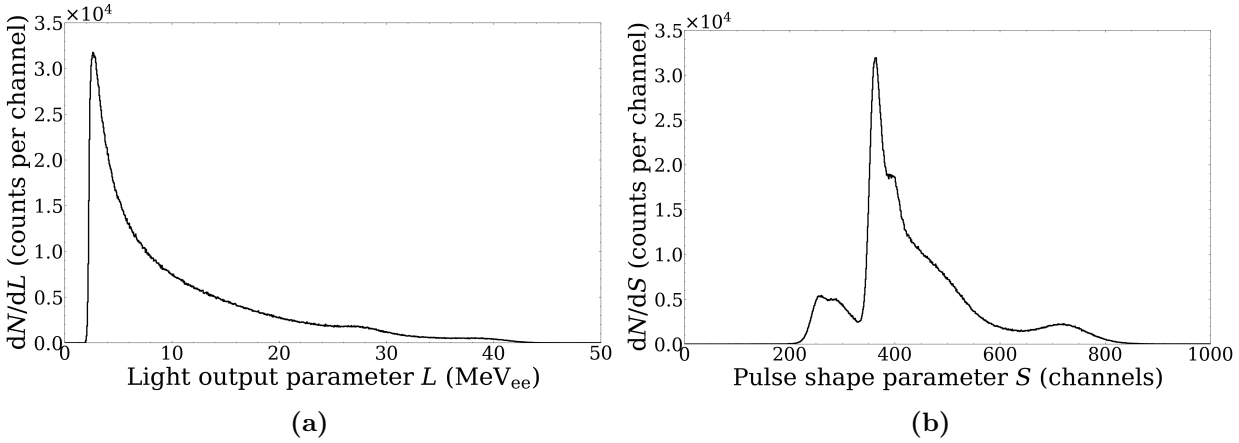

Figure 4.9: Counts as a function of (a) light output parameter L, and (b) pulse shape parameter S, each binned into 1024 channels for measurements of neutrons and gamma rays produced by a 66.48 MeV proton beam irradiating an 8.0 mm lithium target, measured by the the BC501A detector at a distance of 8.000 m from the target at 0°.

Figure 4.10 shows the measured distribution of events as a function of L and S, and the loci associated with different types of charged particles have been identified. The recoil electrons are associated with the Compton scattering and pair production interactions of gamma rays in the detector. Recoil protons are primarily produced from the elastic scattering of neutrons incident on hydrogen nuclei (n-p scattering), and deuterons, tritons and alpha particles are produced via neutron interactions with carbon nuclei. Events occurring between the tritium and alpha particle loci are generally attributed to ^{3}He ions or to the simultaneous detection of multiple charged particles [Comrie et al., 2015]. 'Escaping protons' refers to energetic protons that managed to escape from the detector before depositing all their energy. Protons and heavier charged particles deposit most of their energy in a well-defined 'Bragg peak' at the end of their range in a medium and therefore if they exit the detector before reaching the Bragg peak, the specific energy loss for these particles is lower and the corresponding pulse shape tends closer towards that of lighter particles. A software cut may then be applied to separate neutron and gamma ray events as indicated by the dashed line in Figure 4.10.

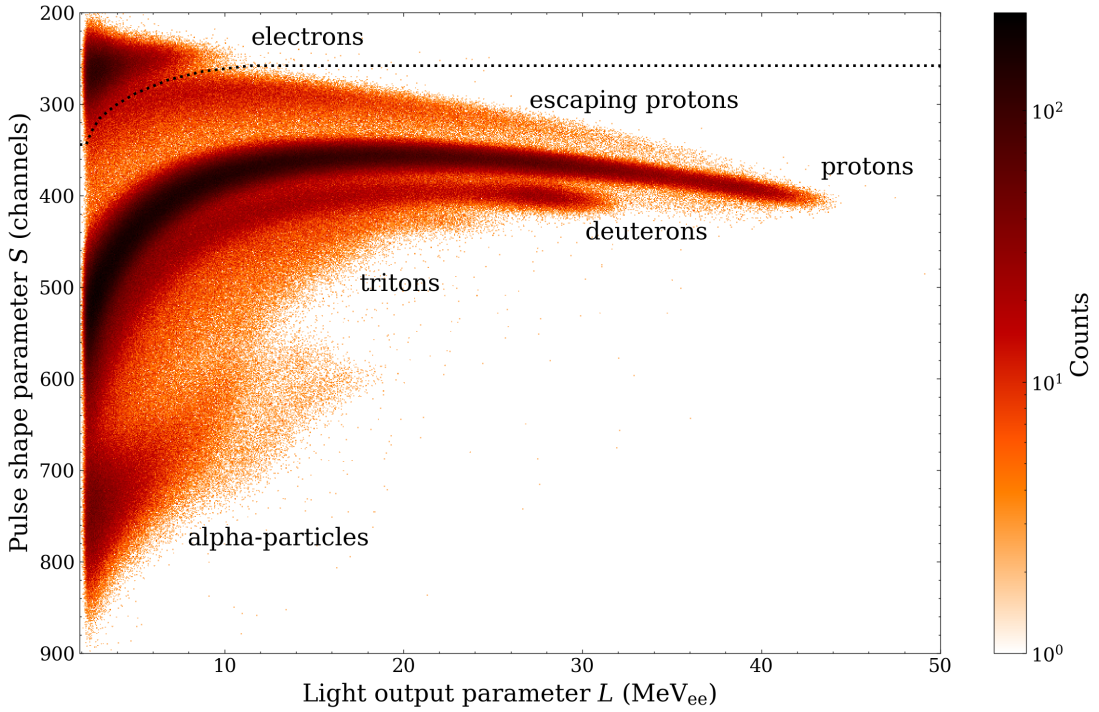

Figure 4.10: Counts as a function of light output parameter L and pulse shape parameter S for measurements of neutrons and gamma rays produced by a 66.48 MeV proton beam irradiating an 8.0 mm lithium target, measured by the BC501A detector at a distance of 8.000 m from the target at 0°. The dotted line indicates the cut that that was applied to separate neutron and gamma-ray induced events.

4.3.4 Time-Of-Flight (TOF) spectroscopy

Time-Of-Flight (TOF) spectroscopy involves determining the energy of a detected particle by measuring the time it takes to travel from the source to the detector. As illustrated in Figure 4.8, TOF information is obtained using the BC501A detector by directing the fast anode signal from the detector into a CFD that produces a timing pulse from the leading edge of the input signal with a width of around 1 ns. This timing pulse is then sent to start a TAC which is subsequently stopped by a suitably delayed pulse from the pulse selector of the SSC such that the amplitude of the output pulse is proportional to the time interval between the start and stop signal. The output pulse is then directed through a DA to an ADC for acquisition of the time-of-flight parameter T.

Figure 4.11 shows the measured distribution of events as a function of L and T, each binned in 1024 channels. For these measurements, the radio frequency (RF) cycle of the SSC was 16.37 MHz and the pulse selector was set to select 1 in 5 proton bunches with a time separation of 305 ns. Since T is determined as the difference between the detected event pulse from the CFD and a suitably delayed pulse selector reference signal, lower values of T correspond to longer times of flight of the detected particle, and higher values of T correspond to shorter times of flight. The small sharp peak around channel 530 that is observed in Figure 4.11 corresponds to gamma rays that are produced in the lithium target. The larger dominant peak around channel 430 in the TOF spectrum is predominantly due to the high-energy neutrons that are produced via direct reaction transitions to the ground or first excited state of ^{7}Be. The 'continuum' at lower channels is largely attributed to lower energy neutrons that are emitted in break-up reactions in the target. A time-independent distribution of gamma rays associated with background in the experimental area is also expected, although these were largely excluded by the chosen pulse height threshold of 2.5 MeV$_{ee}$.

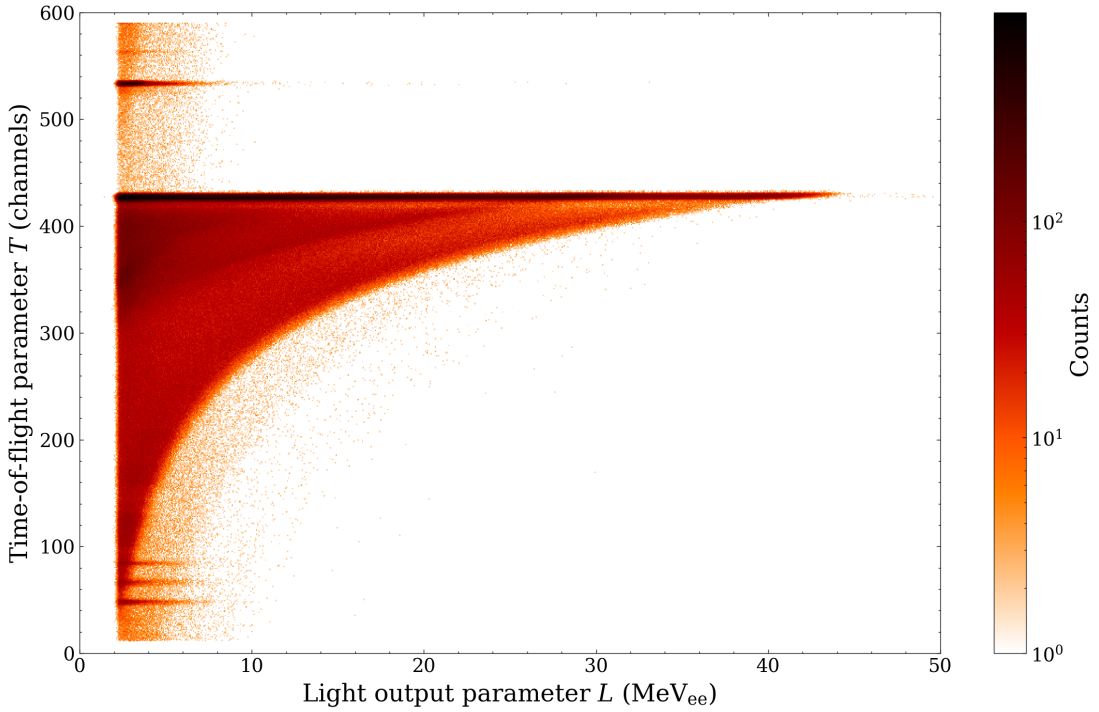

Figure 4.11: Counts as a function of light output parameter L and time-of-flight parameter T for measurements of neutrons and gamma rays produced by a 66.48 MeV proton beam irradiating an 8.0 mm lithium target, measured by the BC501A detector at a distance of 8.000 m from the target at 0°.

To calibrate the TAC output (and hence T) in terms of time, the TAC is run in a self-stopped mode through a calibrated delay to produce sharp peaks every 40 ns over the TAC channel range, as shown in Figure 4.12. For these measurements, the average difference between the maxima of each of the peaks was calculated to be 84.80 ± 0.13 channels, resulting in a time calibration factor of $F = 2.1200 \pm 0.0033$ channels/ns.

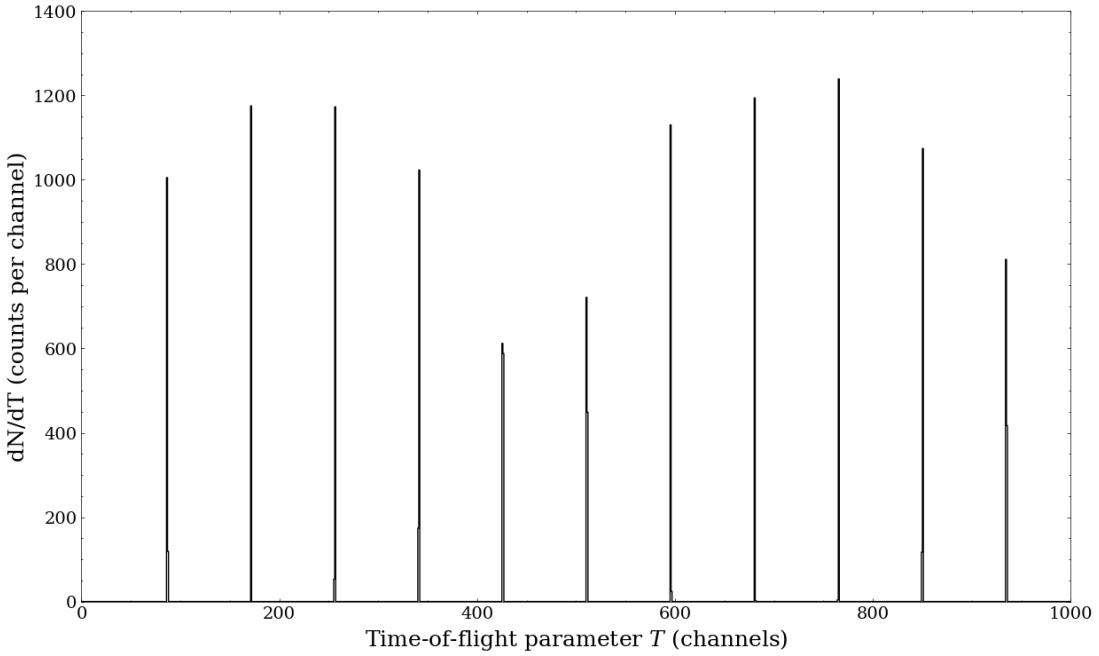

Figure 4.12: Self-stopped TAC calibration using a calibrated delay to produce sharp peaks over the TAC channel range with a separation of 40 ns.

In order to determine the neutron energy spectrum from the TOF spectrum, it is necessary to determine a 'time-zero', denoted T_0, which is the time-of-flight parameter T channel that would correspond to the detection of a (hypothetical) particle that travelled from the source to the detector instantaneously. Utilizing the fact that gamma rays travel at the speed of light, T_0 can be calculated from

$$T_0 = \frac{d}{c}F + T_\gamma, \tag{4.1}$$

where d is the distance from the target to the detector, c is the speed of light, F is the time-calibration factor, and T_γ is the channel number corresponding to centre of the the gamma ray peak that is observed around the TOF channel 530 in Figure 4.11.

In order to determine T_γ from the measured data, a non-linear least squares weighted fit of a Gaussian function to the gamma ray peak region of the measured TOF spectrum was performed. The resulting fit is shown in Figure 4.13, where the uncertainties in the number of measured counts per T bin were calculated as the square root of the measured number of counts, as governed by Poisson statistics. The fitted Gaussian function was found to have a full width at half maximum (FWHM) corresponding to $\Delta T_\gamma = 1.487 \pm 0.046$ ns, which is determined by the time-resolution of the BC501A detector. Using this method, it was found that $T_\gamma = 533.543 \pm 0.054$ channels. The time-zero channel was then determined to be

$$T_0 = 590.08 \pm 0.11 \,\text{channels},$$

using $d = 8.0000 \pm 0.0028$ m, $F = 2.1200 \pm 0.0033$ channels/ns, $c = 0.3$ m/ns, and propagating the associated uncertainties appropriately through the calculation.

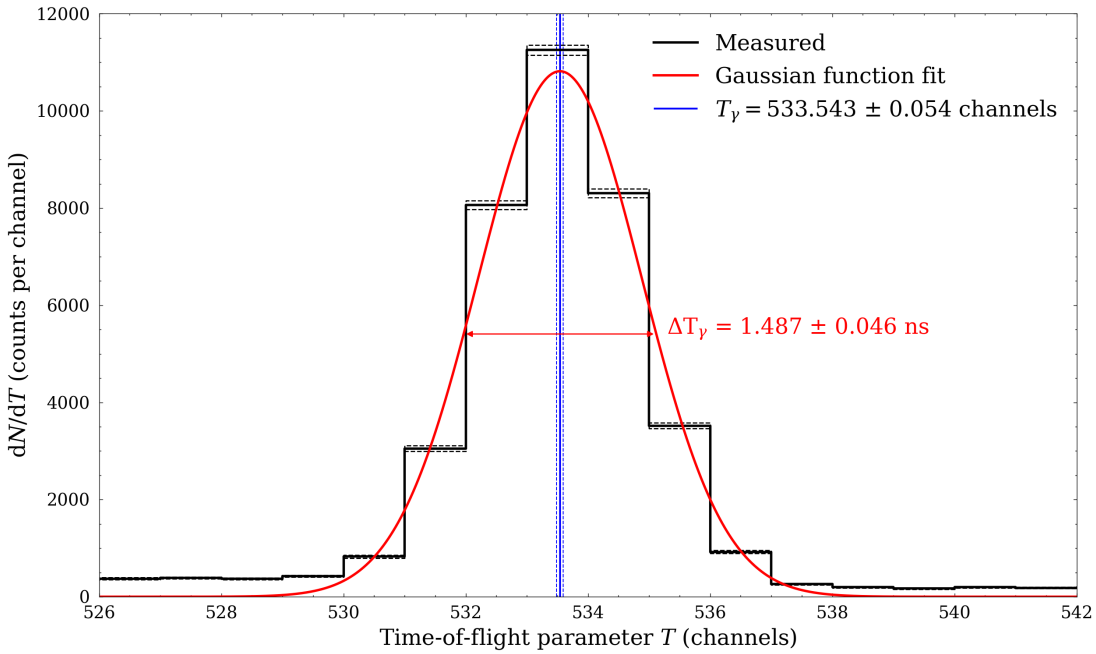

Figure 4.13: Counts as a function of the time-of-flight parameter T in the region of the gamma ray peak for measurements of neutrons and gamma rays produced by a 66.48 MeV proton beam irradiating an 8.0 mm lithium target, measured by the BC501A detector at a distance of 8.000 m from the target at 0°. A Gaussian function has been fitted to the region of the gamma ray peak in order to determine the T channel corresponding to the detected gamma rays that were produced in the target T_γ. The uncertainties are indicated by the dashed lines.

Using the determined values of the time-zero channel T_0 and the time calibration factor F, the TOF parameter T can be calibrated in terms of TOF in ns. Figure 4.14 shows the distribution

of measured events as a function of T (calibrated in terms of both channels and ns) before and after the PSD cut shown in Figure 4.10 was applied to determine the neutron only TOF spectrum.

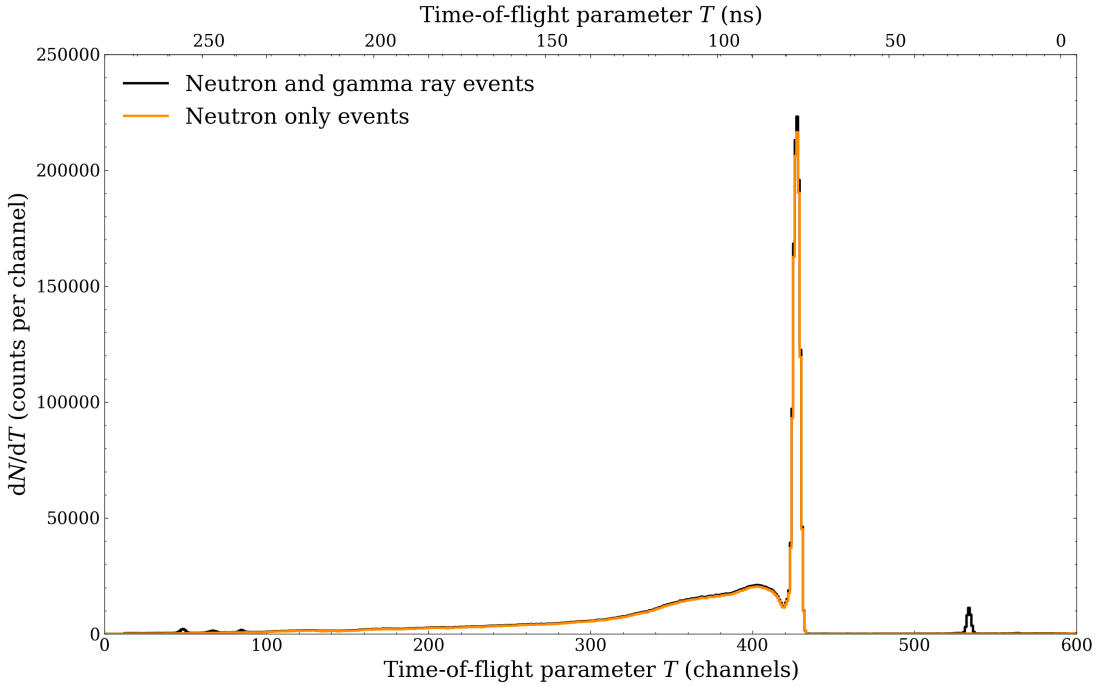

Figure 4.14: Counts as a function of the time-of-flight parameter T for measurements of neutrons and gamma rays produced by a 66.48 MeV proton beam irradiating an 8.0 mm lithium target, measured by the BC501A detector at a distance of 8.000 m from the target at 0°. The "neutron only events" spectrum was obtained by applying the PSD cut shown in Figure 4.10 to exclude gamma ray events.

The velocity v_i corresponding to each channel T_i can then be calculated as

$$v_i = \frac{Fd}{T_0 - T_i}, \tag{4.2}$$

and the corresponding neutron energy can be calculated according to the relativistic formula

$$E_i = m_n \left(\frac{1}{\sqrt{1-\beta^2}} - 1 \right), \tag{4.3}$$

where $\beta = v_i/c$ and $m_n = 939.565\,\mathrm{MeV/c^2}$ is the mass of a neutron.

Rearranging Equations 4.2 and 4.3, the channel T_i corresponding to a particular energy E_i can be calculated as

$$T_i = T_0 - \frac{Fd}{c\sqrt{1-(E_i/m_n+1)^{-2}}}. \tag{4.4}$$

Equation 4.4 was used to calculate the channels T_i corresponding to 0.5 MeV energy bins between 0.0 MeV and 72.5 MeV, as shown in Figure 4.15. The measured data were re-binned into these bins and placed on an energy scale (with a lower threshold of 7.5 MeV) in order to obtain the results shown in Figure 4.16. The uncertainties shown for the number of counts per energy bin include the propagation of the uncertainties of F, d and T_0 through the calculation of E_i, as well as the uncertainty of the number of measured counts per T bin, as governed by Poisson statistics.

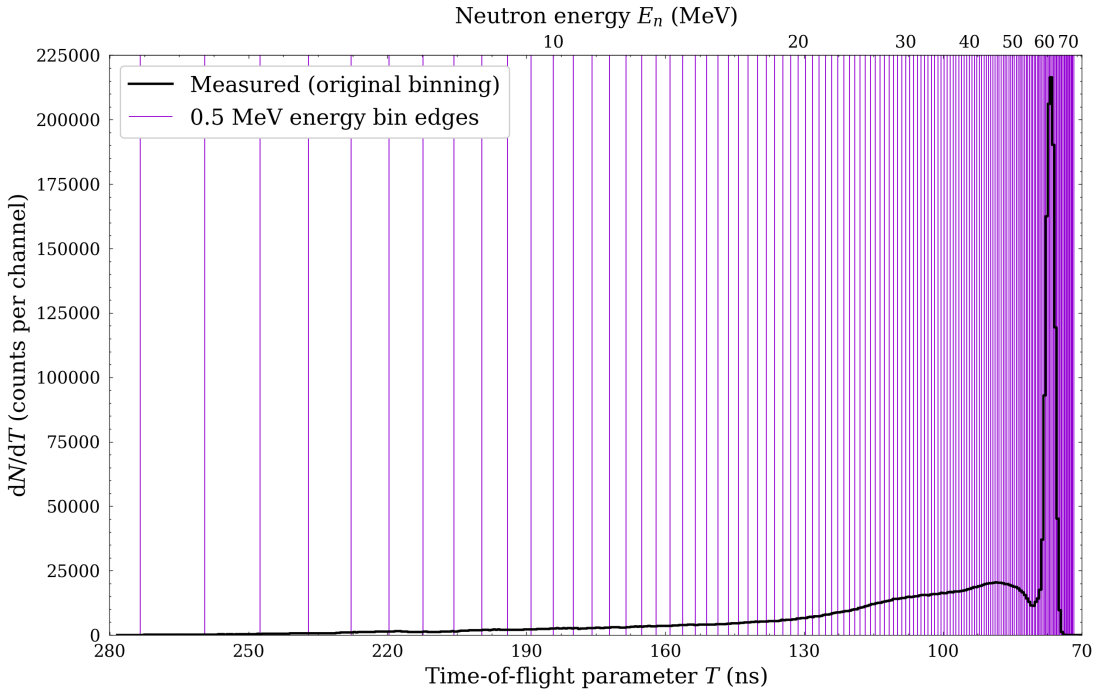

Figure 4.15: Counts as a function of the time-of-flight parameter T for measurements of neutrons produced by a 66.48 MeV proton beam irradiating an 8.0 mm lithium target, measured by the BC501A detector at a distance of 8.000 m from the target at 0°. The measured neutron TOF spectrum is shown alongside the T channel bins that correspond to 0.5 MeV neutron energy bins between 0.0 MeV and 72.5 MeV.

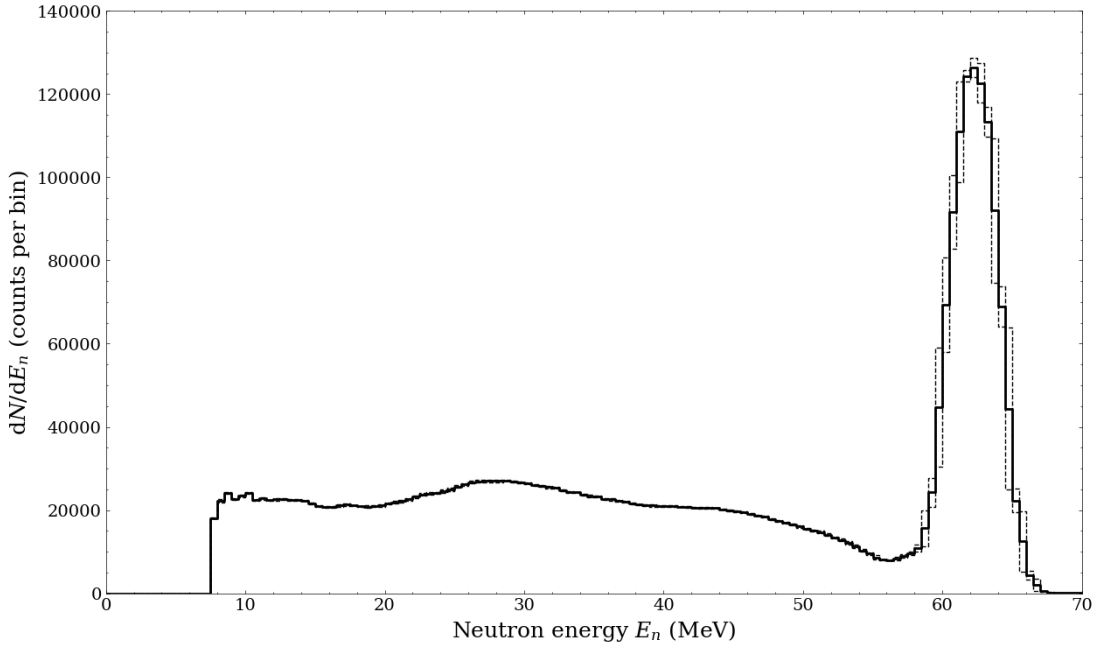

Figure 4.16: Counts as a function of neutron energy E_n for measurements of neutrons produced by a 66.48 MeV proton beam irradiating an 8.0 mm lithium target, measured by the BC501A detector at a distance of 8.000 m from the target at 0°. The uncertainties are indicated by the dashed lines.

4.3.5 Characterisation of the relative neutron spectral fluence distribution

The BC501A detector at iThemba LABS is used to characterise key features of the neutron spectral fluence distribution in terms of neutron spectral fluence per unit total monitor count, which is calculated from the TOF measurements as

$$\frac{\Phi_E^{sc}}{M} = \frac{1}{M}\frac{1}{A_{sc}}\frac{1}{\varepsilon_{sc}(E_n)}\left(\frac{dN}{dE_n}\right), \tag{4.5}$$

where M is the NE102 neutron monitor count (as discussed in Section 4.2), A_{sc} is the cross-sectional area of the active detector volume of the BC501A scintillation detector, $\varepsilon_{sc}(E_n)$ is the detection efficiency of the scintillation detector for neutrons of energy E_n, and dN/dE_n is the detected number of events per neutron energy bin as determined via the TOF analysis discussed in Section 4.3.4. The detection efficiency $\varepsilon_{sc}(E_n)$ of the BC501A detector at iThemba LABS was previously calculated using the Monte Carlo codes SCINFUL and MCNPX along with empirical corrections that were made to improve the agreement with measurements [Nolte et al., 1993]. The results for the efficiency as a function of neutron energy for a 2.5 MeV_{ee} light output L threshold and 0.5 MeV binning in neutron energy are shown in Figure 4.17.

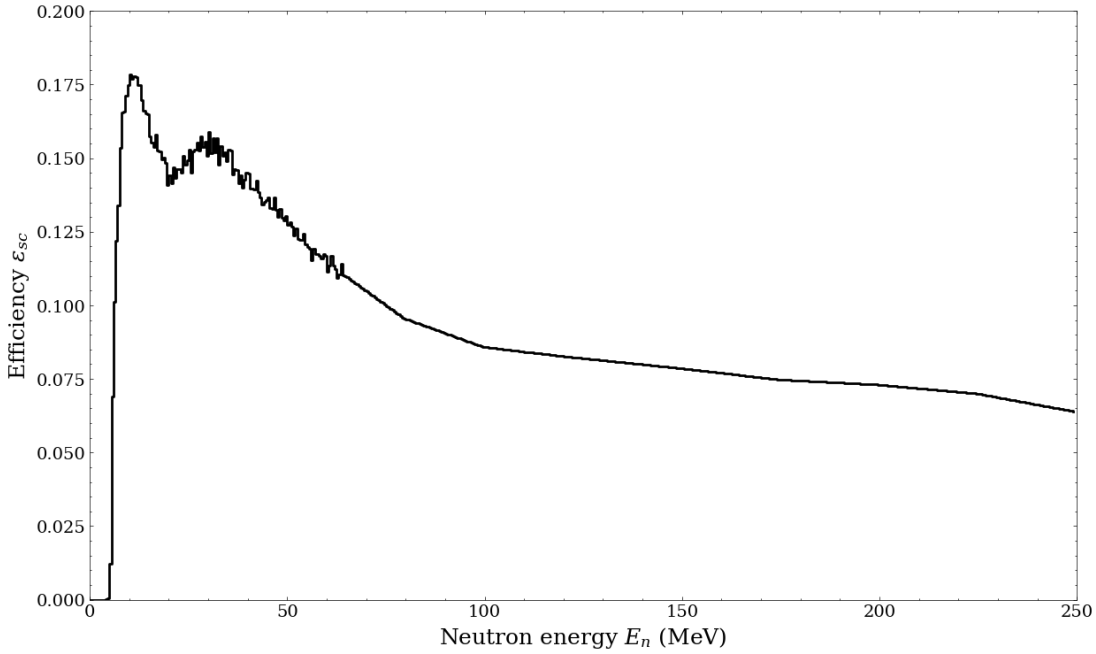

Figure 4.17: Detection efficiency of the BC501A detector at iThemba LABS as a function of neutron energy for a 2.5 MeV_{ee} light output L threshold and 0.5 MeV binning in neutron energy.

Figure 4.18(a) shows the result for the spectral fluence distribution per unit total monitor count Φ_E^{sc}/M obtained using the measured neutron energy spectrum dN/dE_n from Figure 4.16 in Equation 4.5. A horizontal extrapolation of the spectral fluence was used below 7.5 MeV, as motivated by results from [Nolte et al., 2002]. The uncertainties were determined via propagation of the uncertainties for M (as governed by Poisson statistics), A_{sc} (calculated using a triangular probability density function) and dN/dE_n (as shown in Figure 4.16) through the calculation in Equation 4.5. The uncertainties associated with ε_{sc} are not known, but considered to be negligible for the current purpose of calculating the relative fluence distribution for the BC501A measurements.

As discussed in Section 4.1, the neutron energy spectra are comprised of two distinctive components: a high-energy peak and an adjacent low-energy continuum. The width of the high-energy

peak is determined by the TOF resolution of the detector as well the energy loss of the incident protons interacting in the lithium target [Mosconi et al., 2010]. In order to divide the measured spectrum into its respective components $\Phi_E^{sc,peak}/M$ and $\Phi_E^{sc,continuum}/M$, as shown in Figure 4.18(b), a correction was made to compensate for the overlap between 50 MeV and 59 MeV as follows: a Gaussian function was fitted to the peak region above 59 MeV and then the value of the fitted function at the centre of each energy bin was subtracted from the measured spectrum in order to estimate the continuum contribution in this region.

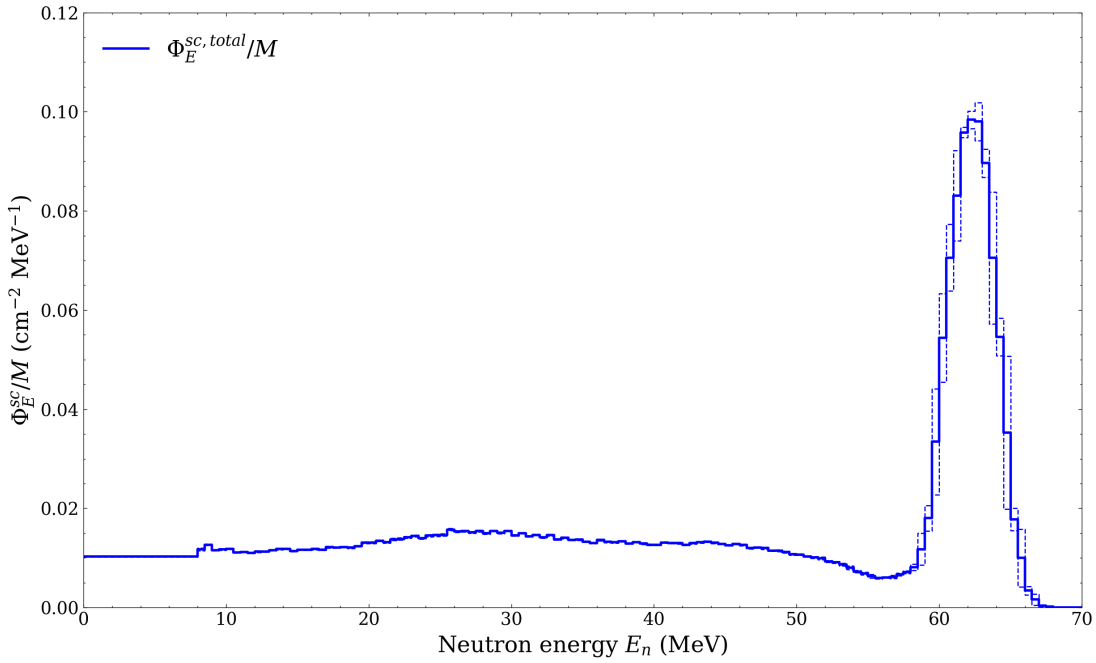

(a)

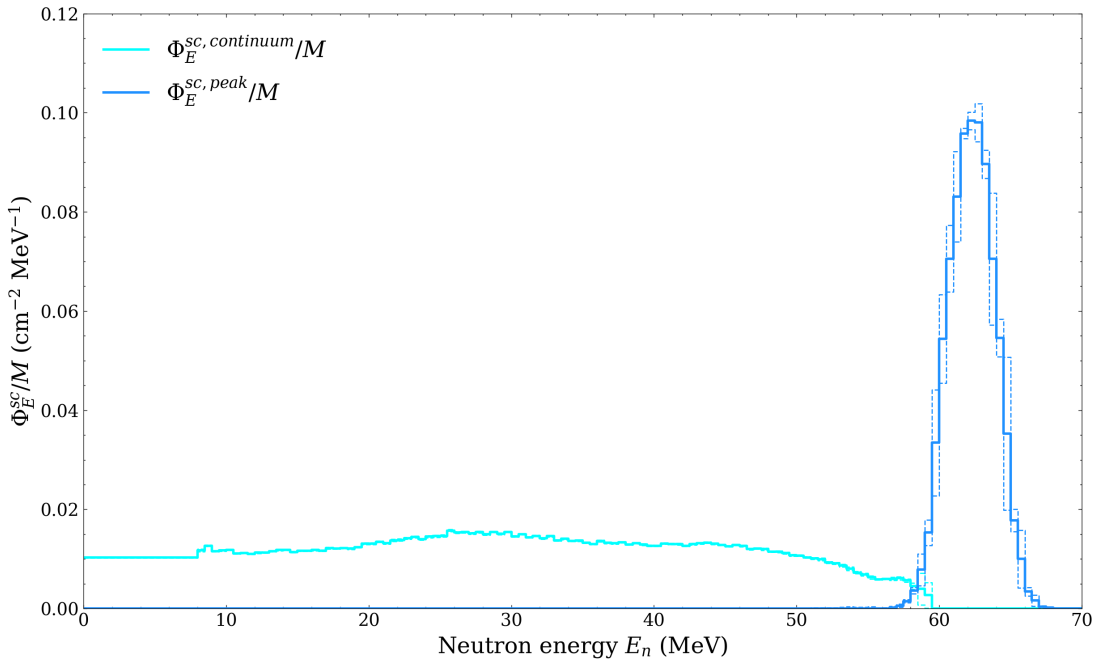

(b)

Figure 4.18: (a) Total and (b) continuum and peak components of the neutron spectral fluence per unit monitor count for measurements of neutrons produced by a 66.48 MeV proton beam irradiating an 8.0 mm lithium target, measured by the BC501A detector at a distance of 8.000 m from the target at 0°. The uncertainties are indicated by the dashed lines.

The key parameters of the measured neutron spectral fluence distribution shown in Figure 4.18 are summarised in Table 4.5, where E_p is the energy of the protons from the SSC, d_{Li} is the thickness of the lithium target, $\langle E \rangle_\Phi$ is the fluence-weighted average energy, $E_{0,exp}$ is the experimental mean energy of the high-energy peak, Θ is the neutron emission angle, and Φ/Φ_0 is the ratio of the total neutron fluence to the peak neutron fluence.

- The experimental mean energy of the high-energy peak $E_{0,exp}$ of the measured spectrum was determined via a non-linear least squares weighted fit of a Gaussian function to the peak region. The calculated uncertainty includes the uncertainty associated with the fit and with the width of the measured peak.

- The total fluence Φ is determined by integration of the spectral fluence over the full energy range:

$$\Phi = \int \Phi_E^{sc,total} dE. \tag{4.6}$$

  The peak fluence Φ_0 is determined by integration of the spectral fluence over the peak component of the spectrum:

$$\Phi_0 = \int \Phi_E^{sc,peak} dE. \tag{4.7}$$

  The ratio of the total neutron fluence to peak neutron fluence can therefore be calculated from the measured spectrum as

$$\frac{\Phi}{\Phi_0} = \frac{\int \Phi_E^{sc,\mathrm{total}}\, dE}{\int \Phi_E^{sc,\mathrm{peak}}\, dE} \approx \frac{\sum_i \Phi_E^{sc,\mathrm{total}}{}_i / M}{\sum_i \Phi_E^{sc,\mathrm{peak}}{}_i / M}. \tag{4.8}$$

$\boldsymbol{E_p}$ (MeV)	$\boldsymbol{d_{Li}}$ (mm)	$\boldsymbol{\langle E \rangle_\Phi}$ (MeV)	$\boldsymbol{E_{0,exp}}$ (MeV)	$\boldsymbol{\Theta}$ (°)	$\boldsymbol{\Phi/\Phi_0}$
66.48	8.0	41.32 ± 0.97	62.34 ± 0.37	0	2.654 ± 0.097

Table 4.5: Summary of the key parameters of spectral fluence distribution of neutrons produced by a 66.48 MeV proton beam irradiating an 8.0 mm lithium target, measured by the BC501A detector at a distance of 8.000 m from the target at 0°.

4.4 Fluence measurements with the ^{238}U fission ionisation chamber

4.4.1 The ^{238}U fission ionisation chamber

The ^{238}U(n, f) cross-section serves as a secondary standard in neutron metrology for fluence measurements over energies extending from thermal up to several hundred MeV [Nolte et al., 2007]. The parallel-plate ^{238}U fission ionisation chamber (FC) at iThemba LABS shown in Figure 4.19 is used to characterise the neutron beam fluence at high beam intensities. The absolute neutron fluence in the high-energy peak Φ_0 is calculated from the FC measurements as

$$\Phi_0 = \frac{N_{f,exp}(\prod_i k_i)}{\sigma N_U}, \tag{4.9}$$

where $N_{f,exp}$ is the measured number of fission counts in the high-energy peak, k_i are a series of correction factors (as discussed in Section 4.4.4), σ is the ^{238}U fission cross section for neutrons in the high-energy peak, and N_U is the number of fissile ^{238}U atoms in the FC [Nolte et al., 2007].

Figure 4.19: The ^{238}U FC in the D-line experimental vault.

Figure 4.20 shows a schematic of a typical parallel plate FC. The FC at iThemba LABS was manufactured at the Institute for Reference Materials and Measurements (IRMM) in Belgium. It contains a stack of ionisation chambers comprising of six platinum-backed cathode plates (carrying the fissile material) that are arranged in alternating layers with the tantalum anode plates. The fissile material consists of $^{238}U_3O_8$ deposits that are produced by electronic spraying onto both sides of the cathode plates. All electrode plates have a sensitive diameter of 76 mm and are separated from each other by a distance of 5 mm. The composition of the uranium in the detector was analysed by the National Bureau of Standards of the United States of America. The total mass of uranium in the FC was reported to be 0.2409 g (specified with a 10% uncertainty), and the relative abundance of ^{238}U atoms in the uranium material was quoted to be 99.9823 $\pm$ 0.0001%.

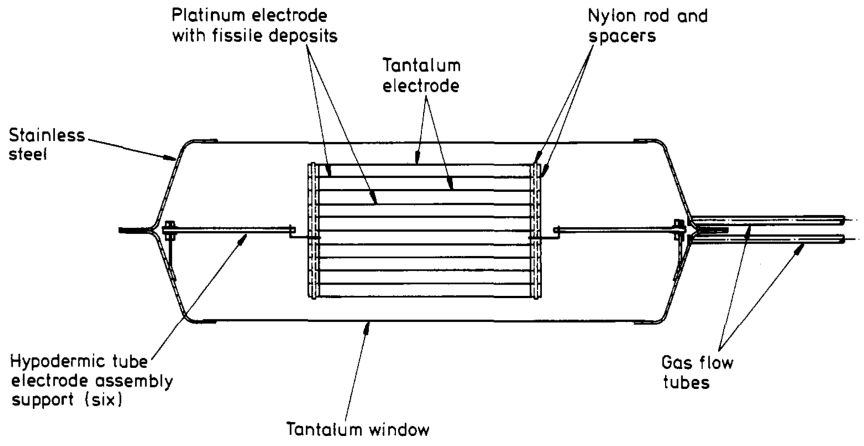

Figure 4.20: Schematic of a typical multi-plate fission ionisation chamber [Gayther, 1990].

The FC is operated with P10 gas (90% Ar and 10% CH_4) in continuous flow mode. Neutrons entering the detector induce fission reactions in the thin ^{238}U deposits and the subsequent fission fragments produce ionisation in the gas. The ^{238}U fission cross-section is almost negligible below 1 MeV and measurements with the FC are therefore insensitive to thermal neutrons as well as gamma rays. The time resolution of the FC is about 5 ns which enables TOF measurements, but with inferior energy resolution to those obtained with the BC501A detector. It has a fluence response of about 10^{-3} cm^2 that makes it suitable for measurements at higher beam intensities, but not at lower currents [Mosconi et al., 2010]. The FC at iThemba LABS has been compared with the ^{238}U fission chamber H21 and proton recoil telescope at the Physikalish-Technische Bundesanstalt (PTB). At a neutron energy of 15 MeV, it was found to be in agreement to better than 1% and to around 1.3% with the H21 fission chamber and the RPT1 respectively [Mosconi et al., 2010].

4.4.2 Experimental setup and data acquisition

The electrical signal from the FC is read out from the anode plate and directed through the electronics modules as illustrated in Figure 4.21. For each detected event, a FAST ComTec MPA is used to record light output L and time-of-flight T, each binned into 1024 channels for further offline analysis. A brief description of how each of these parameters was obtained is given below. For the presented measurements, the front face of the FC was placed 9.515 m from the centre of the lithium target, and measurements were made at proton beam currents of between 200 nA and 850 nA at a neutron emission angle of 0°.

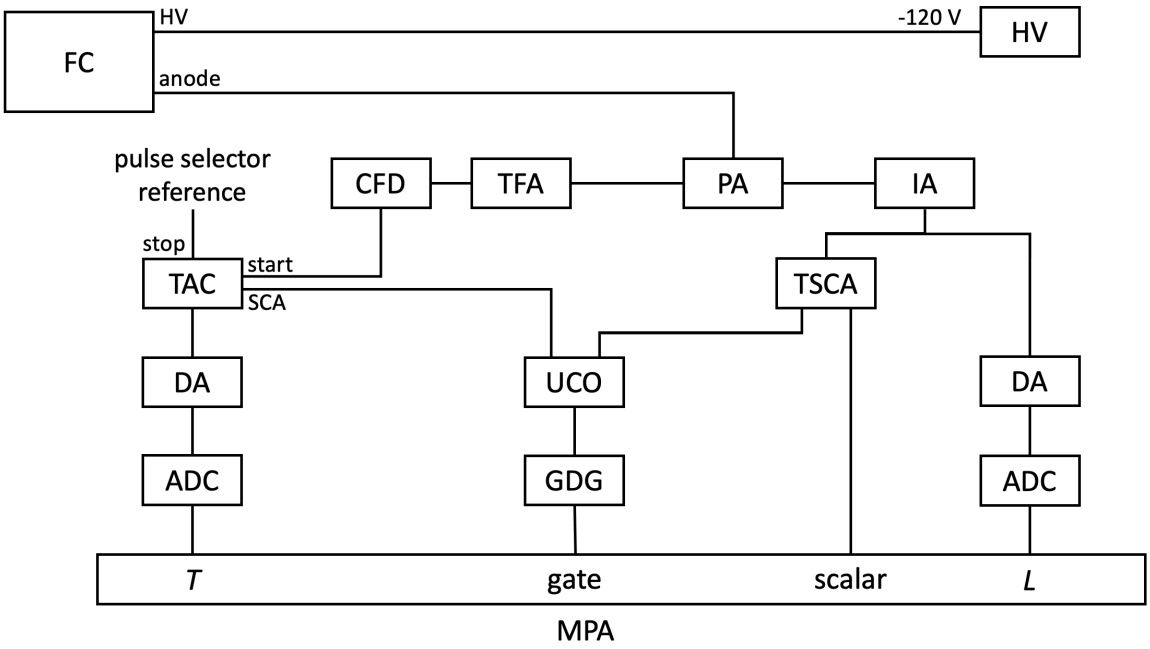

Figure 4.21: Schematic of the arrangement of the electronic modules for acquisition of data from the FC. Table 4.6 contains a key to the abbreviations used in this diagram

.

ADC	analogue-to-digital converter	PA	pre-amplifier
CFD	constant fraction discriminator	SCA	single channel analyser
DA	delay amplifier	T	time-of-flight parameter
GDG	gate and delay generator	TAC	time-to-amplitude converter
HV	high voltage	TFA	differentiating timing filter
IA	integrating amplifier	TSCA	timing single channel analyser
L	light output parameter	UCO	coincidence unit
MPA	multiparameter data acquisition system		

Table 4.6: Key to the abbreviations used in Figure 4.21.

For acquisition of the light output parameter L, the anode signal from the FC is directed through a PA to an Ortec 572 integrating amplifier (IA). The bipolar output signal is then directed through a timing single channel analyser (TSCA) to produce a logic pulse that triggers the data acquisition system to accept an event. The unipolar output signal from the IA is directed through a DA to an ADC for acquisition of the light output parameter L in terms of pulse height. Figure 4.22(a) shows the measured values of L binned into 1024 channels.

For TOF measurements, the anode signal from the FC is directed into an Ortec 474 differentiating timing filter (TFA) and then into a CFD that produces an output timing signal (based on the rise time of the input signal) used to start a TAC. The TAC is subsequently stopped by a suitably delayed pulse from the pulse selector reference from the SSC such that the amplitude of the output pulse is proportional to the time interval between the start and stop signal. The output pulse is then directed through a DA to an ADC for acquisition of the TOF parameter T. Figure 4.22(b) shows the measured values of T binned into 1024 channels.

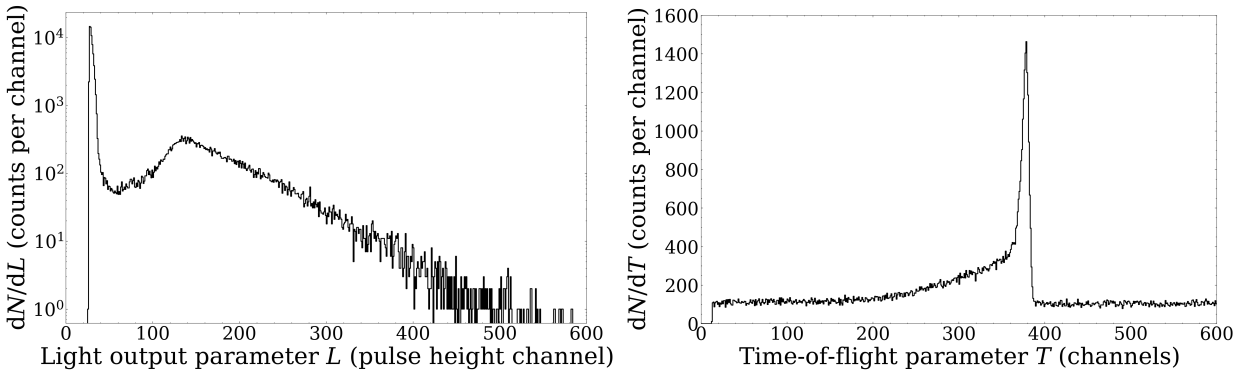

(a) **(b)**

Figure 4.22: Counts as a function of (a) light output parameter L, and (b) time-of-flight parameter T, each binned into 1024 channels for measurements of neutrons and gamma rays produced by a 66.48 MeV proton beam irradiating an 8.0 mm lithium target, measured by the the FC detector at a distance of 9.515 m from the target at 0°.

4.4.3 Determining the measured number of fission counts in the high-energy peak

In order to derive a measurement of the absolute neutron fluence from the FC measurements, it is necessary to determine the measured number of fission counts in the high-energy peak $N_{f,exp}$. As a first step towards determining this quantity, a pulse height threshold is applied to the measured data to eliminate detected events due to the alpha particle background and other light fission reaction products. While the FC is largely insensitive to gamma rays, there is an alpha particle background present in the FC measurements due to the natural decay of ^{238}U. The typical energy of these alpha particles is around 5 MeV, while the energy of the fission fragments is generally much greater, and this can in principle be used to discriminate between detected fission and alpha particle events [Crane and Baker, 1991]. The measured pulse height spectrum for the neutron irradiations, as shown in Figure 4.23 exhibits a broad fission peak, which extends, with decreasing pulse height, down towards a 'plateau' region before the rising rapidly due to the alpha particle background. A threshold based on pulse height can therefore be applied to eliminate the alpha particle background and other light reaction products from the fission events. The position of the pulse height threshold, as shown in Figure 4.23, was chosen based on the recommendation from Gayther [1990], to be at $0.45P$, where P is the pulse height corresponding to the maximum value of the fission peak.

Figure 4.24 shows the neutron-only TOF spectrum that is obtained when the pulse height threshold shown in Figure 4.23 is applied. The neutron-only TOF spectrum exhibits a high-energy peak and lower energy continuum (as described in Section 4.3.5), however the separation of these components is difficult given the inferior timing resolution of FC compared to the BC501A detector. In order to correct for the overlap of the peak and continuum components and estimate the number of fission counts in the high-energy peak, the correction procedure described by Nolte et al. [2007] is followed, as outlined below.

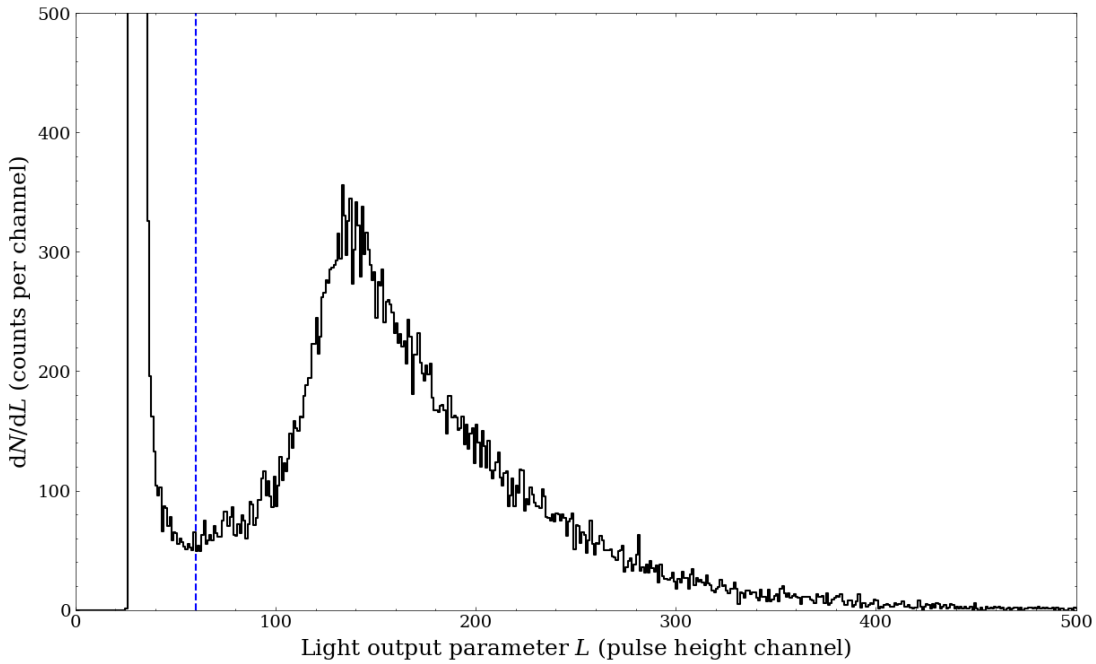

Figure 4.23: Counts as a function of the light output parameter L binned into 1024 channels for measurements of neutrons and gamma rays produced by a 66.48 MeV proton beam irradiating an 8.0 mm lithium target, measured by the FC at a distance of 9.515 m from the target at 0°. The dashed line indicates the pulse height threshold that was chosen to eliminate the alpha particle background and other light reaction products from fission events in the FC.

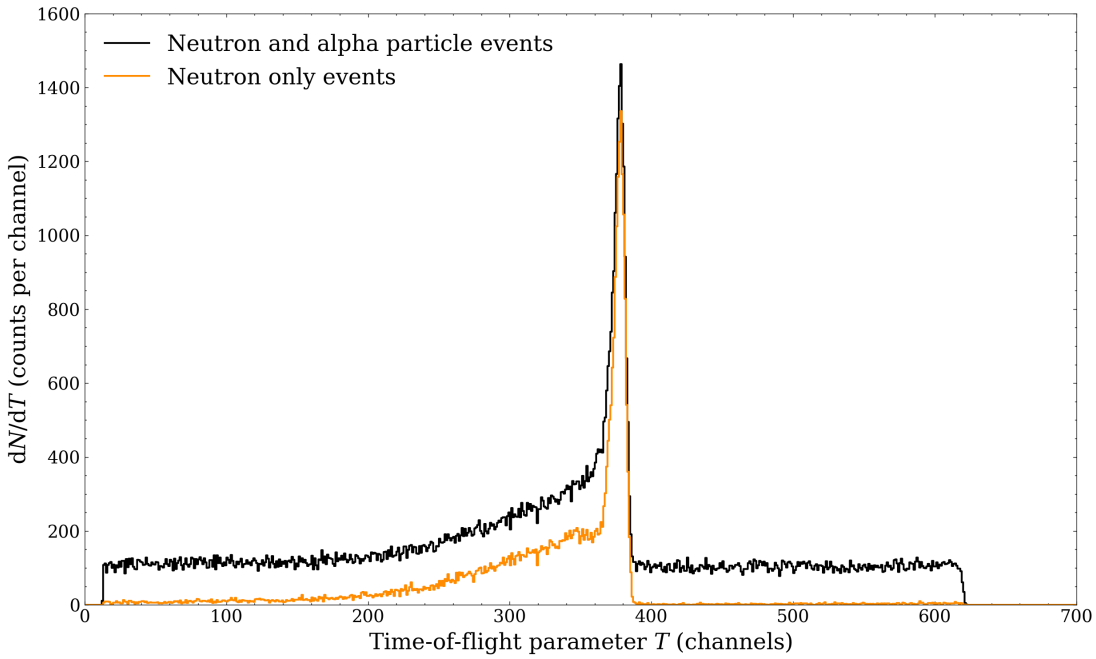

Figure 4.24: Counts as a function of the time-of-flight parameter T binned into 1024 channels for measurements of neutrons and gamma rays produced by a 66.48 MeV proton beam irradiating an 8.0 mm lithium target, measured by the FC at a distance of 9.515 m from the target at 0°. The measurements are shown before and after the pulse height threshold shown in Figure 4.23 was applied to obtain the "neutron only events spectrum".

The detection efficiency of the FC at iThemba LABS has been previously calculated as a function of neutron energy based on Carlson's analytical model [Carlson, 1974] and Prokofiev's parameterisations of experimental data for the kinematical properties of fission by high-energy

neutrons [Prokofiev and Olsson, 2001; Nolte et al., 2007]. Figure 4.25 shows the calculated detection efficiency as a function of neutron energy along with an efficiency curve for the FC as determined via cubic spline interpolation of the calculated data points. The high resolution neutron fluence spectra measured with the BC501A detector at 0° (shown in Figure 4.18) were folded with the efficiency curve in Figure 4.25 to obtain the relative fluence spectra shown in Figure 4.26.

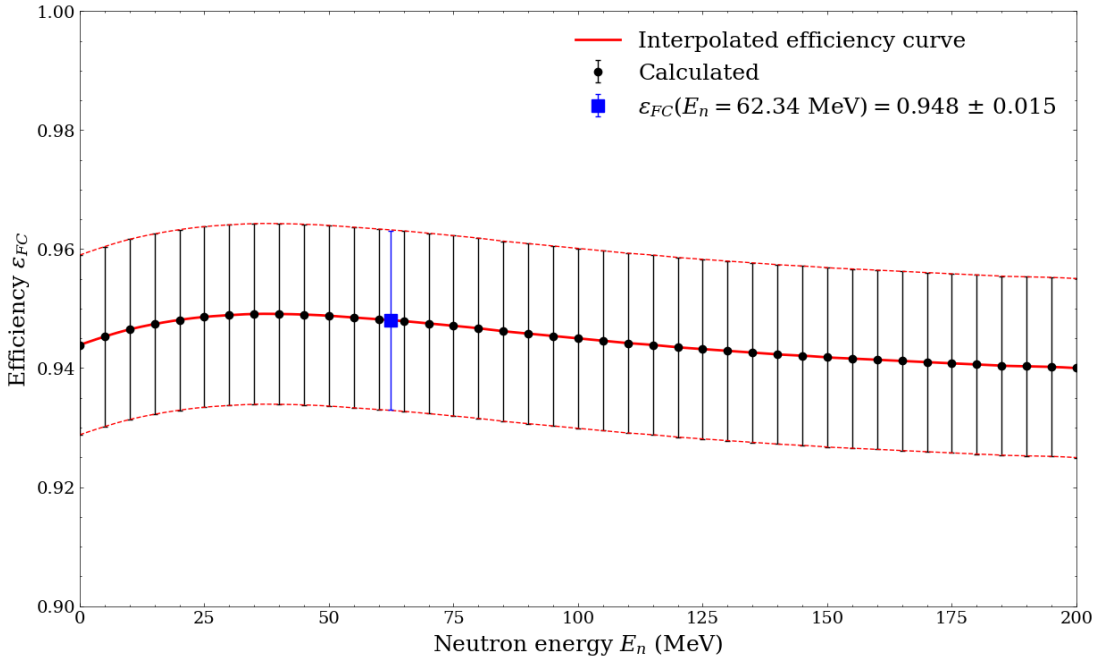

Figure 4.25: The FC efficiency as a function of neutron energy as calculated using Carlson's analytical model [Carlson, 1974] with Prokofiev's parameterisations [Prokofiev and Olsson, 2001].

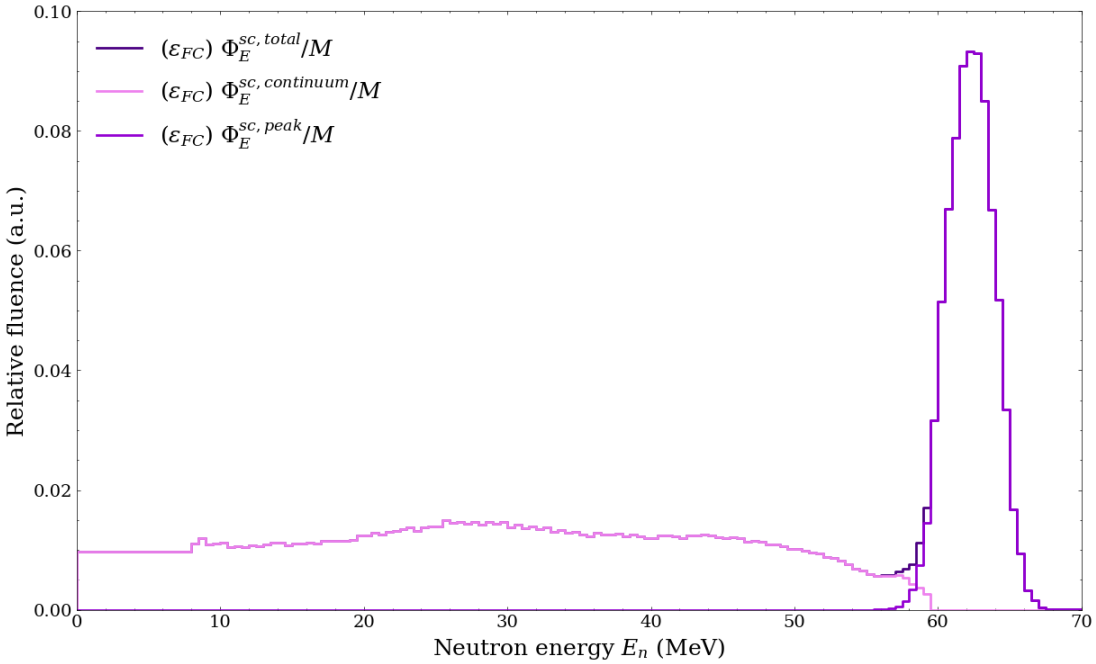

Figure 4.26: Relative fluence spectra obtained by folding the FC efficiency curve (from Figure 4.25) with the spectral fluence for neutrons produced by a 66.48 MeV proton beam irradiating an 8.0 mm lithium target as measured by the BC501A detector at a distance of 8.000 m from the target at 0° (from Figure 4.18).

The fluence spectra shown in Figure 4.26 were subsequently used to calculate the corresponding neutron TOF spectra (as would be detected by the FC) via Monte Carlo simulations in GEANT4. In the simulation, the detection surface of the FC (in the $x-y$ plane) was constructed as a cylinder of air with a diameter of 7.6 cm (corresponding to the sensitive diameter of the electrode plates in the FC and a thickness (in the z-direction) of 10^{-5} cm. The geometry was enclosed in a "world" volume of near-vacuum material (modelled in GEANT4 as 100% H with a density of 10^{25} g/cm^3 [Geant4 Collaboration, 2023a]). The neutron beam was modelled as a square planar source with dimensions of 5 cm $\times$ 5 cm situated in the $x-y$ plane at a distance of 9.515 m (corresponding to the distance at which the FC measurements were made) from the detection surface onto which it was directed. The relative neutron fluence spectra, as shown in Figure 4.26, were normalised and treated as probability distributions from which the energies of the simulated neutrons were randomly sampled. For each simulated neutron that entered the detection volume, the time (since it was generated) at which it entered the volume was recorded. The results for the TOF of 10^8 simulated in this way and binned into 1024 TOF bins are shown by the dashed lines in Figure 4.27.

To compensate for the differing timing resolutions of the BC501A detector and FC, the continuum and peak components of the simulated TOF spectra were independently broadened by sampling from the Gaussian function

$$f(T) = Ce^{-\left(\frac{T-T_0}{A}\right)^2}, \tag{4.10}$$

where T is the broadened TOF, T_0 is the unbroadened TOF (from the simulation), C is a normalization constant, and A is the Gaussian width which is related to the desired FWHM by

$$A = \frac{\text{FWHM}}{2\sqrt{\ln 2}}. \tag{4.11}$$

Since the timing resolution of the BC501A detector is about 1.5 ns (as shown in Figure 4.13), a desired FWHM of 3.5 ns was chosen such that the broadened TOF spectra would correspond to the 5 ns timing resolution of the FC. The results from the Gaussian broadening of the simulated TOF spectra are shown by the solid lines in Figure 4.27.

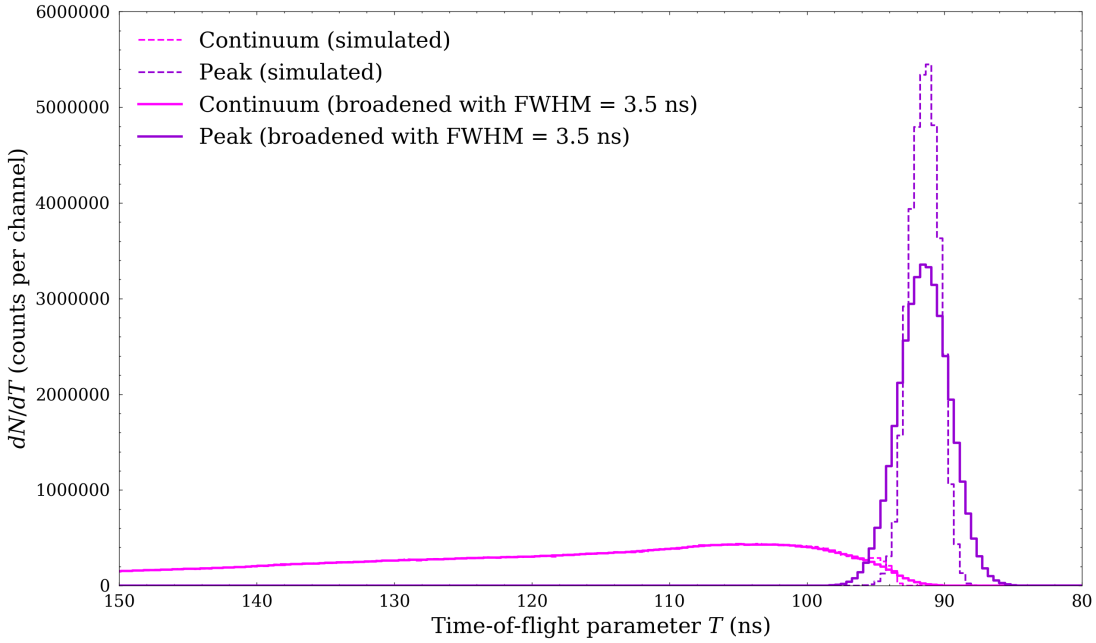

Figure 4.27: Simulated TOF spectrum calculated from the relative fluence spectra shown in Figure 4.26 for neutrons produced at 0° by a 66.48 MeV proton beam irradiating an 8.0 mm lithium target. The dashed/solid lines indicate the results before/after broadening of the data with a Gaussian function with a FWHM of 3.5 ns.

A TAC calibration was not carried out for the FC TOF measurements, and so a time-to-channel calibration of the simulated data was estimated via an alignment of the simulated and measured data in the peak region. Functions for the broadened continuum and peak spectra were obtained via interpolation of the values at the centres of the bins of the histogrammed data. A function $F(T)$ was then defined as

$$F(T) = s_C C(T - h) + s_P P(T - h), \tag{4.12}$$

where C and P are the interpolated continuum and peak functions respectively, T is the TOF channel, h is a horizontal shift, and s_C and s_P are vertical scaling factors for the continuum and peak regions respectively. The function $F(T)$ was then fitted to the overlap region of the measured data using a non-linear least squares weighted fit, with weights determined by the square root of the number of counts per bin as dictated by Poisson statistics. The number of fission counts in the high energy peak $N_{f,exp}$ was then determined via integration of $s_P P(T-h)$. The final results for the fit are shown in Figure 4.28. In order to estimate uncertainties, this procedure was repeated for simulated TOF data that was broadened by Gaussian functions with FWHMs of 2.5 ns and 4.5 ns (corresponding to a FC resolution of approximately 4 ns and 6 ns respectively), and a rectangular probability density function was assumed over this interval. The measured number of fission counts in the high-energy peak was thus determined to be

$$N_{f,exp} = (1.365 \pm 0.095) \times 10^4 \,\text{counts}.$$

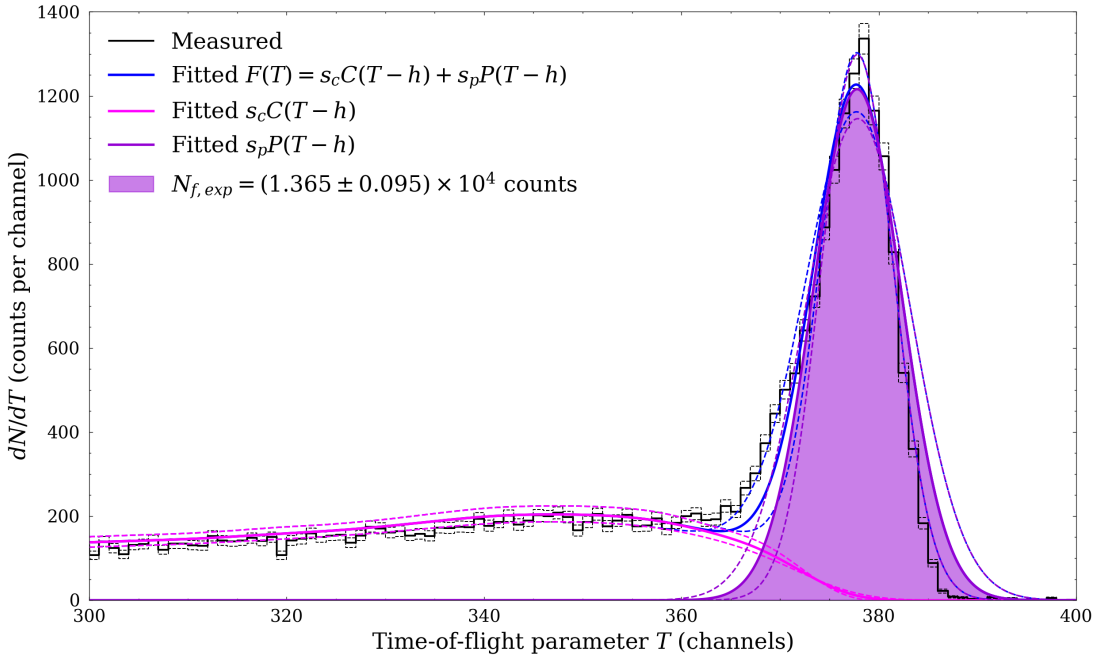

Figure 4.28: Decomposition of the TOF spectrum for neutrons produced by a 66.48 MeV proton beam irradiating an 8.0 mm lithium target, measured by the FC at a distance of 9.515 m from the target at 0°, into continuum and peak components, as obtained via a TOF simulation based on the relative spectral fluence measured with the BC501A detector. Uncertainties are indicated by the dashed lines.

4.4.4 Determining the number of fission counts in the high-energy peak under reference conditions

A series of correction factors k_i are used to relate the measured number of fission counts in the high-energy peak $N_{f,exp}$ to the number of counts that would be obtained under reference conditions as

$$N_f = N_{f,exp} \left(\prod_i k_i \right). \tag{4.13}$$

These correction factors are calculated based on the procedures outlined by Nolte et al. [2007] and Musonza [2011], as described below.

Correction for the efficiency of the FC, k_1

The correction for the efficiency of the FC, k_1, is calculated as

$$k_1 = \frac{1}{\varepsilon_{FC}(E_0)}, \tag{4.14}$$

where ε_{FC} is the detection efficiency of the FC at the peak neutron energy E_0.

As indicated in Figure 4.25, the value of the interpolated FC efficiency curve at the measured peak neutron energy of $E_{0,exp} = 62.34$ MeV was calculated to be $\varepsilon_{FC}(62.34\,\text{MeV}) = 0.948 \pm 0.015$. The correction factor k_1 was determined to be

$$k_1 = 1.055 \pm 0.017.$$

Correction for neutron absorption, multiplication and attenuation in the FC, k_2

The correction for the neutron absorption, multiplication and attenuation due to neutron interactions within the structure of the FC, k_2, is calculated as

$$k_2 = \frac{\sigma(E_0)\Phi_0}{\sigma(E_0)\bar{\Phi}_0 + \int \sigma(E)\Phi_E^{(sec)}(E)dE}, \tag{4.15}$$

where $\bar{\Phi}_0$ denotes the mean fluence of neutrons from the high-energy peak in the FC, $\Phi_E^{(sec)}$ denotes the spectral fluence of low-energy secondary neutrons produced in the structural materials of the FC, and σ is the fission cross-section of ^{238}U for the peak neutron energy E_0 [Nolte et al., 2007].

Defined as above, k_2 is effectively the ratio of the number of fission events expected without the influence of structural materials in the detector to the total number of fission events including influence of the structural materials. The factor k_2 has been previously calculated in MCNPX for a realistic model of the FC at iThemba LABS [Nolte et al., 2007]. The results from these calculations as a function of incident neutron energy are shown in Figure 4.29. The value for k_2 at a neutron energy of 62.34 MeV was determined from the value of the interpolated curve (obtained using cubic spline interpolation) at this energy. The value for k_2 was calculated to be

$$k_2 = 0.9974 \pm 0.0070.$$

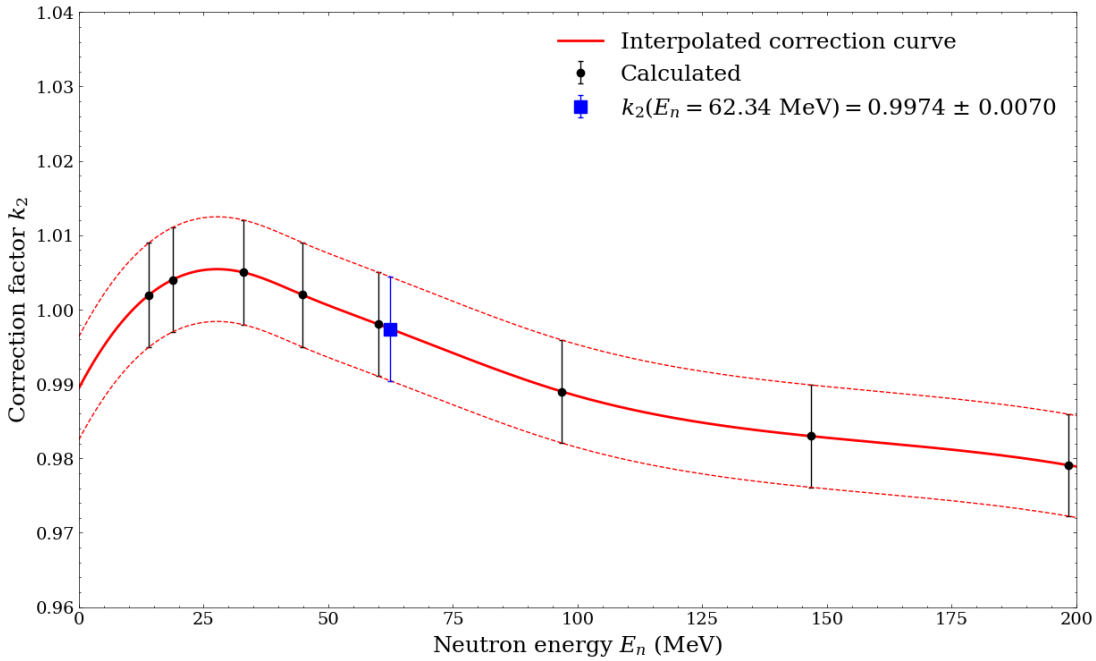

Figure 4.29: Interpolated k_2 correction curve for the FC obtained via cubic spline interpolation of the previously calculated data that was determined using MCNPX. The uncertainties of the interpolated curve are indicated by the dashed lines.

Correction for the applied pulse height threshold k_3

As discussed in Section 4.4.3, a pulse height threshold was applied to the FC measurements in order to eliminate the alpha particle background and other light reaction products from the fission events. To correct for the fission events that occur below, and the background alpha

particle events that extend beyond this threshold, the correction factor k_3 is calculated as

$$k_3 = \frac{N_{Th} - N_\alpha + N_{f,exp}}{N_{f,exp}}, \tag{4.16}$$

where N_{Th} is the number of fission events below the pulse height threshold, and N_α is the number of alpha counts above the pulse height threshold.

As shown in Figure 4.30, N_{Th} is estimated assuming a flat extrapolation from the pulse height threshold to zero pulse height, while N_α is estimated assuming a linear decrease with increasing pulse height. The slope of the linear decrease used to calculate N_α was determined by a linear fit of the measured data in the region just below the pulse height. The value of k_3 was determined to be

$$k_3 = 1.1448 \pm 0.0046,$$

where the uncertainties of N_{Th} and N_α were estimated as the square root of the number of counts of the respective quantities as dictated by Poisson statistics, and propagated appropriately through Equation 4.16.

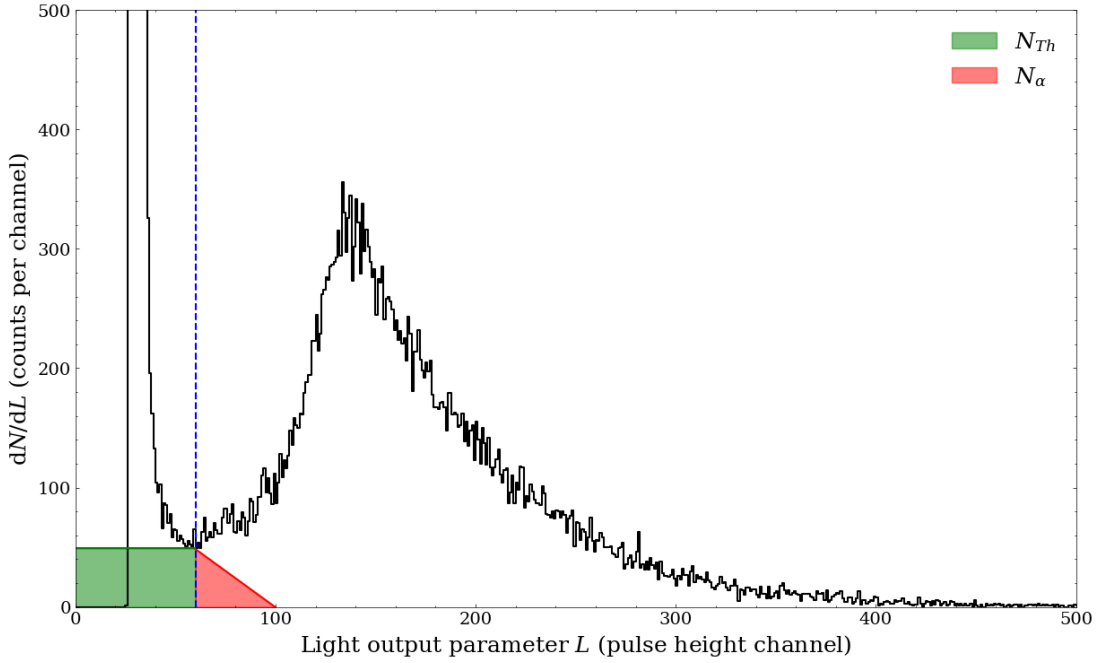

Figure 4.30: Illustration of the calculation of N_{Th} and N_α from the measured FC pulse height spectrum to correct for the fission events occurring below, and the alpha events occurring above, the applied pulse height threshold that is indicated by the dashed line.

Correction for dead time of the FC, k_4

The correction factor k_4 accounts for the dead time of the detector system and is calculated as

$$k_4 = k_{DAQ} k_{analogue}, \tag{4.17}$$

where k_{DAQ} is the correction for the dead time of the digital component of the detector system, and k_{analog} is the correction for the dead time of the analogue components of the detector system. A value of $k_4 = 1.0010 \pm 0.0010$ was used for the purposes of this analysis, as recommended by Musonza [2011].

Correction for reference distance, k_5

In order to account for the dependence of the neutron fluence on the distance at which it is measured, and scale the final fluence to a reference distance, a correction factor k_5 is defined as

$$k_5 = \left(\frac{d_{FC}}{d}\right)^2, \tag{4.18}$$

where d_{FC} is the distance of the FC from the source and d is the reference distance. For $d_{FC} = 9.5150 \pm 0.0028$ m and $d = 4.3000 \pm 0.0028$ m (a measurement position located 30 cm from the collimator exit at 0°), the final result for k_5 was calculated to be

$$k_5 = 4.8964 \pm 0.0070.$$

Correction for neutron beam attenuation in air, k_6

To account for the attenuation of the neutron beam in air between the distance at which the fluence is measured and the reference distance, a correction factor k_6 is calculated as

$$k_6 = \left(\frac{I}{I_0}\right)^{(d-d_{FC})/\mathrm{m}}, \tag{4.19}$$

where I/I_0 is the fluence attenuation in 1 m of air.

The factor I/I_0 was calculated via Monte Carlo simulations in GEANT4 of the attenuation of neutrons in air. In the simulation, the detection volume was modelled as a box with dimensions of 5.0 cm × 5.0 cm in the $x - y$ plane and a thickness of 10^{-5} cm. The neutron beam was modelled as a square planar source with the same $x - y$ dimensions as the detection volume at a z-distance of 1 m away from the detection volume onto which it was directed. Neutrons were generated from a Gaussian distribution with a mean energy of 62.34 MeV and a standard deviation of 0.37 MeV (corresponding to the energy of the high-energy peak measured at 0° by the BC501A detector as shown in Table 4.5). The geometry was enclosed in a "world" volume of air that was modelled in GEANT4 according to its standard properties as specified by the National Institute of Standards and Technology (NIST) [Geant4 Collaboration, 2023a]. For every generated neutron that entered the detection volume, a count was recorded, and at the end of a simulation run, the factor I/I_0 was calculated as the total number of counts divided by the total number of simulated neutrons. Taking the mean value of the results from five runs of 10^7 neutrons, the factor I/I_0 was determined to be 0.99599 ± 0.00074.

Again, taking $d_{FC} = 9.5150 \pm 0.0028$ m and $d = 4.3000 \pm 0.0028$ m, the final value of k_6 was calculated to be

$$k_6 = 1.0212 \pm 0.0040.$$

Correction for the spatial inhomogeneity of the neutron fluence, k_7

A correction factor k_7 used to account for the spatial inhomogeneity of the neutron fluence, is calculated as

$$k_7 = \frac{\Phi}{\Phi_{avg}}, \tag{4.20}$$

where Φ_{avg} is the mean neutron fluence averaged over the detector face, and Φ is the actual neutron fluence at the centre of the detector. This correction factor has been previously calculated based on beam profile measurements and Monte Carlo simulations for the rectangular beam profile in the D-line at a reference distance of 8.000 m [Musonza, 2011]. Beam profile

measurements at the upgraded D-line at the reference distance of interest have not yet been carried out, and for the purposes of this analysis, the previously calculated correction value of $k_7 = 1.037 \pm 0.010$ was used.

Total correction factor, k_{total}

The total correction factor used to relate the measured number of fission counts in the high-energy peak $N_{f,exp}$ to the number of counts that would be obtained under reference conditions, is calculated as

$$k_{total} = \prod_i k_i. \tag{4.21}$$

Using the correction factors discussed above, the total correction factor was calculated to be

$$k_{total} = 6.25 \pm 0.13,$$

where the uncertainty was calculated by propagating the uncertainties of the individual correction factors through the calculation in Equation 4.21. A summary of all the correction factors discussed in this section and their uncertainties is shown in Table 4.7.

Correction	**Description**	**Value**	**Uncertainty**
k_1	Efficiency of the FC	1.055	0.017
k_2	Absorption, multiplication and attenuation in the FC	0.9974	0.0070
k_3	Applied pulse height threshold	1.1448	0.0046
k_4	Dead time of the FC	1.0010	0.0010
k_5	Reference distance	4.8964	0.0070
k_6	Neutron beam attenuation in air	1.0212	0.0040
k_7	Spatial inhomogeneity of the neutron fluence	1.037	0.010
$\boldsymbol{k_{total}}$	Total	6.25	0.13

Table 4.7: Summary of the correction factors used to relate the number of fission counts in the high-energy peak $N_{f,exp}$ measured by the FC at 9.515 m to the number of counts that would be obtained under reference conditions for neutrons produced by a 66.48 MeV proton beam irradiating an 8.0 mm lithium target at a reference distance of 4.300 m from the target at 0°.

4.4.5 The ^{238}U fission cross-section

Figure 4.31 shows the point-wise cross section data for ^{238}U(n, f) reactions for incident neutrons with energies between 2 MeV and 200 MeV, obtained from the International Atomic Energy Agency (IAEA) Neutron Data Standards [Carlson et al., 2018]. Linear interpolation of these data points is recommended by the IAEA and this was used to determine the ^{238}U(n, f) cross-section at the peak neutron energy of $E_{0,exp} = 62.34$ MeV to be

$$\sigma(62.34\,\text{MeV}) = 1.595 \pm 0.040\,\text{b}.$$

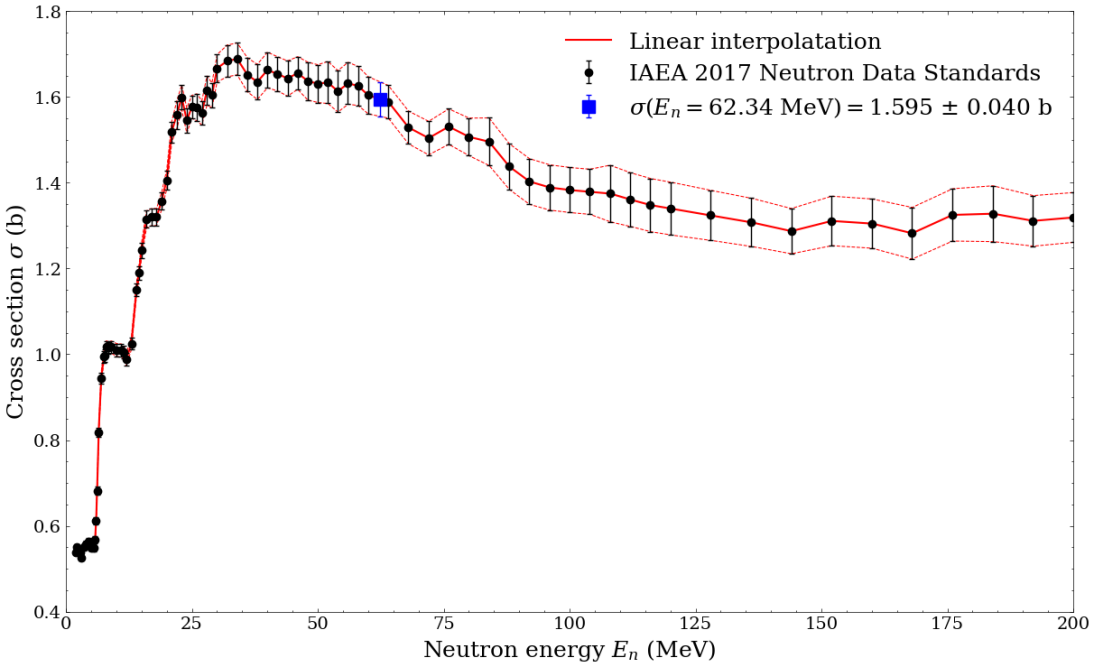

Figure 4.31: Linear interpolation of the IAEA 2017 Neutron Data Standards for ^{238}U(n, f) reaction cross-sections for incident neutrons between 2 MeV and 200 MeV. The uncertainties of the interpolation are indicated by the dashed lines.

4.4.6 Number of ^{238}U atoms in the ^{238}U fission ionisation chamber

The FC at iThemba LABS was obtained from the IRMM, and its composition of uranium was analysed by the National Bureau of Standards of the United States of America. The total mass of uranium in the FC was reported to be $M = 0.24090 \pm 0.02409$ g and the relative abundance of ^{238}U atoms in the uranium material was quoted to be $R = 99.9823 \pm 0.0001\%$ [Musonza, 2011]. Using this information, the number of ^{238}U atoms in the FC can be calculated as

$$N_U = \frac{RMN_A}{M_U} = (6.09 \pm 0.61) \times 10^{20}\,\text{atoms}, \tag{4.22}$$

where $M_U = 238.02891 \pm 0.00003\,\text{g/mol}$ is the molar mass of natural uranium, and $N_A = 6.02214076 \times 10^{23}\,\text{atoms/mol}$ is the Avogadro constant. The standard unit of cross section is the barn (b) and thus N_U can be written in terms of the total atomic area available for neutron fission as

$$N_U = (6.09 \pm 0.61) \times 10^{20} \times \frac{10^{-24}\,\text{cm}^2}{\text{b}} = (6.09 \pm 0.61) \times 10^{-4}\,\text{cm}^2/\text{b}.$$

4.4.7 Measurement of the peak neutron fluence

As stated in Section 4.4.1. The absolute neutron fluence in the high-energy peak is calculated from the FC measurements as

$$\Phi_0 = \frac{N_{f,exp}(\prod_i k_i)}{\sigma N_U}, \tag{4.9}$$

where $N_{f,exp}$ is the measured number of fission counts in the high-energy peak, k_i are a series of correction factors (as discussed in Section 4.4.4), σ is the ^{238}U fission cross section for neutrons in the high-energy peak, and N_U is the number of fissile ^{238}U atoms in the FC [Nolte et al., 2007].

The results discussed in Sections 4.4.3 to 4.4.6 can be used in Equation 4.9 to calculate the absolute peak fluence Φ_0 of neutrons produced produced by a 66.48 MeV proton beam irradiating an 8.0 mm lithium target, scaled to a reference distance of 4.300 m from the target at 0 °. The results for the presented measurements are summarised in Table 4.8, where the calculated peak neutron fluence is scaled with respect to the total number of NE102 monitor counts M during the FC measurement run. The uncertainty of M was taken as $\sqrt{M}$ as described by Poisson statistics.

Parameter	**Value**	**Uncertainty**
$E_{0,exp}$ (MeV)	62.34	0.37
σ (b)	1.595	0.040
$N_u \times 10^{-4}$ (cm^2/b)	6.09	0.61
d_{ref} (m)	4.3000	0.0028
$N_{f,exp} \times 10^4$	1.365	0.095
k_{total}	6.25	0.13
$M \times 10^7$	2.03875	0.00045
$\Phi_0 \times 10^7$ (cm^{-2})	8.8	1.1
Φ_0/M (cm^{-2})	4.32	0.54

Table 4.8: Summary of the key parameters involved in the calculations of the peak neutron fluence per unit monitor count measured by the FC for neutrons produced by a 66.48 MeV proton beam irradiating an 8.0 mm lithium target scaled to a reference distance of 4.300 m from the target at 0°.

5 Quantification of neutron dose at iThemba LABS

Measurements of neutron RBE_M require the determination of the absorbed dose that is delivered by neutrons to the investigated biological samples. This chapter presents an analysis of measurements that were conducted in the D-line in June 2022 in order to establish the absorbed dose delivered to vials of human blood for irradiations with neutrons produced by a 66.48 MeV proton beam impinging on an 8.0 mm lithium target. These are the first dose quantification measurements conducted in the D-line at iThemba LABS since the infrastructural upgrade (described by Ndlovu et al. [2019]) was completed in 2020/2021.

Figure 5.1 shows a schematic layout of the experiment. Metrological neutron beam characterisation was carried out via measurements with the BC501A liquid scintillation detector, ^{238}U fission ionisation chamber (FC), and monitor detectors (a Faraday cup and a NE102 plastic scintillation detector), as discussed in Chapter 4. The blood vials were contained in high density polyethylene phantoms placed 0.30 m from the exits of the beam collimators at 0° and 16°.

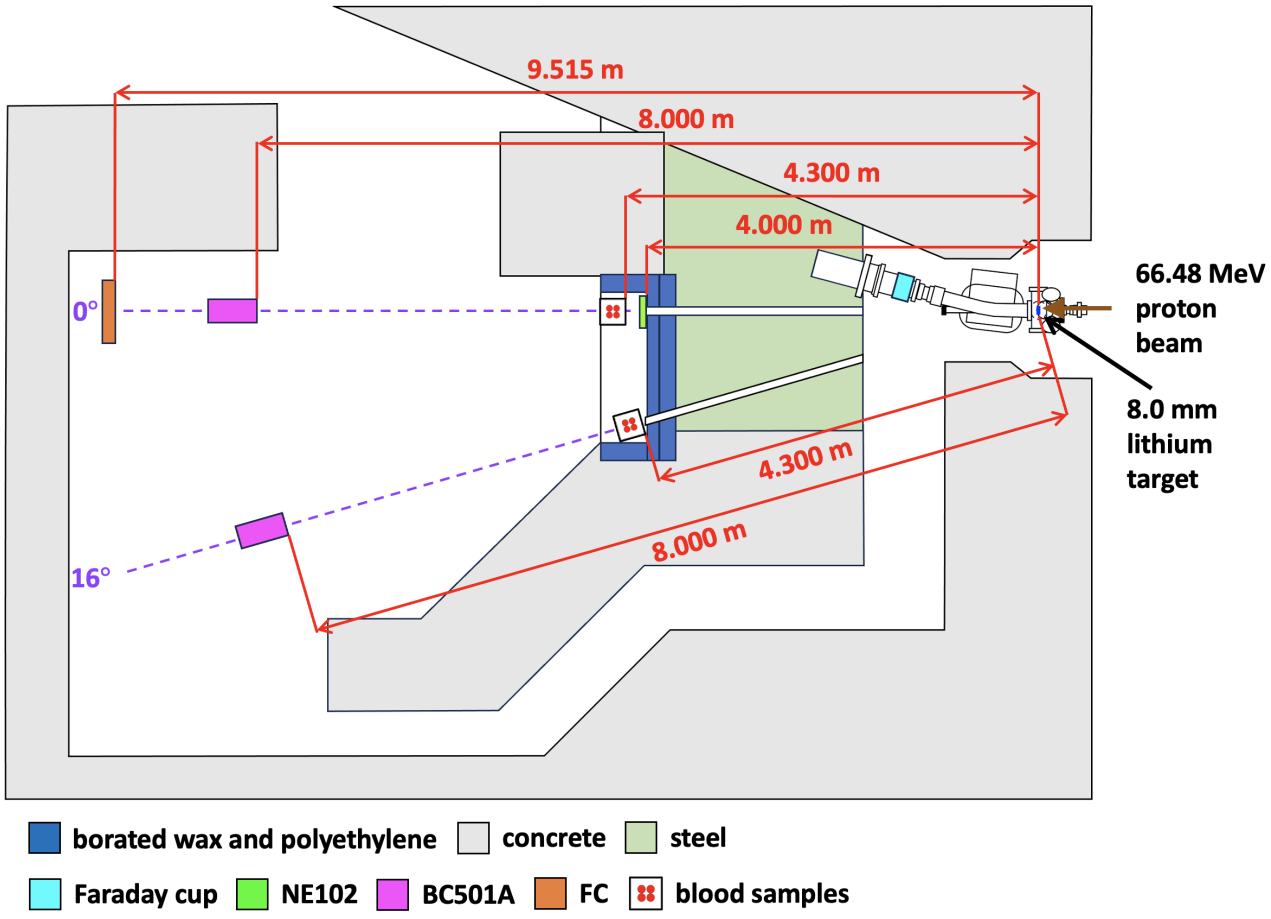

Figure 5.1: Layout of the experimental setup for the dose quantification measurements conducted in the D-line at iThemba LABS in June 2022.

Following the method outlined by Nolte et al. [2005, 2006], the absorbed dose D received by the irradiated blood samples is related to the neutron beam parameters by

$$D = \left(\frac{D}{\Phi}\right)\left(\frac{\Phi}{\Phi_0}\right)\left(\frac{\Phi_0}{M}\right)M, \tag{5.1}$$

where Φ is the total neutron fluence at the front face of the phantom containing the blood vials, Φ_0 is the peak neutron fluence, and M is the neutron monitor count. As discussed in the following sections:

- D/Φ is determined from Monte Carlo simulations in GEANT4 (Section 5.3);
- Φ/Φ_0 is determined from measurements with the BC501A detector (Section 5.1.1);
- Φ_0/M is determined from measurements with the ^{238}U FC (Section 5.1.2); and
- M is determined from an analysis of the monitor count rates recorded throughout the irradiations (Section 5.2.1).

5.1 Characterisation of the neutron beams

A schematic of the experimental setup for the characterisation of the neutron beams is shown in Figure 5.1. Neutrons were produced by directing a 66.48 MeV proton beam from the SSC onto an 8.0 mm lithium target. The RF cycle of the SSC was 16.37 MHz and the pulse selector was set to select 1 in 5 proton bunches with a time separation of 305 ns to enable TOF measurements. The BC501A detector was placed 8.000 m from the centre of the lithium target and high-energy resolution neutron spectral fluence measurements (as described in Section 4.3) were conducted at reduced proton beam currents of around 100 nA for neutron emission angles of 0° and 16°. The FC was placed 9.515 m from the centre of the lithium target and measurements of the peak neutron fluence (as described in Section 4.4) were conducted at increased proton beam currents of between 200 nA and 850 nA for a neutron emission angle of 0°.

5.1.1 Characterisation of the neutron spectral fluence with the BC501A liquid scintillation detector

Figure 5.2 shows the neutron relative spectral fluence measured with the BC501A detector and TOF method (as described in Section 4.3) at neutron emission angles of 0° and 16°. The high resolution spectral fluence measurements at 0° at low currents (as shown in Figure 4.18) were compared to the low resolution FC measurements at high currents (as shown in Figure 4.28), and it was found that the continuum-to-peak ratio had to be increased by factor of 1.17 ± 0.20 at higher beam intensities. This effect is attributed to parasitic neutrons that are produced in the target holder or in structures in the beam line in front of the target that are hit by the halo of the proton beam which varies with beam current and focusing conditions [Nolte et al., 2008]. To correct for this effect at high currents, the continuum component of the spectral fluence as measured with the BC501A detector at 0°, was multiplied by a factor of 1.17 ± 0.20 and the corrected spectrum is shown in Figure 5.2. It was assumed that no such correction was necessary for the 16° measurements because the 16° collimator would shield parasitic neutrons produced in the beam line [Nolte et al., 2008].

The key parameters of the measured neutron spectral fluence distributions shown in Figure 5.2 are summarised in Table 5.1, where E_p is the energy of the protons from the SSC, d_{Li} is the thickness of the lithium target, $E_{0,exp}$ is the experimental mean energy of the high-energy peak, Θ is the neutron emission angle, $\langle E \rangle_\Phi$ is the fluence-weighted average energy, Φ is the total neutron fluence, and Φ_0 is the peak neutron fluence.

E_p (MeV)	d_{Li} (mm)	$E_{0,exp}$ (MeV)	Θ(°)	$\langle E \rangle_\Phi$ (MeV)	Φ/Φ_0	$\Phi_0(16°)/\Phi_0(0°)$
66.48	8.0	62.34 ± 0.37	0	40.11 ± 0.92	2.93 ± 0.11	0.263 ± 0.013
			16	37.26 ± 0.40	6.08 ± 0.20	

Table 5.1: Summary of the key parameters of the spectral fluence distributions shown in Figure 5.2 of neutrons produced by a 66.48 MeV proton beam irradiating an 8.0 mm lithium target, measured by the BC501A detector at a distance of 8.000 m from the target at 0° and 16°.

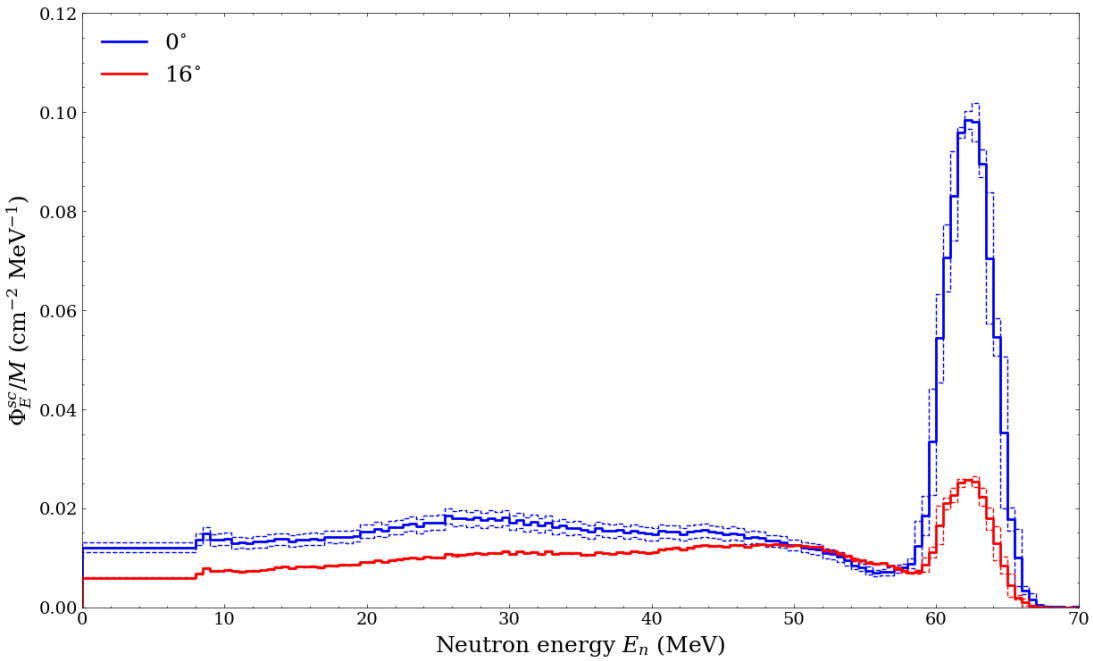

Figure 5.2: Relative spectral fluence per monitor count for measurements of neutrons produced by a 66.48 MeV proton beam irradiating an 8.0 mm lithium target, measured by the BC501A detector at a distance of 8.000 m from the target at 0° and 16°. For consistency with the FC measurements, the height of the low energy continuum region of the 0° distribution was rescaled by a factor of 1.17 ± 0.20. The uncertainties are indicated by the dashed lines.

5.1.2 Characterisation of the neutron fluence measurements with the ^{238}U fission ionisation chamber

Table 5.2 shows the result for the neutron fluence in the high-energy peak Φ_0 per NE102 monitor count M at 0°, calculated from the FC measurements as described in Section 4.4. Measurements with the FC were not made at 16°, and so the result obtained from measurements with the BC501A detector for the ratio of the 16° peak fluence to the 0° peak fluence (as shown in Table 5.1), was used to extrapolate the absolute peak neutron fluence at 16° as shown in Table 5.2.

Θ(°)	d_{ref} (m)	Φ_0/M (cm^{-2})
0	4.3000 ± 0.0028	4.32 ± 0.54
16	4.3000 ± 0.0028	1.13 ± 0.15

Table 5.2: Results for the peak neutron fluence per monitor count calculated from measurements with the FC for neutrons produced by a 66.48 MeV proton beam irradiating an 8.0 mm lithium target, scaled to a reference distance of 4.300 m from the target at 0° and 16°.

5.2 Irradiation of blood samples

A schematic of the experimental setup for the irradiation of the blood samples is shown in Figure 5.1. The blood irradiations were conducted at beam currents of around 1000 nA to 1500 nA under identical beam conditions to those used for the BC501A and FC detector measurements, except that the beam pulse selector was switched off to increase the dose delivered to the blood vials.

Two high density polyethylene phantoms, with dimensions as shown in Figure 5.3, were constructed for holding four "Nest" 1.8 ml cryogenic vials at their centres. Each vial contained isolated peripheral blood mononuclear cells (PBMCs) of the same donor, suspended in 1.8 ml Roswell Park Memorial Institute (RPMI) cell culture media with 20% foetal bovine serum (FBS). During the irradiations, the phantoms were placed with their front faces a distance of 0.300 m from the collimator exits at 0° and 16° (4.300 m from the lithium target).

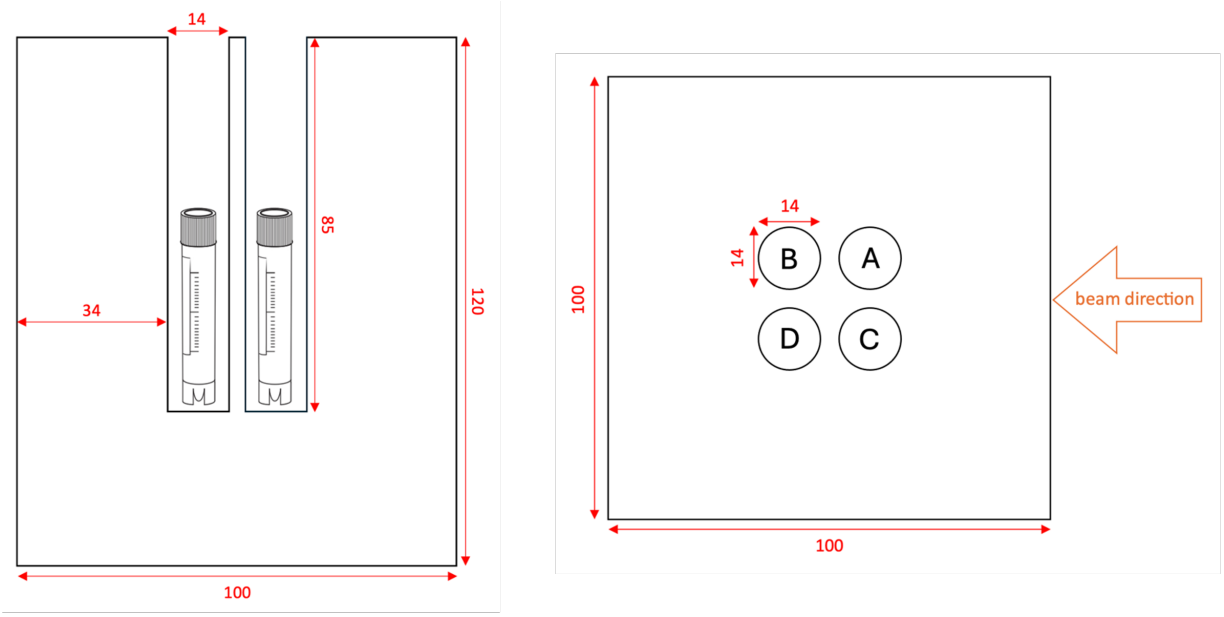

Figure 5.3: Cross-sectional diagrams showing (left) the side view and (right) the top view of the high density polyethylene phantoms that were constructed to contain the blood vials (labelled A, B, C and D) during the neutron irradiations at 0° and 16°. All dimensions are stated in mm.

The blood irradiations were carried out over a total time period of twelve hours. After roughly four hours of irradiation, the vials labelled 'A' in each of the phantoms at 0° and 16° were removed and replaced with water dummy tubes. This procedure was repeated for vials B, C, and D after roughly seven, ten, and twelve hours respectively, to ensure delivery of different levels of absorbed doses to the samples.

5.2.1 Monitoring of the neutron beam conditions during the blood irradiations

Figure 5.4 shows the results for the monitor logger values M_{slow} and M_{fast} normalised to beam charge Q as recorded in 60 s intervals during the irradiation of the blood vials. As discussed in Section 4.2, the beam current should be proportional to the neutron fluence rate if the proton beam is stable and well-focused, however this relationship should be used with caution as leakage currents and the beam focus on the target can vary with time. For this reason, it is necessary to observe the ratios of the different monitors throughout the irradiations, which should be approximately constant if the beam is stable. Figure 5.4 shows that there were times during the irradiations where the beam current was unstable or was switched off completely, either so

that a blood vial could be removed or because it tripped and needed to be restarted. The total 'active' irradiation times of the blood vials, were chosen to correspond to the measurement run periods as indicated by the shaded regions in Figure 5.4 and summarised in Table 5.3.

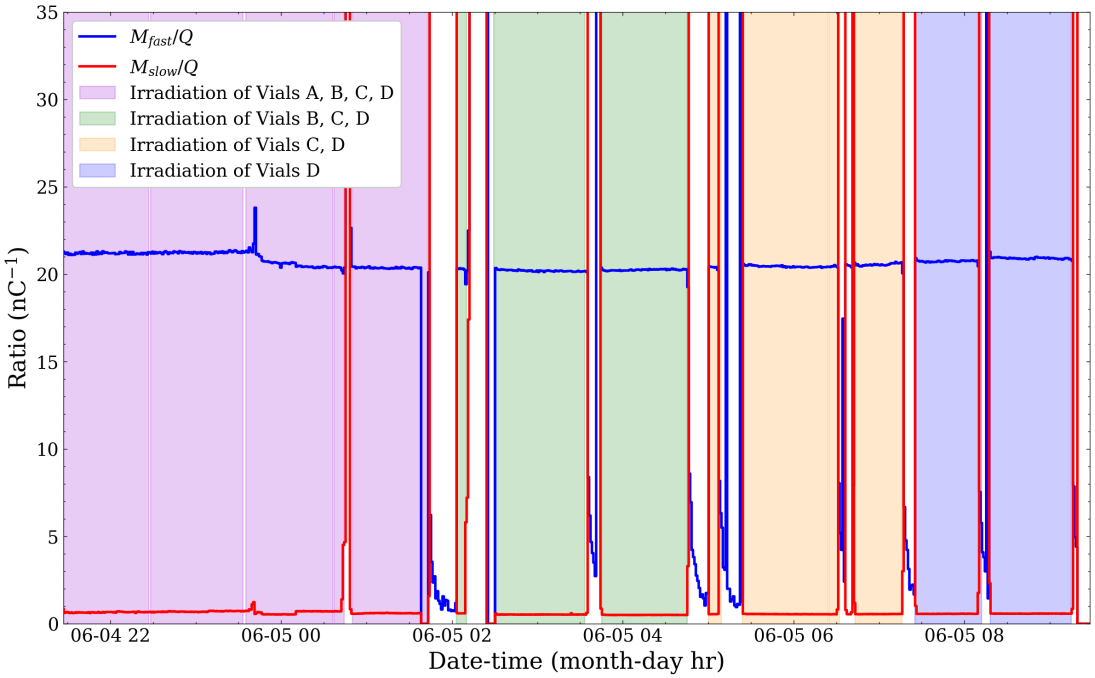

Figure 5.4: Monitor logger values normalised to beam charge as recorded in 60 s intervals during the irradiation of the blood vials. The total 'active' irradiation periods are indicated by the shaded regions.

Vial	**Irradiation time** (hr: min: s)	$\boldsymbol{M}\times10^{8}$
A	04: 05: 34	1.13911 ± 0.00011
B	05: 17: 23	1.71301 ± 0.00013
C	07: 06: 27	2.44552 ± 0.00016
D	08: 53: 02	3.09771 ± 0.00018

Table 5.3: Total 'active' irradiation times of each of the blood vials and the corresponding total number of NE102 monitor counts M, for the irradiations with neutrons produced by a 66.48 MeV proton beam impinging on an 8.0 mm lithium target at a distance of 4.300 m from the target at 0° and 16°.

5.3 Monte Carlo simulations of absorbed dose to the blood samples

Monte Carlo simulations in GEANT4 were used to determine the quantity of absorbed dose to human blood per unit neutron fluence at the front face of the phantom, D/Φ, in Equation 5.1, for each of the blood vials during the neutron irradiations at 0° and 16° respectively. This section outlines how the experimental setup was simulated in GEANT4 and the calculation method used to determine D/Φ and the associated uncertainties for each blood vial.

5.3.1 Simulation geometry

In the simulation, a high density polyethylene phantom was constructed to match the dimensions shown in Figure 5.3. The sample vials placed in the phantom were modelled as cylindrical volumes of ICRP blood with a radius of 0.5 cm, and a height of 2.3 cm, and therefore a total volume of 1.8 cm^3. The polyethylene and ICRP blood materials were modelled in GEANT4 based on their standard properties as specified by the NIST [Geant4 Collaboration, 2023a].

The neutron beam was modelled as a square planar source with dimensions of 5 cm × 5 cm. The beam was situated in the $x - y$ plane at the front face of the phantom such that every generated neutron would be incident on the phantom face. The position and size of the beam relative to the simulated phantom and blood vials is shown in Figure 5.5. The neutron fluence spectra as shown in Figure 5.2, were normalised and treated as probability distributions from which the energies of the simulated neutrons were randomly sampled.

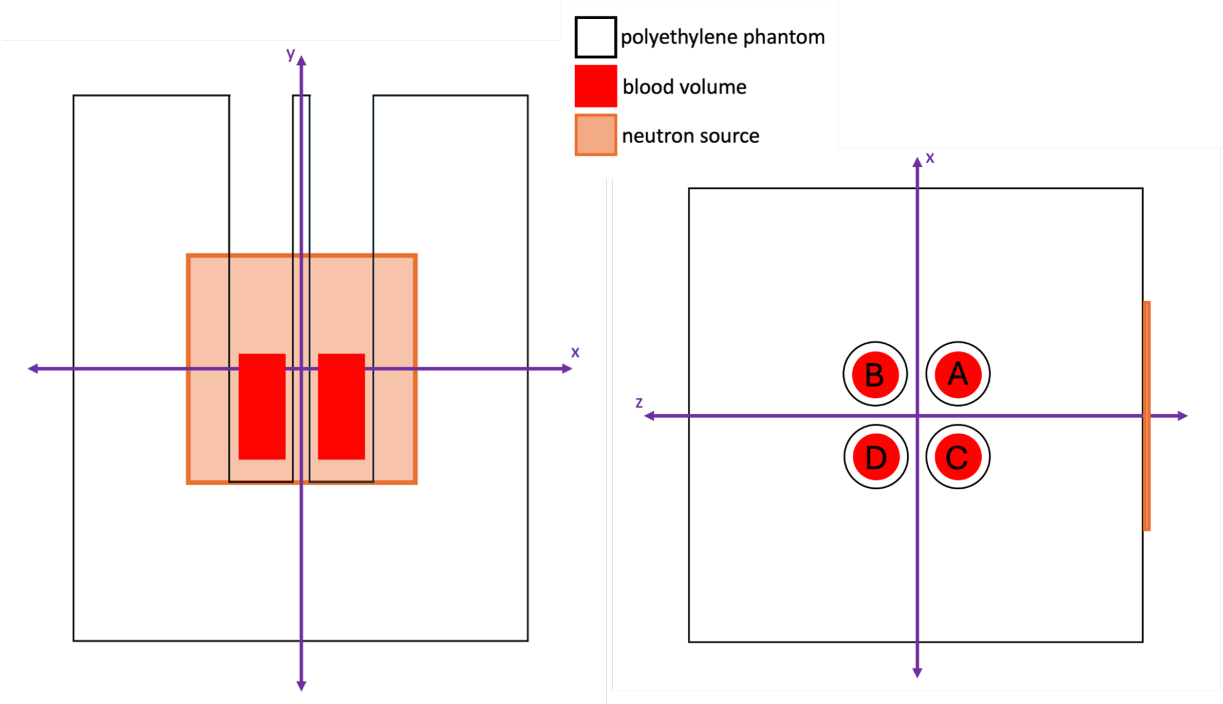

Figure 5.5: Diagrams illustrating the position of the neutron source relative to the high density polyethylene phantom and blood vials as modelled in GEANT4. The dimensions of the phantom are the same as shown in Figure 5.3, the blood samples are modelled as cylindrical volumes with radii of 0.5 cm and heights of 2.3 cm, and the neutron source is a 5 cm × 5 cm planar source placed at the front face of the phantom.

5.3.2 Modelling physical interactions in Geant4: Choice of Physics List

GEANT4 offers a wide range of physics models, or 'Physics Lists' that are responsible for specifying the particles that are used in the simulation together with the processes assigned to their physical interactions. While the user can have a large amount of flexibility in terms of specifying the physics environment of their simulation, there are a number of 'reference' Physics Lists that are well-maintained, extensively validated, and recommended for use in specific applications. For the current simulations, the reference Physics List, QGSP_BIC_AllHP was used.

The hadronic component of the QGSP_BIC_AllHP list consists of elastic, inelastic, and capture processes that are built from a set of cross-section sets and interaction models. For the interactions of neutrons with energies below 20 MeV, it uses a high precision transport and cross-section model based on data from a combination of different standard evaluated neutron data libraries. The interactions of protons, deuterons, tritons, ^{3}He ions and alpha particles, are also simulated based on a high precision data-driven model at energies below 200 MeV [Geant4 Collaboration, 2020]. For hadronic interactions with energies extending beyond the limitations of the high precision models sets up to 10 GeV, the QGSP_BIC_AllHP list uses the theory-based Binary Cascade Model, which is an intranuclear cascade model for propagating primary and secondary particles in a nucleus. The model in GEANT4 simulates the initial interaction of the particle with individual nucleons of the nucleus, and the subsequent production of high-energy secondary particles, leaving the nucleus in an excited state. The propagation of particles is done via numerically solving the equation of motion and once the intranuclear cascade terminates (when the energies of secondary particles drop below a particular threshold), the remaining fragment is handled with various pre-compound and de-excitation models [Geant4 Collaboration, 2023b].

The electromagnetic component of the QGSP_BIC_AllHP list uses the "standard" GEANT4 electromagnetic physics. Similarly, the decay of all long-lived hadrons and leptons is handled by standard GEANT4 decay processes. Further details on this physics list can be found in the GEANT4 Physics List User Manual [Geant4 Collaboration, 2020].

5.3.3 Method of calculation

The basic unit of simulation in GEANT4 is called an event. At the beginning of an event, the track of a primary particle is generated. This track contains the physical quantities corresponding to the physical properties of the particle and is updated in 'steps' throughout the event, along with any secondary tracks that are created as the primary particle and subsequent secondary particles interact within the simulated environment. The steps that are used to update a particular track contain 'delta' information, like energy loss or gain, of a particle between two points.

At the beginning of each event, a neutron was generated at an initial position that was randomly sampled from a uniform distribution across the planar source. Each neutron was generated with an energy sampled from a probability distribution based on the measured BC501A neutron spectral fluence distributions at 0° and 16° (as shown in Figure 5.2), and with an initial momentum in the z-direction. The tracks of the primary neutron and any secondary tracks created were followed throughout the event either until they exited out of the world volume (defined as a 1 m^3 box of air containing the simulated geometry), disappeared, or reached zero kinetic energy. The blood vials of interest were set as scoring volumes such that every time a step resulted in energy being deposited in the blood, the amount of energy deposited in that step was recorded. At the end of each event, the energy deposited in the blood vial throughout

that event was summed up to determine the total energy deposited per simulated event. The total energy deposited over an entire 'run' of N simulated neutrons could then be determined by summing up the total energy deposited per event.

Since neutrons are indirectly ionising radiation, they do not deposit energy in the blood vials directly. Rather, they interact with the nuclei of the material in the phantom and blood vials to transfer their energy to a mixed field of secondary radiation particles which are subsequently responsible for depositing energy via the ionisation and excitation of atoms and molecules. The energy deposited per event that was calculated in the simulation is therefore the sum of the energy deposited by these secondary charged particles. Figure 5.6 shows the energy deposited per event in vial A by different charged particles for a run of 10^8 incident neutrons sampled from the 0° fluence spectrum. It should be noted that the events where no energy was deposited were excluded from this histogram because they dominate the events where energy is deposited. Neutrons are highly penetrating and can travel through many centimetres of matter without any interaction. For a run of 10^8 events, only 0.84% of the events resulted in energy being deposited in vial A.

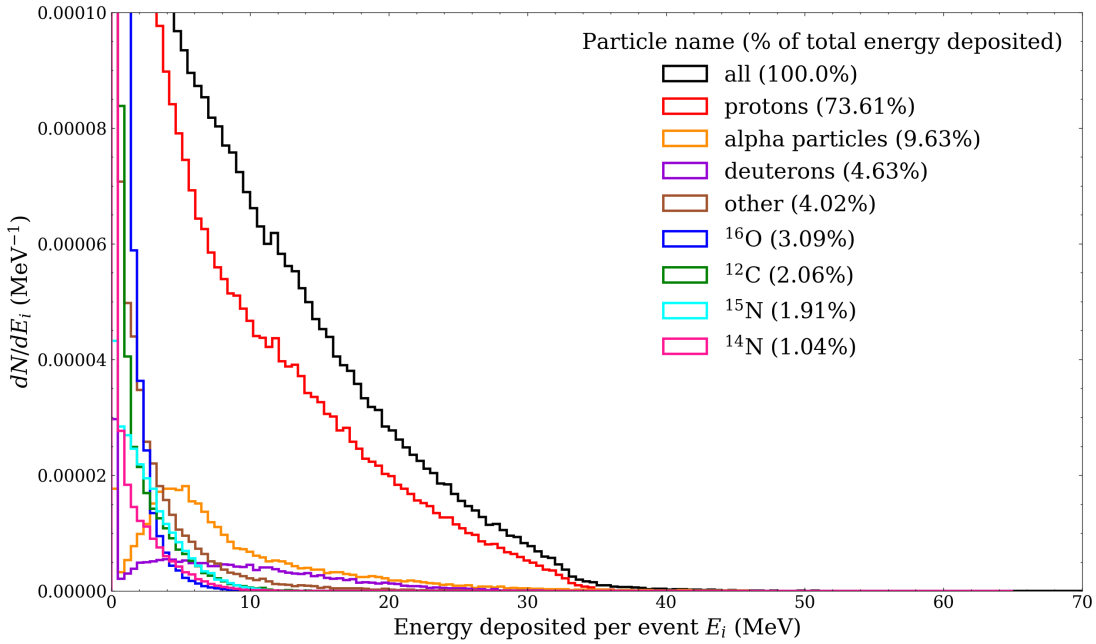

Figure 5.6: Energy deposited in vial A by different charged particles in per event for a simulation run of 10^8 incident neutrons sampled from the fluence spectrum for neutrons produced by a 66.48 MeV proton beam irradiating an 8.0 mm lithium target measured by the BC501A detector at 0°. "All" refers to the energy deposited by all charged particles during the event, and "other" includes particles that individually contributed $< 1\%$ to the total energy deposited.

The absorbed dose deposited in a blood vial over a run of N simulated neutrons (which corresponds to N events) was calculated as

$$D = \frac{\sum_{i=1}^{N} E_i}{M_b}, \tag{5.2}$$

where E_i is the energy deposited in the blood vial in event i and M_b is the mass of the blood vial.

The fluence of incident neutrons on the front face of the phantom was calculated as

$$\Phi = \frac{N}{A}, \tag{5.3}$$

where N is the number of simulated neutrons (which corresponds to the number of incident neutrons since the source was placed at the phantom surface) and A is the cross-sectional area of the beam.

Combining Equations 5.2 and 5.3, the absorbed dose D to human blood per unit neutron fluence Φ at the front face of the phantom was therefore calculated as

$$\frac{D}{\Phi} = \frac{A}{M_b}\left(\frac{1}{N}\sum_{i=1}^{N} E_i\right) \equiv \frac{A}{M_b}\bar{E}, \tag{5.4}$$

where $\bar{E}$ is defined as the sample mean energy deposited per event.

5.3.4 Estimation of the Monte Carlo precision

Monte Carlo methods rely on repeated random sampling to obtain numerical results that represent an average of the contributions from all the histories that are sampled throughout the problem. The statistical uncertainty that is inherent in this process was estimated by assessing the sample standard deviation of the Monte Carlo result for the sample mean energy deposited per event $\bar{E}$ as defined in Equation 5.4. The sample standard deviation of the mean $\bar{E}$ was calculated as

$$S_{\bar{E}} = \sqrt{\frac{S^2}{N}}, \tag{5.5}$$

where S^2 is the sample variance, and was calculated as

$$S^2 = \frac{\sum_{i=1}^{N}(E_i - \bar{E})^2}{N-1} \approx \frac{\sum_{i=1}^{N} E_i^2 - \frac{1}{N}(\sum_{i=1}^{N} E_i)^2}{N-1}, \tag{5.6}$$

where the approximation was obtained using a standard numerical algorithm for computing the sample variance as specified in Chan et al. [1983].

Based on Equation 5.4, the statistical uncertainty in the result for D/Φ caused by the statistical fluctuations of the amount of energy deposited per event for the portion of the physical phase space that has been sampled by the Monte Carlo process was calculated as

$$u\left(\frac{D}{\Phi}\right)_{stat} = \frac{A}{M_b} S_{\bar{E}}. \tag{5.7}$$

A key characteristic of Monte Carlo simulations is that the 68% confidence interval defined by the uncertainty as calculated in Equation 5.7, is only valid if the physical phase space has been 'adequately sampled' by the Monte Carlo process. The result from the simulation should approach the 'true' result as the number of simulated events N approaches infinity, however there is a trade-off in computational time and so it is often up to the discretion of the user to decide when adequate events have been simulated to allow for the convergence of the result on a statistically valid solution.

There are a number of 'statistical checks' that can be conducted to assess the statistical behaviour of the final result of the Monte Carlo simulation and the validity of the corresponding confidence intervals. For this purpose, seven of the 'statistical checks' recommended in Kulesza et al. [2022] were carried out to assess the validity of the results obtained for D/Φ in the Monte Carlo simulation in GEANT4 for various numbers of simulated neutrons. The statistical tests and their results for the current simulations are discussed in detail in Appendix A. Failing several of these tests is typically an indication that the determined confidence of the final results

is less likely to be correct. As discussed in Appendix A, it was found that all seven tests were passed for $N = 2 \times 10^9$ simulated events, and so this N was chosen to obtain the final results for D/Φ. Figure 5.7 shows the results for D/Φ for each blood vial at 0° and 16° plotted with the corresponding statistical uncertainties as a function of the number of simulated neutrons N.

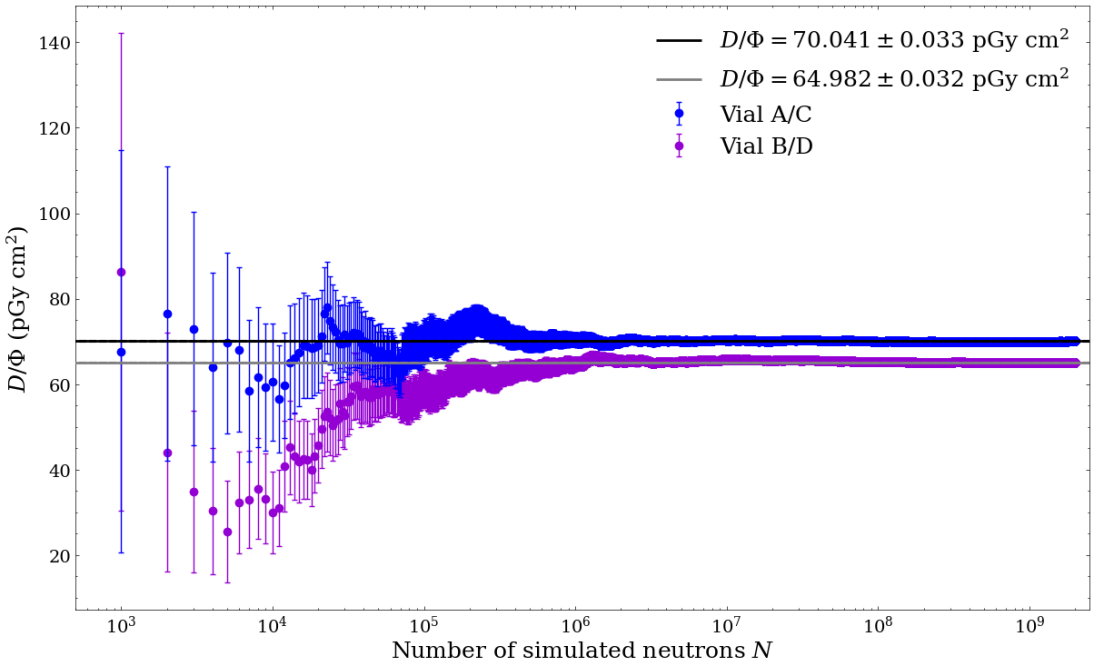

(a)

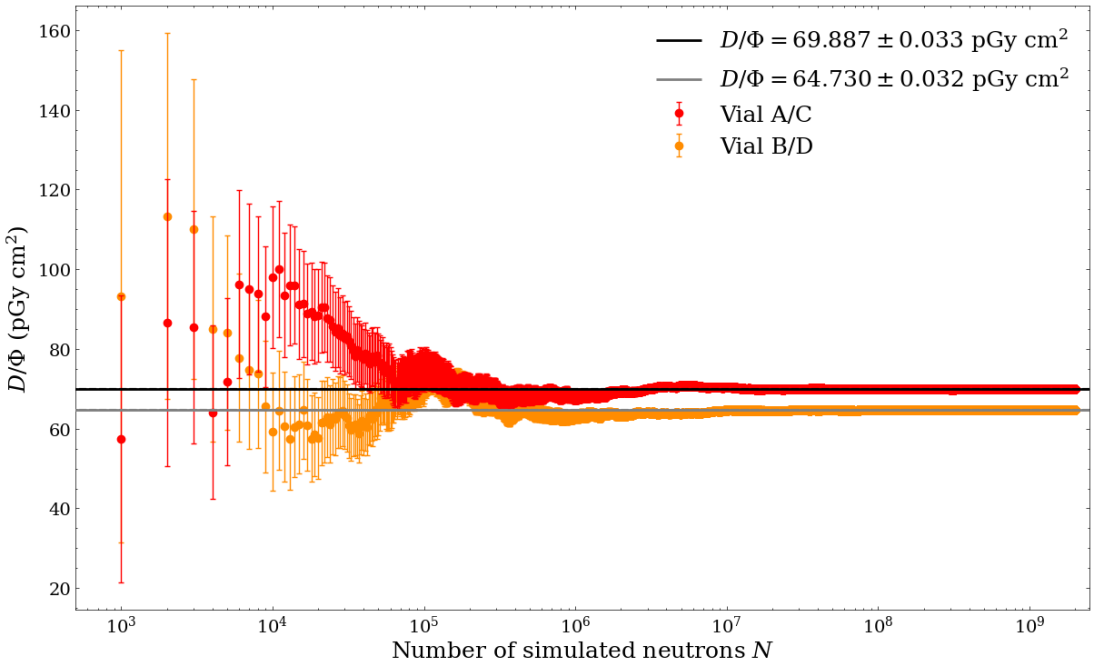

(b)

Figure 5.7: The simulation results with statistical uncertainties for D/Φ in each blood vial as a function of the number of simulated neutrons N with energies sampled from (a) the 0° fluence spectrum, and (b) the 16° fluence spectrum, shown in Figure 5.2. The horizontal lines indicate the result for D/Φ for 2×10^9 incident neutrons.

5.3.5 Simulation results for D/Φ

The results for the absorbed dose to human blood in each of the blood vials per unit neutron fluence at the front face of the phantom, D/Φ, as required for the calculation in Equation 5.1 for the irradiations at 0° and 16°, are summarised in Table 5.4.

As motivated in Section 5.3.4, the results were obtained for simulation runs of 2×10^9 incident neutrons sampled from the 0° or 16° fluence spectra shown in Figure 5.2. The final uncertainties involve both the statistical uncertainty $u\left(D/\Phi\right)_{stat}$ associated with the Monte Carlo process (as discussed in Section 5.3.4), as well as the uncertainty associated with the BC501A detector measurements of the neutron fluence spectra $u\left(D/\Phi\right)_{\Phi_E^{sc}}$ that were used as input spectra. The values of $u\left(D/\Phi\right)_{\Phi_E^{sc}}$ were obtained by running the simulation with the upper and lower bounds of the Φ_E^{sc} measurements (as indicated by the dashed lines in Figure 5.2) as the input spectra from which the energies of the simulated neutrons were sampled. As shown in Table 5.4, the uncertainties associated with the Φ_E^{sc} measurements (arising from the TOF measurements as discussed in Section 4.3.4) dominated the statistical uncertainties in all cases.

Θ (°)	**Vial**	$\boldsymbol{D/\Phi}$ (pGy cm^2)	$\boldsymbol{u(D/\Phi)}$ (pGy cm^2)	
0	A/C	70.03	$u(stat)$	0.033
			$u(\Phi_E^{sc})$	0.11
			0.11	
	B/D	64.97	$u(stat)$	0.032
			$u(\Phi_E^{sc})$	0.10
			0.10	
16	A/C	69.89	$u(stat)$	0.033
			$u(\Phi_E^{sc})$	0.15
			0.15	
	B/D	64.73	$u(stat)$	0.032
			$u(\Phi_E^{sc})$	0.17
			0.17	

Table 5.4: Summary of the Monte Carlo simulation results for D/Φ in each blood vial obtained for simulation runs of 2×10^9 incident neutrons sampled from the 0° and 16° spectra shown in Figure 5.2.

5.4 Calculation of the absorbed dose delivered to the irradiated blood samples

5.4.1 Calculation of the total absorbed dose delivered to the irradiated blood samples

Table 5.5 presents a summary of the results obtained in Sections 5.1 to 5.3. The absorbed dose D in each blood sample was calculated using Equation 5.1, with associated uncertainties determined via the propagation of the uncertainties of each quantity through the calculation. As shown in Table 5.5, the total relative uncertainties of the absorbed dose values D ranged between 12.9% and 13.7% for all irradiations.

Vial	$\boldsymbol{\Phi/\Phi_0}$	$\boldsymbol{\Phi_0/M}$ (cm^{-2})	$\mathbf{D/\Phi}$ (pGy cm^2)	$\boldsymbol{M} \times 10^8$	$\boldsymbol{D}$ (mGy)
0° irradiation position					
A	2.93 ± 0.11	4.32 ± 0.54	70.03 ± 0.11	1.13911 ± 0.00011	101 ± 13
B			64.97 ± 0.10	1.71301 ± 0.00013	141 ± 18
C			70.03 ± 0.11	2.44552 ± 0.00016	217 ± 28
D			64.97 ± 0.10	3.09771 ± 0.00018	255 ± 33
16° irradiation position					
A	6.08 ± 0.20	1.13 ± 0.15	69.89 ± 0.15	1.13911 ± 0.00011	54.7 ± 7.5
B			64.73 ± 0.17	1.71301 ± 0.00013	76 ± 10
C			69.89 ± 0.15	2.44552 ± 0.00016	117 ± 16

Table 5.5: Summary of the results obtained in Sections 5.1 to 5.3 that were used in Equation 5.1 to calculate the total absorbed dose D that was delivered to each blood vial during the irradiations with neutrons produced by a 66.48 MeV proton beam impinging on an 8.0 mm lithium target, with the front faces of the phantoms containing the blood vials placed 4.300 m from the target at 0° and 16°.

5.4.2 Estimation of the absorbed dose rate in the irradiated blood samples

The absorbed dose in each blood vial was calculated as a function of 'active' irradiation time using the cumulative number of NE102 monitor counts per measurement run as M in Equation 5.1 along with the other quantities shown in Table 5.5. These results are shown in Figure 5.8. As discussed in Section 5.2.1, the absorbed dose rate in the blood vials was not constant due to the variation of the stability of the neutron beam during the irradiations. However, an approximate absorbed dose rate in each blood vial was estimated by fitting the data shown in Figure 5.8 to a linear function of the form

$$D = Rt, \tag{5.8}$$

where t is the irradiation time and R is the absorbed dose rate. The results for the estimated absorbed dose rate in each blood vial at 0° and 16° are shown in Figure 5.8 and summarised in Table 5.6.

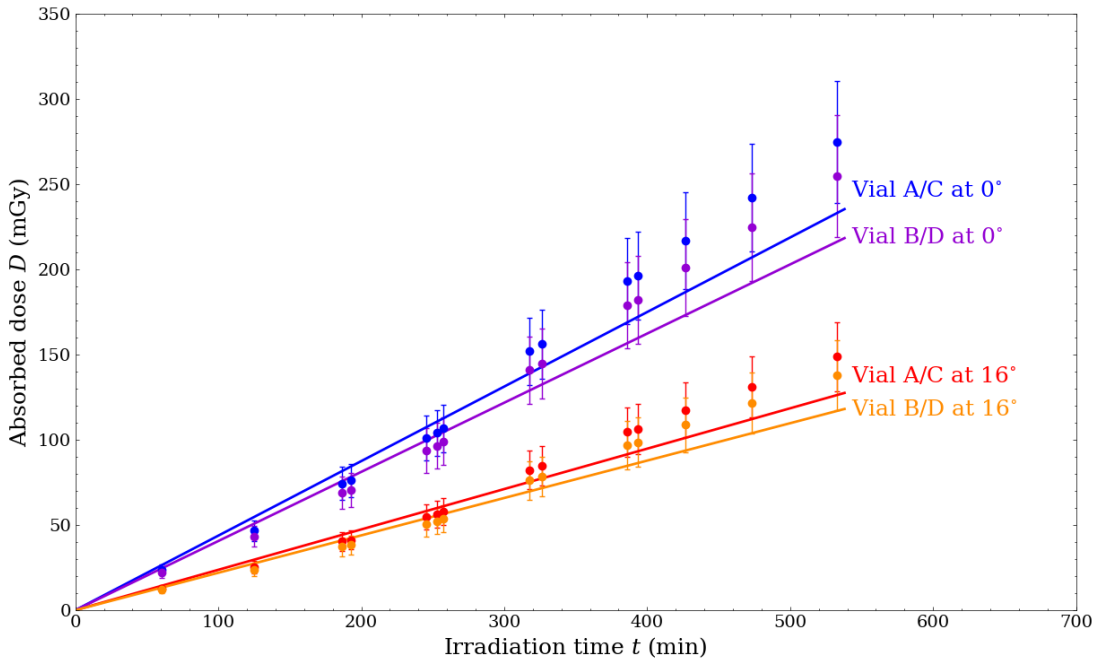

Figure 5.8: Absorbed dose in the blood vials contained in the polyethylene phantoms (as shown in Figure 5.3) as a function of irradiation time for neutrons produced by a 66.48 MeV proton beam impinging on an 8.0 mm lithium target, measured at a distance of 4.300 m from the target at 0° and 16°. Linear functions are fitted to the data to obtain an estimate of the absorbed dose rate R in each blood vial at 0° and 16°, as shown in Table 5.6.

Θ (°)	**Vial**	$\boldsymbol{R}$ (mGy/min)
0	A/C	0.437 ± 0.014
	B/D	0.406 ± 0.013
16	A/C	0.2369 ± 0.0076
	B/D	0.2194 ± 0.0070

Table 5.6: Results for the estimated absorbed dose rate R in each blood vial contained in the polyethylene phantoms (as shown in Figure 5.3) for irradiations with neutrons produced by a 66.48 MeV proton beam impinging on an 8.0 mm lithium target, measured at a distance of 4.300 m from the target at 0° and 16°.

5.5 Recommendations for future neutron dose quantification measurements at iThemba LABS

Section 5.4 summarises the results from the first neutron dose quantification measurements that have been conducted in the D-line at iThemba LABS since the completion of the infrastructural upgrade in 2020/2021. This section presents a discussion surrounding a number of potential sources of uncertainties that were not taken into account in the analysis presented in this chapter, and recommendations for improving the quantification of neutron dose in the D-line in the future.

5.5.1 Characterisation of the neutron spectral fluence at low energies

The relative neutron fluence spectra measured with the BC501A detector were obtained from the TOF analysis with a lower energy threshold of 7.5 MeV as discussed in Section 4.3.4. A horizontal extrapolation of the spectral fluence was used below 7.5 MeV, as motivated by results from Nolte et al. [2002], where Bonner sphere spectrometers were used to characterise the low-energy tail of the energy distributions of quasi-monoenergetic neutron beams between 20 MeV and 100 MeV produced by the ^{7}Li(p, n)^{7}Be reaction. Such measurements have not been conducted at iThemba LABS since the infrastructural upgrade of the D-line. Since neutrons in the low-energy continuum are expected to demonstrate a relatively high biological effectiveness compared to neutrons in the high-energy peak (as illustrated in Figure 3.4), any neutron RBE measurements will be particularly sensitive to the shape of the spectral distribution at low energies. It is therefore recommended that a detailed characterisation of the neutron spectral distribution at energies below the threshold of 7.5 MeV be carried out with Bonner sphere spectrometers in order to reduce the potential uncertainties associated with the contributions of these neutrons to the dose received by the biological samples.

5.5.2 Fluence measurements with the ^{238}U fission ionisation chamber

There are a number of improvements that could be made to reduce the uncertainties associated with the absolute fluence per unit monitor count that is obtained from an analysis of measurements made with the FC.

The procedure that was used to correct for the overlap of the peak and continuum components in the FC TOF spectrum, in order to estimate the number of fission counts in the high-energy peak was described in Section 4.4.3. To reduce the uncertainties associated with the result for $N_{f,exp}$ obtained using this method, it is recommended that a TAC calibration be carried out for future FC measurements to allow for a more precise comparison of the simulated TOF spectrum (based on the high resolution measurements with the BC501A detector) and the FC TOF measurements. It is also recommended that the FC measurements should be obtained over a longer period of time than was the case for the presented measurements ($\sim$ 43 minutes), in order to reduce the uncertainties associated with the number of counts per channel in the measured TOF and light output spectra.

The series of correction factors used to relate the measured number of fission counts in the high-energy peak $N_{f,exp}$ to the number of counts that would be obtained under reference conditions, were described in Section 4.4.4. For the presented measurements, a previously calculated value for the correction for the spatial inhomogeneity of the neutron fluence k_7, was used. For future measurements, it is recommended that this factor should be re-calculated based on updated beam profile assessments and Monte Carlo simulations of the beam profile in the recently upgraded D-line at a reference distance that corresponds to the distance at

which the relevant blood irradiations are carried out.

The calculation of the absolute neutron fluence in the high-energy peak, as given in Equation 4.9, involves using the recommended value of the ^{238}U fission cross section at the neutron energy of interest. For the present measurements, this value was obtained via a linear interpolation of the IAEA 2017 Neutron Data Standards for ^{238}U(n, f) reactions (as shown in Figure 4.31), however it should be noted that the database for these standards still needs improvement as there is a significant lack of experimental data for neutron energies above 20 MeV [Carlson et al., 2018]. Measuring the ^{238}U fission cross section relative to the n-p elastic scattering cross-section in order to reduce the existing uncertainties in the energy range of 35 MeV to 100 MeV is the subject of ongoing work that is being carried out within the Metrological and Applied Sciences University Research Unit (MeASURe) at the University of Cape Town (UCT).

5.5.3 Effect of parasitic neutrons

Previous experiments in the D-line at iThemba LABS have revealed that the fraction of neutrons produced in the low-energy continuum for a fixed proton beam energy can vary with the beam current [Mosconi et al., 2010]. This effect is attributed to parasitic neutrons that are produced in the target holder or in structures in the beam line in front of the target that are hit by the halo of the proton beam which varies with beam current and focusing conditions. In Figure 5.2, the energy spectrum measured by the BC501A detector at 0° at low beam currents was corrected for this effect via a rescaling of the height of the low energy continuum region for consistency with the FC measurements. It should be noted however, that for the presented experiment, the BC501A detector measurements at 0° were conducted at beam currents of 89 nA to 110 nA, while the FC measurements were performed at currents of 200 nA to 850 nA, and the blood irradiations at currents of 1000 nA to 1500 nA. Given the variations of the beam current during these measurements and the corresponding potential variation in the contribution of the low-energy continuum to the dose received by the blood samples, a more careful correction procedure should be considered. This is particularly important for RBE measurements since the low-energy continuum is expected to contribute significantly to the observed biological effects. In order to more closely monitor the effects of the parasitic neutrons, it is recommended that empty target runs be performed regularly and that the beam characterisation measurements be carried out at stable beam currents, with the FC measurements being conducted at a current that is as close as possible to that used for the blood irradiations.

5.5.4 Phantom design

Figure 5.9 shows the results from a GEANT4 simulation for dose deposited by 66.48 MeV protons as a function of depth in a solid polyethylene phantom. The depth at which the blood vials were located in the polyethylene phantom used for the presented measurements are indicated on the plot. These results illustrate that if the neutron beam was contaminated with charged particles from the incident 66.48 MeV proton beam, then this could contribute to the dose received by the blood samples. This is particularly important to consider with regards to making RBE measurements, as protons are known to have significant biological effects and deposit most of their energy at the end of their range in what is known as the Bragg peak. For future measurements, it is recommended that the thickness of the phantom layers in front of and behind the blood samples be chosen to correspond to the range of the incident beam protons in the phantom (3.70 cm for 66.48 MeV protons). This condition allows for the irradiations to be carried out under conditions close to longitudinal charged particle equilibrium, thereby reducing the sensitivity of the dose received by the blood samples to contamination of the neutron beam

with charged particles, and producing a well-defined spectral distribution of charged particles in the samples [Nolte et al., 2008].

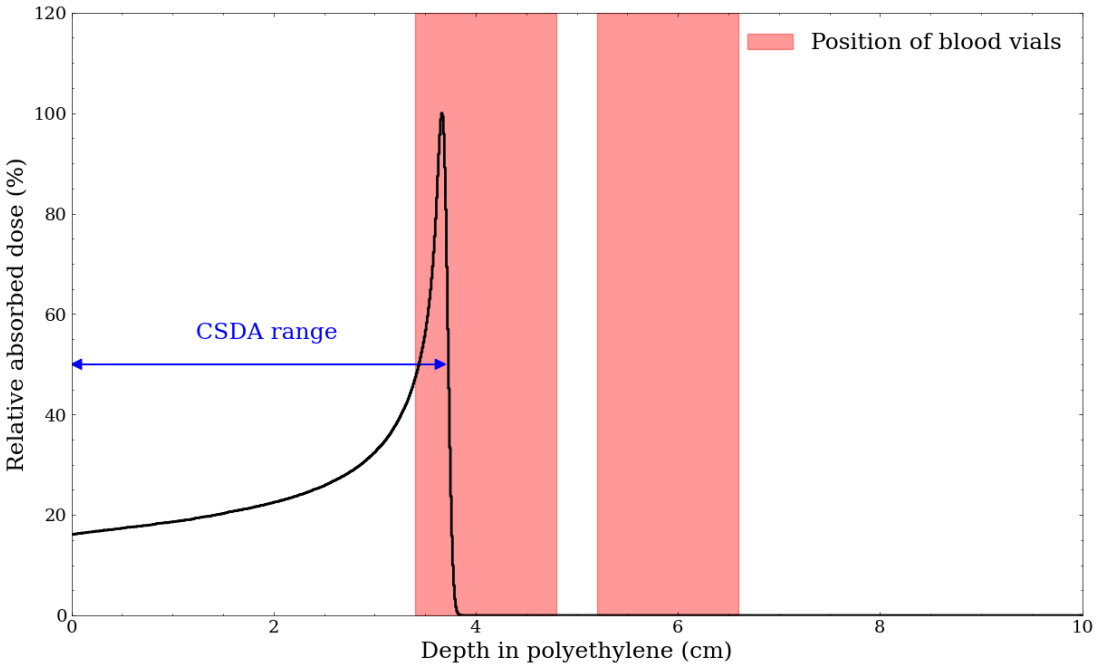

Figure 5.9: Simulation results for absorbed dose deposited by 66.48 MeV protons as a function of depth in a solid polyethylene phantom. The depths at which the blood vials were located for the presented measurements are shown and compared to the continuous slowing down approximation (CSDA) range of 3.70 cm for 66.48 MeV protons in polyethylene [Berger et al., 2017].

5.5.5 Gamma ray contribution to the absorbed dose in the irradiated blood vials

The technique of PSD was used to separate events induced by neutrons from events induced by gamma rays in the BC501A detector (as shown in Figure 4.10), however the contribution of these gamma rays to the absorbed dose in the irradiated blood samples was not accounted for in the presented analysis. Gamma rays in the neutron beam result from proton interactions in the lithium target and neutron interactions in the surrounding structural materials. The gamma ray light output spectra for the presented measurements at 0° and 16° are shown in Figure 5.10. By comparison of these spectra to the gamma ray response functions for a similar detector to the BC501A detector at iThemba LABS, it can be deduced that the gamma rays have a maximum energy of around 11.5 MeV.

Nolte et al. [2005] conducted neutron RBE measurements with a 60 MeV quasi-monoenergetic neutron beam at the Université Catholique de Louvain (UCL) and calculated that the gamma ray dose in their blood samples was only 0.7% of the neutron dose, and could thus be neglected. It is recommended that a similar procedure be followed to assess the dose from gamma rays in the D-line at iThemba LABS for the neutron energies of interest. This would require measurements being made with a detector for which the gamma ray response functions have been calculated so that the spectral fluence can be determined via an unfolding of the measured light output spectra (separated from the neutron spectra using PSD) as shown in Figure 5.10. The resulting gamma ray spectral fluence could then be used in a simulation similar to that discussed in Section 5.3 to establish the absorbed dose from gamma rays per unit photon fluence and subsequently the total gamma ray dose in the irradiated blood samples.

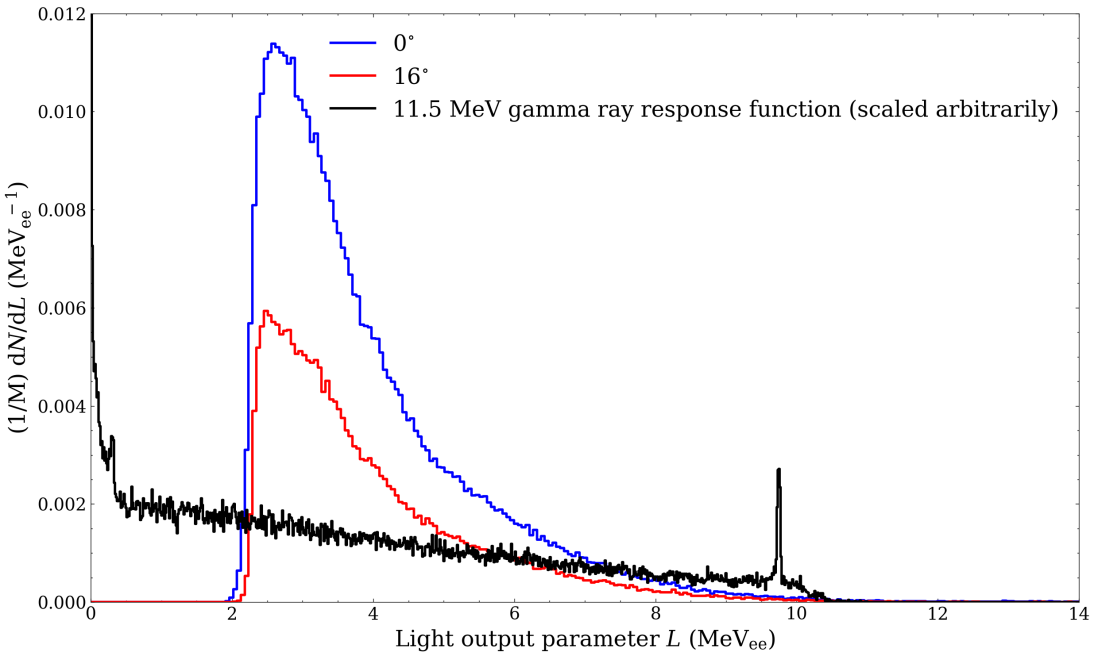

Figure 5.10: Counts as a function of light output parameter L for measurements of gamma rays produced by a 66.48 MeV proton beam irradiating an 8.0 mm lithium target, measured by the BC501A detector at a distance of 8.000 m from the target at 0° and 16°. The measured counts per light output channel are normalized per unit neutron monitor count. The calculated response function for a detector similar to BC501A detector for incident monoenergetic 11.5 MeV gamma rays is plotted alongside the measured data.

5.5.6 Contribution of the background from neutron moderation to the absorbed dose in the irradiated blood vials

Before the infrastructural upgrade of the D-line at iThemba LABS, a background from moderated neutrons was observed in the experimental area of the neutron beam facility and attributed to the scattering of high-energy neutrons off the walls of the passage between the target vault and experimental area [Mosconi et al., 2010]. The infrastructural upgrade of the facility included improving the shielding on neutrons from the target area specifically aimed at reducing the effect of the moderated neutron background [Ndlovu et al., 2019], however a full characterisation of the neutron background in the experimental area has not been conducted since the upgrade.

The dose quantification analysis presented in this chapter was based on the assumption that all the neutrons irradiating the blood samples were contained in a uniform neutron beam incident on the phantom surface. Furthermore, it was assumed that the neutron spectral fluence at the position of the front face of the phantom containing the blood samples (4.300 m from the lithium target) was identical to that measured by the BC501A detector at 8.000 m from the lithium target. The presence of a background from neutron moderation as described by Mosconi et al. [2010] would challenge the validity of both of these assumptions. Given the sensitivity of RBE measurements to the effects of low-energy neutrons, it is recommended that a full characterisation of the neutron background in the D-line be conducted to assess the intensity and energy distribution of the moderated neutron background and how these vary with location in the experimental area. It is suggested that this characterisation be conducted in a similar manner to the assessments of the neutron background before the infrastructural upgrade, which included measurements with a Bonner sphere spectrometer and LB-6411 rem counter, as described by Ndlovu et al. [2019] and Mosconi et al. [2010] respectively.

5.5.7 Beam profile measurements

In the Monte Carlo simulations discussed in Section 5.3, the neutron beam was modelled as a square planar source at the front face of the phantom with dimensions of 5.0 cm × 5.0 cm. In the absence of more detailed information, the shape and size of the simulated neutron beam were chosen based on a rough estimate of how the neutron beam may diverge upon emerging from the 4.5 cm × 4.5 cm collimator exit and travelling the 30 cm distance to the front face of the phantom. Figure 5.11 shows that when the simulated neutron beam dimensions are varied between 4.5 cm × 4.5 cm and 6.0 cm × 6.0 cm, the calculated absorbed dose at 0° varies by up to 3.0% of the results presented in Table 5.5 for vials A and C, and up to 4.3% of the results presented in Table 5.5 for vials B and D. For future RBE experiments, it is recommended that measurements should be conducted to characterise the spatial beam profile at the neutron energy of interest at the position of the phantoms containing the blood vials so that the measured beam profile can be included in the Monte Carlo simulations. Such measurements have been conducted in the D-line in the past (before the completion of the upgrade) using image plates mounted behind a 2 mm polymethyl methacrylate (PMMA) plate and thermo-luminescent diodes in the PMMA holder [Mosconi et al., 2010; Musonza, 2011].

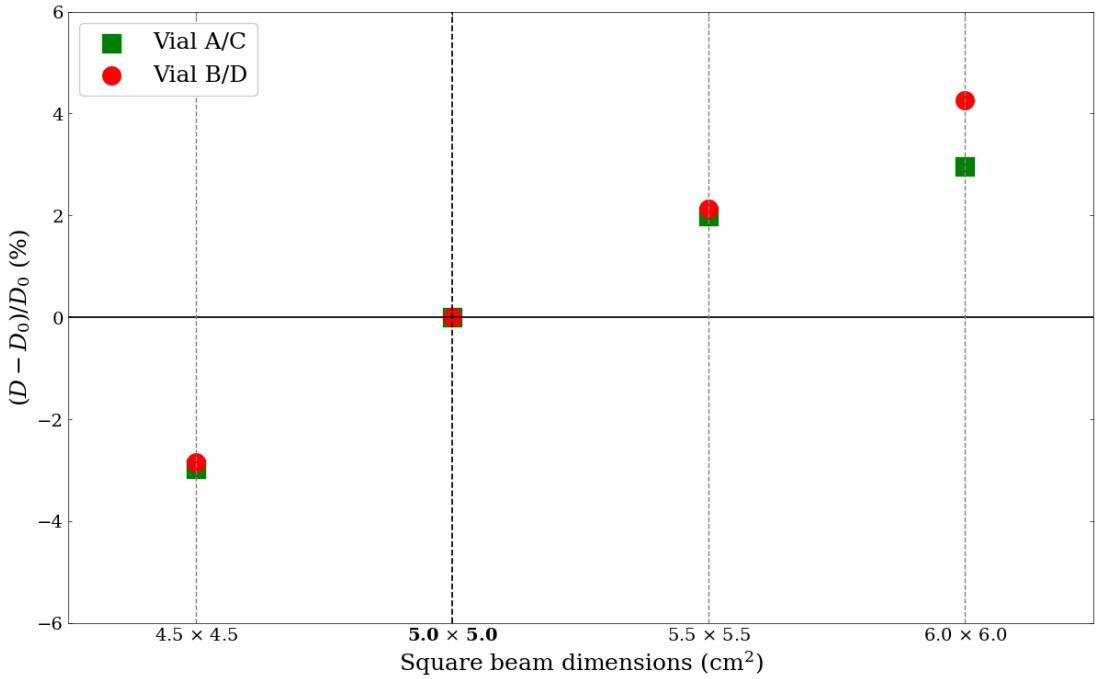

Figure 5.11: Variation in the calculated absorbed dose in each blood vial that results from varying the dimensions of the simulated neutron beam at 0° at the front face of the phantom containing the blood vials, as described in Section 5.3. The quantity D_0 refers to the absorbed dose calculated from the results of the simulation with a 5.0 cm × 5.0 cm beam, as was used to obtain the results presented in Table 5.6.

5.5.8 Validation of computational simulations

The chosen 'Physics List' in the GEANT4 simulation (as discussed in Section 5.3.2) is responsible for specifying the particles that are used in the Monte Carlo simulation together with the processes assigned to their physical interactions. The GEANT4 reference Physics Lists are based on various data-driven, parametrisation-driven, and theory-driven models for hadronic interactions, and it is important to be aware of the limitations and applicability of these models in the applications and energy ranges of interest, and how this may affect the calculated dose in the irradiated blood vials.

The QGSP_BIC_AllHP list that was chosen for the presented analysis (as described in Section 5.3.2) uses high precision transport and cross-section models based on data from a combination of different standard evaluated data libraries for the interactions of neutrons below 20 MeV, and the interactions of protons and other light ions below 200 MeV [Geant4 Collaboration, 2020]. The upper limits of the high precision models are set by the nuclear data libraries on which these models are based. At higher energies, experimental cross-section data are scarce and so the simulation of hadronic interactions in GEANT4 relies entirely on theoretical models. In the medium energy range up to 10 GeV, there are three different intranuclear cascade models available to simulate the interactions of primary hadronic particles: the Binary, Bertini, and Liège Intranuclear Cascade models [Lerendegui-Marco et al., 2016].

Figure 5.12 shows that the results for the calculated absorbed doses to human blood in the irradiated vials vary by up to 7.96% in vials A/C, and 8.17% in vials B/D, when a range of different GEANT4 physics lists are implemented in the Monte Carlo simulation. The inclusion of "BERT", "BIC", or "INCLXX" in the physics lists name indicates whether the physics list implements the Bertini, Binary, or Liège Intranuclear Cascade models in the medium energy range up to 10 GeV respectively. Similarly, "HP" indicates that high precision models based on standard evaluated data libraries are used for the interactions of neutrons below 20 MeV. More information about these Physics Lists can be found in Geant4 Collaboration [2020], but Figure 5.12 indicates that the most significant differences in the absorbed dose in blood vials result from which intranuclear cascade model is implemented in the chosen physics list. The chosen QGSP_BIC_AllHP physics list uses the Binary Cascade model in the neutron energy range of interest above 20 MeV and was chosen because this cascade model is often recommended for applications with hadrons and ions with energies below 1 GeV, although it should be noted that these recommendations are based on very limited experimental data [Apostolakis et al., 2009].

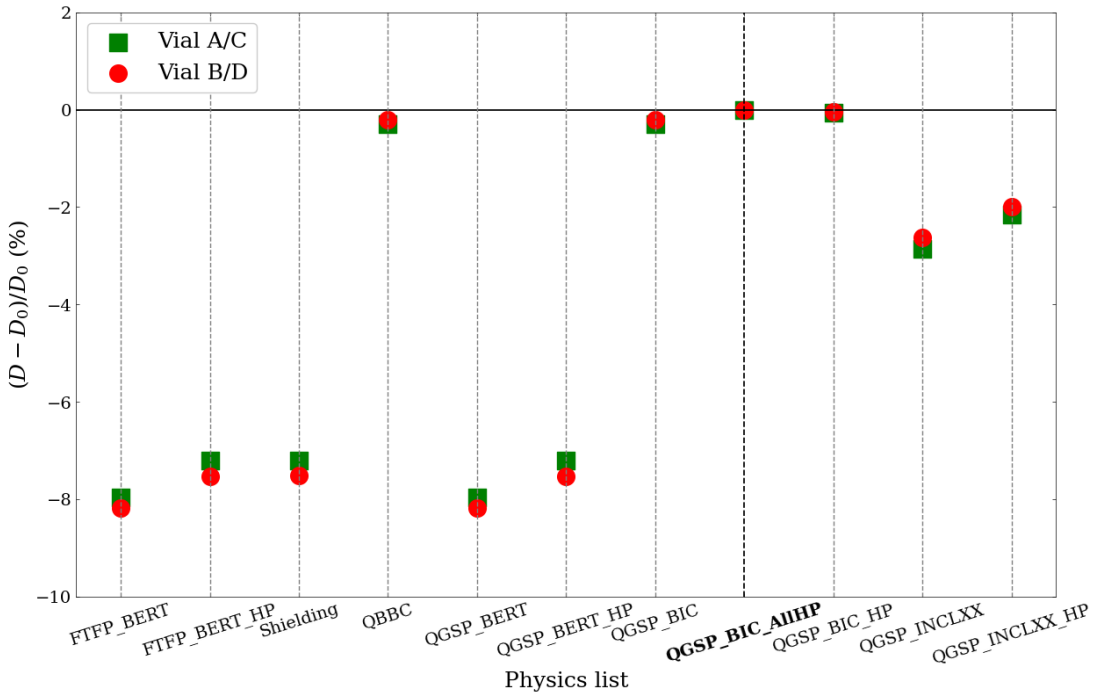

Figure 5.12: Variation in the calculated absorbed dose in each blood vial that results from implementing different GEANT4 reference Physics Lists in the Monte Carlo simulation. The quantity D_0 refers to the absorbed dose calculated from the results of the simulation using the QGSP_BIC_AllHP physics list, as was used to obtain the results presented in Table 5.5.

Given the limitations of relying on Monte Carlo simulations with limited neutron data sets for calculations of the absorbed dose to the blood vials, it is recommended that future calculations be validated with reference to direct measurements of the energy deposition by heavy charged particles at the position of the blood vials. The development of a compact scintillator-based neutron spectrometer capable of characterising neutron spectral fluence between 1 MeV and 120 MeV is an ongoing project within MeASURe at UCT [Buffler et al., 2024]. A potential means of verifying the presented Monte Carlo dose simulations could involve making measurements with this detector (or other "traditional" neutron dosimeters such as Bonner spheres, Bubble detectors, or tissue-equivalent proportional counters [Hälg and Schneider, 2020]) placed in the phantom at the position of the irradiated blood vials, in order to characterise charged particle energy deposition in the detector material and compare it to the simulation results.

6 Towards neutron Relative Biological Effectiveness (RBE) measurements at iThemba LABS

Radiation weighting factors for the induction of stochastic effects at low doses are typically selected based on experimentally determined values of the maximum Relative Biological Effectiveness, $\mathrm{RBE_M}$ (as described in Section 3.3). Measurements of neutron $\mathrm{RBE_M}$ require the establishment of dose-response relationships for a relevant biological endpoint for both the neutron and reference radiations, from which the $\mathrm{RBE_M}$ is then calculated as

$$\mathrm{RBE_M} = \frac{\alpha_n}{\alpha_{ref}}, \tag{3.5}$$

where α_n and α_{ref} are the initial slopes of the dose-response curves for the neutrons and reference radiation respectively [Valentin, 2003].

The dose-quantification measurements (from the June 2022 exploratory experiment) that were presented in Chapter 5 were accompanied by a radiobiology analysis of the induction of DNA DSBs in the irradiated blood samples via the γ-H2AX foci assay. The results from this assay were used to determine the "biological response" which was subsequently related to the absorbed dose in the samples such that the linear yield coefficient α_n for the neutron irradiations in the D-line (with neutrons produced by a 66.48 MeV proton beam impinging on a 8.0 mm lithium target) could be determined as is required in the calculation of the $\mathrm{RBE_M}$. This chapter presents the results from the radiobiology analysis and the corresponding dose-response relationships that were established, and includes a discussion as to how these results can be used to inform the preparation for neutron RBE experiments at iThemba LABS in the future.

6.1 Radiobiology measurements at iThemba LABS

6.1.1 The γ-H2AX foci assay

There are a variety of endpoints that can be investigated in a chosen biological system in order to assess the biological impact of ionising radiation exposure. The γ-H2AX foci assay that was used in the experiments conducted at iThemba LABS in June 2022 is a protein modification based technique. It relies on the detection of a fluorescent labelled phosphorylated DNA repair protein called γ-H2AX. When a DNA DSB is induced in a cell, it triggers a DNA damage response that involves the phosphorylation of the histone protein component H2AX to form γ-H2AX as one of the initial steps. This process spreads rapidly, resulting in the phosphorylation of many more H2AX histone proteins which interact with other proteins and protein complexes to form γ-H2AX foci in the region of the DSB. There is a close correlation between the number of DNA DSBs and the number of γ-H2AX foci which can be identified via immunofluorescence microscopy techniques [Noubissi et al., 2021]. Figure 6.1 shows example images of slides showing γ-H2AX foci as a function of dose for human lymphocytes exposed to ^{60}Co gamma rays.

The γ-H2AX foci assay has been well-established as a reliable biomarker for the detection of DNA DSBs [Nair et al., 2021]. It is one of the most sensitive biological assays for the

detection of DNA damage in the low-dose range, with dose-dependent numbers of γ-H2AX foci having been detected in experiments with fibroblasts and lymphocytes following radiation doses as low as 1 mGy [Rothkamm and Löbrich, 2003]. It also offers the advantage of having a rapid turnaround time, with results being obtained within a few hours, in comparison to many other cytogenetic techniques where results can only be obtained after a couple of days [Nair et al., 2021]. Along with the availability of the required equipment and expertise at iThemba LABS, its sensitivity at low doses was the primary reason why the γ-H2AX foci assay was selected for the experiments conducted at iThemba LABS in June 2022, where the expected dose to the biological samples was not known prior to the neutron irradiations.

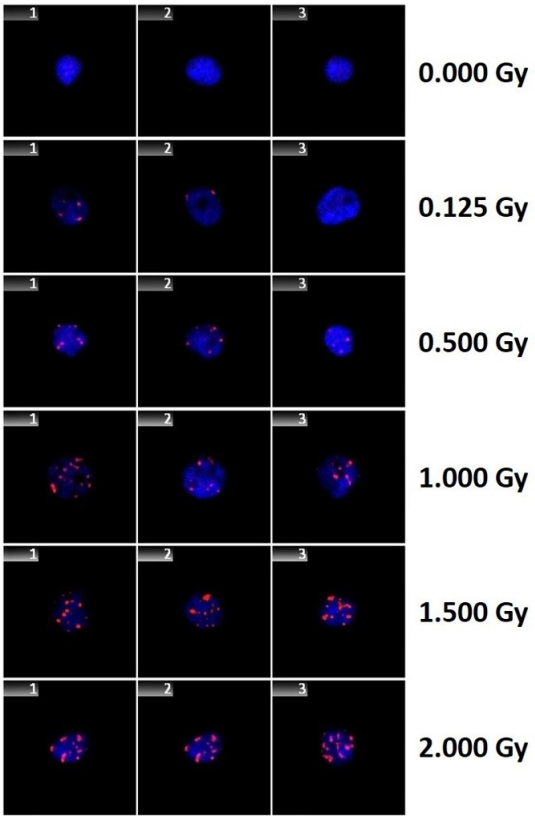

Figure 6.1: Example images of slides showing γ-H2AX foci as a function of dose for human lymphocytes exposed to ^{60}Co gamma rays. The blue region in each slide is a singular cell, and the pink spots are the detected γ-H2AX foci per cell [Nair et al., 2021].

6.1.2 Experimental procedure and analysis of results

The radiobiology components of the experiment conducted in the D-line in June 2022, were carried out by members of the Radiation Biophysics group at iThemba LABS.

The irradiated blood samples consisted of isolated PBMCs of the same healthy adult donor, suspended in 1.8 mL of RPMI cell culture media supplemented with 20% FBS. The samples were contained in sterile 1.8 mL cryogenic vials (NEST Biotechnology Co., Ltd) and kept at 37°C in a water bath prior to irradiation. The samples were placed in the polyethylene phantoms and irradiated with neutrons as discussed in Section 5.2, and the irradiations were carried out at room temperature. Following irradiation, the samples were incubated inside a water bath at 37°C for 30 minutes before being stored in a fridge until further analysis. A non-irradiated control sample was kept at room temperature during the twelve hours over which the other samples were irradiated, before being incubated and stored for the same amount of time as the irradiated samples.

The slide preparation, fixation and immunofluorescence γ-H2AX staining were performed following the protocol outlined by Nair et al. [2021]. Two or three slides were prepared for each sample and their analysis was carried out using the automated scanning and analysis platform with an integrated fluorescence microscope as described by Nair et al. [2021]. For each sample, the scanning system returns the number of cells scanned per slide, the average number of γ-H2AX foci per cell in each slide, and the resulting weighted means and standard deviations of the number of γ-H2AX foci scored per cell. The results of the analysis for the irradiated samples at 0° and 16°, and the control sample, are shown in Table 6.1. The quantity y_i represents the mean number of γ-H2AX foci per cell for each sample. The associated uncertainty $u(y_i)$ was calculated as the experimental standard deviation of the mean based on the variation in the results from each slide that was analysed.

Vial	D (mGy)	Slide no.	No. of cells	y_s (foci/cell)	y_i (foci/cell)	$u(y_i)$ (foci/cell)
0° irradiation position						
A	101 ± 13	1	269	1.985130	2.01	0.26
		2	1001	2.190809		
		3	262	1.320611		
B	141 ± 18	1	538	3.135688	1.99	0.56
		2	736	1.921196		
		3	745	1.233557		
C	217 ± 28	1	424	2.391509	3.48	0.56
		2	1001	4.29171		
		3	670	2.968657		
D	255 ± 33	1	1002	3.73553	3.63	0.11
		2	1002	3.52295		
16° irradiation position						
A	54.7 ± 7.5	1	617	1.254457	1.308	0.092
		2	256	1.4375		
B	76 ± 10	1	521	1.592105	1.575	0.021
		2	380	1.550864		
C	117 ± 16	1	872	1.988532	1.965	0.070
		2	178	1.848315		
Control room						
Control	0	1	351	1.396011	1.02	0.25
		2	1003	0.887338		

Table 6.1: Results from the γ-H2AX foci assay analysis of the irradiated blood samples contained in polyethylene phantoms placed 30 cm from the exits of the 0° and 16° collimators for irradiations with neutrons produced by a 66.48 MeV proton beam impinging on an 8.0 mm lithium target. The quantity D is the absorbed dose delivered to each blood vial (as calculated in Table 5.5), y_s is the number of foci per cell observed in a single slide, y_i is the mean number of γ-H2AX foci per cell per sample, and $u(y_i)$ is the uncertainty associated with y_i. The control sample was kept as a reference out of the beam during the irradiations.

6.1.3 Improving the quality of results from the γ-H2AX foci assay

Table 6.1 shows that the relative uncertainties associated with the mean number of foci scored per cell in each blood sample range between 1.3% and 28.1%. To reduce the uncertainties associated with the results from the γ-H2AX foci assay in future measurements, it is recommended that the quality control suggestions outlined by Nair et al. [2021] be followed such that three slides per sample are prepared and 1000 cells per slide are scanned. It is also recommended that multiple measurements be conducted over the same dose range with blood from the same donor to improve statistics and demonstrate the reproducibility of the results. Ideally, the experi-

ment should also be repeated with blood from different donors to account for inter-individual variations in the biological response.

For future experiments, it is also recommended that multiple control samples are used to account for the time-dependence of the spontaneous yield of γ-H2AX foci. For the presented measurements, a single non-irradiated control sample was kept at room temperature during the twelve hours over which the blood irradiations were carried out in the D-line. However, the individual blood samples were removed from the irradiated phantoms after roughly four, seven, ten, and twelve hours, and so a single control sample does not account for how the spontaneous yield of γ-H2AX foci may have varied over these time frames.

6.1.4 Choice of biological endpoint

While the γ-H2AX foci assay is a reliable and sensitive indicator of initial DNA damage, it is not considered the most appropriate biological assay for RBE_M measurements that are intended to inform the risk of long-term stochastic effects associated with a particular radiation exposure. As discussed in Section 3.3.4, radiation weighting factors for stochastic effects are generally based on the analysis of chromosome aberrations in human peripheral blood lymphocytes. For neutron RBE_M measurements in the future, it is recommended that the induction of unstable aberrations (through dicentric analysis) and/or the induction of stable aberrations (through translocation analysis) in human peripheral blood lymphocytes be used as the measured biological endpoint in order to enhance the ultimate impact of the RBE_M results. These cytogenetic analysis techniques were discussed in detail in Section 3.3.4.

The production of dicentric chromosomes in human lymphocytes is the method that was previously used by Nolte et al. [2006] to make measurements of neutron RBE_M, and indeed forms the basis for many RBE_M experiments pertaining to stochastic effects [Stricklin et al., 2021]. Conducting neutron RBE_M measurements with this endpoint would therefore offer the advantage of enabling direct comparisons of the results with other measurements. Dicentric analysis is verified to be sensitive to doses as low as 100 mGy [Herate and Sabatier, 2020] - a threshold that would require at least four hours of irradiation time to reach in the D-line at 0° for the experimental setup described in Chapter 5 (based on the measured average dose rate to human blood of around 0.4 mGy as quoted in Table 5.6).

Although it requires a more time-consuming and expensive analysis procedure, the study of stable aberrations is potentially more relevant with regards to long-term health effects like cancer development [Gasparini et al., 2007]. The induction of translocation aberrations following neutron radiation is of particular interest with regards to space radiation studies, as this endpoint could be observed in an astronaut's blood sample years after returning from space travel, and directly compared to data from Earth-based experiments. While its applicability at low doses still needs to be further investigated, the lower detection limit for translocation analysis is generally estimated to be around 300 mGy [Herate and Sabatier, 2020] - a threshold that would require at least 12.5 hours of irradiation time to reach in the D-line at 0° for the experimental setup described in Chapter 5 (based on the measured average dose rate to human blood of around 0.4 mGy as quoted in Table 5.6).

iThemba LABS currently does not have the appropriate equipment and expertise required to conduct these analyses, so irradiated samples would need to undergo fixation and slide preparation at iThemba LABS before being transported to a facility where the analysis can be performed. Such facilities exist within the radiobiology laboratories at GSI, for example, with whom the Radiation Biophysics group at iThemba LABS maintains a working relationship.

6.2 Determination of the linear yield coefficients for the neutron irradiations

The results obtained from the measurements and simulations as shown in Table 6.1 were used to plot the absorbed dose in each blood vial, D, versus the corresponding yield of γ-H2AX foci per cell, $y_i - y_0$, where y_0 is the spontaneous yield of γ-H2AX foci as measured in the (unirradiated) control sample. The resulting plot is shown in Figure 6.2. Linear functions of the form

$$y = \alpha D \tag{6.1}$$

were fitted to the yield data, $y_i^{(0°)} - y_0$ and $y_i^{(16°)} - y_0$, in order to determine the linear yield coefficients $\alpha_n^{(0°)}$ and $\alpha_n^{(16°)}$ for the irradiations at 0° and 16° respectively. The results, as shown in Figure 6.2 are:

$$\alpha_n^{(0°)} = 10.12 \pm 0.63\,\text{Gy}^{-1}; \text{ and}$$
$$\alpha_n^{(16°)} = 7.45 \pm 0.66\,\text{Gy}^{-1}.$$

Given appropriate reference radiation measurements conducted to establish α_{ref} (as will be discussed in Section 6.5), $\alpha_n^{(0°)}$ and $\alpha_n^{(16°)}$ could be used in Equation 3.5 in order to calculate the neutron RBE_M for irradiations with neutrons at 0° and 16°, which have fluence weighted average energies of 40.11 ± 0.92 MeV and 37.26 ± 0.40 MeV respectively.

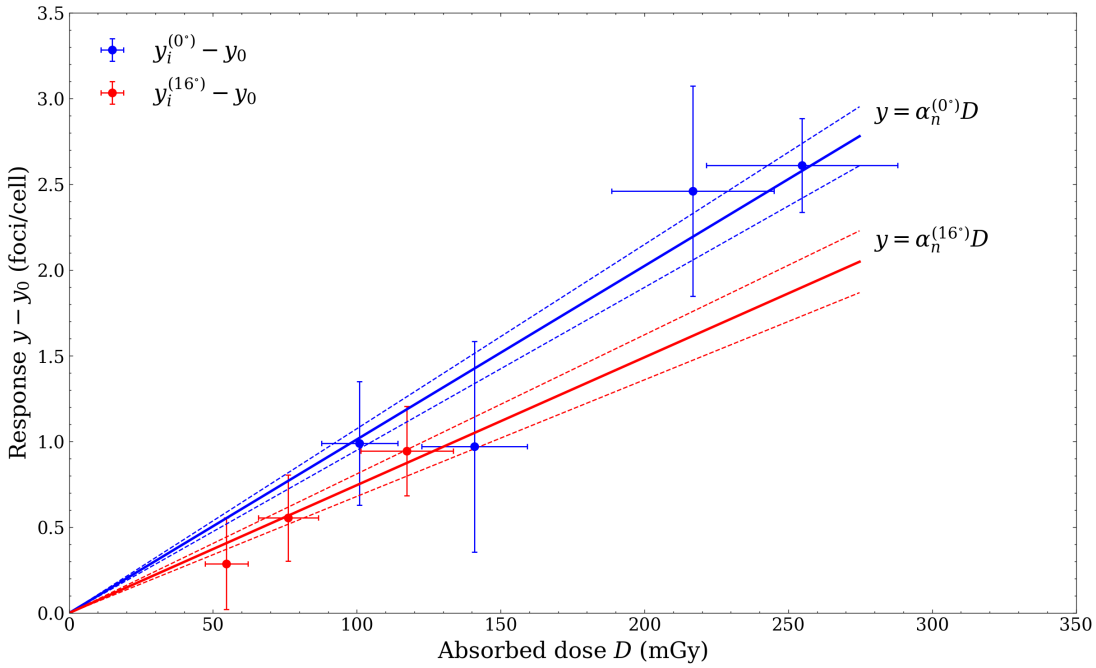

Figure 6.2: Yield of γ-H2AX foci in human PBMCs as a function of absorbed dose in blood vials contained in polyethylene phantoms for irradiations with neutrons produced by a 66.48 MeV proton beam impinging on an 8.0 mm lithium target, measured at a distance of 4.300 m from the target at 0° and 16°. Linear functions of the form $y = \alpha D$ were fitted to the data resulting in linear yield coefficients of 10.12 ± 0.63 Gy^{-1} and 7.45 ± 0.66 Gy^{-1} at 0° and 16° respectively. The solid lines indicate the weighted fits and the dashed lines indicate the corresponding uncertainties.

6.3 Measurements of neutron Relative Biological Effectiveness (RBE) with quasi-monoenergetic neutrons

The original motivation behind making measurements at both 0° and 16° was so that the subtraction procedure outlined by Nolte et al. [2006] could be applied to discriminate the effects of lower-energy continuum neutrons from those of the neutrons in the high-energy peak and thus determine the effect of the quasi-monoenergetic neutron beam. Although the radiation field to which astronauts will be exposed in space will never be a monoenergetic single-ion beam, it is relevant to conduct experiments with monoenergetic (or quasi-monoenergetic) high-energy neutrons in order to generate meaningful data sets regarding the biological responses at specific neutron energies that can contribute towards the establishment of the radiation weighting factors used by regulatory bodies.

This section discusses how application of the subtraction procedure outlined by Nolte et al. [2006] to the data from the June 2022 exploratory measurements raises some questions pertaining to the validity of his method, and further work that is required in order to answer these questions and move towards making measurements with quasi-monoenergetic neutrons in the future.

6.3.1 Subtraction procedure to determine the linear yield coefficient for the quasi-monoenergetic difference spectrum

In this section, the subtraction procedure, outlined by Nolte et al. [2006], is applied to the data from the 2022 exploratory experiment (as discussed in Section 6.1 in an attempt to correct for the effect of neutrons from the low-energy break-up continuum and determine the linear yield coefficient for the (0° - 16°) difference spectrum, with a peak energy of 62.34 ± 0.37 MeV.

Figure 6.3 shows the spectral fluences per monitor count $(\Phi_E^{sc}/M)^{(0°)}$ and $(\Phi_E^{sc}/M)^{(16°)}$ as measured using the BC501A detector at 0° and 16° respectively. Also shown is the (0° - 16°) difference spectrum, calculated by subtracting $(\Phi_E^{sc}/M)^{(16°)}$ from $(\Phi_E^{sc}/M)^{(0°)}$ at each energy bin.

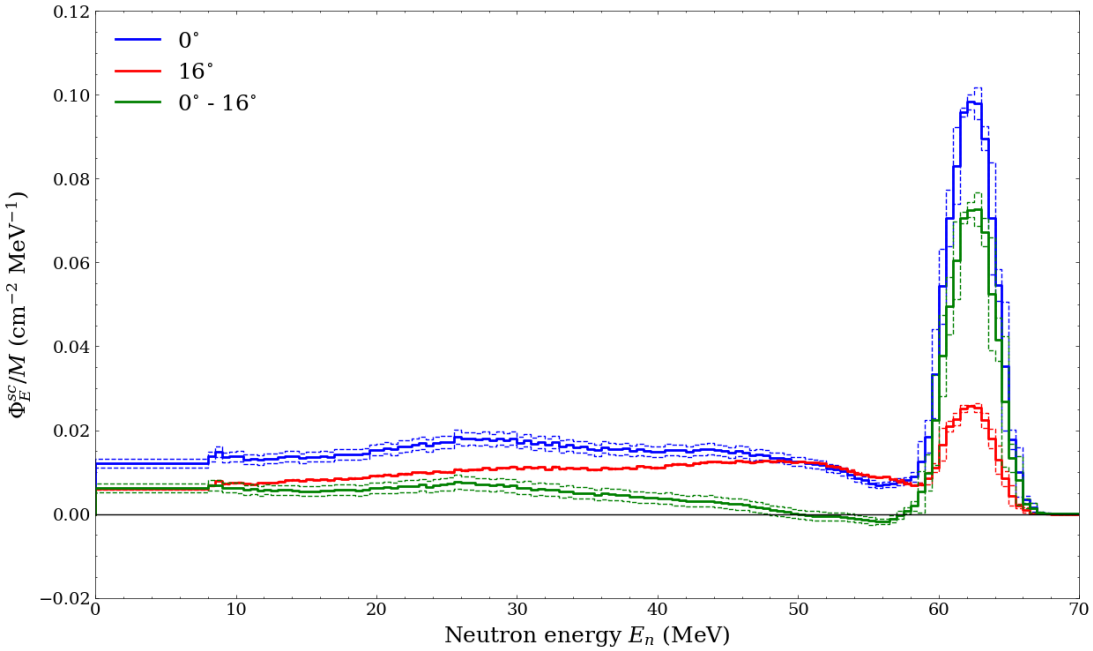

Figure 6.3: Relative spectral fluence per monitor count for measurements of neutrons produced by a 66.48 MeV proton beam irradiating an 8.0 mm lithium target, measured by the BC501A detector at a distance of 8.000 m from the target at 0° and 16° (as shown in Figure 5.2). The (0° - 16°) spectral fluence was obtained by subtracting the measured spectral fluence at 16° from that at 0°. The uncertainties are indicated by the dashed lines.

In a similar manner to that discussed in Sections 5.1 to 5.4, Equation 5.1 was used with the quantities shown in Table 6.2, to calculate the absorbed dose D that would be received by each blood sample if the vials had been irradiated with neutrons from the (0° - 16°) difference spectrum. The quantity Φ/Φ_0 was calculated by applying Equation 4.8 to the difference spectrum, Φ_0/M was determined using the FC measurement of the peak neutron fluence along with the ratio of the difference spectrum peak fluence to the 0° spectrum peak fluence, and D/Φ was calculated via Monte Carlo simulations as discussed in Section 5.3, but with the difference spectrum used as the input fluence spectrum from which the energies of the simulated neutrons were sampled. As shown in Table 6.2, the total relative uncertainties of the absorbed dose values D, again obtained via propagation of the uncertainties of each quantity through the calculation of Equation 5.1, were around 15% for all irradiations. The γ-H2AX foci yield data for the difference spectrum were calculated according to:

$$y_i^{(0°-16°)} = (y_i^{(0°)} - y_0) - (y_i^{(16°)} - y_0). \tag{6.2}$$

Vial	$\boldsymbol{\Phi/\Phi_0}$	$\boldsymbol{\Phi_0/M}$ (cm^{-2})	$\boldsymbol{D/\Phi}$ (pGy cm^2)	$\boldsymbol{M} \times 10^8$	$\boldsymbol{D}$ (mGy)	$\boldsymbol{y_i^{(0°-16°)}}$ (foci/cell)
(0° - 16°) difference spectrum						
A	1.82 ± 0.10	3.16 ± 0.44	70.27 ± 0.14	1.13911 ± 0.00011	46.0 ± 6.9	0.70 ± 0.45
B			65.48 ± 0.13	1.71301 ± 0.00013	64.5 ± 9.7	0.42 ± 0.66
C			70.27 ± 0.14	2.44552 ± 0.00016	99 ± 15	1.52 ± 0.67

Table 6.2: Summary of the results used to determine the relationship between the absorbed dose and the yield of γ-H2AX foci for the $(0° - 16°)$ difference spectrum from measurements with neutrons produced by a 66.48 MeV proton beam impinging on an 8.0 mm lithium target with the front faces of the phantoms containing the blood vials placed 4.300 m from the target at 0° and 16°.

The data in Table 6.2 were used to plot the absorbed dose in each blood vial D versus the corresponding yield of γ-H2AX foci per cell $y_i^{(0°-16°)}$ as shown in Figure 6.4. Again, a linear function of the form in Equation 6.1 was fitted to the yield data to determine the linear yield coefficient $\alpha_n^{(0°-16°)}$. The result, as shown in Figure 6.4 is

$$\alpha_n^{(0°-16°)} = 13.3 \pm 2.6\,\mathrm{Gy}^{-1}.$$

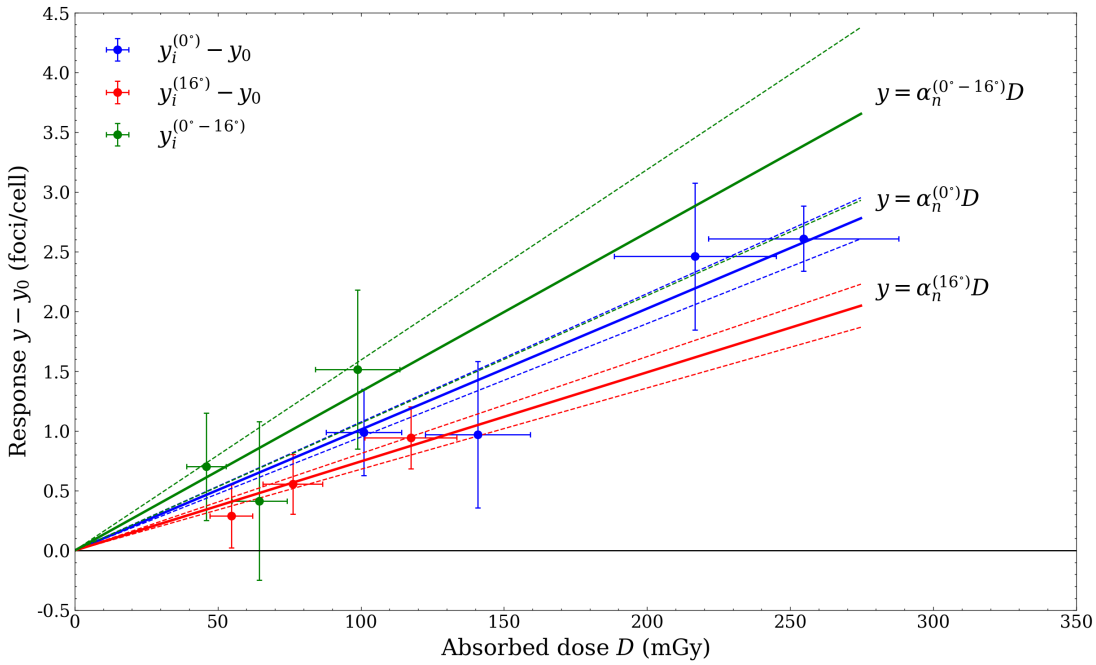

Figure 6.4: Yield of γ-H2AX foci in human PBMCs as a function of absorbed dose in blood vials contained in polyethylene phantoms for irradiations with neutrons produced by a 66.48 MeV proton beam irradiating an 8.0 mm lithium target, measured at a distance of 4.300 m from the target at 0° and 16°. The $(0° - 16°)$ difference spectrum data were calculated using the subtraction procedure outlined by Nolte et al. [2006]. Linear functions of the form $y = \alpha D$ were fitted to the data resulting in linear yield coefficients of 10.12 ± 0.63 Gy^{-1}, 7.45 ± 0.66 Gy^{-1}, and 13.3 ± 2.6 Gy^{-1} at 0°, 16°, and $(0° - 16°)$ respectively. The solid lines indicate the weighted fits and the dashed lines indicate the corresponding uncertainties.

6.3.2 Interpretation and discussion of subtraction procedure

The result from applying the subtraction procedure outlined by Nolte et al. [2006] to the data from the exploratory experiment indicates that the linear yield coefficient $\alpha_n^{(0°-16°)}$, and hence the RBE for the $(0° - 16°)$ difference spectrum is greater than that measured at 0° and at 16°. This is a surprising result given that currently recommended ICRP neutron radiation weighting factors, as shown in Figure 6.5, indicate that the low-energy break-up continuum should have a greater biological effect than neutrons in the high-energy peak. It should be noted that the data were taken as an exploratory experiment and the uncertainty associated with the individual data points are relatively large. Although preliminary, this surprising result raises a number of questions and concerns surrounding the validity of applying the subtraction procedure, which is motivated by fluence difference measurements, to biological effects.

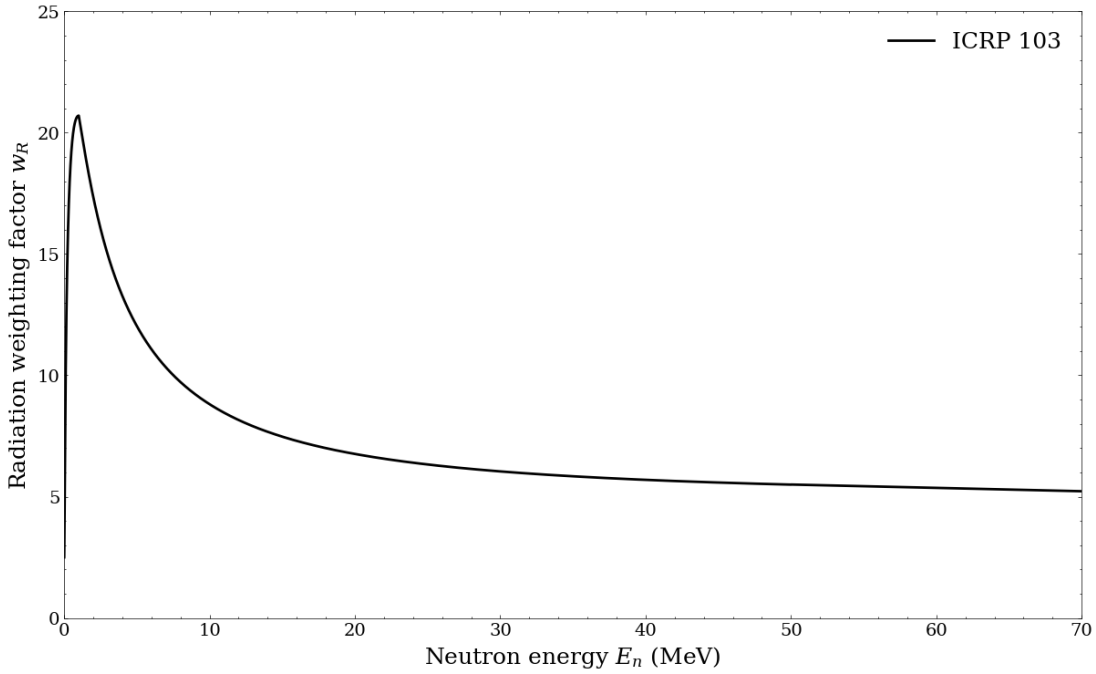

Figure 6.5: Radiation weighting factors for stochastic effects as currently recommended by the ICRP for neutrons with energies between 0 MeV and 70 MeV [Valentin, 2007].

The subtraction procedure outlined by Nolte et al. [2006] relies on being able to observe a statistically significant difference between the measured data at 0° and 16°, and it should be noted that the data from the exploratory experiment does not provide clear evidence that this can be observed for 62.34 MeV neutrons. The linear yield coefficients $\alpha_n^{(0°)}$ and $\alpha_n^{(16°)}$ were obtained by independently fitting the data measured at 0° and at 16°. However, there were only four data points at 0° and three at 16°, and owing to the differing dose rates at these neutron emission angles, they do not cover the same dose range. In order to obtain statistically significant results for $\alpha_n^{(0°)}$ and $\alpha_n^{(16°)}$ and confirm that a clear difference in RBE measurements can be observed at the two angles, the measurements would need to be repeated over a wider and comparable dose range with a more precise dosimetric and radiobiology analysis (following the recommendations outlined in Sections 5.5 and 6.1 respectively).

Based on the preliminary results, the slope of the data set measured at 16° is smaller than that at 0°, however one would actually expect this to be the other way around. Figure 6.6 shows the calculated relative contributions of neutrons from the continuum and peak regions of the energy spectra at 0° and 16° to the total fluence at the front face of the phantom and to the absorbed dose in blood vial A/C. For a given absorbed dose, the continuum region contributes a greater percentage of the total dose at 16° than at 0°. According to the weighting factors shown in Figure 6.5, the continuum region is expected to have a more significant biological effect than the peak region, and it is therefore expected that at a given absorbed dose (on the x-axis in Figure 6.4), the biological effect (on the y-axis in Figure 6.4) should be greater at 16° than at 0°, and therefore one would expect that $\alpha_n^{(0°)} < \alpha_n^{(16°)}$. This discrepancy in the measurements was also observed in the results from Nolte et al. [2006] and noted in Nolte et al. [2008], where the effect was attributed to parasitic neutrons produced by drifts in the proton beam transport during the long irradiation time. If this were the case, then the absorbed dose as calculated using Equation 5.1 would underestimate the dose delivered to the blood samples at 0°, and thus the measured $\alpha_n^{(0°)}$ would only represent an upper limit [Nolte et al., 2008]. This matter emphasizes the importance of all RBE measurements being accompanied by a detailed metrology characterisation and careful monitoring of the beam conditions during the irradi-

ation. For the 2022 exploratory experiment, the BC501A detector measurements at 0° were conducted at beam currents of 89 nA to 110 nA, while the FC measurements were conducted at currents of 200 nA to 850 nA, and the blood irradiations at currents of 1000 nA to 1500 nA. As discussed in Section 5.5.3, the relative fluence spectra measured by the BC501A detector were corrected for the effects of parasitic neutrons at higher beam currents for consistency with the FC measurements, but given the variations of the beam current during these measurements and during the irradiation of the blood samples, a more careful correction procedure should be considered.

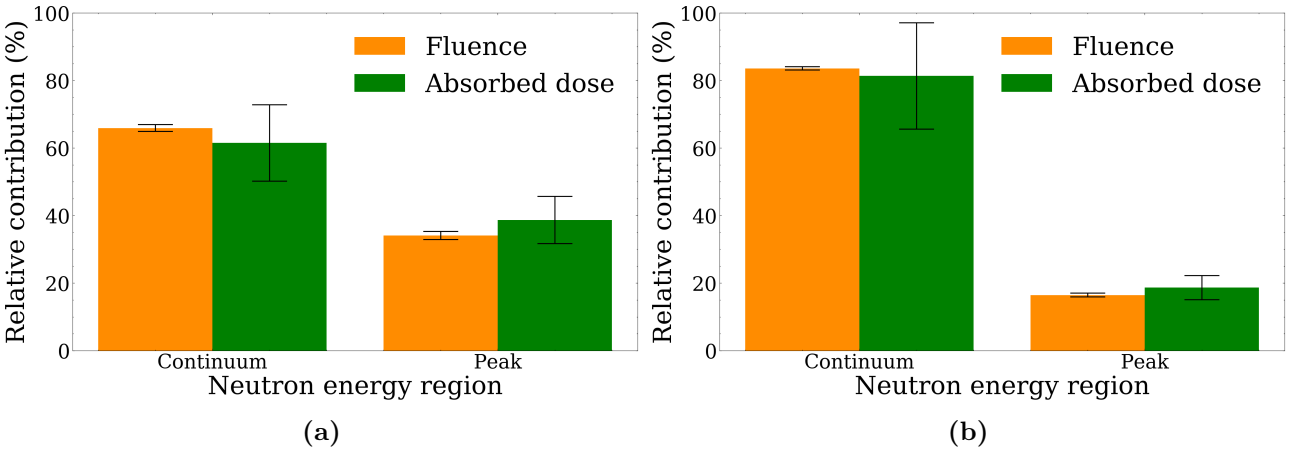

Figure 6.6: Calculated relative contributions of neutrons from the continuum and peak regions of the neutron energy spectra at (a) 0° and (b) 16° to the total fluence at the front face of the phantom and to the absorbed dose in blood vials A and C.

The above discussion makes it clear that application of the subtraction procedure as outlined in Nolte et al. [2006] requires careful consideration. As discussed above, if a statistically significant biological difference can be observed and $\alpha_n^{(16°)} > \alpha_n^{(0°)}$ (as expected based on the currently recommended neutron radiation weighting factors), then it would be more appropriate to calculate the difference in biological response via a $(16° - 0°)$ subtraction of the biological effects rather than a $(0° - 16°)$ subtraction as given in Equation 6.2. In this case, it may make more sense to determine the RBE of the quasi-monoenergetic spectrum via a simple subtraction of $\alpha_n^{(0°)}$ from $\alpha_n^{(16°)}$ although it is not immediately clear if this simple subtraction fully accounts for the intricate energy dependence of the biological yield. An analysis conducted in this way would need to be validated through comparison with other methods to correct for the contributions of the continuum neutrons and estimate the effects of the quasi-monoenergetic peak. Such a correction procedure is outlined in Nolte et al. [2005] and Nolte et al. [2008] where measurements at two different angles relative to the incident neutron beam were not possible. It should be noted that this method relies on RBE measurements having been conducted with the same biological endpoint at lower neutron energies so that these data can be interpolated and combined with an extrapolation scheme to estimate the linear yield coefficient for quasi-monoenergetic neutrons as a function of energy $\alpha(E)$.

6.4 Measurements of neutron Relative Biological Effectiveness (RBE) over a range of energies

Experimental verification of the shape of the neutron radiation weighting factor function that is currently recommended by the ICRP ultimately requires neutron RBE experiments to be conducted with similar irradiation conditions for the same biological endpoints over a range of neutron energies. While the presented measurements from the exploratory experiment in June 2022 involved irradiations of a lithium target with a 66.48 MeV proton beam (resulting in neutrons with a peak energy of 62.34 ± 0.37 MeV), the available proton beams from the SSC at iThemba LABS allow for a neutron energy range from around 30 MeV to 200 MeV to be covered almost continuously [Ndlovu et al., 2019].

Figure 6.7 shows the neutron fluence energy spectra derived from TOF measurements with the BC501A detector (as described in Section 4.3) that were conducted in the D-line in 2009. The fluence spectra are shown for measurements of neutrons that were produced by 65.99 MeV, 99.44 MeV, and 203.33 MeV proton beams respectively, impinging on both a 6.0 mm lithium target and a 8.0 mm carbon target, illustrating the range of different neutron energies that can be covered and characterised at iThemba LABS.

Varying thicknesses of lithium and beryllium targets are traditionally used in the D-line to produce neutron spectra that have the characteristic high-energy peak and lower-energy continuum, which are measured at different neutron emission angles in order to simulate a quasi-monoenergetic neutron spectrum, as discussed in Section 4.1 [Ndlovu et al., 2019]. As discussed in Section 6.3, the validity of the 'subtraction procedure', based on irradiating the biological samples at different neutron emission angles from the lithium target to determine the linear yield coefficient of neutrons in the high-energy peak, still needs to be assessed. Figure 6.7 illustrates that a carbon target can be alternatively used to produce a continuous energy distribution of neutrons without a high-energy peak, covering a range of energies similar to a portion of the low-energy continuum that is observed for the lithium target at the same proton beam energy. Conducting neutron RBE measurements with both the lithium and carbon targets for a particular proton beam energy presents a potentially interesting alternative prospect for future RBE measurements at iThemba LABS, as the absence of the high-energy peak in the carbon target spectra could allow for the biological effects of the low-energy continuum to be directly investigated and distinguished from those of the high-energy peak neutrons.

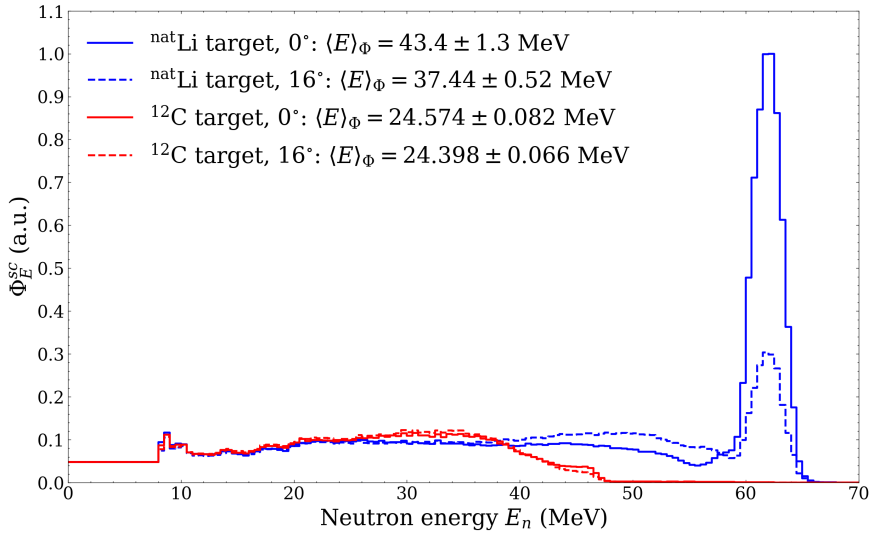

(a)

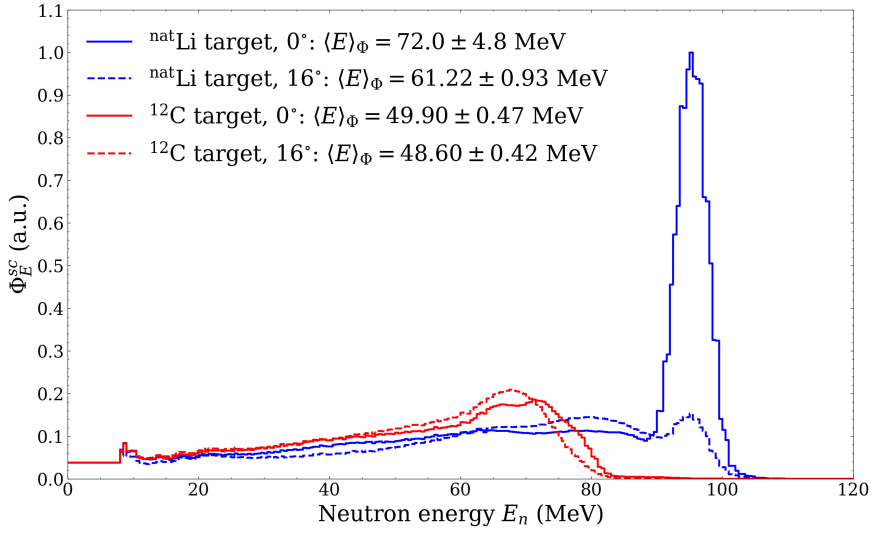

(b)

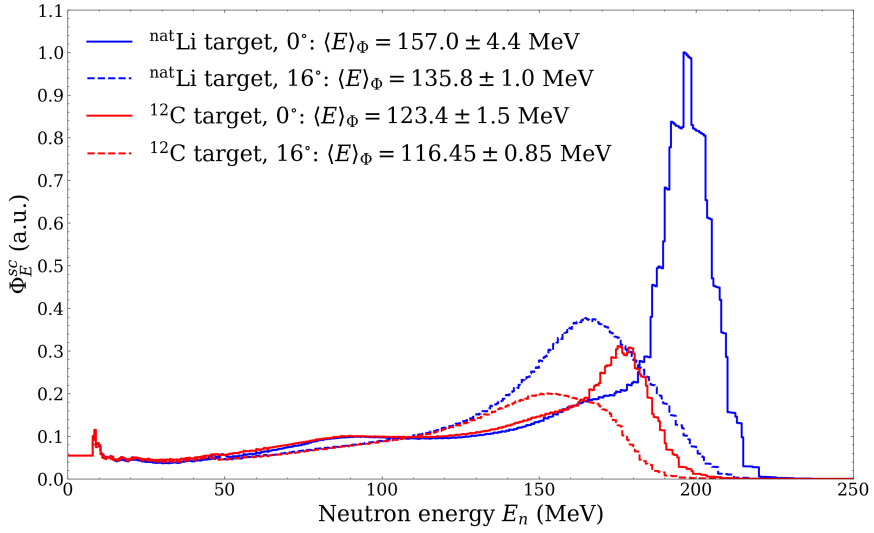

(c)

Figure 6.7: Relative spectral fluence for measurements of neutrons produced by a (a) 65.99 MeV, (b) 99.44 MeV, and (c) 203.33 MeV proton beam irradiating a 6.0 mm lithium target (blue) and an 8.0 mm carbon target (red), measured by the BC501A detector at a distance of (a, b) 9.1586 m and (c) 8.0000 m from the target at 0°, and 8.0500 m from the target at 16°. The heights of the measured spectra have been arbitrarily scaled to match in the region below 7.5 MeV. The quantity $\langle E \rangle_\Phi$ indicates the fluence-weighted average energy of each spectrum.

6.5 Reference radiation measurements

As defined in Equation 3.5, measurements of neutron RBE_M require the establishment of dose-response relationships for the relevant biological endpoint for both the neutron and reference radiations. While there is no international recommendation for the specific sources that should be used, the reference radiation is typically a low-LET photon radiation such as gamma rays or X-rays [Valentin, 2003].

Within the context of radiation weighting factors, a value of $w_R = 1$ is assigned to a range of low-LET radiations over a range of energies, as differences in the effectiveness of these radiations are not considered significant enough for general radiation protection purposes [Valentin, 2003]. This assumption is restricted to the definition of w_R and does not imply that all low-LET radiations are equally effective. In fact, it is well-established that particularly at low doses, different low-LET radiations can have substantially different effects, and therefore the magnitude of RBE values depend significantly on the chosen reference radiation [Valentin, 2003].

Neutron RBE results have been shown to be influenced not only by the type of reference radiation, but also by the specific characteristics of the irradiation that can influence the interpretation of the neutron biological effectiveness. Schmid et al. [2000, 2002] investigated how neutron RBE_M results are directly affected by use of different reference radiations under differing exposure conditions including irradiation temperatures, dose rates, and experimental setups that affect the spectral distribution of the photons. Their results emphasise that RBE_M studies should not assume universal applicability of linear yield coefficients for reference radiations unless the experimental conditions are directly comparable. It is therefore necessary to report RBE_M measurements alongside detailed specifications of the type of reference radiation and the corresponding experimental conditions that may have influenced the results.

In order to minimise potential confounding factors and facilitate the comparability of experimental results for neutron RBE_M determined via cytogenetic analysis in *in vitro* cell systems, it is recommended that where possible, the neutron and corresponding reference irradiations should be performed under 'head-to-head' conditions, that is [Schmid et al., 2002, 2003; Nolte et al., 2005]:

1. Using blood from the same donor;
2. Using matched culture and evaluation conditions; and
3. Using similar irradiation times.

At iThemba LABS, a ^{60}Co gamma radiation source from a *Theratron 780-C* cobalt therapy unit and a *XRAD 320* X-ray irradiator are available as reference radiation qualities for neutron RBE measurements.

While there is no exclusive convention, there are a number of arguments to favour hard gamma rays as a reference radiation for neutron RBE measurements [Valentin, 2003], and the previous high-energy neutron RBE experiments conducted by Nolte et al. [2005, 2006] were carried out with ^{60}Co as a reference radiation. For ease of comparability with these previous neutron RBE experiments, it is recommended that the ^{60}Co gamma radiation source from the *Theratron 780-C* cobalt therapy unit should be used as a reference radiation for measurements of high-energy neutron RBE at iThemba LABS in the future. The proximity of the cobalt therapy unit to both the iThemba LABS Radiation Biophysics laboratories and the D-line, will enable consistent culture and evaluation conditions to be established for both the neutron and

reference irradiations, as is required for 'head-to-head' conditions.

Fulfilling the third requirement for 'head-to-head' conditions, i.e. that both the neutron and reference irradiations are carried out at similar dose rates, is more complicated. In January 2024, the dose output to water from the cobalt therapy unit at iThemba LABS (for the standard experimental setup that is used for radiobiology experiments at the facility) was measured to be 233.3 ± 21.7 mGy/min. This dose rate is over 500 times greater than the measured average dose rates to blood vials A/C from neutrons in the D-line at 0° as quoted in Table 5.6.

Appendix B discusses simulations of the cobalt therapy unit at iThemba LABS that were constructed in GEANT4, as shown in Figure 6.8, in order to assess the feasibility of lowering the dose rate from this unit to match those expected for neutrons in the D-line so that future neutron RBE experiments could be carried out under 'head-to-head' conditions.

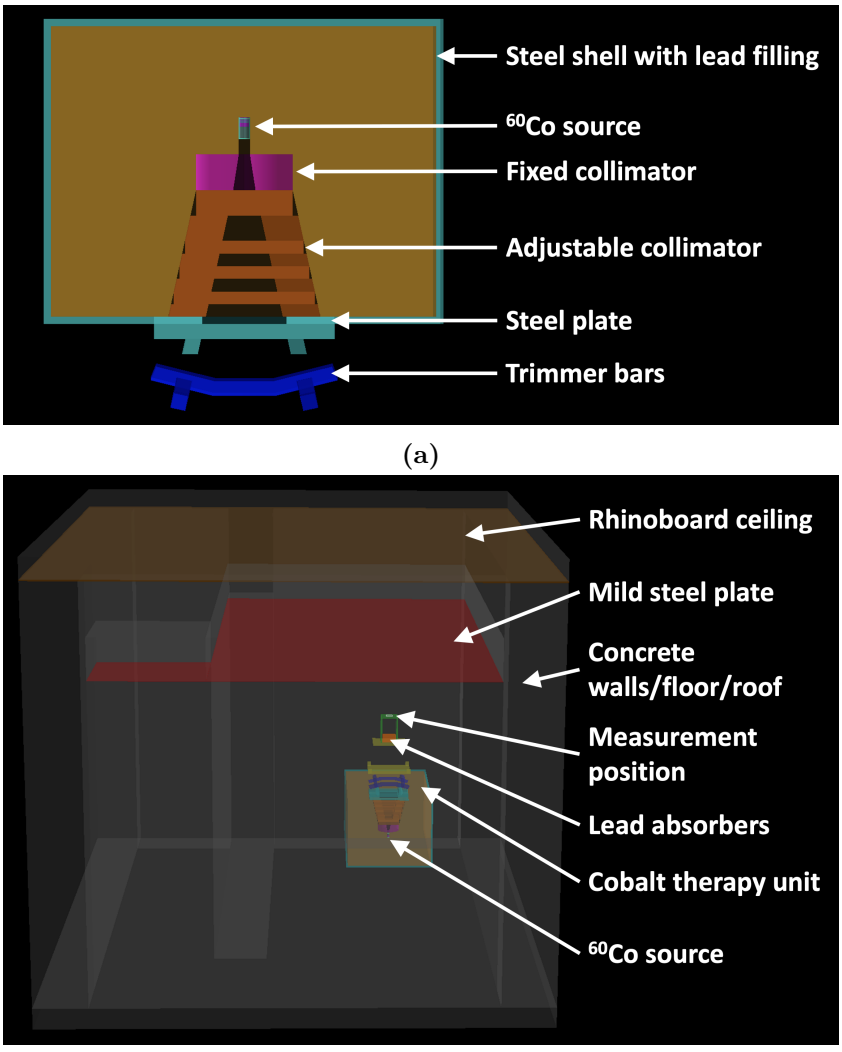

Figure 6.8: Simplified model constructed in GEANT4 of (a) the cobalt therapy unit and (b) the cobalt therapy unit and the room in which it is housed at iThemba LABS for the experimental 'Setup B' that is described in Appendix B.

The simulations of the cobalt therapy unit at iThemba LABS are discussed in detail in Appendix B, and the results show that while the desired dose rates could theoretically be achieved by altering the experimental setup and placing lead absorbers between the ^{60}Co source and irradiated blood samples, doing so could result in significant changes to the features

of ^{60}Co gamma ray spectrum. Most concerning is the observed potential increased contribution to the dose from scattered gamma rays from around the room in which the unit is housed. This is illustrated in Figure 6.9, which shows simulated photon fluence spectra at a particular measurement position with fluence-weighted average energies that vary between 1.037 MeV and 0.737 MeV, for lead absorber thicknesses of 0 cm and 10 cm respectively, when the room is not included in the simulation; and between 1.025 MeV and 0.504 MeV, for lead absorber thicknesses of 0 cm and 10 cm respectively, when the room is included in the simulation.

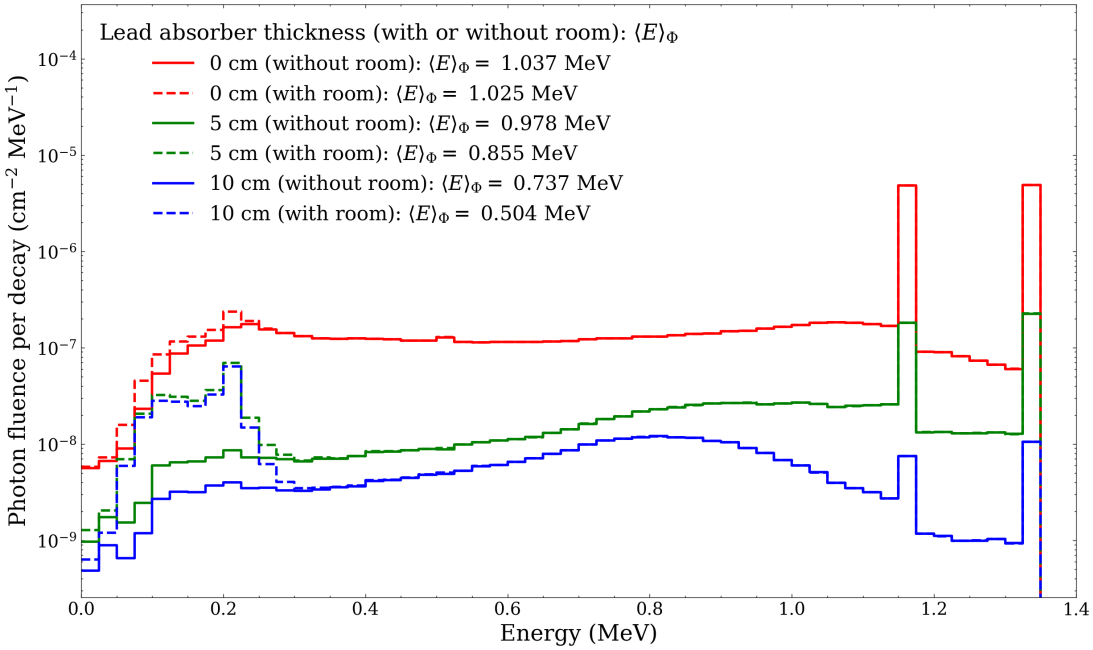

Figure 6.9: Simulated photon fluence spectra scored on a 5 cm × 5 cm plane at the indicated measurement position for the simulation setup shown in Figure 6.8(b) for a field size of 35 cm × 35 cm (at a source-surface distance (SSD) of 80 cm) and different thicknesses of lead absorbers. The results are shown for simulations with and without the inclusion of the room in which the cobalt therapy unit at iThemba LABS is housed, and the fluence-weighted average energy $\langle E \rangle_\Phi$ of each spectrum is indicated. Further details about these simulations are discussed in Appendix B.

Conducting neutron and reference irradiations under 'head-to-head' conditions is generally recommended to facilitate the ease of comparability of experimental results for neutron RBE_M measurements [Schmid et al., 2002, 2003; Nolte et al., 2005]. However, the results in Appendix B show that changing the experimental setup at the cobalt therapy unit at iThemba LABS to achieve the desired dose rates, could significantly alter the spectrum of ^{60}Co gamma rays with which the investigated biological samples are irradiated. Moving away from a 'standard' ^{60}Co spectrum will potentially introduce more complications to the inter-laboratory comparisons of RBE_M results than using different dose rates. Indeed, Schmid et al. [2002] concluded that a differing spectral distribution of ^{60}Co gamma rays (due to different experimental setups) had a more significant impact on their observed reference radiation yield coefficients than their differing dose rates. For these reasons, it is recommended that reference radiation measurements with the cobalt therapy unit at iThemba LABS be conducted with the experimental setup that is typically used for radiobiology experiments at the facility for which the dose rate, although significantly higher than that of the neutron irradiations, is well-known and samples are directly irradiated with ^{60}Co gamma rays. What is most important is that the RBE_M results are quoted alongside a detailed specification of the type of reference radiation and the irradiation conditions used, in order to allow for comparisons with other measurements and existing knowledge of the biological effects of ^{60}Co gamma rays.

7 Conclusion

The presented thesis focused on synthesising existing literature pertaining to the production and the biological effects of high-energy neutrons in space, and the development of a standardised procedure to measure the maximum neutron Relative Biological Effectiveness (RBE_M) at the iThemba LABS high-energy neutron facility at energies between 30 MeV and 200 MeV.

Review of the current state of knowledge surrounding the production of high-energy neutrons in space and their biological effects

The neutron radiation environment in space is challenging to characterise for astronaut radiation protection purposes owing to the variety of factors that collectively influence its key characteristics at a specific location, environment, and time. Neutrons in space occur as secondary radiation produced via the interactions of galactic cosmic radiation (GCR) and solar energetic particles (SEPs) with matter. The interactions of GCR and SEPs generally result in astronaut exposure to chronic and acute doses of neutrons respectively, but with energies and intensities that vary significantly depending on both the space weather conditions over differing temporal scales at a particular location in the heliosphere, and the specific environment and corresponding neutron production mechanisms that contribute to a given radiation exposure scenario. As discussed in Chapter 2, a number of experimental and computational studies have been conducted to investigate the production of neutrons in Earth's atmosphere, in spacecraft shielding materials, in Lower Earth Orbit, on the Moon, and on Mars. Measured or extrapolated neutron dose equivalent rates for chronic exposures in space over extended time periods significantly exceed the recommended limits (for all radiation types) for the general public on Earth, by factors ranging from 7.3 to 71.5, depending on the specific exposure scenario. While experimental data are limited, neutrons that are produced in spallation/fragmentation reactions with energies greater than 10 MeV and extending up to several hundred MeV, have been predicted to contribute approximately 50% of the total neutron dose equivalent in the investigated scenarios.

Energetic neutrons pose a significant concern with regards to astronaut radiation protection owing to their ability to penetrate through typical spacecraft shielding, and to induce considerably more biological damage than less densely ionising radiation, like photons. The development of radiation health-risk models for space exploration requires the quantification of the biological effects of neutrons, and in the current radiation protection framework, this is achieved via measurements of the neutron Relative Biological Effectiveness (RBE). Experimentally determined values of RBE are utilised by the International Commission on Radiological Protection (ICRP) to inform the selection of radiation weighting factors that relate absorbed dose from ionising radiation in human tissue to the risk of both stochastic and deterministic effects. However, measuring neutron RBE is complicated, given that it depends on a number of both physical and biological variables. Current radiation health risk models developed within the context of future space exploration involve considerable uncertainties surrounding our knowledge of the biological effects of neutron radiation at relevant energies, doses, dose-rates, biological systems and endpoints, as discussed in Chapter 3.

This project aimed to address the significant uncertainties associated with the biological effects of neutrons with energies above 20 MeV. The available neutron RBE data in this energy range (which is an important component of the neutron energy spectrum in space) are extremely

limited, having been obtained from radiobiology experiments conducted in mixed radiation and neutron energy fields under varying radiation exposure conditions for different biological systems, biological endpoints, and reference radiations (as discussed in Section 3.3.1). The existing uncertainties surrounding neutron RBE at high energies call for dedicated radiobiology experiments to be conducted with well-characterised neutron fields and comparable experimental conditions over a range of neutron energies above 20 MeV. The high-energy neutron facility (D-line) at iThemba LABS is uniquely capable of providing neutron beams with energies between 30 MeV and 200 MeV, and has the potential to be instrumental in providing the required experimental data.

While there are a range of health effects that are of concern regarding human exposure to ionising radiation in space, the presented thesis focused on evaluating the carcinogenic effects of neutrons. Carcinogenesis, identified as a critical research priority in space exploration health-risk assessments [Cucinotta and Durante, 2013b], is a stochastic radiation effect - assumed to have no threshold dose - and is typically evaluated through measurements of the maximum neutron Relative Biological Effectiveness ($\mathrm{RBE_M}$), the limiting maximum value of RBE that is approached at low doses. Such measurements require the determination of the linear yield coefficients α_n and α_{ref} from the radiation dose-response curves for both the neutron and reference radiations respectively, from which the $\mathrm{RBE_M}$ is calculated as

$$\mathrm{RBE_M} = \frac{\alpha_n}{\alpha_{ref}}. \tag{3.5}$$

The presented thesis built on previous neutron $\mathrm{RBE_M}$ experiments by Nolte et al. [2005] and Nolte et al. [2006] to outline a standardised approach for measuring the neutron linear yield coefficient α_n in the D-line at iThemba LABS – a task that involves the harmonisation of both physics (in terms of a detailed characterisation of the measured neutron field) and radiobiology (in terms of understanding and quantifying the associated biological effects).

Results from the exploratory experiment conducted as preparation for measuring neutron $\mathrm{RBE_M}$ at iThemba LABS

The characterisation of the neutron beam energy distribution and fluence in the D-line was achieved via Time-Of-Flight (TOF) spectroscopy using a BC501A liquid scintillation detector (for high energy resolution spectral fluence measurements at low beam intensities) and a ^{238}U fission ionisation chamber (FC) (for standardised neutron fluence measurements at high beam intensities), in combination with a Faraday cup and NE102 plastic scintillation detector that are used to monitor the beam conditions during experiments. In Chapter 4, these metrological methods were illustrated via their application to data from an exploratory experiment that was conducted in the D-line in June 2022, involving measurements of neutrons with a peak energy of 62.34 ± 0.37 MeV produced by a 66.48 MeV proton beam irradiating an 8.0 mm lithium target at neutron emission angles of 0° and 16° relative to the incident beam direction.

In Chapter 5, the results from the metrological characterisation of the neutron beam were used in combination with Monte Carlo simulations developed in GEANT4, in order to establish the absorbed dose delivered to vials of human blood contained in high density polyethylene phantoms that were irradiated 4.300 m from the collimator exits for different time intervals during the exploratory experiment. The absorbed dose values (from 54 mGy to 255 mGy) were calculated with total relative uncertainties of around 13%, predominantly arising from uncertainties inherent in the TOF procedure to determine the measured spectra, and the correction factors involved in estimating the peak neutron fluence from the FC measurements. The measured average dose rates in human blood ranged between 0.406 ± 0.013 mGy/min and 0.437 ± 0.014 mGy/min at

0°, and between 0.2369 ± 0.0076 mGy/min and 0.2194 ± 0.0070 mGy/min at 16°, depending on the blood vial position in the phantom. These are the first neutron dose-quantification measurements that have been conducted in the D-line since the infrastructural upgrade (described by Ndlovu et al. [2019]) was completed in 2020/2021.

The determined values of neutron dose to the blood vials irradiated during the June 2022 exploratory experiment were related to the results from a corresponding radiobiology analysis of the induction of DNA DSBs in the irradiated blood samples, via the γ-H2AX foci assay, such that a dose-response relationship could be established for the irradiations, as discussed in Chapter 6. The resulting neutron linear yield coefficients were calculated to be $\alpha_n^{(0^\circ)} = 10.12 \pm 0.63$ Gy^{-1} and $\alpha_n^{(16^\circ)} = 7.45 \pm 0.66$ Gy^{-1} for irradiations with neutrons with fluence-weighted average energies of 40.11 ± 0.92 MeV (at 0°) and 37.26 ± 0.40 MeV (at 16°) respectively.

Recommendations for future neutron RBE experiments at iThemba LABS

Although preliminary, the results from the exploratory experiment were not consistent with the expectation that $\alpha_n^{(0^\circ)}$ should be less than $\alpha_n^{(16^\circ)}$ since the low-energy neutron continuum region, which should have a higher RBE according to the ICRP weighting factors, contributes a greater percentage of the total dose at 16° than at 0°. Similar discrepancies in the results for the linear yield coefficients measured at different angles were previously observed in the experiments by Nolte et al. [2006] and Nolte et al. [2008], where the effect was attributed to parasitic neutrons produced by drifts in the proton beam during the extended irradiation time. These results emphasize the importance of all neutron RBE measurements being accompanied by a detailed metrology characterisation and careful monitoring of the beam conditions during the irradiations in order to accurately determine the absorbed dose received by the investigated biological samples. With this goal in mind, Section 5.5 included a discussion surrounding a number of potential sources of uncertainties that were not taken into account in the presented dose-quantification analysis, and recommendations for improving the quantification of the neutron dose in the D-line at iThemba LABS in the future. Section 6.1 included recommendations for improving the radiobiology analysis, particularly noting that future measurements should investigate the induction of unstable aberrations and/or stable aberrations as alternative and more appropriate biological endpoints than the γ-H2AX assay for $\mathrm{RBE_M}$ assessments. Given the lack of appropriate equipment and expertise required to conduct these assays at iThemba LABS, irradiated samples would need to undergo fixation and slide preparation before being transported to a facility where the analyses can be performed (such as the GSI Helmholtz Centre for Heavy Ion Research).

The original motivation behind making measurements at both 0° and 16° was so that the subtraction procedure outlined by Nolte et al. [2006] could be applied to discriminate the effects of continuum neutrons from those of high-energy neutrons and thus determine the effect of the quasi-monoenergetic neutron beam. As discussed in Section 6.3, applying the subtraction procedure to the data from the exploratory experiment resulted in a linear yield coefficient for irradiations with the quasi-monoenergetic difference spectrum (with a peak energy of 62.34 ± 0.37 MeV) of $\alpha_n^{(0^\circ - 16^\circ)} = 13.3 \pm 2.6$ Gy^{-1}. The fact that $\alpha_n^{(0^\circ - 16^\circ)}$ is greater than both $\alpha_n^{(0^\circ)}$ and $\alpha_n^{(16^\circ)}$ is surprising given that the low-energy continuum is expected to have a greater biological effect than neutrons in the high-energy peak. Although preliminary, this result raises a number of questions and concerns surrounding the validity of applying the subtraction procedure, which is motivated by fluence difference measurements, to biological effects. It is recommended that future measurements of radiation dose-response curves should be re-

peated over a wider and comparable dose range with more precise dosimetric and radiobiology analysis (following the recommendations discussed in Section 5.5 and Section 6.1) in order to confirm that a statistically significant difference can be observed between the measured data at 0° and 16°. Furthermore, even if a statistically significant difference is observed, it is not immediately clear if the relatively simple subtraction procedure fully accounts for the intricate energy dependence of the biological yield. It is recommended that the procedure be validated through comparison with other methods such as that outlined by Nolte et al. [2005], or by directly investigating the effects of the low-energy continuum neutrons by making measurements of neutrons produced in a carbon target (which do not exhibit a high energy peak) at the same proton beam energy as measurements of neutrons produced in a lithium target (which exhibit the characteristic low-energy continuum and high-energy peak on which the subtraction procedure is based).

Neutron RBE_M measurements require the determination of the linear yield coefficient for a reference radiation α_{ref} for the investigated biological endpoint. At iThemba LABS, the available reference radiation sources are a ^{60}Co gamma radiation source from a *Theratron 780-C* cobalt therapy unit and an *XRAD 320* X-ray irradiator. Hard gamma rays are preferred for comparability with previous neutron RBE experiments [Nolte et al., 2005, 2006], and therefore it is recommended that the ^{60}Co gamma radiation source be used as the reference radiation for future neutron RBE measurements at iThemba LABS. As discussed in Section 6.5, neutron RBE_M measurements should ideally be conducted under 'head-to-head' conditions, using blood from the same donor, matched culture and evaluation conditions, and similar irradiation times for neutron and reference irradiations. The proximity of the cobalt therapy unit to the D-line at iThemba LABS facilitates the first two conditions. However, matching dose rates poses a challenge, as the dose output of the cobalt therapy unit exceeds that measured in the D-line (as discussed in Chapter 5) by over 500 times. GEANT4 simulations indicate that reducing the dose rate to match the neutron irradiations by changing the experimental setup could significantly alter the ^{60}Co gamma-ray spectrum. Moving away from a 'standard' ^{60}Co spectrum will potentially introduce more complications to the inter-laboratory comparisons of RBE_M results than the differing dose rates. For this reason, it is recommended to conduct reference radiation measurements at iThemba LABS using the standard experimental setup used for radiobiology experiments at the cobalt therapy unit facility, for which the dose rate, although significantly higher than that of the neutron irradiations, is well-known and samples are directly irradiated with an unmodified ^{60}Co gamma ray spectrum.

A comprehensive interpretation of existing neutron RBE data at energies greater than 20 MeV is challenging given the varied experimental conditions under which the measurements have been performed. To experimentally validate the shape of the neutron radiation weighting factor function currently recommended by the ICRP, it is necessary to conduct neutron RBE experiments under consistent irradiation conditions, targeting identical biological endpoints, across a range of neutron energies above 20 MeV. While the exploratory measurements presented in this thesis involved neutrons with a peak energy of 62.34 ± 0.37 MeV, the proton beams available from the SSC at iThemba LABS enable nearly continuous coverage of neutron energies from around 30 MeV to 200 MeV. Although the subtraction procedure used to determine the RBE_M of quasi-monoenergetic neutrons still requires validation, conducting neutron RBE_M experiments in well-characterised, mixed-energy radiation fields remains valuable. Such studies will allow for comparison of the energy-dependent variation in neutron RBE_M against predictions based on the currently-recommended ICRP neutron radiation weighting factor function for stochastic effects. This thesis outlined a standardised methodology for conducting neutron RBE_M measurements in the D-line at iThemba LABS. The results of such

measurements over the range of available neutron energies at iThemba LABS will be critical in reducing the existing uncertainties associated with the biological effects of high energy neutrons within the context of future space exploration, as well as aviation and proton therapy.

A The statistical convergence of Monte Carlo simulations

Section 5.3 describes the Monte Carlo simulations that were constructed in GEANT4 in order to calculate the absorbed dose per unit neutron fluence at the front face of the phantom D/Φ and the associated uncertainties for each blood vial for the experimental setup described in Section 5.2. As mentioned in Section 5.3.4, the 68% confidence associated with the statistical uncertainty of the result for D/Φ (calculated using Equation 5.7) is only valid if the physical space has been 'adequately sampled' by the Monte Carlo process and it is often up to the discretion of the user to decide when a sufficient number of events have been simulated to allow for the convergence of the result on a statistically valid solution. In order to choose an appropriate number of events to simulate to obtain the results for D/Φ that are presented in Section 5.3, seven of the 'statistical tests' recommended by Kulesza et al. [2022] were conducted for simulation runs of $N = 2 \times 10^3$ $N = 2 \times 10^6$, and $N = 2 \times 10^9$ simulated neutrons.

The criteria for passing the statistical tests are summarised in Table A.1, and involve three calculated quantities:

- The estimated 'mean' result for D/Φ (as defined in Equation 5.4);
- The estimated relative error R defined as

$$R = \frac{S_{\bar{E}}}{\bar{E}}, \tag{A.1}$$

  where $S_{\bar{E}}$ is the sample standard deviation of the sample mean energy deposited per event (as defined in Equation 5.5), and $\bar{E}$ is the sample mean energy deposited per event (as defined in Equation 5.4); and
- The relative variance of the variance VOV, defined as

$$VOV = \frac{S^2(S^2_{\bar{E}})}{S^4_{\bar{E}}}, \tag{A.2}$$

  where $S^2_{\bar{E}}$ is the estimated variance of $\bar{E}$ and $S^2(S^2_{\bar{E}})$ is the estimated variance in $S^2_{\bar{E}}$.

Value	Test number	Criteria
Mean	1	Estimated mean shows non-monotonic behaviour as a function of N for the last half of the problem.
R	2	Final magnitude of R is < 0.10.
	3	R decreases monotonically as a function of N for the last half of the problem.
	4	R decreases as $1/\sqrt{N}$ for the last half of the problem.
VOV	5	Final magnitude of VOV is < 0.10.
	6	VOV decreases monotonically as a function of N for the last half of the problem.
	7	VOV decreases as $1/N$ for the last half of the problem.

Table A.1: Summary of the criteria for passing the 'statistical tests' that are recommended for assessing the statistical validity of the results obtained from a Monte Carlo simulation [Kulesza et al., 2022].

Figures A.1, A.2, and A.3, show the mean result for D/Φ, the estimated relative error R, and the relative variance of the variance VOV, respectively, plotted as a function of N for the last half of the problem for simulation runs of (a) $N = 2 \times 10^3$, (b) $N = 2 \times 10^6$, and (c) $N = 2 \times 10^9$ incident neutrons sampled from the 16° fluence spectrum shown in Figure 5.2. Table A.2 provides a summary of the results for the statistical tests that were obtained based on the results shown in Figures A.1 to and A.3. Failing several of these tests is typically an indication that the determined confidence interval of the final result is less likely to be correct. As shown in Table A.2, all seven tests were passed for $N = 2 \times 10^9$ simulated events, and so this N was chosen to obtain the final results for D/Φ that are presented in Section 5.3.5.

Value	Test number	Result		
		$N = 2 \times 10^3$	$N = 2 \times 10^6$	$N = 2 \times 10^9$
Mean	1	Failed	Passed	Passed
R	2	Failed	Passed	Passed
	3	Failed	Passed	Passed
	4	Failed	Failed	Passed
VOV	5	Failed	Passed	Passed
	6	Failed	Failed	Passed
	7	Failed	Failed	Passed

Table A.2: Summary of the results for the 'statistical tests' described in Table A.1 that were obtained based on the results shown in Figures A.1, A.2, and A.3.

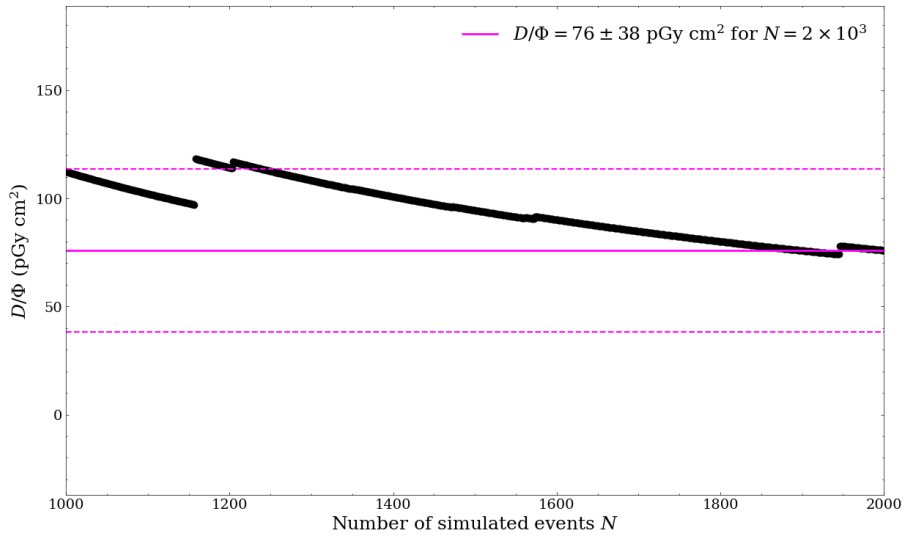

(a)

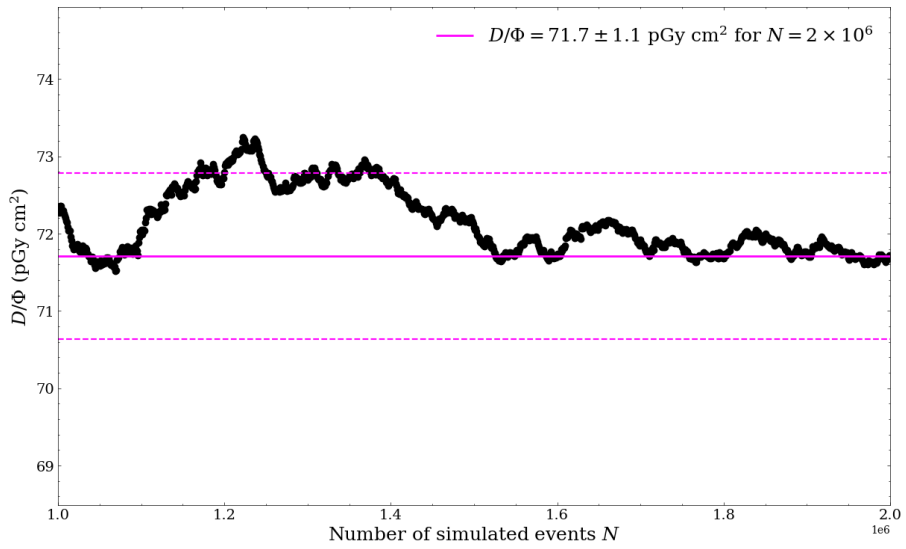

(b)

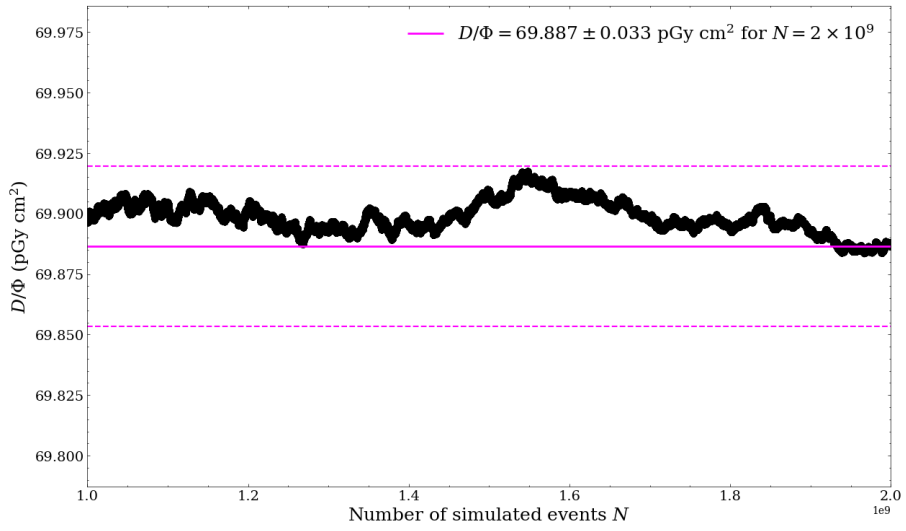

(c)

Figure A.1: The 'mean' result for D/Φ plotted as a function of N for the last half of the problem for simulation runs of (a) $N = 2 \times 10^3$, (b) $N = 2 \times 10^6$, and (c) $N = 2 \times 10^9$ incident neutrons sampled from the 16° fluence spectrum shown in Figure 5.2.

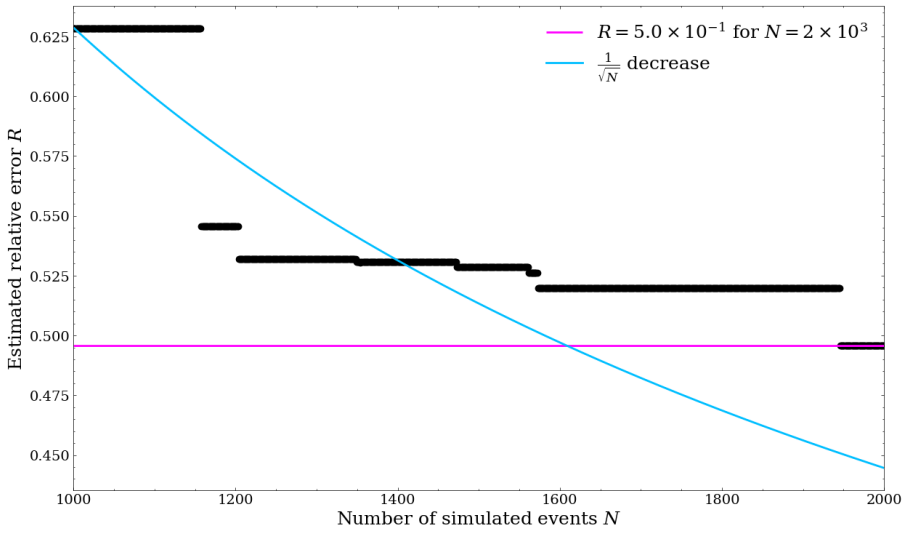

(a)

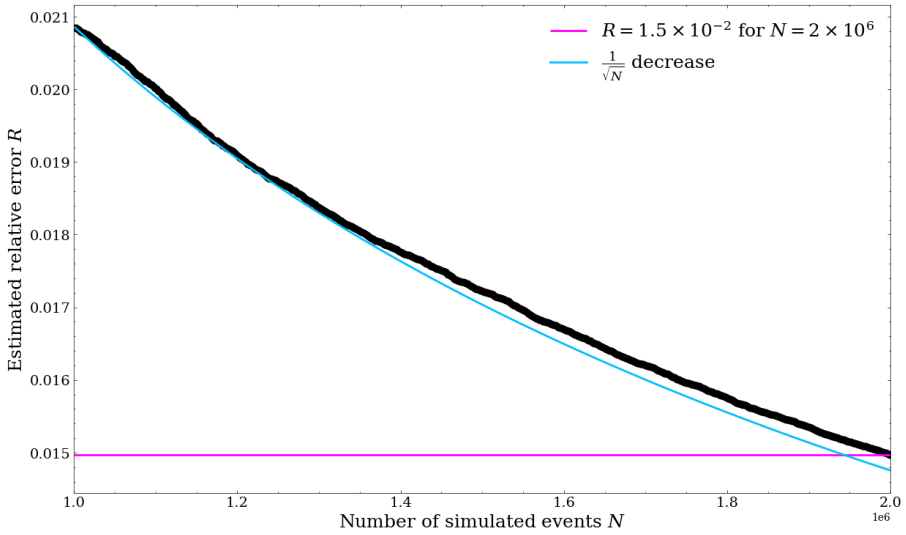

(b)

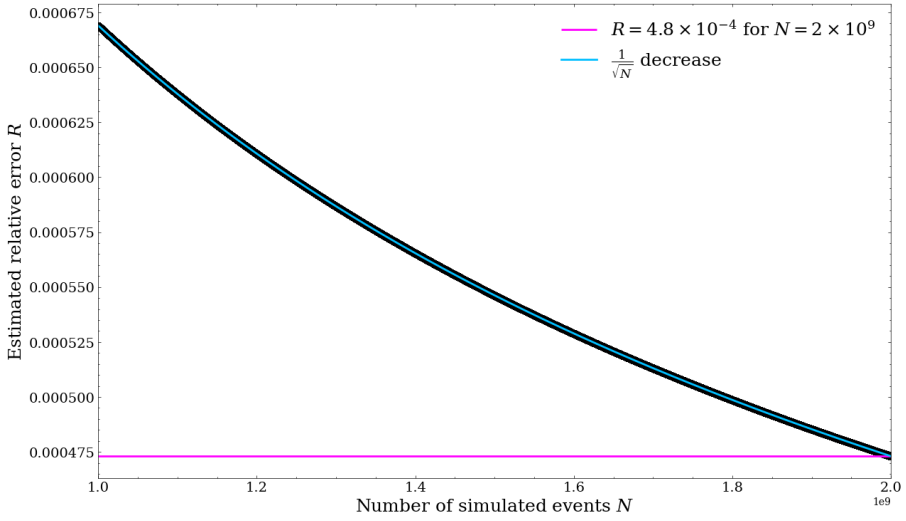

(c)

Figure A.2: The estimated relative error R plotted as a function of N for the last half of the problem for simulation runs of (a) $N = 2 \times 10^3$, (b) $N = 2 \times 10^6$, and (c) $N = 2 \times 10^9$ incident neutrons sampled from the 16° fluence spectrum shown in Figure 5.2.

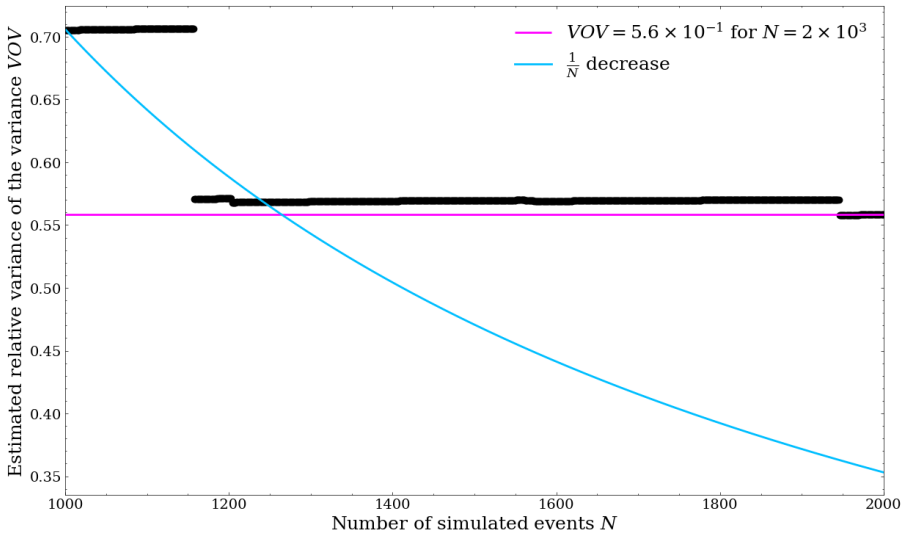

(a)

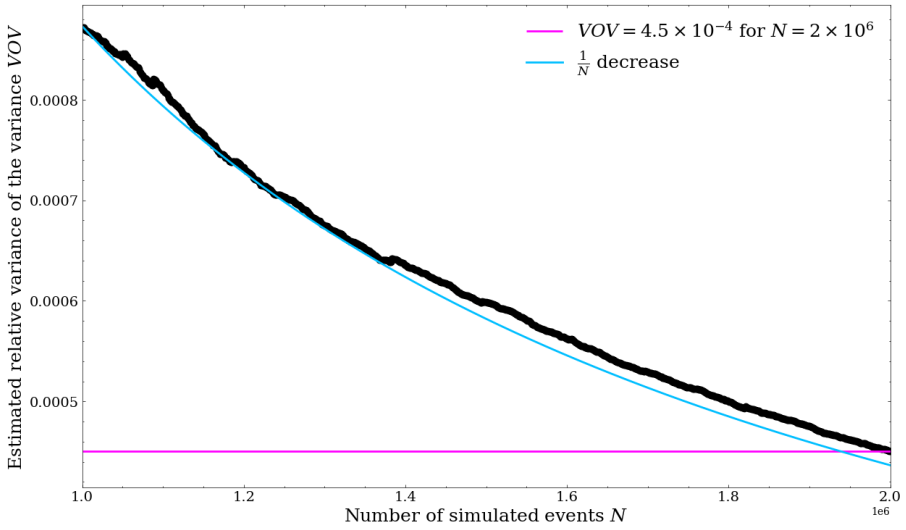

(b)

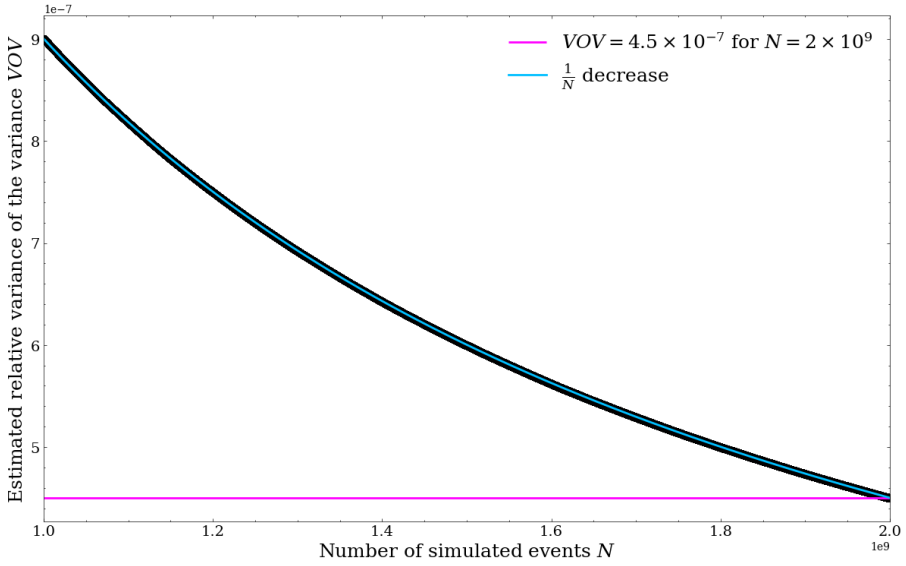

(c)

Figure A.3: The relative variance of the variance VOV plotted as a function of N for the last half of the problem for simulation runs of (a) $N = 2 \times 10^3$, (b) $N = 2 \times 10^6$, and (c) $N = 2 \times 10^9$ incident neutrons sampled from the 16° fluence spectrum shown in Figure 5.2.

B Simulations of the cobalt therapy unit at iThemba LABS

The Radiation Biophysics department at iThemba LABS houses a *Theratron 780-C* cobalt therapy unit. This appendix describes simulations of this cobalt therapy unit that were constructed in GEANT4 in order to investigate the feasibility of lowering the dose rate from this unit to match that expected for neutrons in the D-line so that future neutron RBE experiments could be carried out under 'head-to-head' conditions (as described in Section 6.5) using this unit as a reference radiation source.

B.1 Simulation geometry

The construction of the *Theratron 780-C* cobalt therapy unit in GEANT4 was based on a combination of information obtained from Sichani and Sohrabpour [2004] and Miró et al. [2005], and from provided computer-aided design (CAD) drawings for the treatment head and collimator assembly of the unit. There are significant uncertainties and discrepancies in the information from these three sources, and these are noted in the outline of the simulation setup below. Owing to the limited information about specific construction features of the unit, the current simulations focus on providing a rough approximation of the facility's key characteristics. Therefore, all results should be regarded as an approximate rather than a detailed characterisation.

The simulated *Theratron 780-C* cobalt therapy unit consists of a source capsule, fixed and adjustable collimators, and lead shielding in the unit head, as described in detail below. For certain simulations investigating the contributions of scattered photons at the measurement point of interest, the room in which the unit at iThemba LABS is housed was also simulated. The properties of the materials modelled in the simulations that are not NIST standard materials (referred to in italics throughout the rest of this section) are listed in Table B.1.

Material	**Composition**	**Density** (g/cm^3)
depleted uranium	99.8% ^{238}U; 0.2% ^{235}U; 0.001% ^{234}U	19.10
mild steel	0.17% C; 0.75% Mn; 0.02% P; 0.025% S; 99.035% Fe	7.87
Rhinoboard	67% H_2O; 33% $CaSO_4$	0.76
stainless steel (no. 316L)	0.03% C; 17% Cr; 10% Ni; 2% Mo; 2% Mn; 1% Si; 0.1% N; 0.045% P; 0.015% S; 67.81% Fe	8.00
tungsten alloy	90% W; 6% Ni; 4% Cu	16.90

Table B.1: Properties of the (non-NIST standard) materials that were modelled in GEANT4 for the simulations of the cobalt therapy unit at iThemba LABS.

B.1.1 Source

A diagram of the source capsule, which was simulated in a cylindrical geometry about the beam axis (z-axis), is shown in Figure B.1, along with the dimensions used. The active region

of ^{60}Co was simulated as a uniform medium made of cobalt where two gamma rays with energies 1.173 MeV and 1.332 MeV were generated simultaneously with random directions and at uniformly random positions in the volume at the beginning of each event. The source capsule consisted of two coaxial cylinders made of *stainless steel (no. 316L)*. On top of the source, there were tungsten plates and *stainless steel (no. 316L)* plates. On the bottom of the source, there was a thin *stainless steel (no. 316L)* plate that allows more particles to emerge in the downward direction.

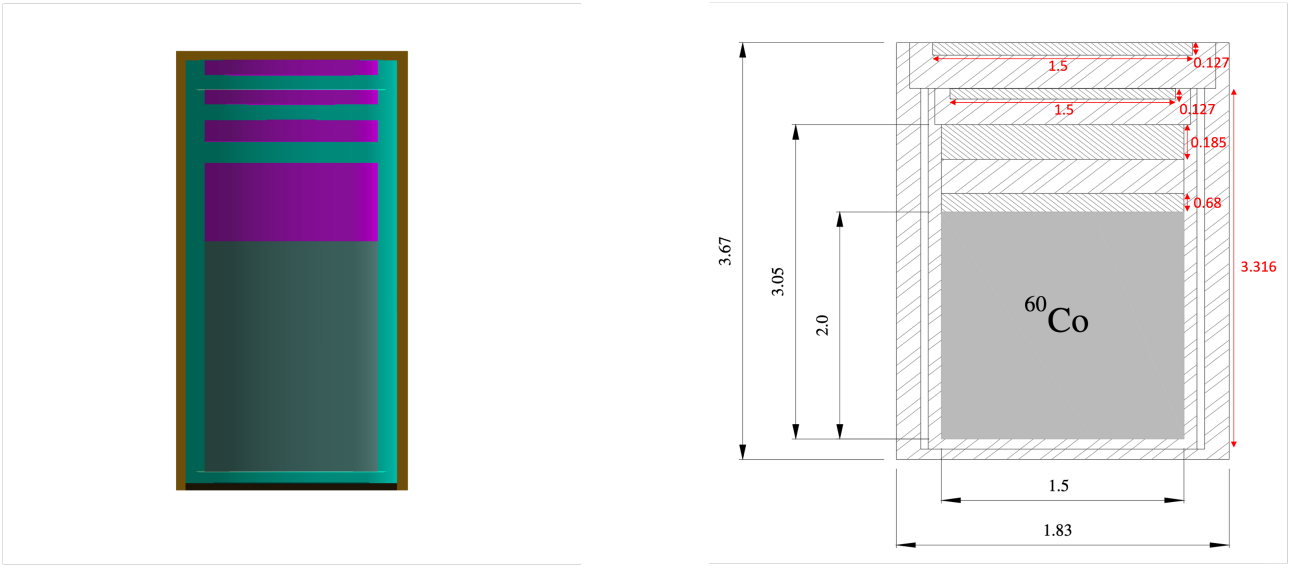

(a) **(b)**

Figure B.1: (a) ^{60}Co source capsule simulated in GEANT4 including the active material, tungsten shielding, steel spacers, and surrounding capsule. (b) The dimensions (in cm) used in the simulation. The diagram is taken from Sichani and Sohrabpour [2004] and the dimensions in red were chosen based on more detailed information that was available from Miró et al. [2005].

B.1.2 Fixed collimator

A 2.5 cm air gap separates the source capsule from the fixed collimator, which is constructed as a solid cylinder made from a tungsten alloy, with a trapezoidal shaped hole and dimensions as shown in Figure B.2.

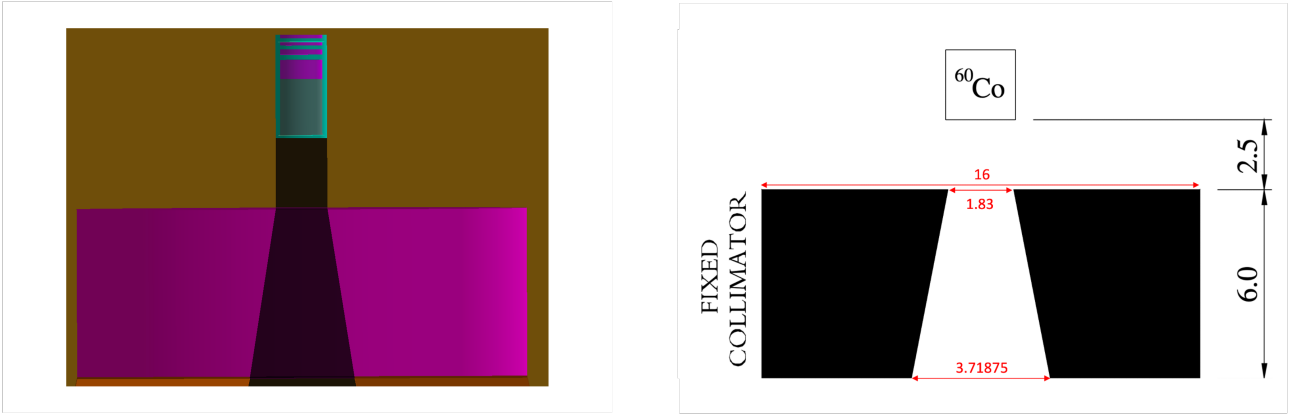

(a) **(b)**

Figure B.2: (a) Source capsule and fixed collimator simulated in GEANT4. (b) The dimensions (in cm) used in the simulation. The diagram is taken from Sichani and Sohrabpour [2004] and the dimensions in red were chosen to obtain a field size of 35 cm × 35 cm at a SSD of 80 cm.

B.1.3 Adjustable collimator, steel plate, and trimmer bars

The adjustable collimator follows immediately after the fixed collimator and is constructed of four sets of interleaved lead vanes that move in the $x - y$ plane perpendicular to the z-direction of the beam. The lead vanes are constructed in GEANT4 as parallelepiped volumes with x-dimensions of 6.1 cm, z-dimensions of 4.2 cm / 2.1 cm / 2.1 cm / 2.1 cm (for each set - based on information obtained from the CAD drawings), and y-dimensions and θ angles chosen depending on the desired field size (such that the inner edges of the collimator vanes are angulated to follow the beam divergence).

Following the lead vanes, there is a 1.2 cm thick *stainless steel no. 316L* plate with a 14 cm $\times$ 14 cm opening that is followed by a set of two layers of trimmer bars. The trimmer bars were modelled as curved parallelepiped volumes with dimensions of 2.5 cm x 30.0 cm x 2.5 cm to extend the total source-to-diaphragm distance to 45 cm. Based on information provided by Sichani and Sohrabpour [2004], the two sets of trimmer bars are made of *stainless steel no. 316L* and *depleted uranium* respectively.

The head of the treatment unit in which the source and collimation system are enclosed was modelled as a rectangular *stainless steel (no. 316L)* shell with dimensions of 120.0 cm x 66.0 cm x 50.7 cm that is filled with lead. The centre of the ^{60}Co source sits at a location of (30.00 cm, 0.00 cm, -6.45 cm) relative to the centre of this volume. The resulting model of the cobalt therapy unit in GEANT4 is shown in Figure B.3.

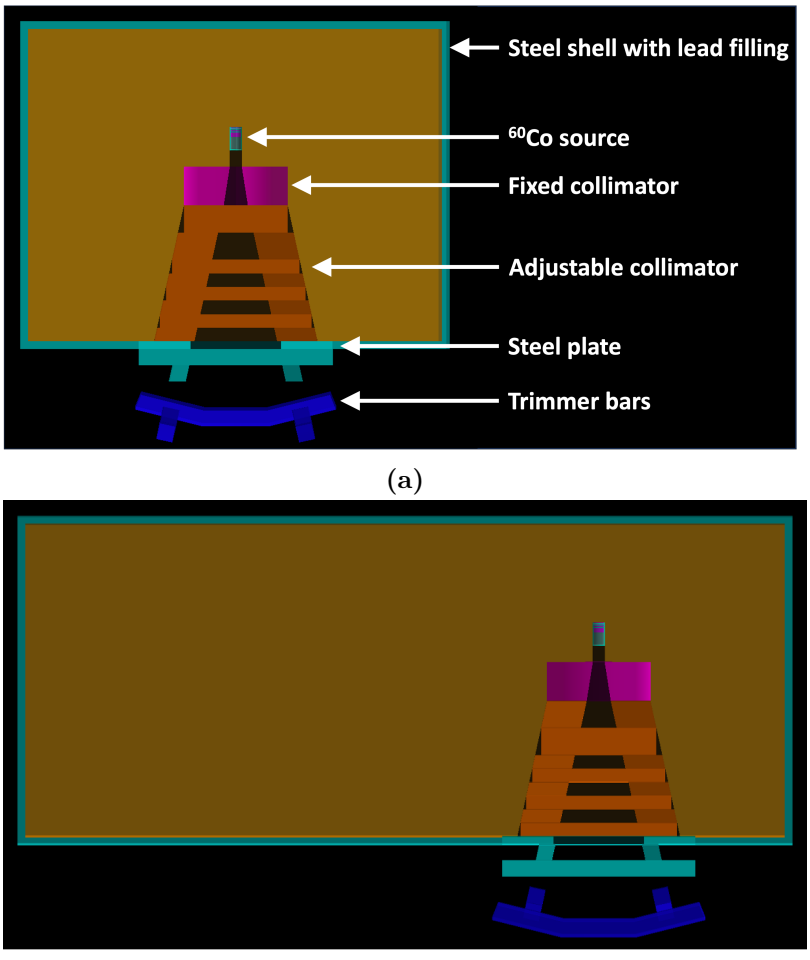

(a)

(b)

Figure B.3: Model of the cobalt therapy unit at iThemba LABS as constructed in GEANT4 and viewed in (a) the $y - z$ plane, and (b) the $x - z$ plane.

The simulated model of the cobalt therapy unit was designed such that the geometry of the adjustable collimators and trimmer bars could be easily adjusted to achieve field sizes ranging from 5 cm × 5 cm to 35 cm × 35 cm at a SSD of 80 cm. Figure B.4 illustrates the final simulation setup for three different field sizes.

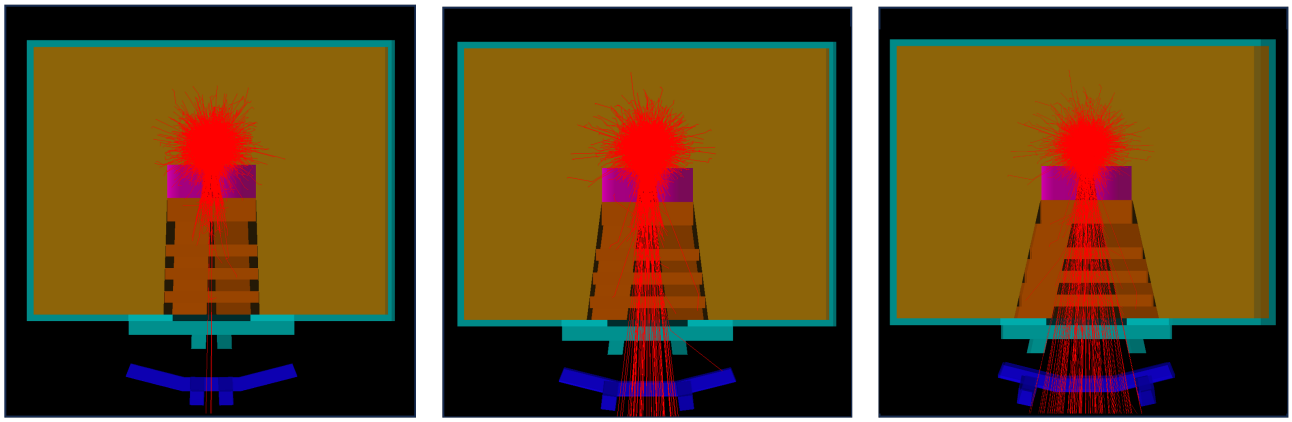

(a) **(b)** **(c)**

Figure B.4: Simulation setup in GEANT4, as viewed in the $y - z$ plane, for different field sizes of (a) 5 cm × 5 cm, (b) 10 cm × 10 cm, and (c) 35 cm × 35 cm at a SSD of 80 cm. The tracks of gamma rays in the geometry for 10^4 simulated ^{60}Co decays are shown in red.

B.1.4 Specific experimental setups at iThemba LABS

The simulations in GEANT4 involved modelling two specific experimental setups at iThemba LABS. The properties of these experimental setups, which will be referred to as "Setup A" and "Setup B" throughout the rest of this section, are summarised in Table B.2, and the resulting models in GEANT4 are shown in Figure B.5.

	Setup A	Setup B
Description	Typical experimental setup that is used for radiobiology experiments at iThemba LABS.	Experimental setup at iThemba LABS that can support the addition of lead absorbers without damaging the cobalt therapy unit.
Geometry	The gantry of the cobalt therapy unit is rotated such that the beam is directed vertically upwards. This setup includes a 32.50 cm × 30.00 cm × 0.58 cm Perspex build-up plate at a distance of 49.80 cm from the source, followed by four 4.25 cm × 4.35 cm × 2.95 cm Perspex spacer blocks that support a 29.80 cm × 29.90 cm × 4.96 cm Perspex backscatter block at its corners.	The gantry of the cobalt therapy unit is rotated such that the beam is directed vertically upwards. This setup includes the Perspex build-up plate and Perspex spacer blocks positioned as described for Setup A. It also includes a 25.00 cm × 25.00 cm × 0.90 cm Perspex table top at a distance of 72.12 cm from the source that supports 10.00 cm × 10.00 cm lead absorbers with variable thickness and a polyethylene mini table with two 13.00 cm × 1.00 cm × 19.00 cm legs and a 13.00 cm × 13.00 cm × 1.00 cm table top.
Field size	35 cm × 35 cm at a SSD of 80 cm.	Variable.
Measurement position	On top of the Perspex build-up plate at an SSD of 50.09 cm.	On top of the polyethylene mini table at a SSD of 92.57 cm.

Table B.2: Description of two specific experimental setups at the cobalt therapy unit at iThemba LABS that were modelled in GEANT4. "Geometry" refers to the components of the GEANT4 geometry that were added to the simulation in addition to those described in Sections B.1.1 to B.1.3.

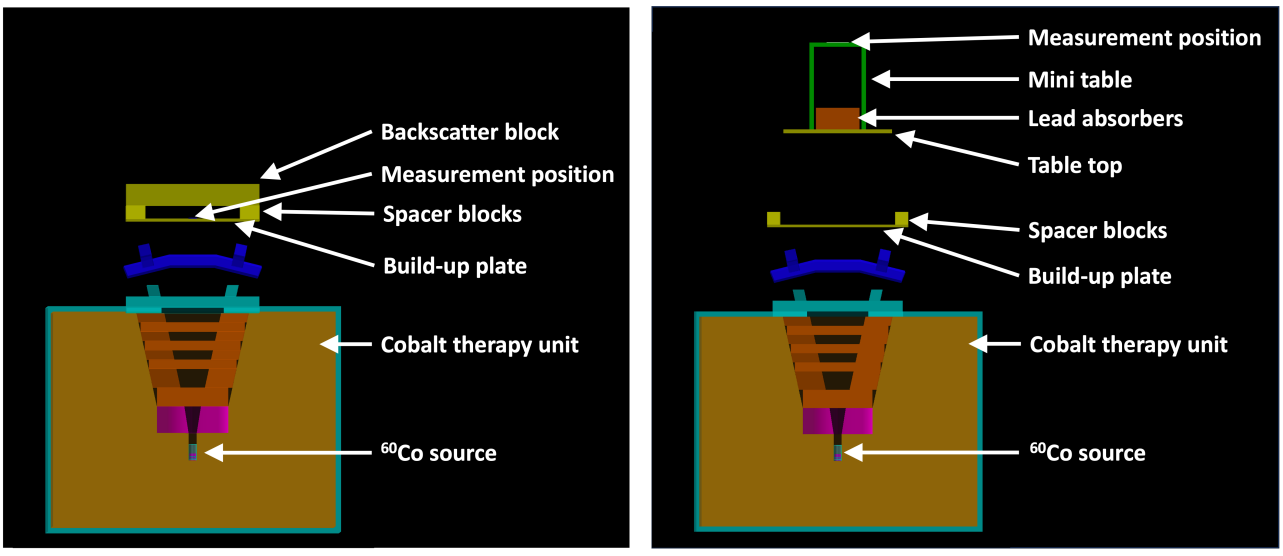

(a) **(b)**

Figure B.5: Model of the experimental setups (a) A and (b) B for the cobalt therapy unit at iThemba LABS, constructed in GEANT4 as described in Table B.2, and viewed from the $y - z$ plane.

B.1.5 Room

A simplified model of the room in which the cobalt therapy unit at iThemba LABS is housed (including the vault where the unit sits and the concrete passageway at the entrance) was also included in some of the simulations in order to investigate the effects of scattered photons from around this room. The floor plan of the room and the corresponding simulation in GEANT4 are shown in Figure B.6. The walls are concrete with dimensions as shown in Figure B.6(a). The roof of the vault consists of a 0.3 cm mild steel plate, with concrete bricks above the steel plate that are 30.0 cm thick. The ceiling of the entire room is made from 1.0 cm thick Rhinoboard beneath 15.0 cm thick concrete bricks. The concrete floor of the room is assumed to be 15.0 cm thick. The distance from the floor to the roof of the vault is 223.0 cm, and the distance from the floor to the Rhinoboard ceiling is 297.0 cm. The gantry is rotated such that the centre of the ^{60}Co source sits 75.0 cm from the ground and the beam is directed vertically upwards.

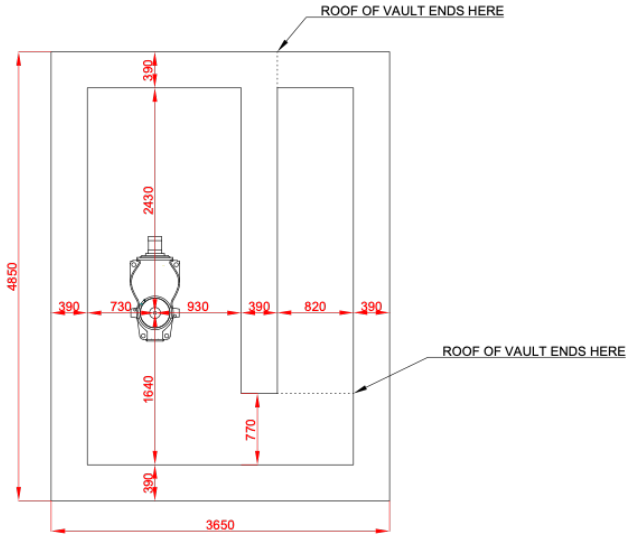

(a)

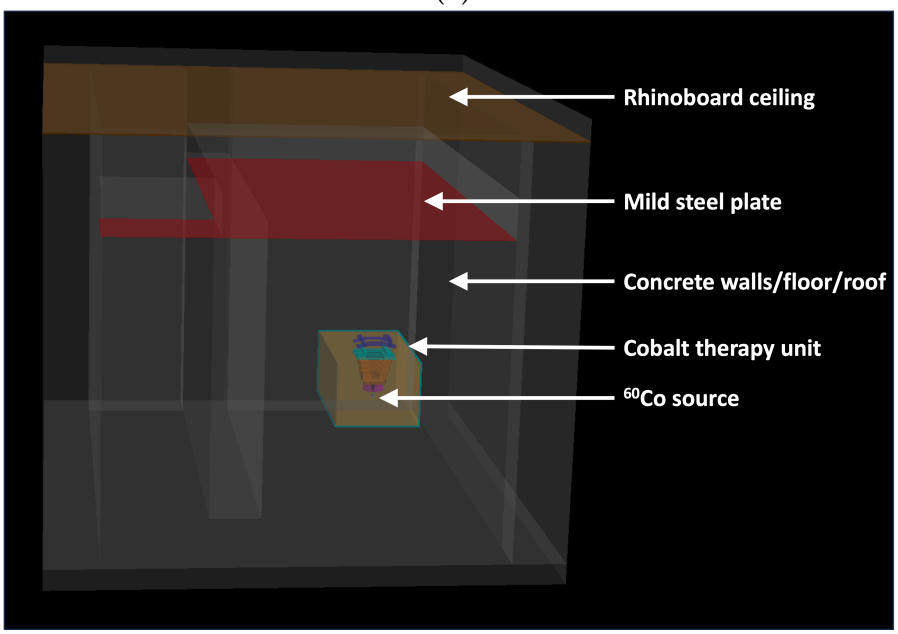

(b)

Figure B.6: The floor plan showing the dimensions (in mm) of the room in which the cobalt therapy unit at iThemba LABS is housed, and (b) the simplified model of this unit and room that was constructed in GEANT4.

B.2 Estimating the activity of the ^{60}Co source at iThemba LABS

An estimate of the activity of the ^{60}Co source in the cobalt therapy unit at iThemba LABS is required in order to estimate the corresponding dose rate to human blood under different experimental conditions based on the simulations in GEANT4.

In January 2024, the dose output to water from this unit for Setup A was measured by an IBA FC65-G Farmer type ionization chamber to be 233.3 ± 21.7 mGy/min. In order to estimate the corresponding activity of the ^{60}Co source, GEANT4 was used to roughly simulate the experimental conditions, by including in the simulation of Setup A (without the room in which the unit is housed) a cylindrical volume of water with a radius of 0.95 cm and a height of 0.23 cm (corresponding to the dimensions of the sensitive volume of the ionization chamber) at the reference measurement position. By running the simulation for 2×10^9 simulated ^{60}Co decays, the absorbed dose per decay in the water volume was found to be

$$(2.889 \pm 0.041) \times 10^{-16}\,\text{Gy/decay},$$

where the uncertainty was calculated in a similar manner to that described in Section 5.3.4. By folding this result with the measured dose rate of 233.3 ± 21.7 mGy/min, the corresponding source activity was estimated to be approximately

$$(1.35 \pm 0.13) \times 10^{13}\,\text{Bq}.$$

B.3 Investigating possible ways of reducing the dose rate from the cobalt therapy unit at iThemba LABS

As discussed in Section 6.5, one of the requirements for conducting neutron RBE measurements under 'head-to-head' conditions is that both the neutron and reference irradiations are carried out at similar dose rates. As shown in Table 5.6, the average dose rate to human blood was measured to be around 0.4 mGy/min for neutrons in the D-line at 0° for the experimental setup discussed in Chapter 5. The measured dose rate to water from the iThemba LABS cobalt therapy unit for Setup A corresponds to a dose rate in human blood of around 231 mGy/min (determined by replacing the sensitive volume of water described in Section B.2 with an equivalent volume of human blood and folding the resulting simulation result for the dose per ^{60}Co decay with the estimated activity of the source). This section presents an assessment of the feasibility of reducing the dose rate from the cobalt therapy unit to match that measured for neutrons in the D-line. There are three possible ways of altering the experimental setup to reduce the dose rate from the cobalt therapy unit at iThemba LABS:

Option 1: Reduce the field size by adjusting the collimator system

The cobalt therapy unit at iThemba LABS has an adjustable collimation system that can be moved to obtain field sizes that range between 5 cm × 5 cm and 35 cm × 35 cm at a SSD of 80 cm. For Setup A (that corresponds to a dose rate of 231 mGy/min in human blood), the jaws of the collimator system were set to obtain the maximum field size of 35 cm × 35 cm (SSD = 80 cm). By rerunning the simulation for the minimum field size of 5 cm × 5 cm (SSD = 80 cm) and again folding the result for the dose to the blood volume per simulated ^{60}Co decay with the estimated activity of the source (as determined in Section B.2), it was found that changing to the minimum field size decreased the dose rate to around 106 mGy/min, which is still 265 times greater than desired for 'head-to-head' measurements.

Option 2: Increase the distance to the irradiated biological samples

Assuming that the dose rate from the cobalt therapy unit roughly follows an inverse square law, a back-of-the-envelope calculation shows that if the dose rate at a distance of d_1 is R_1, then at a different distance d_2, the dose rate is given by

$$R_2 = R_1 \left(\frac{d_1}{d_2}\right)^2. \tag{B.1}$$

Based on this rough calculation, the minimum distance from the source that would be required to achieve the desired dose rate of 0.4 mGy/min for field sizes of 5 cm × 5 cm and 35 cm × 35 cm (at SSD = 80 cm) is estimated to be around 8.2 m and 12.0 m respectively.

Option 3: Place lead absorbers between the ^{60}Co source and the irradiated biological samples

The above discussion makes it clear that in order to achieve the required dose rate a sensible distance to the source, it will be necessary to place a lead attenuator between the source and the irradiated samples. GEANT4 simulations were conducted to investigate the thickness of lead that would be required to achieve the desired dose rate, by including a lead block with $x - y$ dimensions of 10 cm × 10 cm with variable thickness in the z-direction in Setup A as shown in Figure B.7. The absorbed dose in the blood volume on top of the lead block per simulated ^{60}Co decay was determined and multiplied by the activity of the source (as estimated in Section B.2) to determine the dose rate in the blood volume as a function of lead absorber thickness. The results shown in Figure B.8 indicate that lead absorbers with a thickness of between 8 cm and 9 cm would be required for the minimum field size of 5 cm × 5 cm at an SSD of 80 cm.

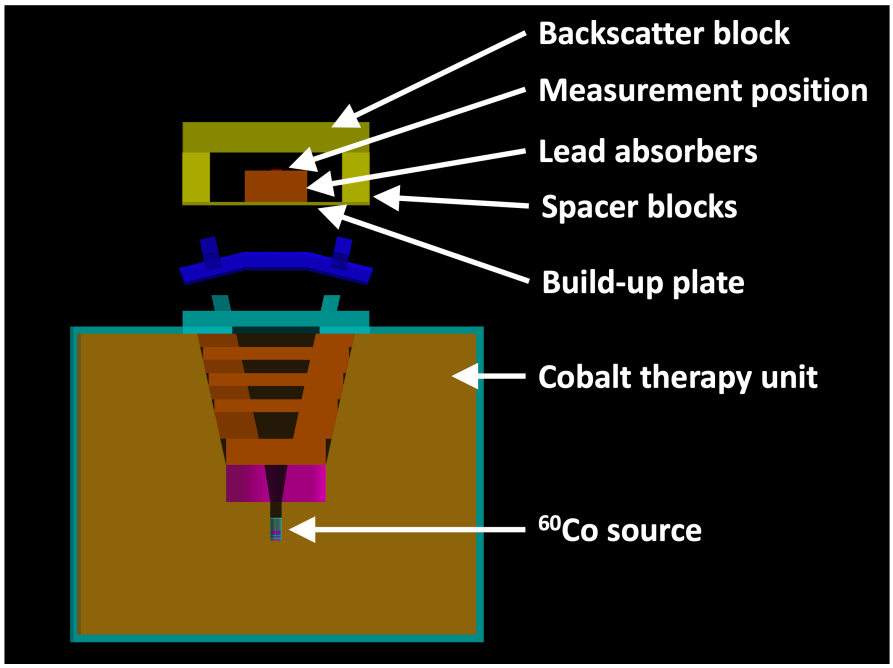

Figure B.7: Simulation setup in GEANT4, as viewed in the y-z plane for Setup A including a lead block of variable thickness, that was used to assess the thickness of lead required to achieve the desired dose rate to carry out reference irradiations under 'head-to-head' conditions.

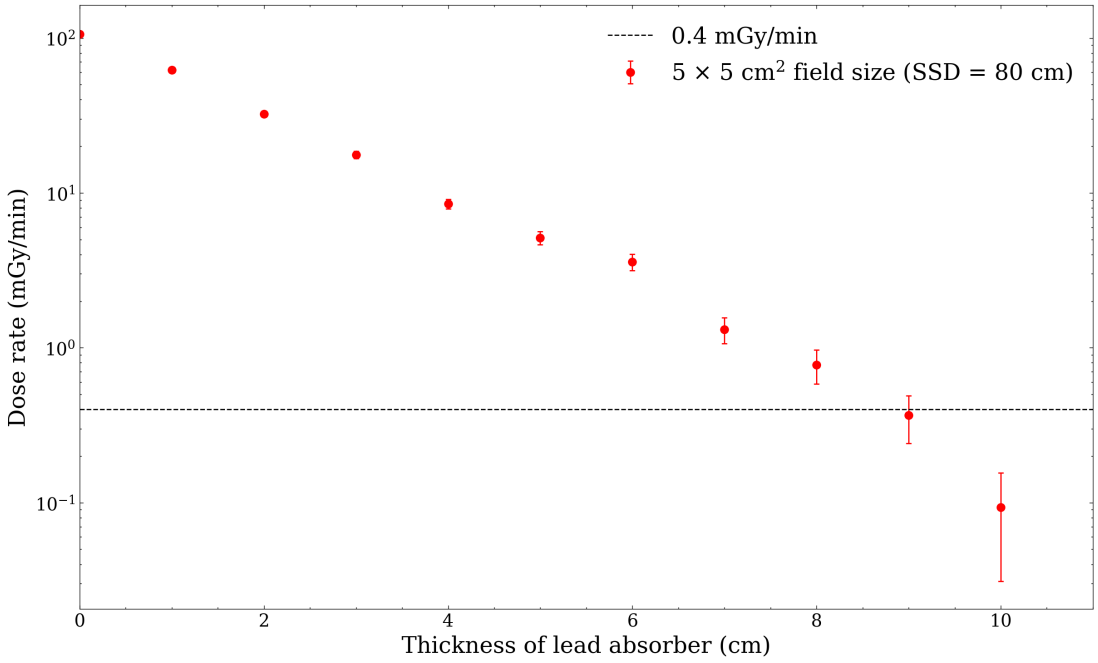

Figure B.8: GEANT4 simulation results for the dose rate to human blood for the experimental setup shown in Figure B.7 as a function of thickness of lead absorber for the minimum 5 cm × 5 cm field size. These results are compared to the approximate average measured dose rate of 0.4 mGy/min for neutrons in the D-line at 0° for the experimental setup discussed in Chapter 5.

B.4 Investigating the effects of changing the experimental setup on the ^{60}Co gamma ray energy spectrum

The discussion in Section B.3 shows that based on the GEANT4 simulations of the cobalt therapy unit at iThemba LABS, it is possible to reduce the dose rate from this unit by adjusting the collimation system to decrease the field size, increasing the distance to the irradiated biological samples, placing lead absorbers between the source and the biological samples, or a combination of all three. This section presents the results from simulations that were run to investigate the effects of changing the experimental setup on the spectrum of ^{60}Co gamma rays with which the biological samples are irradiated. Figure B.9 shows photon energy fluence spectra that were scored on a 5 cm × 5 cm plane at the reference measurement position for Setup A for the minimum and maximum field sizes of 5 cm × 5 cm and 35 cm × 35 cm, for which the fluence-weighted average energies $\langle E \rangle_\Phi$ vary between 1.072 MeV and 0.993 MeV respectively.

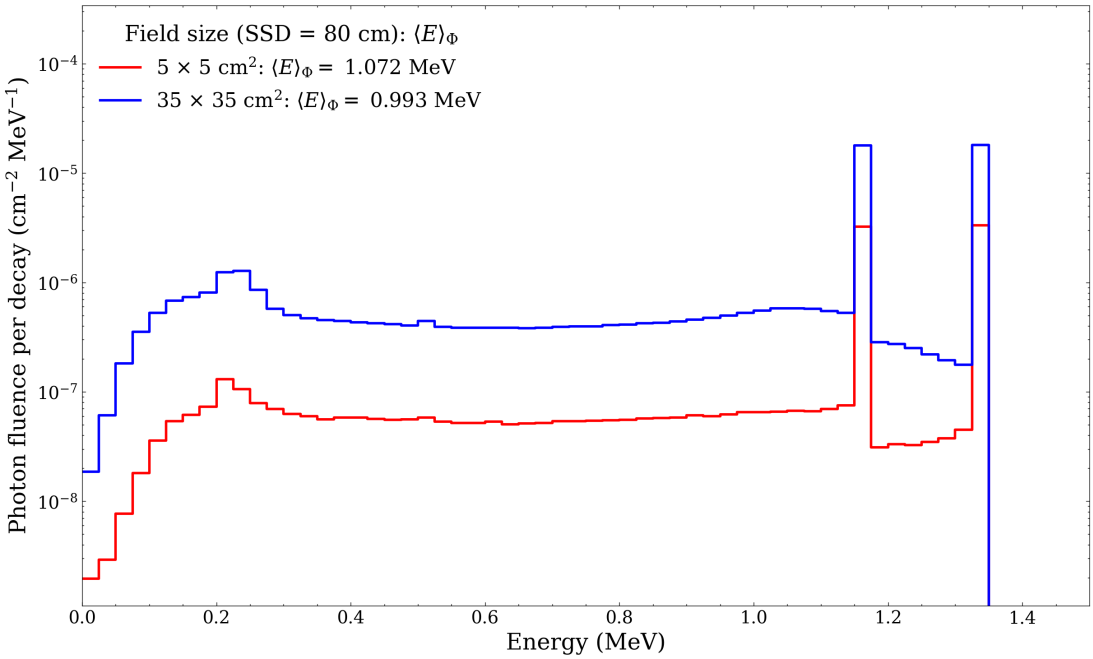

Figure B.9: Photon fluence spectra determined on a 5 × 5 cm plane at the measurement position for Setup A for the minimum and maximum field sizes that are possible with the cobalt therapy unit at iThemba LABS. The fluence-weighted average energy $\langle E \rangle_\Phi$ of each spectrum is indicated.

As discussed in Section B.3, the combined impact of reducing the field size and increasing the distance between the source and irradiated biological samples will not be sufficient to reduce the dose rate to match that from neutrons in the D-line. In order to achieve this, it will become necessary to place lead absorbers between the source and irradiated biological samples. Depending on the mass of lead that is required, the typical Setup A, for which the Perspex setup table rests on the head of the cobalt therapy unit, may not be able to safely support both the lead and irradiated samples. Setup B represents a practical option for both increasing the distance between source and irradiated biological samples, and safely supporting the lead absorbers over the cobalt therapy unit. Figure B.10 shows the simulation results for the photon fluence energy spectra that were determined on a 5 cm × 5 cm plane at the measurement position for this experimental setup for different field sizes. These results were obtained for simulations run both with and without including the room in which the unit is housed at iThemba LABS in order to investigate the contributions of photons that are scattered from around the room. The results show how changing this experimental setup and varying the lead absorber thickness affects the spectrum of ^{60}Co gamma rays with which biological

samples are irradiated. Particularly for larger field sizes, adding lead absorbers could result in a significant contribution to the dose from photons that are scattered from around the room. It should be noted that the models constructed in GEANT4 are simplified versions of the actual experimental setup, and in reality, the scattering of photons from around the room could have a more significant influence on the shape of the ^{60}Co spectrum. The implications of such effects for reference radiation measurements for neutron RBE studies are discussed in Section 6.5.

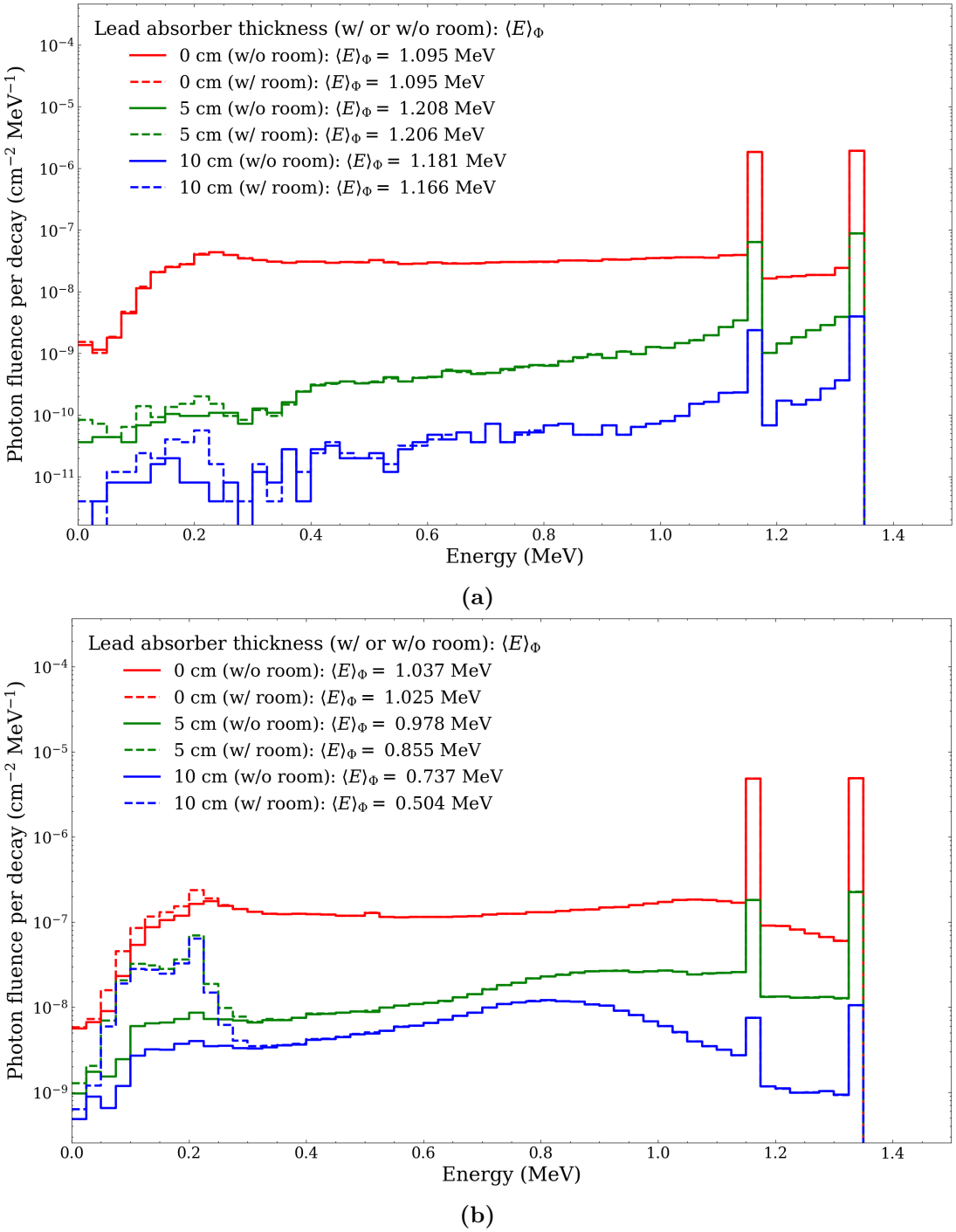

Figure B.10: Photon fluence spectra determined on a 5 cm × 5 cm plane at the measurement position for Setup B for different thicknesses of lead absorbers and field sizes of (a) 5 cm × 5 cm and (b) 35 cm × 35 cm at a SSD of 80 cm. The results are shown for simulations with and without the inclusion of the room in which the cobalt therapy unit at iThemba LABS is housed, and the fluence weighted mean energy $\langle E \rangle_\Phi$ of each spectrum is indicated.

Acronyms

ADC analogue-to-digital converter. 72–74, 84

BBND Bonner Ball Neutron Detector. 25

BER base excision repair. 37

CAD computer-aided design. 144, 146

CFD constant fraction discriminator. 72–74, 84

CI confidence interval. 52

CMEs coronal mass ejections. 11, 13

CSDA continuous slowing down approximation. 113

D-line iThemba LABS fast neutron facility. 64, 65, 67–70, 93, 94, 97, 111–115, 119, 122, 129, 131, 132, 135–137, 144, 151–153

DA delay amplifier. 72–74, 84

DDREF dose and dose-rate effectiveness factor. 56, 57

DLA delay line amplifier. 72

DNA deoxyribonucleic acid. 37, 38, 42, 43, 45, 46, 54, 56, 57, 59, 118, 119, 122, 136

DSBs double-strand breaks. 37, 45, 46, 56, 57, 59, 118, 136

FBS foetal bovine serum. 101, 119

FC fission ionisation chamber. 64, 82–95, 97, 99–101, 111, 112, 125, 128, 135

FISH Fluorescence In-Situ Hybridization. 61

FWHM full width at half maximum. 76, 88, 89

GCR galactic cosmic radiation. 9–14, 17–24, 27–29, 33, 34, 134

GSI GSI Helmholtz Centre for Heavy Ion Research. 22, 23, 122

HEND High Energy Neutron Detector. 31, 32

HR homologous recombination. 37

IA integrating amplifier. 84

IAEA International Atomic Energy Agency. 94, 95, 112

ICRP International Commission on Radiological Protection. 7, 9, 21, 34, 35, 40, 43–47, 55, 58, 103, 126, 127, 129, 134, 136, 137

ICRU International Commission on Radiation Units and Measurements. 18, 21, 29

IRMM Institute for Reference Materials and Measurements. 82, 95

ISS International Space Station. 10, 16, 17, 23–26, 40

iThemba LABS iThemba Laboratories for Accelerator Based Sciences. 8, 48, 63–66, 70, 79, 82, 83, 86, 91, 95, 97, 111–114, 118, 119, 122, 129, 131–138, 144, 146–151, 153, 154

LANSCE Los Alamos Nuclear Science Centre. 47, 48

LED light-emitting diode. 67, 70

LEO Lower Earth Orbit. 6, 9, 16, 23, 24, 34, 40, 51

LET linear energy transfer. 42, 43, 45, 46, 53–56, 131

LND Lunar Lander Neutron and Dosimetry. 26, 27

LP Lunar Prospector. 27, 28

MeASURe Metrological and Applied Sciences University Research Unit. 112, 117

mFISH multicolour fluorescence in-situ hybridization. 61, 62

MPA multiparameter data acquisition system. 71, 83

MSL Mars Science Laboratory. 21, 22, 30

NASA National Aeronautics and Space Administration. 6, 40, 41

NCRP National Council on Radiation Protection and Measurements. 47

NHEJ non-homologous end-joining. 37

NIST National Institute of Standards and Technology. 93, 103, 144

PA pre-amplifier. 72, 73, 84

PBMCs peripheral blood mononuclear cells. 101, 119, 123, 126

PMMA polymethyl methacrylate. 115

PSD pulse shape discrimination. 70–72, 77, 113

RAD Radiation Assessment Detector. 6, 21, 22, 26, 30–32

RBE Relative Biological Effectiveness. 7–9, 37, 40, 43–51, 53–59, 61–63, 111–115, 118, 126–129, 131, 132, 134–137, 144, 151, 154

RBE_M maximum Relative Biological Effectiveness. 8, 43, 44, 47–49, 55, 63, 97, 118, 122, 123, 131, 133–137

RF radio frequency. 74, 99

RPMI Roswell Park Memorial Institute. 101, 119

SEPs solar energetic particles. 9, 11–14, 23, 27, 34, 134

SPEs solar particle events. 11, 13, 34

SSBs single-strand breaks. 37

SSC Separated Sector Cyclotron. 64, 65, 74, 81, 84, 99, 129, 137

SSD source-surface distance. 133, 145, 147, 148, 151, 154

STS Space Shuttle. 16, 17, 24

TAC time-to-amplitude converter. 73–75, 84, 89, 111

TFA differentiating timing filter. 84

TOF Time-Of-Flight. 8, 64–66, 68, 69, 71, 74, 76–80, 83–85, 88–90, 99, 108, 111, 129, 135

TSCA timing single channel analyser. 84

U.S. NRC United States Nuclear Regulatory Commission. 7, 21, 44–46, 58

UCT University of Cape Town. 112, 117

References

Ainsbury, E., Barquinero, J., Beinke, C., Blakely, W., Braselmann, H., Carr, Z., Di Giorgio, M., Fenech, M., Garcia, L. O., Kodama, Y., et al. (2011). Cytogenetic dosimetry: Applications in preparedness for and response to radiation emergencies.

Apostolakis, J., Asai, M., Bogdanov, A., Burkhardt, H., Cosmo, G., Elles, S., Folger, G., Grichine, V., Gumplinger, P., Heikkinen, A., et al. (2009). Geometry and physics of the Geant4 toolkit for high and medium energy applications. *Radiation Physics and Chemistry*, 78(10):859–873.

Arena, C., De Micco, V., Macaeva, E., and Quintens, R. (2014). Space radiation effects on plant and mammalian cells. *Acta Astronautica*, 104(1):419–431.

Armstrong, T. and Colborn, B. (2001). Predictions of secondary neutrons and their importance to radiation effects inside the International Space Station. *Radiation Measurements*, 33(3):229–234.

Badhwar, G. D. (1997). The radiation environment in Low-Earth Orbit. *Radiation Research*, 148(5s):S3–S10.

Badhwar, G. D., Keith, J. E., and Cleghorn, T. F. (2001). Neutron measurements onboard the Space Shuttle. *Radiation Measurements*, 33(3):235–241.

Baiocco, G., Barbieri, S., Babini, G., Morini, J., Alloni, D., Friedland, W., Kundrát, P., Schmitt, E., Puchalska, M., Sihver, L., et al. (2016). The origin of neutron biological effectiveness as a function of energy. *Scientific Reports*, 6(1):34033.

Baiocco, G., Barbieri, S., Babini, G., Morini, J., Friedland, W., Kundrát, P., Schmitt, E., Puchalska, M., Giesen, U., Nolte, R., et al. (2018). At the physics-biology interface: The neutron affair. *Radiation Protection Dosimetry*, 180(1-4):278–281.

Berger, M., Coursey, J., Zucker, M., and Chang, J. (2017). Stopping-Power & Range Tables for Electrons, Protons, and Helium Ions. *NIST Standard Reference Database 124*.

Berger, T., Matthiä, D., Burmeister, S., Zeitlin, C., Rios, R., Stoffle, N., Schwadron, N. A., Spence, H. E., Hassler, D. M., Ehresmann, B., et al. (2020). Long term variations of galactic cosmic radiation on board the International Space Station, on the Moon and on the surface of Mars. *Journal of Space Weather and Space Climate*, 10:34.

Bizzarri, M. and Cucina, A. (2008). Biological effects of cosmic radiation during stratospheric flights. *Memorie della Societa Astronomica Italiana*, 79:812.

Boscolo, D., Scognamiglio, D., Horst, F., Weber, U., Schuy, C., Durante, M., La Tessa, C., Kozlova, E., Sokolov, A., Dinescu, I., et al. (2020). Characterization of the secondary neutron field produced in a thick aluminum shield by 1 GeV/u Fe-56 ions using TLD-based ambient dosimeters. *Frontiers in Physics*, 8:365.

Brenner, D. J. and Hall, E. J. (2008). Secondary neutrons in clinical proton radiotherapy: A charged issue. *Radiotherapy and Oncology*, 86(2):165–170.

Brooks, F. (1979). Development of organic scintillators. *Nuclear Instruments and Methods*, 162(1-3):477–505.

Buffler, A., Hutton, T., Jarvie, E., and Babut, R. (2024). A compact scintillator-based detector for high energy neutron spectrometry. *Radiation Physics and Chemistry*, 220:111698.

Buffler, A., Reitz, G., Röttger, S., Smit, F., and Wissmann, F. (2016). Irradiations at the high-energy neutron facility at iThemba LABS. *EURADOS Report*, 2:2016.

Carlson, A. D., Pronyaev, V. G., Capote, R., Hale, G. M., Chen, Z.-P., Duran, I., Hambsch, F.-J., Kunieda, S., Mannhart, W., Marcinkevicius, B., et al. (2018). Evaluation of the neutron data standards. *Nuclear Data Sheets*, 148:143–188.

Carlson, G. W. (1974). The effect of fragment anisotropy on fission-chamber efficiency. *Nuclear Instruments and Methods*, 119:97–100.

Carroll, B. W. and Ostlie, D. A. (2017). *An Introduction to Modern Astrophysics*. Cambridge University Press.

Chan, T. F., Golub, G. H., and LeVeque, R. J. (1983). Algorithms for computing the sample variance: Analysis and recommendations. *The American Statistician*, 37(3):242–247.

Chancellor, J. C., Scott, G. B., and Sutton, J. P. (2014). Space radiation: The number one risk to astronaut health beyond Low Earth Orbit. *Life*, 4(3):491–510.

Clement, C., Fujita, H., Harrison, J., Balonov, M., Bochud, F., Martin, C., Menzel, H., Ortiz-Lopez, P., Smith-Bindman, R., Simmonds, J., and Wakeford, R. (2021). Use of Dose Quantities in Radiological Protection: ICRP Publication 147. *Ann. ICRP*, 50:1–86.

Comrie, A., Buffler, A., Smit, F., and Wörtche, H. (2015). Digital neutron/gamma discrimination with an organic scintillator at energies between 1 MeV and 100 MeV. *Nuclear Instruments and Methods in Physics Research Section A: Accelerators, Spectrometers, Detectors and Associated Equipment*, 772:43–49.

ComTec (1974). Pulse Shape Discriminator. Model 2160 A Operating Manual. *Nuclear Instruments and Methods*, 116(1):55–59.

Crane, T. and Baker, M. (1991). Neutron detectors. *Passive Nondestructive Assay of Nuclear Materials*, 13:1–28.

Cucinotta, F. A. and Durante, M. (2013a). Evidence report: Risk of acute or late central nervous system effects from radiation exposure. *Human Health and Performance Risks of Space Exploration Missions*, pages 191–212.

Cucinotta, F. A. and Durante, M. (2013b). Evidence report: Risk of radiation carcinogenesis. *Human Health and Performance Risks of Space Exploration Missions*, pages 119–170.

De Saint-Hubert, M., Saldarriaga Vargas, C., Van Hoey, O., Schoonjans, W., De Smet, V., Mathot, G., Stichelbaut, F., Manessi, G., Dinar, N., Aza, E., et al. (2016). Secondary neutron doses in a proton therapy centre. *Radiation Protection Dosimetry*, 170(1-4):336–341.

Dietze, G., Bartlett, D., Cool, D., Cucinotta, F., and Jia, X. (2013). Assessment of Radiation Exposure of Astronauts in Space: ICRP Publication 123. *Ann. ICRP*, 42:1–339.

Dobynde, M., Shprits, Y., Drozdov, A., Hoffman, J., and Li, J. (2021). Beating 1 sievert: Optimal radiation shielding of astronauts on a mission to Mars. *Space Weather*, 19(9):e2021SW002749.

Dobynde, M. I. and Guo, J. (2021). Radiation environment at the surface and subsurface of the moon: Model development and validation. *Journal of Geophysical Research: Planets*, 126(11):e2021JE006930.

Ehresmann, B., Hassler, D., Zeitlin, C., Guo, J., Wimmer-Schweingruber, R., Khaksari, S., and Loeffler, S. (2021). Natural radiation shielding on Mars measured with the MSL/RAD instrument. *Journal of Geophysical Research: Planets*, 126(8):e2021JE006851.

Eljen Technology (2016). Neutron/Gamma PSD EJ-301, EJ-309. *Eljen Technology*.

Engelbrecht, M., Ndimba, R., De Kock, M., Miles, X., Nair, S., Fisher, R., Du Plessis, P., Bolcaen, J., Botha, M. H., Zwanepoel, E., et al. (2021). DNA damage response of haematopoietic stem and progenitor cells to high-LET neutron irradiation. *Scientific Reports*, 11(1):20854.

Ferrari, C., Manenti, G., and Malizia, A. (2023). Sievert or gray: Dose quantities and protection levels in emergency exposure. *Sensors*, 23(4):1918.

Fisher, R., Baselet, B., Vermeesen, R., Moreels, M., Baatout, S., Rahiman, F., Miles, X., Nair, S., du Plessis, P., Engelbrecht, M., et al. (2020). Immunological changes during space travel: A ground-based evaluation of the impact of neutron dose rate on plasma cytokine levels in human whole blood cultures. *Frontiers in Physics*, 8:568124.

Fogtman, A., Baatout, S., Baselet, B., Berger, T., Hellweg, C. E., Jiggens, P., La Tessa, C., Narici, L., Nieminen, P., Sabatier, L., et al. (2023). Towards sustainable human space exploration—priorities for radiation research to quantify and mitigate radiation risks. *npj Microgravity*, 9(1):8.

Gasparini, P., Sozzi, G., and Pierotti, M. A. (2007). The role of chromosomal alterations in human cancer development. *Journal of Cellular Biochemistry*, 102(2):320–331.

Gayther, D. (1990). International intercomparison of fast neutron fluence-rate measurements using fission chamber transfer instruments. *Metrologia*, 27(4):221.

Geant4 Collaboration (2020). Geant4 Reference Physics Lists.

Geant4 Collaboration (2023a). Geant4 Material Database.

Geant4 Collaboration (2023b). The Geant4 Binary Cascade Model.

Gersey, B., Sodolak, J., Hada, M., Saganti, P., Wilkins, R., Cucinotta, F., and Wu, H. (2007). Micronuclei induction in human fibroblasts exposed in vitro to Los Alamos high-energy neutrons. *Advances in Space Research*, 40(11):1754–1757.

Goldhagen, P., Clem, J., and Wilson, J. (2004). The energy spectrum of cosmic-ray induced neutrons measured on an airplane over a wide range of altitude and latitude. *Radiation Protection Dosimetry*, 110(1-4):387–392.

Goodhead, D. T. (2019). Neutrons are forever! Historical perspectives. *International Journal of Radiation Biology*, 95(7):957–984.

Grieder, P. K. (2001). *Cosmic Rays at Earth*. Elsevier.

Guo, J., Lillis, R., Wimmer-Schweingruber, R. F., Zeitlin, C., Simonson, P., Rahmati, A., Posner, A., Papaioannou, A., Lundt, N., Lee, C. O., et al. (2018). Measurements of Forbush decreases at Mars: Both by MSL on ground and by MAVEN in orbit. *Astronomy & Astrophysics*, 611:A79.

Guo, J., Zeitlin, C., Wimmer-Schweingruber, R., Hassler, D. M., Köhler, J., Ehresmann, B., Böttcher, S., Böhm, E., and Brinza, D. E. (2017). Measurements of the neutral particle spectra on Mars by MSL/RAD from 2015-11-15 to 2016-01-15. *Life Sciences in Space Research*, 14:12–17.

Guo, J., Zeitlin, C., Wimmer-Schweingruber, R. F., Hassler, D. M., Ehresmann, B., Rafkin, S., Freiherr von Forstner, J. L., Khaksarighiri, S., Liu, W., and Wang, Y. (2021). Radiation environment for future human exploration on the surface of Mars: The current understanding based on MSL/RAD dose measurements. *The Astronomy and Astrophysics Review*, 29:1–81.

Hada, M., Gersey, B., Saganti, P., Wilkins, R., Cucinotta, F., and Wu, H. (2010). mBAND analysis of chromosome aberrations in human epithelial cells induced by γ-rays and secondary neutrons of low dose rate. *Mutation Research/Genetic Toxicology and Environmental Mutagenesis*, 701(1):67–74.

Hälg, R. A. and Schneider, U. (2020). Neutron dose and its measurement in proton therapy - current state of knowledge. *The British Journal of Radiology*, 93(1107):20190412.

Hall, E. J. and Giaccia, A. (2019). Radiobiology for the radiologist 8th ed.

Heilbronn, L. H., Borak, T. B., Townsend, L. W., Tsai, P.-E., Burnham, C. A., and McBeth, R. A. (2015). Neutron yields and effective doses produced by Galactic Cosmic Ray interactions in shielded environments in space. *Life Sciences in Space Research*, 7:90–99.

Heimers, A. (1999). Cytogenetic analysis in human lymphocytes after exposure to simulated cosmic radiation which reflects the inflight radiation environment. *International Journal of Radiation Biology*, 75(6):691–698.

Herate, C. and Sabatier, L. (2020). Retrospective biodosimetry techniques: Focus on cytogenetics assays for individuals exposed to ionizing radiation. *Mutation Research/Reviews in Mutation Research*, 783:108287.

Horst, F., Boscolo, D., Cartechini, G., Durante, M., Hartel, C., Kozlova, E., La Tessa, C., Missiaggia, M., Pierobon, E., Radon, T., et al. (2022a). A multi-detector experimental setup for the study of space radiation shielding materials: Measurement of secondary radiation behind thick shielding and assessment of its radiobiological effect. In *EPJ Web of Conferences*, volume 261, page 03002. EDP Sciences.

Horst, F., Boscolo, D., Durante, M., Luoni, F., Schuy, C., and Weber, U. (2022b). Thick shielding against galactic cosmic radiation: A Monte Carlo study with focus on the role of secondary neutrons. *Life Sciences in Space Research*, 33:58–68.

Huff, J. and Cucinotta, F. A. (2013). Risk of degenerative tissue or other health effects from radiation exposure. *Human Health and Performance Risks of Space Exploration Missions*, pages 213–235.

Joiner, M. C. and van der Kogel, A. J. (2019). *Basic Clinical Radiobiology*. Taylor Francis Group.

Juerß, D., Zwar, M., Giesen, U., Nolte, R., Kriesen, S., Baiocco, G., Puchalska, M., van Goethem, M.-J., Manda, K., and Hildebrandt, G. (2017). Comparative study of the effects of different radiation qualities on normal human breast cells. *Radiation Oncology*, 12:1–10.

Keith, J. E., Badhwar, G. D., and Lindstrom, D. J. (1992). Neutron spectrum and dose-equivalent in shuttle flights during solar maximum. *International Journal of Radiation Applications and Instrumentation. Part D. Nuclear Tracks and Radiation Measurements*, 20(1):41–47.

Kim, M.-H., Atwell, W., Tylka, A. J., Dietrich, W. F., and Cucinotta, F. A. (2010). Radiation dose assessments of solar particle events with spectral representation at high energies for the improvement of radiation protection. In *38th COSPAR Scientific Assembly Conference*, number JSC-CN-20952.

Knoll, G. F. (2010). *Radiation Detection and Measurement*. John Wiley & Sons.

Köhler, J., Ehresmann, B., Zeitlin, C., Wimmer-Schweingruber, R., Hassler, D., Reitz, G., Brinza, D., Appel, J., Böttcher, S., Böhm, E., et al. (2015). Measurements of the neutron spectrum in transit to Mars on the Mars Science Laboratory. *Life Sciences in Space Research*, 5:6–12.

Köhler, J., Zeitlin, C., Ehresmann, B., Wimmer-Schweingruber, R. F., Hassler, D. M., Reitz, G., Brinza, D., Weigle, G., Appel, J., Böttcher, S., et al. (2014). Measurements of the neutron spectrum on the Martian surface with MSL/RAD. *Journal of Geophysical Research: Planets*, 119(3):594–603.

Koshiishi, H., Matsumoto, H., Chishiki, A., Goka, T., and Omodaka, T. (2007). Evaluation of the neutron radiation environment inside the International Space Station based on the Bonner Ball Neutron Detector experiment. *Radiation Measurements*, 42(9):1510–1520.

Kuhne, W. W., Gersey, B. B., Wilkins, R., Wu, H., Wender, S. A., George, V., and Dynan, W. S. (2009). Biological effects of high-energy neutrons measured in vivo using a vertebrate model. *Radiation Research*, 172(4):473–480.

Kulesza, J. A., Adams, T. R., Armstrong, J. C., Bolding, S. R., Brown, F. B., Bull, J. S., Burke, T. P., Clark, A. R., Forster III, R. A. A., Giron, J. F., et al. (2022). MCNP® code version 6.3.0 theory & user manual. Technical report, Los Alamos National Lab.(LANL), Los Alamos, NM (United States).

Lerendegui-Marco, J., Lo Meo, S., Guerrero, C., Cortés-Giraldo, M., Massimi, C., Quesada, J., Barbagallo, M., Colonna, N., Mancusi, D., Mingrone, F., et al. (2016). Geant4 simulation of the n_TOF-EAR2 neutron beam: Characteristics and prospects. *The European Physical Journal A*, 52:1–10.

Li, X., Jiao, T., Li, W., Zheng, Q., Ni, N., Zhao, S., Zhao, S., Cheng, F., Yang, L., Yu, H., et al. (2023). Spectrum measurement of secondary neutron induced by ^{9}Be(p, n) reaction in Low-Earth Orbit. *Nuclear Instruments and Methods in Physics Research Section A: Accelerators, Spectrometers, Detectors and Associated Equipment*, 1047:167783.

Litvak, M., Mitrofanov, I., Golovin, D., Pekov, A., Mokrousov, M., Sanin, A., Tretyakov, V., Dachev, T. P., and Semkova, Y. (2022). Long-period variations of the neutron component of the radiation background in the area of the International Space Station according to the data of the BTN-Neutron space experiment. *Cosmic Research*, 60(3):174–184.

Lund, C. M., Famulari, G., Montgomery, L., and Kildea, J. (2020). A microdosimetric analysis of the interactions of mono-energetic neutrons with human tissue. *Physica Medica*, 73:29–42.

Martinez Sierra, L., Jun, I., Ehresmann, B., Zeitlin, C., Guo, J., Litvak, M., Harshman, K., Hassler, D., Mitrofanov, I., Matthiä, D., et al. (2023). Unfolding the neutron flux spectrum on the surface of Mars using the MSL-RAD and Odyssey-HEND data. *Space Weather*, 21(8):e2022SW003344.

Matthiä, D., Burmeister, S., Przybyla, B., and Berger, T. (2023). Active radiation measurements over one solar cycle with two DOSTEL instruments in the Columbus laboratory of the International Space Station. *Life Sciences in Space Research*, 39:14–25.

Matthiä, D., Ehresmann, B., Lohf, H., Köhler, J., Zeitlin, C., Appel, J., Sato, T., Slaba, T., Martin, C., Berger, T., et al. (2016). The Martian surface radiation environment - a comparison of models and MSL/RAD measurements. *Journal of Space Weather and Space Climate*, 6:A13.

Matthiä, D., Hassler, D. M., de Wet, W., Ehresmann, B., Firan, A., Flores-McLaughlin, J., Guo, J., Heilbronn, L. H., Lee, K., Ratliff, H., et al. (2017). The radiation environment on the surface of Mars-Summary of model calculations and comparison to RAD data. *Life Sciences in Space Research*, 14:18–28.

Maurice, S., Feldman, W., Lawrence, D., Elphic, R., Gasnault, O., d'Uston, C., Genetay, I., and Lucey, P. (2000). High-energy neutrons from the Moon. *Journal of Geophysical Research: Planets*, 105(E8):20365–20375.

Miller, J., Taylor, L., Zeitlin, C., Heilbronn, L., Guetersloh, S., DiGiuseppe, M., Iwata, Y., and Murakami, T. (2009). Lunar soil as shielding against space radiation. *Radiation Measurements*, 44(2):163–167.

Miró, R., Soler, J., Gallardo, S., Campayo, J., Diez, S., and Verdu, G. (2005). MCNP simulation of a Theratron 780 radiotherapy unit. *Radiation Protection Dosimetry*, 116(1-4):65–68.

Mitaroff, A. and Silari, M. (2002). The CERN-EU high-energy reference field (CERF) facility for dosimetry at commercial flight altitudes and in space. *Radiation Protection Dosimetry*, 102(1):7–22.

Moldwin, M. (2022). *An Introduction to Space Weather*. Cambridge University Press.

Mosconi, M., Musonza, E., Buffler, A., Nolte, R., Röttger, S., and Smit, F. (2010). Characterisation of the high-energy neutron beam at iThemba LABS. *Radiation Measurements*, 45(10):1342–1345.

Musonza, E. T. (2011). Measurement of fluence at the D-line fast neutron facility at iThemba LABS.

Nair, S., Cairncross, S., Miles, X., Engelbrecht, M., du Plessis, P., Bolcaen, J., Fisher, R., Ndimba, R., Cunningham, C., Martínez-López, W., et al. (2021). An automated microscopic scoring method for the γ-H2AX foci assay in human peripheral blood lymphocytes. *JoVE (Journal of Visualized Experiments)*, (178):e62623.

Nair, S., Engelbrecht, M., Miles, X., Ndimba, R., Fisher, R., du Plessis, P., Bolcaen, J., Nieto-Camero, J., de Kock, E., and Vandevoorde, C. (2019). The impact of dose rate on DNA double-strand break formation and repair in human lymphocytes exposed to fast neutron irradiation. *International Journal of Molecular Sciences*, 20(21):5350.

Naito, M., Kusano, H., and Kodaira, S. (2023). Global dose distributions of neutrons and gamma-rays on the Moon. *Scientific Reports*, 13(1):13275.

Ndlovu, N., Boso, A., Buffler, A., Geduld, D., Hutton, T., Lacoste, V., Leadbeater, T., Maleka, P., and Smit, F. (2019). Upgrade of the iThemba LABS neutron beam vault to a metrology facility. In *22nd International Conference on Cyclotrons and their Applications (CYC2019)*, page TUP012.

Niwa, O., Barcellos-Hoff, M., and Globus, R. (2015). Stem cell biology with respect to carcinogenesis aspects of radiological protection: ICRP Publication 131. *Ann. ICRP*, 44:7–357.

Nolte, R., Allie, M., Binns, P., Brooks, F., Buffler, A., Dangendorf, V., Meulders, J.-P., Roos, F., Schuhmacher, H., and Wiegel, B. (2002). High-energy neutron reference fields for the calibration of detectors used in neutron spectrometry. *Nuclear Instruments and Methods in Physics Research Section A: Accelerators, Spectrometers, Detectors and Associated Equipment*, 476(1-2):369–373.

Nolte, R., Allie, M., Brooks, F., Buffler, A., Dangendorf, V., Meulders, J.-P., Schuhmacher, H., Smit, F., and Weierganz, M. (2007). Cross sections for neutron-induced fission of ^{235}U, ^{238}U, ^{209}Bi, and $^{\text{nat}}$Pb in the energy range from 33 to 200 MeV measured relative to n-p scattering. *Nuclear Science and Engineering*, 156(2):197–210.

Nolte, R., Brede, H., Schrewe, U., and Schuhmacher, H. (1993). Neutron spectrometry with liquid scintillation detectors at neutron energies between 20 MeV and 70 MeV. A status report.

Nolte, R., Dangendorf, V., Buffler, A., Brooks, F., Slabbert, J., Smit, F., Haney, M., Schmid, E., and Stephan, G. (2006). Relative biological efficiency of 192 MeV neutron radiation for the induction of chromosome aberrations in human lymphocytes of the peripheral blood. *Proceedings of Science*.

Nolte, R., Dangendorf, V., Schmid, E., Slabbert, J., Smit, F., and Stephan, G. (2008). Low-dose RBE for the induction of dicentric chromosomes in human lymphocytes by quasi-monoenergetic 100 MeV and 200 MeV neutron radiation. *Unpublished notes*.

Nolte, R., Mühlbradt, K.-H., Meulders, J.-P., Stephan, G., Haney, M., and Schmid, E. (2005). RBE of quasi-monoenergetic 60 MeV neutron radiation for induction of dicentric chromosomes in human lymphocytes. *Radiation and Environmental Biophysics*, 44(3):201–209.

Norbury, J. W., Slaba, T. C., Aghara, S., Badavi, F. F., Blattnig, S. R., Clowdsley, M. S., Heilbronn, L. H., Lee, K., Maung, K. M., Mertens, C. J., et al. (2019). Advances in space radiation physics and transport at NASA. *Life Sciences in Space Research*, 22:98–124.

Noubissi, F. K., McBride, A. A., Leppert, H. G., Millet, L. J., Wang, X., and Davern, S. M. (2021). Detection and quantification of γ-H2AX using a dissociation enhanced lanthanide fluorescence immunoassay. *Scientific Reports*, 11(1):8945.

Ottolenghi, A., Baiocco, G., Smyth, V., and Trott, K. (2015). The ANDANTE project: a multidisciplinary approach to neutron RBE. *Radiation Protection Dosimetry*, 166(1-4):311–315.

Paganetti, H. (2018). *Proton Therapy Physics*. CRC press.

Papadopoulos, A., Kyriakou, I., Incerti, S., Santin, G., Nieminen, P., Daglis, I. A., Li, W., and Emfietzoglou, D. (2023). Space radiation quality factor for Galactic Cosmic Rays and typical space mission scenarios using a microdosimetric approach. *Radiation and Environmental Biophysics*, 62(2):221–234.

Pomp, S., Bartlett, D., Mayer, S., Reitz, G., Röttger, S., Silari, M., Smit, F., Vincke, H., and Yasuda, H. (2014). High-energy quasi-monoenergetic neutron fields: existing facilities and future needs. *Radiation Protection Dosimetry*, 161(1-4):62–66.

Prokofiev, A. and Olsson, N. (2001). Fission fragment detection efficiency of thin-film breakdown counters in sandwich geometry. *UU-NF015*.

Proteintech (2024). Cell cycle and checkpoint controls. *Proteintech*.

Restier-Verlet, J., El-Nachef, L., Ferlazzo, M. L., Al-Choboq, J., Granzotto, A., Bouchet, A., and Foray, N. (2021). Radiation on earth or in space: what does it change? *International Journal of Molecular Sciences*, 22(7):3739.

Röstel, L., Guo, J., Banjac, S., Wimmer-Schweingruber, R. F., and Heber, B. (2020). Subsurface radiation environment of Mars and its implication for shielding protection of future habitats. *Journal of Geophysical Research: Planets*, 125(3):e2019JE006246.

Rothkamm, K. and Löbrich, M. (2003). Evidence for a lack of DNA double-strand break repair in human cells exposed to very low x-ray doses. *Proceedings of the National Academy of Sciences*, 100(9):5057–5062.

Rühm, W., Azizova, T., Bouffler, S., Cullings, H. M., Grosche, B., Little, M. P., Shore, R. S., Walsh, L., and Woloschak, G. E. (2018). Typical doses and dose rates in studies pertinent to radiation risk inference at low doses and low dose rates. *Journal of Radiation Research*, 59(suppl_2):ii1–ii10.

Schmid, E., Regulla, D., Guldbakke, S., Schlegel, D., and Bauchinger, M. (2000). The effectiveness of monoenergetic neutrons at 565 keV in producing dicentric chromosomes in human lymphocytes at low doses. *Radiation Research*, 154(3):307–312.

Schmid, E., Regulla, D., Guldbakke, S., Schlegel, D., and Roos, M. (2002). Relative biological effectiveness of 144 keV neutrons in producing dicentric chromosomes in human lymphocytes compared with ^{60}Co gamma rays under head-to-head conditions. *Radiation Research*, 157(4):453–460.

Schmid, E., Schlegel, D., Guldbakke, S., Kapsch, R.-P., and Regulla, D. (2003). RBE of nearly monoenergetic neutrons at energies of 36 keV–14.6 MeV for induction of dicentrics in human lymphocytes. *Radiation and Environmental Biophysics*, 42:87–94.

Schneider, U. and Hälg, R. (2015). The impact of neutrons in clinical proton therapy. *Frontiers in Oncology*, 5:235.

Schneider, U. and Walsh, L. (2009). Cancer risk above 1 Gy and the impact for space radiation protection. *Advances in Space Research*, 44(2):202–209.

Shavers, M., Semones, E., Tomi, L., Chen, J., Straube, U., Komiyama, T., Shurshakov, V., Li, C., and Rühm, W. (2023). Space agency-specific standards for crew dose and risk assessment of ionising radiation exposures for the International Space Station. *Zeitschrift für Medizinische Physik*.

Sichani, B. T. and Sohrabpour, M. (2004). Monte Carlo dose calculations for radiotherapy machines: Theratron 780-C teletherapy case study. *Physics in Medicine & Biology*, 49(5):807.

Slaba, T. C., Bahadori, A. A., Reddell, B. D., Singleterry, R. C., Clowdsley, M. S., and Blattnig, S. R. (2017). Optimal shielding thickness for Galactic Cosmic Ray environments. *Life Sciences in Space Research*, 12:1–15.

Slaba, T. C., Blattnig, S. R., and Clowdsley, M. S. (2011). Variation in lunar neutron dose estimates. *Radiation Research*, 176(6):827–841.

Slabbert, J. P., August, L., Vral, A., and Symons, J. (2010). The relative biological effectiveness of a high energy neutron beam for micronuclei induction in T-lymphocytes of different individuals. *Radiation Measurements*, 45(10):1455–1457.

Slabbert, J. P., Theron, T., Zölzer, F., Streffer, C., and Böhm, L. (2000). A comparison of the potential therapeutic gain of p (66)/Be neutrons and d (14)/Be neutrons. *International Journal of Radiation Oncology* Biology* Physics*, 47(4):1059–1065.

Smith, M., Akatov, Y., Andrews, H., Arkhangelsky, V., Chernykh, I., Ing, H., Khoshooniy, N., Lewis, B., Machrafi, R., Nikolaev, I., et al. (2013). Measurements of the neutron dose and energy spectrum on the International Space Station during expeditions ISS-16 to ISS-21. *Radiation Protection Dosimetry*, 153(4):509–533.

Smith, M., Khulapko, S., Andrews, H., Arkhangelsky, V., Ing, H., Koslowksy, M., Lewis, B., Machrafi, R., Nikolaev, I., and Shurshakov, V. (2016). Bubble-detector measurements of neutron radiation in the international space station: ISS-34 to ISS-37. *Radiation Protection Dosimetry*, 168(2):154–166.

Stevens, D. L., Bradley, S., Goodhead, D. T., and Hill, M. A. (2014). The influence of dose rate on the induction of chromosome aberrations and gene mutation after exposure of plateau phase V79-4 cells with high-LET alpha particles. *Radiation Research*, 182(3):331–337.

Straube, U., Berger, T., Reitz, G., Facius, R., Fuglesang, C., Reiter, T., Damann, V., and Tognini, M. (2010). Operational radiation protection for astronauts and cosmonauts and correlated activities of ESA Medical Operations. *Acta Astronautica*, 66(7-8):963–973.

Stricklin, D. L., VanHorne-Sealy, J., Rios, C. I., Scott Carnell, L. A., and Taliaferro, L. P. (2021). Neutron radiobiology and dosimetry.

University of Waikaito (2011). DNA, chromosomes and gene expression. *Science Learning Hub*.

Valentin, J. (2003). Relative biological effectiveness (RBE), quality factor (Q), and radiation weighting factor (w_R): ICRP Publication 92. *Ann. ICRP*, 33:1–121.

Valentin, J. (2007). The 2007 Recommendations of the International Commission on Radiological Protection: ICRP Publication 103. *Ann ICRP*.

Vandersickel, V., Beukes, P., Van Bockstaele, B., Depuydt, J., Vral, A., and Slabbert, J. (2014). Induction and disappearance of γH2AX foci and formation of micronuclei after exposure of human lymphocytes to ^{60}Co γ-rays and p (66)+ Be (40) neutrons. *International Journal of Radiation Biology*, 90(2):149–158.

Von Rosenvinge, T. and Cane, H. V. (2006). Solar energetic particles: An overview. *Geophysical Monograph Series*, 165:103–114.

Vykydal, Z., Andrlík, M., Bártová, H., Králík, M., Šolc, J., and Vondráček, V. (2016). Measurement of secondary neutrons generated during proton therapy. *Radiation Protection Dosimetry*, 172(4):341–345.

Walker, S. A., Townsend, L. W., and Norbury, J. W. (2013). Heavy ion contributions to organ dose equivalent for the 1977 galactic cosmic ray spectrum. *Advances in Space Research*, 51(9):1792–1799.

Walsh, L., Schneider, U., Fogtman, A., Kausch, C., McKenna-Lawlor, S., Narici, L., Ngo-Anh, J., Reitz, G., Sabatier, L., Santin, G., et al. (2019). Research plans in Europe for radiation health hazard assessment in exploratory space missions. *Life Sciences in Space Research*, 21:73–82.

Wu, H., Huff, J. L., Casey, R., Kim, M.-H., and Cucinotta, F. A. (2013). Risk of acute radiation syndromes due to solar particle events. *Human Health and Performance Risks for Space Explorations*, pages 171–190.

Zeitlin, C., Castro, A., Beard, K., Abdelmelek, M., Hayes, B., Johnson, A., Stoffle, N., Rios, R., Leitgab, M., and Hassler, D. (2023). Results from the Radiation Assessment Detector on the International Space Station, Part 2: The fast neutron detector. *Life Sciences in Space Research*, 39:76–85.

Zeman, E. M., Schreiber, E. C., and Tepper, J. E. (2020). Basics of Radiation Therapy. In *Abeloff's Clinical Oncology*, pages 431–460. Elsevier.

Zhang, J., Guo, J., Dobynde, M. I., Wang, Y., and Wimmer-Schweingruber, R. F. (2022). From the top of Martian Olympus to deep craters and beneath: Mars radiation environment under different atmospheric and regolith depths. *Journal of Geophysical Research: Planets*, 127(3):1–19.

Zhang, S., Wimmer-Schweingruber, R. F., Yu, J., Wang, C., Fu, Q., Zou, Y., Sun, Y., Wang, C., Hou, D., Böttcher, S. I., et al. (2020). First measurements of the radiation dose on the lunar surface. *Science Advances*, 6(39):1–5.